UNIVERSITÀ DEGLI STUDI DI PADOVA

Sede Amministrativa: Università degli Studi di Padova

Dipartimento di Fisica e Astronomia “Galileo Galilei”

CORSO DI DOTTORATO DI RICERCA IN: FISICA
CICLO XXIX

The bispectrum of Large Scale Structures: modelling, prediction and estimation

Tesi redatta con il contributo finanziario della Fondazione Cassa di Risparmio di Padova e Rovigo (CARIPARO)

Coordinatore: Ch.mo Prof. Gianguido Dall'Agata
Supervisore: Ch.mo Dr. Michele Liguori

Dottorando : Dionysios Karagiannis

Abstract

In this thesis we study the higher-order statistics of Large Scale Structures (LSS). In particular, we examine the potential of the bispectrum (Fourier transform of the three-point correlator) of galaxies for both probing the non-linear regime of structure growth and setting constraints on primordial non-Gaussianity.

The starting step is to construct accurate models for the power spectrum (Fourier transform of the two-point correlator) and bispectrum of galaxies by using the predictions of perturbation methods. In addition, the recent developments on the relation between dark matter and galaxy distributions (*i.e.* bias) are discussed and incorporated into the modelling, in order to have an accurate theoretical formalism on the galaxy formation. In order to build models that are as realistic as possible, we take into account additional non-linear effects, such as redshift space distortions. The analysis is mainly restricted to the large and intermediate scales.

Furthermore, we investigate forecasted constraints on primordial non-Gaussianity and bias parameters from measurements of galaxy power spectrum and bispectrum in future radio continuum (EMU and SKA) and optical surveys (Euclid, DESI, LSST and SPHEREx). In the galaxy bispectrum modelling, we consider the bias expansion for non-Gaussian initial conditions up to second order, including trispectrum (Fourier transform of the four-point correlator) scale-dependant contributions, originating from the galaxy bias expansion, where for the first time we extend such correction to redshift space. We study the impact of uncertainties in the theoretical modelling of the bispectrum expansion

and of redshift space distortions (*theoretical errors*), showing that they can all affect the final predicted bounds.

We find that the bispectrum generally has a strong constraining power and can lead to improvements up to a factor ~ 5 over bounds based on the power spectrum alone. Our results show that constraints for local-type PNG can be significantly improved compared to current limits: future radio (*e.g.* SKA) and photometric surveys could obtain a measurement error on $f_{\rm NL}^{\rm loc}$, $\sigma(f_{\rm NL}^{\rm loc}) \approx 0.2 - 0.3$. More specifically, near future optical spectroscopic surveys, such as Euclid, will also improve over *Planck* by a factor of a few, while LSST will provide competitive constraints to radio continuum. In the case of equilateral PNG, galaxy bispectrum constraints are very weak, and current constraints could be tightened only if significant improvements in the redshift determinations of large volume surveys could be achieved. For orthogonal non-Gaussianity, expected constraints are comparable to the ones from *Planck*, *e.g.* $\sigma(f_{\rm NL}^{\rm orth}) \approx 18$ for radio surveys.

In the last part of the thesis we development a pipeline that measures the bispectrum from N-body simulations or galaxy surveys, which is based on the *modal estimation* formalism. This computationally demanding task is reduced from $\mathcal{O}(N^6)$ operations to $\mathcal{O}(N^3)$, where N is the number of modes per dimension inside the said simulation box or survey. The main idea of the modal estimator is to construct a suitable basis ("modes") on the domain defined by the triangle condition and decompose on it the desired theoretical or observational bispectrum. This allows for massive data compression, making it an extremely useful tool for future LSS surveys. We show the results of tests performed to improve the performance of the pipeline and the convergence of the modal expansion. In addition, we present the measured bispectrum from a set of simulations with Gaussian initial condition, where the small amount of modes needed to accurately reconstruct the matter bispectrum shows the power of the modal expansion. The effective $f_{\rm NL}$ value, corresponding to the bispectrum of the non-linear gravitational evolution, comes at no computational cost. In order to further test the pipeline, we proceed in measuring the

bispectrum of a few realisations with non-Gaussian initial conditions of the local type. We show that the modal decomposition can accurately separate the primordial signal, from the late-time non-Gaussianity, and put tight constraints on its amplitude.

Declaration

This document is the Ph.D. thesis of Dionysios Karagiannis.

No part of this thesis has previously been submitted for a degree at this or any other university.

Contents

1 Introduction **1**

2 The Standard Cosmological Model **7**

2.1 The Cosmological Principle 7

2.2 The expanding Universe 8

2.2.1 FLRW metric 8

2.2.2 Hubble flow and redshift 11

2.2.3 Cosmic distances 13

2.2.4 Cosmological horizons 15

2.3 Dynamics of the expansion 16

2.3.1 Friedmann equation 19

2.3.2 Continuity equation 21

2.4 The inflationary paradigm 23

2.4.1 Early accelerating expansion 25

2.4.2 Dynamics of Inflation 26

2.4.3 Primordial fluctuations from inflation 30

2.4.4 Primordial non-Gaussianity 35

3 Cosmological Perturbation Theory **43**

3.1 Introduction 43

3.2 Eulerian Perturbation Theory 44

3.2.1 Linear solution . . . 46
3.2.2 Non-linear solution . . . 50
3.3 Lagrangian Perturbation theory . . . 53
3.3.1 Linear Solution . . . 55
3.3.2 Second-order solution . . . 57
3.4 MPTbreeze . . . 58
3.5 Statistical description of the cosmic fields . . . 61
3.5.1 Random fields . . . 62
3.5.2 Two-point correlation function and power spectrum . . . 67
3.5.3 Three-point correlation function and bispectrum . . . 73
3.5.4 Tree-level trispectrum . . . 81

4 Structure formation and bias 85
4.1 Introduction . . . 85
4.2 Mass function . . . 86
4.3 Large-Scale halo bias . . . 89
4.3.1 Bias evolution . . . 92
4.3.2 General bias expansion . . . 96
4.3.3 Peak-background split . . . 100
4.4 Effects of primordial Non-Gaussianity . . . 103
4.4.1 Non-Gasusian mass function . . . 103
4.4.2 Non-Gaussian bias . . . 105

5 Fisher matrix predictions from LSS surveys 113
5.1 Introduction . . . 113
5.2 Galaxy statistics . . . 116
5.2.1 Real space . . . 118
5.2.2 Redshift space . . . 130

5.3 Fisher information matrix formalism . . . 136
5.4 Theoretical Errors . . . 145
5.5 Galaxy Surveys . . . 149
5.5.1 Future radio surveys . . . 149
5.5.2 Future optical surveys . . . 153
5.6 Summary of the analysis method . . . 161
5.7 Results . . . 163
5.7.1 Radio continuum surveys forecasts . . . 164
5.7.2 Optical surveys forecasts . . . 182
5.8 Conclusions . . . 194

6 The modal estimator **199**
6.1 Introduction . . . 199
6.2 Statitical estimator . . . 201
6.3 Modal estimation formalism . . . 204
6.3.1 The modal estimator . . . 205
6.3.2 Modal decomposition . . . 209
6.3.3 Testing the pipeline and the modal expansion . . . 215
6.4 Measuring the bispectrum from N-body simulations . . . 221
6.4.1 Modal decomposed bispectrum and PNG measurements . . . 223

7 Conclusion **233**

Bibliography **237**

List of Figures

2.1 The inflationary potential. 29

3.1 The linear growth factor. 47

3.2 The logarithmic growth rate. 49

3.3 The smoothed variance. 68

3.4 Triangle configurations. 75

3.5 The reduced bispectrum. 76

4.1 Halo bias parameters as a function of mass. 103

4.2 Third one-point cumulant. 104

5.1 The shape of the galaxy bispectrum for Gaussian initial conditions 122

5.2 The shape of the non-Gaussian part of the galaxy bispectrum for local PNG. 126

5.3 The shape of the non-Gaussian part of the galaxy bispectrum for equilateral PNG. 127

5.4 The shape of the non-Gaussian part of the galaxy bispectrum for orthogonal PNG. 128

5.5 Galaxy bias used in the predictions for SKA and EMU like surveys. 152

5.6 True redshift distribution for LSST 158

5.7 The linear and quadratic bias terms for the optical surveys considered. . . 160

5.8 The effect of theoretical errors. 165

5.9 The ratio of the 1σ forecasts between including and excluding the theoretical errors in the Fisher matrix. 167

5.10 The effect of redshift space distortions in forecasts. 170
5.11 FOG and redshift error dumping factor. 174
5.12 Forecast on the three PNG shapes, including trispectrum corrections in the monopole approximation, from the two radio continuum surveys. 177
5.13 Forecast on the three PNG shapes, including trispectrum corrections in the RSD bispectrum, from the two radio continuum surveys. 180
5.14 Forecast on the three PNG shapes, assuming the monopole approximation model, from the Euclid and DESI surveys. 184
5.15 Forecast on the three PNG shapes, assuming the monopole approximation model, from the LSST and SPHEREx surveys. 185
5.16 Contour plot for the degeneracies between $f_{\rm NL}$ and bias parameters, after the inclusion of the trispectrum term, in the case of the two small volume optical surveys. 186
5.17 Forecast on the three PNG shapes, using the full redshift space treatment and including the trispectrum term, from the Euclid and DESI surveys. . . 191
5.18 Forecast on the three PNG shapes, using the full redshift space treatment and including the trispectrum term, from the LSST and SPHEREx surveys. 192
6.1 The tetrahedral domain. 207
6.2 The modal polynomials. 211
6.3 The shape correlator of a few bispectra. 217
6.4 Tests on the stabilization of the modal decomposition. 220
6.5 Modal decomposition coefficients. 227
6.6 Decomposed modal bispectrum. 228
6.7 Modal decomposition coefficients for the tree-level and 1-loop bispectrum. . 230
6.8 Modal decomposition coefficients for a simulation with local non-Gaussian initial conditions. 231

List of Tables

2.1 Density and scale factor evolution for all the components of the Universe. . 22

5.1 Details of the radio continuum surveys. 151

5.2 Basic specifications for Euclid survey. 154

5.3 Basic specifications for DESI. 156

5.4 Basic specifications for a LSST like survey. 159

5.5 Constraints on the three PNG shapes including theoretical errors. 166

5.6 Effect of RSD and redshift errors. 171

5.7 PNG forecasts with trispectrum corrections from radio continuum surveys. 178

5.8 PNG forecasts with trispectrum corrections from radio continuum surveys in redshift space. 181

5.9 The full effect of theoretical errors after using the optical surveys considered here. 183

5.10 Forecasts for all three PNG types, after considering the monopole approximation and including the trispectrum term, from all the optical surveys considered here. 189

5.11 Forecasts for all three PNG types, after considering the redshift space model and including the trispectrum term, from all the optical surveys considered here. 193

5.12 Final Fisher matrix forecasts on the local, equilateral and orthogonal PNG for all surveys (radio and ortical) considered here. 196

6.1 Measurements on the amplitude of the effective non-Gaussianity. 229

6.2 Measurements on the amplitude of the effective non-Gaussianity. 232

Chapter 1 | *Introduction*

One of the biggest challenges of cosmology is to explain the origin of the observable structures in the Universe, namely galaxies, galaxy clusters, filament structures and voids. The current picture suggests that their source can be traced back to small primordial density perturbations over a homogeneous and isotropic background. The gravitational evolution of these initial fluctuations subsequently produces today's observed structures.

The *Hot Big Bang* model (HBB) is the theoretical framework of standard cosmology. It successfully describes the evolution of the Universe from a hot, dense, radiation dominated initial state (~ 14 billion year ago), to a cool, low-density, non-relativistic dominated present state. The most notable success of HBB is the prediction of a relic radiation, called the *Cosmic Microwave Background* (CMB). Its discovery by Penzias and Wilson (1965) lead to the direct observational confirmation of the validity of the HBB scenario. The observed temperature anisotropies of the CMB provided compelling evidence that primordial inhomogeneities are not just a theoretical construction used to describe the origin of structures, but they are the actual seeds of all observed structures in the Universe. An other success of HBB, besides the CMB, is its the prediction of the abundance of light elements (*e.g.* Deuterium, Helium and Lithium) that are created during the first few minutes after the HBB through the framework of the Big-Bang Nucleosynthesis (BBN) (Gamow, 1946).

Besides its success, the standard HBB model cannot provide a fully sufficient description of the early Universe, or explain the origin of the primordial inhomogeneities that seed the observed structures. The inflationary paradigm came as a supplement to the HBB model and elegantly solved its major problems (Sec. 2.4). Inflation is an era in the early history of the universe that provides a mechanism for driving an exponentially

accelerated expansion. The first model of cosmological inflation was introduced by Guth in 1981 (Guth, 1981) as a solution to the horizon and flatness problems, which arose from the standard cosmological model. Moreover, an improved inflationary model, called *"new" inflation*, was introduced soon after (Linde, 1982; Albrecht and Steinhardt, 1982). The greatest success of inflation, besides solving the major cosmological problems, such as the horizon and the flatness problems (see Sec. 2.4.3), was to provide an explanation for the production of the primordial density fluctuations. In this picture, during the inflation epoch, the universe is dominated by one or more scalar fields and their self-interaction potential. Primordial perturbations can be created by quantum fluctuations of the scalar fields that drive the accelerated expansion. These fluctuations are stretched then during inflation from Planckian size to cosmological scales, maintaining their initial amplitudes nearly unchanged.

A vast landscape of different inflationary scenarios exists (see *e.g.* (Martin et al, 2014) and references therein). Depending on the specific inflationary scenario (*i.e.* single or multifield, different interaction potentials, canonical or non-canonical kinetic terms, vacuum initial state), the statistical distribution of the primordial perturbation follows a Gaussian or a non-Gaussian description (see Sec. 2.4.4 for details). The latter is in particular an important and general prediction of inflationary theories. It is a direct product of any kind of non-linear interaction occurring during the inflationary or reheating stage. Maps of temperature and polarization CMB anisotropies, as measured by ESA's *Planck* survey (Planck Collaboration et al, 2016a), provided the tightest constraints on the amount of deviation from Gaussianity. In this way, *Planck* probed directly the distribution of the primordial perturbation field.

In alternative to the CMB, inflationary non-Gaussianity can also be probed by exploiting observations of *Large-Scale Structures* (LSS): for example gravitational lensing or galaxy distribution measurements. LSS data have can have indeed great potential, based on the fact that 3D LSS surveys, covering large volumes and probing a wide range

of scales, have in principle access to a much larger amount of modes, with respect to 2D CMB maps. Up to now, LSS surveys have mainly relied on the two-point correlation function (see Sec. 3.5.2) to retrieve cosmological information. However, additional information can be extracted from higher-order correlation functions, such as the three-point correlation function (see Sec. 3.5.3) and in particular its Fourier transformation the *bispectrum*. This is in general the most important statistic to consider when studying inflationary non-Gaussianity, as explained in detail in Chapters 2 and 5 of the thesis.

The bispectrum of the primordial curvature perturbation field, arising from interactions during inflation, is characterized by a dimensionless, amplitude parameter, $f_{\rm NL}$, and by a shape function $F(k_1, k_2, k_3)$. While $f_{\rm NL}$ defines the strength of the primordial *non-Gaussianity* (NG) signal, the shape describes the functional dependence of the bispectrum on different Fourier space triangles. Both of them are strongly model dependent and provide significant information on the physical mechanisms at work during inflation.

As promising as it looks, measuring primordial non-Gaussianity from LSS surveys, via bispectrum studies, will be very challenging. The gravitational non-Gaussian signal, originating from a LSS dataset, is far larger (orders of magnitude) than the primordial component. Therefore, these late-time, non-linear contributions need to be understood and subtracted with exquisite accuracy.

The potential of the LSS bispectrum for both probing the non-linear regime of structure growth and setting constraints on primordial non-Gaussianity is the main topic of this thesis. The steps we will take to this purpose are the following: we start by constructing an accurate model for the power spectrum and bispectrum of galaxies by using perturbation methods for the dark matter correlators. In addition, account for recent developments on galaxy bias (see Sec. 4.3.2 for a discussion) in order to have a theoretical formalism that links dark matter distribution to the actual galaxy statistics measured by a LSS survey. Our analysis is restricted to the large and intermediate scales, where the available perturbation theories have been heavily tested and give predictions that are

in agreement with simulation and past LSS surveys. Constructing accurate models for the non-linear evolution of galaxies, as sourced by gravitational interactions, is crucial in order to distinguish the primordial non-Gaussian signal from the late time non-linearities.

We then produce accurate Fisher forecasts (see Sec. 5.3 for a review on the formalism) on the amplitude of primordial non-Gaussianity coming from future LSS surveys. Using the previously discussed formalism, we choose two future radio continuum surveys (*i.e.* SKA and EMU) due to their appealing features for this kind of measurements, *i.e.* very large volumes and high redshift estimation, where a larger amount of modes are in the linear regime. In addition, we choose future or proposed optical galaxy surveys, such as Euclid, DESI, SPHEREx and LSST, in order to have a more complete picture on the future and potential improvements on current $f_{\rm NL}$ constraints from LSS surveys. We pay particular attention in testing many effects that can affect the Fisher matrix predictions, as well as consistently include all the important elements and produce as complete and realistic as possible primordial NG forecasts, combining power spectrum and bispectrum constraints. After this extensive analysis, we move on from forecasting to the problem of actually producing accurate statistical estimate of non-Gaussian parameters from actual datasets.

Measuring the actual bispectrum from N-body simulations or galaxy surveys presents peculiar challenges and is computationally very demanding. The full bispectrum of a dataset contains a large number of Fourier space triangles, formed by all the modes inside a survey or a simulation. The larger the volume of the said dataset, the more the triangles one can build up to the chosen small scale limit. For large volume surveys this can increase tremendously the computational effort of the bispectrum measurements. More precisely, the numerical measurement of the bispectrum needs $\mathcal{O}(N^6)$ operations, where N is the number of modes per dimension inside a simulation box or a LSS survey. Future LSS surveys will have a growing size in their volume (*e.g.* Euclid). This makes the development of a fast, efficient, optimal, bispectrum pipeline for forthcoming LSS

datasets a crucial task.

Therefore, the final step we take in this thesis is the development of such a pipeline. Our approach is based on the *modal estimation* formalism, proposed initially for the measurement of the CMB bispectrum (Fergusson and Shellard, 2009; Fergusson et al, 2010a,b). The modal estimator was actually used to measure the non-Gaussian amplitude from *Planck* CMB temperature and polarization maps (Planck Collaboration et al, 2016a). The advantages of this approach are that it reduced the computational cost to $\mathcal{O}(N^3)$ operations, which makes the measurement of the bispectrum a manageable task. In addition, it gives directly the best fit value of the $f_{\rm NL}$ parameter, besides allowing for full bispectrum reconstruction. The main idea of modal estimation consists of finding a suitable basis of bispectrum templates and write higher order correlations as a linear combination of such templates ("modes"). By properly choosing the templates it is always possible to achieve fast convergence. Although the modal estimator was developed for measuring primordial $f_{\rm NL}$ parameters, its appealing features make it ideal to measure any kind of galaxy bispectrum. The modal decomposition applies both to the theoretical prediction and to the bispectrum extracted from the dataset. Expanding both on the same basis we can achieve a fast, efficient comparison by only comparing the coefficient of the expansion instead of comparing all the triangles. This allows for massive data compression (from billions of triangles to hundred/thousand coefficients), making it an extremely useful tool for future LSS surveys, such as Euclid and SKA.

This thesis is structured as follows: in Chapter 2 we present the standard cosmological model and the dynamics of the expanding background. Furthermore, we review the inflationary scenario by describing the field interactions and dynamics during that era and showing the non-Gaussian predictions from different inflationary theories. In Chapter 3 we review different perturbation theories and their statistical predictions for the two, three and four-point correlators. For Chapter 4 we discuss structure formation, from primordial density fluctuations to the formation of galaxies. In addition, we review the details on the

relationship between matter and galaxy statistics (*i.e.* bias expansion),presenting recent developments in this field. In Chapter 5 we obtain expressions for galaxy power spectra and bispectra considering all the relevant effects discussed in the previous chapters (*e.g.* redshift space distortions, redshift uncertainties, trispectrum corrections). We then define Fisher matrix forecasts several LSS surveys, both optical and radio (Euclid, DESI, LSST, SPHEREx, SKA and EMU). One of the main goals of this chapter, is explaining how to account for theoretical errors in the forecasts. In Chapter 6 we review the modal estimator formalism and we discuss the details and technicalities of the pipeline. We present tests performed to improve the performance of the pipeline and the convergence of the modal expansion. In addition, we show the measured bispectrum for a set of N-body simulations, by reconstructing modal coefficients, which hold the compressed information about the three-point correlator. Furthermore, we show both the measured primordial non-Gaussian amplitude and the effective $f_{\rm NL}$ value from non-linear gravitational evolution, for a set of N-body realisations with non-Gaussian initial conditions. In this way we show the power of the modal estimator in separating these two contributions, cleaning in this way the primordial signal from the late-time non-Gaussianity. Finally, we summarize the main conclusions of this thesis in Chapter 7.

Chapter 2

The Standard Cosmological Model

2.1 The Cosmological Principle

The main pillar of cosmology is the "*Cosmological Principle*". It states that on sufficiently large scales, larger than those probed by LSS, the Universe is statistically homogeneous and isotropic. This assumption was introduced by the early cosmologists, in the absence of data, in order to construct simplified models that could describe the Universe.

The property of homogeneity means that the Universe is identical in different spatial locations, in an average sense, when one looks at a large patch. Isotropy, on the other hand, is the feature of the Universe to look the same in every direction. There are observational evidence supporting the latter, coming from the radiation of the CMB, which has been proved to be near-isotropic with small temperature variations between different directions of the order $\Delta T/T \sim 10^{-5}$. Nevertheless the evident near-isotropy cannot alone imply homogeneity without invoking the additional assumption of the "*Copernican Principle*" (Coles and Lucchin, 2002), which states that the observer does not occupy a special place in the Universe.

The presence of planets, stars, galaxies, clusters, *etc.* indicate that the validity of cosmological principle breaks down on small scales, since they shouldn't exist in a perfectly homogeneous scenario. Nonetheless, galaxy statistics have shown that on scales larger than 70-80 Mpc/h (*i.e. homogeneity scale*) (Hogg et al, 2005; Sarkar et al, 2009; Scrimgeour et al, 2012) the Universe becomes smooth and a fractal distribution is excluded,

i.e. statistically on large scales cosmological principle is valid. An opposite argument to the claimed homogeneity also exists in the work of (Labini et al, 2009; Labini, 2010; Maartens, 2011), where they claim that homogeneity is inconsistent[1] with their findings for scales smaller than 100 Mpc/h. We will discuss shortly the statistical argument they used in Sec. 3.5.

In this chapter we will provide a short introduction to the standard cosmological model and the formalism behind it. In addition we will also introduce useful notation that we will use in the main body of this thesis. The reader is advised to a series of books and reviews (Peebles, 1993; Coles and Lucchin, 2002; Mukhanov, 2005; Linde, 2005; Liddle and Lyth, 2000; Martin et al, 2014), that provide a deep analysis on the topics that we will discuss shortly in this chapter.

2.2 The expanding Universe

2.2.1 FLRW metric

The assumption of statistical homogeneity and isotropy, leads to a non-static Universe (*i.e.* contracting or expanding). The *Friedmann–Lemaître–Robertson–Walker* (*FLRW*) metric was developed independently by (Friedmann, 1922; Lemaître, 1927; Robertson, 1935; Walker, 1937) and is an exact elegant solution of the Einstein field equations under the assumptions of the cosmological principle. The dynamics of the expanding Universe are incorporated in the Einstein equations after plugging in the *FLRW* metric and solving for the scale factor $a(t)$ (also referred as Robertson-Walker scale factor), as we will see in Sec. 2.3. It is convenient to use a coordinate system that is *comoving* with the Hubble expansion. The comoving observers will be free-falling and will see the Universe isotropic and homogeneous, where their spatial coordinates will be constant in time. In other words

[1] However they point out (Labini, 2010) that the inhomogeneous structures can be compatible with isotropy and homogeneity for a relaxed version of the cosmological principle.

in the comoving frame the uniform expansion of the Universe is factored out and the distance between two spatial points is constant over time, independently of the expansion rate.

In differential geometry the space-time infinitesimal interval between two point x^i and $x^i + dx^i$ is given by:

$$ds^2 = g_{\mu\nu}(x) dx^\mu dx^\nu, \tag{2.1}$$

where $\mu, \nu = 0, 1, 2, 3$ and the Einstein index convention is used as usual. The metric $g_{\mu\nu}$, determines how the distance are measured in the considered manifold. The most general metric in a Universe that obeys the cosmological principle is the *FLRW* metric (Weinberg, 2008), where the line element is given by:

$$ds^2 = (cdt)^2 - a^2(t) \left(\frac{dr^2}{1 - Kr^2} + r^2 (d\theta^2 + \sin^2 \theta d\phi^2) \right), \tag{2.2}$$

where the metric is diagonal with each element being:

$$g_{00} = c,\ g_{rr} = -\frac{a^2(t)}{1 - Kr^2},\ g_{\theta\theta} = -a^2(t) r^2,\ g_{\phi\phi} = -a^2(t) r^2 \sin^2 \theta, \tag{2.3}$$

where c is the speed of light, r, θ, and ϕ are the spherical polar coordinates in a comoving frame, t is the *proper time* and the constant K is the curvature parameter. It can take the following values, depending on the spatial geometry of the Universe:

$$K = \begin{cases} < 0 & \text{Open (Hyperbolic)} \\ 0 & \text{Flat (Euclidean)} \\ > 0 & \text{Closed (Spherical)} \end{cases} \tag{2.4}$$

The value of K in *FLRW* is a free parameter to be measured by an experiment. The recent results of Planck Collaboration et al (2016b) indicate that the spatial curvature of the Universe is very close to flat, where the presence of errors in the measured parameter

prevent an absolute claim on the exact geometrical properties of the Universe. For the rest of the thesis we will assume a spatial Euclidean geometry.

Under the assumptions provided by the cosmological principle, one can define a proper time such that the spatial part of ds^2, $dl^2 = \gamma_{ij} dx^i dx^j$ with $i, j = 1, 2, 3$, defines a spatial interval that is the same at all directions and places. The interval dl^2 can be seen as a comoving distance. The *proper distance* $d_p(t)$ at a constant time t ($dt = 0$) can be defined as the distance from the origin, which can be chosen at $r_0 = 0$ due to the homogeneity of space, to an object with spherical coordinates[2] $(r, 0, 0)$ as:

$$d_p(t) = a(t) \int_0^r \frac{dr}{\sqrt{1 - Kr^2}} = a(t) d_c, \tag{2.5}$$

where $d_c = \sinh r$, r or $\sin r$ for $K < 0$, $K = 0$, $K > 0$ respectively and is calculated at some reference time t_0. The proper distance between two points at t can now be understood as their separation at that particular time (Hogg, 1999). However, it is of little operational significance, since one cannot measure simultaneously the coordinates separating the two points (Coles and Lucchin, 2002). One can see now that the dimensionless cosmic scale factor parametrises the relative expansion of the Universe and by construction becomes unity at the reference time (*i.e.* $a(t_0) = a_0 = 1$), which is set to present. Taking the time derivative of Eq. (2.5) we can get the radial velocity of an object with respect to the origin as:

$$u_r = \dot{a}(t) d_c = \frac{\dot{a}}{a} d_p. \tag{2.6}$$

It will be useful, for the following chapters, to define here the *conformal time* as:

$$\tau = \int \frac{dt}{a(t)}, \tag{2.7}$$

[2]Geodesics that pass through $r_0 = 0$ are lines of constant θ and ϕ and therefore $d\theta = 0$, $d\phi = 0$. Note here that, objects do not only recede radially from an observer, but they also move in the other two spatial directions (*i.e.* peculiar motion).

where we have used the units $c = 1$.

2.2.2 Hubble flow and redshift

The first observational indication for an expanding Universe came from the work of (Slipher, 1914, 1915) and was independently confirmed by (Hubble, 1929). Hubble found that there is a simple proportional relation between the radial velocity of galaxies and their distance from an observer on Earth. The observation was encoded in the so called *Hubble's law*, which is simply given by

$$u_r = H_0 r, \tag{2.8}$$

where the proportionality constant at the present time, $H(t_0) = H_0$, is called the *Hubble constant*. As we have shown in the previous section, one can end up to the same relation just by considering the assumptions of the cosmological principle and by using the appropriate metric (*i.e. FLRW* metric). Due to isotropy, the radial nature of the recession velocity is ensured, while homogeneity provides the freedom of choosing the coordinates of the origin and hence establish the proportional relation between the radial velocity and comoving distance.

The observational results of Hubble showed that the constant H_0 does not have an arbitrary sign but it is a positive one, providing the proof of an expanding Universe. The recession velocity must be understood not as the velocity of a galaxy that moves in space-time away from us in the radial direction due to the effect of some force field, but rather than as the velocity inherited to the galaxy due to the expansion of space-time itself. In other words galaxies are objects at rest in an expanding Universe. The pedagogical analogy between a raisin bread and the Universe, where raisins play role of galaxies, is most intuitively.

The value of the expansion rate as incorporated in the Hubble constant at present time, after parametrizing it by means of a pure number h, $H_0 = 100h\,\frac{\mathrm{km/s}}{\mathrm{Mpc}}$), can only be

measured by experiments. The tightest constraint up to date was given by the *Planck* CMB satellite (Planck Collaboration et al, 2016b):

$$h = 0.6774 \pm 0.0046, \tag{2.9}$$

at 68% confidence level confidence level. This will be the fiducial value for the Hubble constant used throughout this thesis. Comparing Eq. (2.6) with the Hubble's law we can derive a more general form for the Hubble flow, where the Hubble parameter is at any given time

$$H(t) = \frac{\dot{a}}{a}, \tag{2.10}$$

where the dot denotes a derivative with respect to the proper time. The *Hubble time* is defined as the inverse of the Hubble parameter as:

$$t_H = \frac{1}{H_0} = 14.7\,\mathrm{Gyr}, \tag{2.11}$$

where it is a rough estimate of the age of the Universe, since it is the age it would have if the expansion was linear and didn't vary. However, this is not the case and the current age of the Universe is, $t_0 = 13.799 \pm 0.021\,\mathrm{Gyr}$ (Planck Collaboration et al, 2016b). This is derived after integrating $dt = da/(aH(t))$ [Eq. (2.10)]. Nevertheless, the Hubble age is a good proxy of the current age of the Universe.

Hubble flow will Doppler shift the radiation wavelength, λ_0, of a luminous object observed at present time with respect to the wavelength, λ_e, at emission time. The observed shift will be towards the red part of the spectrum, due to the movement of the source with the expansion of the Universe. This can be taken into account by defining a new variable related to the scale factor, which is a direct observable. The *redshift* is given by:

$$z = \frac{\lambda_0 - \lambda_e}{\lambda_e} = \frac{a_0}{a(t)} - 1. \tag{2.12}$$

From the definition of the scale factor, the redshift at present time is $z = 0$. After taking into account the normalization of the scale factor, we can get the following simplified relation, $a(t) = 1/(1+z)$. The expansion redshift can be measured directly from the electromagnetic spectrum of a source that moves with the Hubble flow, rendering it a very useful quantity, since it can be directly related to the comoving distance of the object. Recent spectroscopic galaxy surveys, like 2DF (Colless et al, 2001), SDSS (York et al, 2000) and BOSS (Dawson et al, 2013), have provided a plethora of accurate redshift measurements, allowing us to gain a full 3D information on the distribution of luminous matter.

2.2.3 Cosmic distances

In Sec. 2.2.1 we commented on our inability to measure the proper distances of objects, since the emitted light takes a finite amount of time to reach to us and hence we cannot know the proper time of the travelling light. However we can define other distances that, in principle, can be related to observables. The light emitted by distant galaxies at a time $t_e < t_0$ is propagated along the null geodesic ($ds^2 = 0$) in a space-time described by the *FLRW* metric. After choosing appropriately the origin coordinates[3] ($d\theta = 0$, $d\phi = 0$) we can write Eq. (2.2) as:

$$c\int_{t_e}^{t_0} \frac{dt}{a(t)} = \int_0^r \frac{dr}{\sqrt{1 - Kr^2}} = d_c. \tag{2.13}$$

The comoving distance does not change with time by definition, therefore two photons that are emitted with a small time difference (t_e and $t_e + dt_e$) will cover the same comoving distance. This means that the quantity $dt/a(t)$ is conserved along the light cone. Using

[3]The isotropy of the Universe makes the choice of the origin coordinates (θ_0, ϕ_0) irrelevant.

the relation between redshift and scale factor (*i.e.* $dz = -da/a^2$), as well as Eq. (2.10), we can derive a relation between the comoving distance and a measured variable (*i.e.* redshift)

$$d_c(z) = c\int_0^z \frac{dz}{H(z)} = \frac{c}{H_0}\int_0^z \frac{dz}{E(z)}, \tag{2.14}$$

where $E(z) = H(z)/H_0$ (Peebles, 1980). This relation show that the comoving distance of an object depends on the expansion history of the Universe, as governed by $H(z)$, between the emission and observation time. Taylor expanding the integral $\int dz/E(z)$ around $z = 0$ we can get a simplified relation between redshift and comoving distance for $z \ll 1$

$$d_c \simeq \frac{c}{H_0} z. \tag{2.15}$$

An other important distance in cosmology is the *angular diameter* distance, d_A which is defined as

$$d_A = \frac{\Delta x}{\Delta\theta}, \tag{2.16}$$

where Δx is the physical size of an object transverse to the line-of-sight and $\Delta\theta$ is its angular size measured in radians. In an *FLRW* space-time the object lies on the surface of a sphere with the observer in the centre and a radius the size of comoving distance. Therefore the size Δx at time t is given by (Weinberg, 1972; Peebles, 1993)

$$\begin{aligned} &\Delta x = a(t) f_K(d_c)\Delta\theta \Rightarrow \\ &d_A = \frac{f_K(d_c)}{1+z}, \end{aligned} \tag{2.17}$$

where the function $f_K(x)$ is defined, after using the relation between proper and comoving distance [Eq. (2.5)], as:

$$f_K(x) = \begin{cases} \frac{1}{\sqrt{K}} \sin(\sqrt{K}x) & K > 0 \\ x & K = 0 \\ \frac{1}{\sqrt{|K|}} \sin(\sqrt{|K|}x) & K < 0 \end{cases}, \tag{2.18}$$

where $f_K(d_c)$ is denoted in the literature as the *transverse comoving distance* (Hogg, 1999).

2.2.4 Cosmological horizons

The *Hubble radius* can be defined as the distance light travels in a Hubble time, along a straight line and inside a flat space-time. It is given by:

$$d_H(t) = \frac{c}{H(t)}, \tag{2.19}$$

where we have used the Hubble law at an arbitrary time t to derive it. It defines a boundary between particles moving with a speed smaller than light's and those with a super-luminar motion. The latter can acquire such velocities due to the Hubble flow without violating special relativity. An object outside the Hubble radius is not able to interact with those that are inside, defining a sphere of causality. For a slow expansion, an increasing number of regions will be able to be in causal contact, while in the case of an accelerating expansion two regions that are separated with a distance larger than the Hubble radius they will never be in a causal relation from now on. Due to the causal nature of the Hubble radius, it is often referred as a horizon, without though being one due to its comoving properties. A comoving horizon can be also defined by dividing d_H with the scale factor (*i.e.* $d_{H,c} = d_H/a(t)$).

The maximum comoving spatial distance travelled by a particle/photon from a time $t_{\min}$ in the past till now defines the *particle horizon*

$$d_{ph} = c \int_{t_{\min}}^{t_0} \frac{dt}{a(t)}. \tag{2.20}$$

Setting $t_{\min}$ to the time of the last scattering, which is the time the Universe became transparent to light, the particle horizon represents the size of the visible Universe and thus defines the furthest distance in the past from which we can acquire information. The particle horizon defers from the Hubble horizon, since it is not simply the age of the universe times the speed of light but the product between the speed of light and the conformal time.

Finally the cosmic *event horizon* is the largest comoving distance a particle will travel from the present time till it reaches an observer in the future and it is given by:

$$d_{eh} = c \int_{t_0}^{t_{\max}} \frac{dt}{a(t)}. \tag{2.21}$$

The particle and event horizons have the same integrands in their definitions, where the integration limits are what differs between the two. This indicates that they correspond to different conformal times, *i.e.* particle horizon resides in our past light cone while the event horizon lies on our future one.

2.3 Dynamics of the expansion

The dynamics of the Universe is encoded in the equations of motion (EOM) of the scale factor $a(t)$. Its time evolution can be derived from the solution of the Einstein field equations:

$$R_{\mu\nu} - \frac{1}{2} g_{\mu\nu} R \equiv G_{\mu\nu} = 8\pi G\, T_{\mu\nu} + \Lambda g_{\mu\nu}, \tag{2.22}$$

where G is Newton's gravitational constant, $G_{\mu\nu}$ is the Einstein tensor, $T_{\mu\nu}$ is the total energy-momentum tensor for all the components in the Universe (*i.e.* a sum over the

energy-momentum tensors of baryons, photons, neutrinos, cold dark matter and dark energy) and Λ is the *cosmological constant*. The form of the field equation are derived assuming $c = 1$. For the rest of this section we will use these units. The left hand side of the Einstein equations [Eq. (2.22)] describes the geometry of the Universe, while the right hand side the energy and momenta of the different species inside it.

The *Ricci tensor* $R_{\mu\nu}$ is constructed by summing over repeated indices (*i.e.* contraction) of the four-rank Riemann tensor and is defined as:

$$R_{\mu\nu} = \frac{\partial \Gamma^{\alpha}{}_{\mu\nu}}{\partial x^{\alpha}} - \frac{\partial \Gamma^{\alpha}{}_{\mu\alpha}}{\partial x^{\nu}} + \Gamma^{\alpha}{}_{\beta\alpha}\Gamma^{\beta}{}_{\mu\nu} - \Gamma^{\alpha}{}_{\beta\nu}\Gamma^{\beta}{}_{\mu\alpha}\,, \tag{2.23}$$

where the *affine connection* is given by

$$\Gamma^{\mu}{}_{\alpha\beta} = \frac{g^{\mu\nu}}{2}\left(\frac{\partial g_{\alpha\nu}}{\partial x^{\beta}} + \frac{\partial g_{\beta\nu}}{\partial x^{\alpha}} - \frac{\partial g_{\alpha\beta}}{\partial x^{\nu}}\right). \tag{2.24}$$

The scalar curvature (*i.e. Ricci scalar*) is given by the contraction of the Ricci tensor as:

$$R = g^{\mu\nu}R_{\mu\nu}. \tag{2.25}$$

For a isotropic and homogeneous Universe described by the *FLRW* metric in comoving coordinates, the only non-zero components of the affine connection are:

$$\Gamma^{0}{}_{ij} = a\dot{a}\gamma_{ij}, \quad \Gamma^{i}{}_{0j} = \Gamma^{i}{}_{j0} = H\delta^{i}_{j}, \quad \Gamma^{1}{}_{11} = \frac{Kr}{1-Kr^2}, \quad \Gamma^{1}{}_{22} = -r(1-Kr^2), \tag{2.26}$$

$$\Gamma^{1}{}_{33} = -r(1-Kr^2)\sin^2\theta, \quad \Gamma^{2}{}_{33} = -\sin\theta\cos\theta, \tag{2.27}$$

$$\Gamma^{2}{}_{12} = \Gamma^{2}{}_{21} = \Gamma^{3}{}_{13} = \Gamma^{3}{}_{31} = \frac{1}{r}, \quad \Gamma^{3}{}_{23} = \Gamma^{3}{}_{32} = \cot\theta. \tag{2.28}$$

The non-zero component of the Ricci tensor and Ricci scalar are respectively

$$R_{00} = -3\frac{\ddot{a}}{a}, \quad R_{0i} = R_{i0} = 0, \quad R_{ij} = (a\ddot{a} + 2a\dot{a}^2 + 2K)\gamma_{ij}, \tag{2.29}$$

$$R = -6(\frac{\ddot{a}}{a} + H^2 + \frac{K}{a^2}), \tag{2.30}$$

where δ^{μ}_{ν} is the Kronecker's delta ($\delta^{\mu}_{\nu}=1$ for $\mu=\nu$ and $\delta^{\mu}_{\nu}=0$ for $\mu\neq\nu$). The Latin indexes i, j run from 1 to 3 while the Greek μ, ν from 0 to 3.

The total energy-momentum tensor must have a form dictated by the symmetries of the *FLRW* metric. This means that $T_{\mu\nu}$ must be diagonal in the rest frame of the fluid (*i.e.* shearing terms, generated *e.g.* by viscosity, are zero). The isotropy of space-time imposes the requirement that the spatial part of the tensor must be equal. The simplest case satisfying these conditions is the energy-momentum tensor of a *perfect fluid*, given by:

$$T_{\mu\nu}=(\rho+P)U_{\mu}U_{\nu}-Pg_{\mu\nu}, \tag{2.31}$$

where the energy density ρ and pressure P are time-dependent quantities in the rest-frame, while U_{μ} is the four-velocity relative to the observer. Note that, an imperfect fluid would also satisfy the symmetries imposed by the *FLRW* metric (Kolb and Turner, 1990). The above relation can be reduced in the rest frame[4] to $T^{\mu}_{\nu}=g^{\mu\alpha}T_{\alpha\nu}=\mathrm{diag}(\rho,-P,-P,-P)$, which is valid for every reference frame because Eq. (2.31) is a tensor equation. The *equation of state* (*i.e.* the pressure/density ratio) of a perfect fluid is characterized by a dimensionless constant:

$$w_i=\frac{P_i}{\rho_i}. \tag{2.32}$$

The value of the parameter w depends on the type of fluid we consider. In the case of "matter", which consists of all non-relativistic species ($|P|\ll\rho$) in the cosmic fluid, *i.e.* baryonic matter and cold dark matter, $w=0$ and hence $P=0$. For relativistic components, *e.g.* photons, neutrinos, *etc.*, where the energy density is dominated by kinetic energy, the equation of state is $P=\frac{1}{3}\rho$ ($w=1/3$). Today, the Universe seems to be dominated by a negative pressure component with $P=-\rho$ ($w=-1$), called *dark energy*, which drives the observed accelerated expansion.

[4]For a comoving observer the four-velocity is $U_{\mu}=(1,0,0,0)$.

2.3.1 Friedmann equation

The time-time component of the Einstein equations [Eq. (2.22)] is the only equation needed to understand the time evolution of the scale factor. The *Friedmann equation* is given by:

$$R_{00} - \frac{1}{2} g_{00} R = 8\pi G T_{00} + \Lambda g_{00} \quad \Rightarrow$$
$$H^2 = \frac{8\pi G}{3}\rho - \frac{K}{a^2}, \tag{2.33}$$

where ρ is the total energy density ($\rho = \sum_i \rho_i$) of all the species in the Universe. The spatial part of the Einstein equations will give the *acceleration equation*:

$$\frac{\ddot{a}}{a} = -\frac{4\pi G}{3}(\rho + 3P), \tag{2.34}$$

where P is again the total pressure coming from all the components in the Universe.

The cosmological constant term in the Friedmann equation [Eq. (2.33)] has been absorbed in the total energy density ($\rho_\Lambda = \frac{\Lambda}{8\pi G}$) considering it as a separate component. This can be also done in the Einstein equations by breaking the total energy-momentum tensor into a "matter" and Λ component, $T_{\mu\nu} = T^{(M)}_{\mu\nu} + T^{(\Lambda)}_{\mu\nu} = T^{(M)}_{\mu\nu} + \rho_\Lambda g_{\mu\nu}$. The cosmological constant component behaves like a species with negative pressure (*i.e.* $P_\Lambda = -\rho_\Lambda, \quad w_\Lambda = -1$), therefore we can identify the nature of dark energy with that of a cosmological constant. In the absence of matter, the *vacuum energy* (*i.e.* the energy of empty space) can reproduce the effect of a cosmological constant, according to quantum field theory. The vacuum energy cannot have a preferred direction and its energy-momentum tensor must be Lorentz invariant, therefore it has a form, $T^{\rm vac}_{\mu\nu} = \rho_{\rm vac} g_{\mu\nu}$. The energy-momentum tensor [Eq. (2.31)] takes the form of a perfect fluid, since vacuum looks like one, and hence the equation of state of vacuum is the same with that of a negative pressure fluid, *i.e.* $P_{\rm vac} = -\rho_{\rm vac}$. The concept of cosmological constant is interchangeable with the vacuum energy ($\rho_{\rm vac} = \rho_\Lambda = \frac{\Lambda}{8\pi G}$). Unfortunately the predicted energy density

of the vacuum, coming from quantum field theory, is completely off from the observed density of a cosmological constant ($\rho_{\rm vac}/\rho_\Lambda = 10^{120}$). The dark energy sector is considered throughout this thesis to be the cosmological constant with a fixed pressure/density ratio, accepting the predictions of the *Lambda Cold Dark Matter* (ΛCDM) framework.

For a flat Universe ($K = 0$) we can define a *critical density* as

$$\rho_{\rm crit}(t) = \frac{3H^2}{8\pi G}, \tag{2.35}$$

The present time value of the critical density is

$$\rho_{\rm crit,0} = 1.878h^2 \times 10^{-26}\,\frac{\rm kg}{\rm m^3} = 2.775h^{-1} \times 10^{11}\,\frac{\rm M_\odot}{\rm (Mpc/h)^3}, \tag{2.36}$$

where the index "0" denotes the value of the parameter in the present time $t = t_0$. Note that, in general the critical density depends on time. We can use the critical density to define a dimensionless *density parameter* as

$$\Omega_\alpha(t) = \frac{\rho_{\alpha,}(t)}{\rho_{\rm crit}(t)}, \tag{2.37}$$

where α denotes the different species. The sum of all density parameters for all species at any time t is equal to

$$\Omega(t) - 1 = \frac{K}{a^2H^2}, \tag{2.38}$$

where the contribution of the spatial curvature can be treated as a fictitious component with an energy density $\rho_K = -\frac{3K}{8\pi G a^2}$ and a density parameter defined as, $\Omega_K = -\frac{K}{a^2H^2}$. For a flat Universe the total density parameter is equal to unity (*i.e.* $\Omega_{\rm tot} = 1$), while for $K > 0$ and $K < 0$ it is $\Omega_{\rm tot} > 1$ and $\Omega_{\rm tot} < 1$ respectively.

The Friedmann equation can be expressed with respect to the density parameters as:

$$H^2(t) = H_0^2\left(\Omega_{R,0}a^{-4} + \Omega_{m,0}a^{-3} + \Omega_{K,0}a^{-2} + \Omega_{\Lambda,0}\right). \tag{2.39}$$

Writing this relation with respect to redshift we can get the expression for $E(z)$ in Eq. (2.14). In this thesis we will use the values for the density parameters as measured by (Planck Collaboration et al, 2016b)

$$\Omega_{b,0}\,h^2 \;=\; 0.02230 \pm 0.00014\,, \qquad\qquad \Omega_{c,0}\,h^2 \;=\; 0.1188 \pm 0.001\,, \tag{2.40}$$

where the subscripts c and b denotes cthe cold dark matter and baryons respectively. In addition, we define the critical density of matter as the sum of the two, *i.e.* $\Omega_{m,0} = \Omega_{b,0} + \Omega_{c,0}$. The critical density of dakr energy is then given by $\Omega_{\Lambda,0} = 1 - \Omega_{\mathrm{M},0} = 0,6925$ with $w_\Lambda = -1$, while we consider a perfectly flat Universe ($\Omega_K = 0$). Moreover, we ignore the photon and neutrino contributions (*i.e.* $\Omega_\gamma = 0$, $\Omega_\nu = 0$).

2.3.2 Continuity equation

The conservation laws demand that the covariant derivative (denoted with a semi-column ;) of the energy-momentum tensor must be equal to zero:

$$T^{\mu}_{\nu;\mu} = \frac{\partial T^{\mu}_{\nu}}{\partial x^{\mu}} + \Gamma^{\mu}{}_{\alpha\mu} T^{\alpha}_{\nu} - \Gamma^{\alpha}{}_{\nu\mu} T^{\mu}_{\alpha}. \tag{2.41}$$

Only the $\nu = 0$ equation is meaningful, due to the isotropy of the Universe, giving the *continuity equation*:

$$\dot{\rho} = 3\frac{\dot{a}}{a}(\rho + P) = 0. \tag{2.42}$$

The above can be derived also from the first law of thermodynamics. After rearranging the continuity equation, substituting the equation of state for a general species and finally integrating it, we yield:

$$\rho_i \propto a^{-3(1+w_i)}, \tag{2.43}$$

Component	w_i	$\rho(a)$	$a(t)$
Non-Relativistic/Matter	0	$\propto a^{-3}$	$\propto t^{2/3}$
Relativistic/Radiation	1/3	$\propto a^{-4}$	$\propto t^{1/2}$
Curvature	-1/3	$\propto a^{-2}$	$\propto t$
Cosmological constant	-1	$\propto a^{0}$	$\propto \exp Ht$

Table 2.1 – The energy density and scale factor time evolution.

where we can immediately see that the energy density of cosmological constant/vacuum is constant with respect to the scale factor. This indicates that it will come to dominate the Universe at some late time. Using the Friedman equation, together with the above result, we can get the time evolution of the scale factor:

$$a(t) = a_*[1+\frac{3}{2}(1+w)H_*(t-t_*)]^{\frac{2}{3}(1+w_i)}, \tag{2.44}$$

where the "$*$" subscript denotes the quantity at some initial time and $H_* = \sqrt{8\pi G/3}\rho_*$. The integration constant a_* is not important and can be normalized to unity ($a_* = a_0 = 1$). In the case of cosmological constant we can assume, $w = -1+\varepsilon$ and derive the limit:

$$\begin{aligned}\lim_{w\to-1} a(t) &= [1+\frac{3}{2}\varepsilon H_*(t-t_*)]^{-\frac{2}{3}\varepsilon} \\ &= \exp[H_*(t-t_*)] \propto e^{Ht}.\end{aligned} \tag{2.45}$$

The scale factor in this case is the de Sitter solution (vacuum energy solution of *FLRW*) and provides, in the case of cosmological constant, a description for the observed recent accelerating expansion. A summary of the results of the density and scale factor evolution can be found in Table 2.1 for all the components.

We can identify immediately two important events during the history of the Universe, the matter-radiation and the matter-Λ equality. The redshift and scale factor of the matter-radiation equality can be found, after equating the energy density evolution of the

two species, to be:

$$a_{\rm EQ} = \frac{4.15 \times 10^{-5}}{\Omega_m h^2}, \tag{2.46}$$

$$1 + z_{\rm EQ} = 2.4 \times 10^4 \Omega_m h^2. \tag{2.47}$$

The time of equality can be pushed further to the past (higher redshifts) in the case of an increasing Ω_m, although it must be smaller that the redshift of CMB ($z \sim 1000$). The redshift of equality between matter and cosmological constant can be found to be, $z_\Lambda = 1.26$,for the values of $\Omega_{m,0}$ and $\Omega_{\Lambda,0}$ considered here. The event of the cosmological constant dominance, and hence the accelerating expansion, is very recent in the history of the Universe.

2.4 The inflationary paradigm

The HBB model besides its great successes (most notable *e.g.* the black body spectrum of CMB and and the abundance of light nuclei), does not provide a description for the initial conditions of the Universe. A set of problems arise from this, listed as follows:

Horizon problem: The observations of CMB temperature spectrum show that at the time of recombination, the Universe was nearly homogeneous at an impressive precision (a part over 10^5 independent of the direction). These inhomogeneities, as we will show in the next Chapter, are gravitationally unstable and grow with time. This means that the Universe must have been even more homogeneous in the past. However, at the redshift of CMB, the size of the particle horizon was roughly one degree on the microwave sky. How could causally disconnected parts on the sky came to create a CMB which has the same temperature almost everywhere? Why do we live in a homogeneous Universe, even though there was no time to create such a characteristic?

Flatness problem: The Universe as observed by CMB is very close to flat. Using Eq. (2.38), one can see that in the standard HBB model the curvature component is dominated

at late times, *i.e.* $\Omega(t)$ grows away from unity with time. The $\Omega = 1$ point is an attractor in the past, therefore in order to get $\Omega_0 \approx 1$ the Universe must have been even more close to flat in the past. This however, imposes a fine tuning. Thus, a problem arises when one attempts to explain the near flat observations of present time only from within the framework of HBB.

Structure problem: Both these problems show the deficiency on the predictability of the HBB model. However, they can be overcome by assuming homogeneity and flatness in the initial conditions without giving any explanations. The real problem arises when one wishes to explain the origin of observable structures, as well as the small anisotropies observed in the CMB. Naturally, initial density fluctuations can be assumed to be the seeds for both cases. Nevertheless, their origin cannot be explained from the HBB model.

Cosmic *inflation* was introduced by Guth (1981) to solve the problems of the standard HBB model. It is a period of exponential acceleration of the early Universe ($\sim 10^{-34}$ sec), before the radiation dominated era. During this epoch, the Universe is dominated by a scalar field ϕ, called the *inflaton*, and its self-interaction potential $\mathrm{V}(\phi)$ which can be related to the vacuum energy density of the quantum field. The Universe undergoes a phase transition while ϕ slowly rolls down $\mathrm{V}(\phi)$ from an unstable false-vacuum state, with high energy density, towards a stable vacuum state, represented by a local minimum at $\mathrm{V}(\phi_0)$. The slope of the potential must be quite flat so inflation can last enough time to solve the HBB model problems, without spoiling the successful predictions of the HBB. So the inflationary era must smoothly reach to an end (graceful exit) and into a Friedmann expansion stage. The number of inflationary models is large enough (see (Martin et al, 2014) for a review) to give inflation the character of a paradigm. Note that, up to now there is really no viable alternative.

In this section we will review the main aspects of inflation and the generation of the initial fluctuations. Details on the technicalities can be found in textbooks like (Kolb and Turner, 1990; Mukhanov, 2005; Liddle and Lyth, 2000). Finally, we will present the main

aspects on primordial non-Gausianity, generated from the different inflationary scenarios, which is one of the most powerful tools to put constraints on the inflationary era.

2.4.1 Early accelerating expansion

A way to solve the horizon problem would be to assume that the different patches on the sky separated by large distances, and hence unable to communicate, were at some point in the past in causal contact, *i.e.* inside the comoving Hubble radius ($d_{H,c} = c/(aH)$). This means that, a brief time period in the early Universe, before the radiation domination (BBN happens during this epoch), could be added in order to decrease sufficiently the comoving Hubble radius. Following this assumption we get:

$$\frac{d(aH)}{dt} = \ddot{a} > 0 \implies \rho + 3P < 0, \tag{2.48}$$

which is nothing more than a de Sitter space. In such case, the singularity observed for ordinary matter fields ($\rho + 3P > 0 \Rightarrow \ddot{a} < 0$) in the HBB model does not exist, but it is approached asymptotically for $t \to -\infty$. Therefore, when we state that inflation starts at t_*, we really mean time t_* after the HBB singularity. The equation of state of the fluid that governs the inflationary epoch must have a negative pressure (from Eq. (2.48) we get $w < -1/3$). This matches the case of the vacuum described in the previous section, leading to a treatment similar to a cosmological constant dominated Universe. In fact, using the second Friedmann equation [Eq. (2.34)] together with Eq. (2.44) we can get:

$$H^2 + \dot{H} > 0, \tag{2.49}$$

with the exact solutions being:

- $\dot{H} < 0 \implies \dot{H} + H^2 > 0 \implies w = \text{const} \Rightarrow a \propto t^{\alpha}$, $\alpha > 1$
- $\dot{H} = 0 \implies H^2 > 0 \implies w = -1 \Rightarrow a \propto e^{H(t-t_*)}$

- $\dot{H} > 0 \implies H^2 + \dot{H} > 0 \implies w < -1 \Rightarrow a \propto |t - t_*|^{-\alpha}$, $\alpha > 0$.

The second case is the pure de Sitter phase. For the inflationary models we have $-1 < w < -1/3$, where in most of the cases w is close to -1, but never exactly. Therefore, inflation is a phase close to de Sitter with $H \approx$ const.

The minimum requirement for solving the horizon problem is that the largest scales that enter the horizon today must have been inside $d_{H,c}$ during inflation. In other words, the comoving horizon during inflation must be larger than today. This means that inflation has a minimum duration that must be satisfied, given by:

$$\begin{aligned} d_{H,c}(t_i) \geq d_{H,c}(t_0) \;\Rightarrow\; & \frac{a_0}{a_i}(a_i d_{H,c}(t_i)) \geq H_0^{-1} \;\Rightarrow \\ & \frac{a_f}{a_i}\frac{a_0}{a_f} H_I^{-1} \geq H_0^{-1}, \end{aligned} \tag{2.50}$$

where subscripts i and f stand for the initial and final time of the inflationary epoch. The ratio, $N = \ln(a_f/a_i)$, defines the duration of inflation. In order to acquire a nearly flat Universe today the number of *e-folds* must be $N \gtrsim 60$.

The solution to the flatness problem comes for free. Inflation makes now $\Omega = 1$ an attractor in the future and therefore whatever is the initial value of K it will always make the Universe flat after its end [5]. This can be seen as follows from the ratio:

$$\frac{\Omega_f - 1}{\Omega_i - 1} = \frac{d_{H,c}^2(t_f)}{d_{H,c}^2(t_i)} = \frac{a^2(t_i)}{a^2(t_f)} \simeq e^{-2N} \tag{2.51}$$

The solution of inflation to the structure problem will be discussed in Sec. 2.4.3.

2.4.2 Dynamics of Inflation

The inflationary scenario solves the problems of standard HBB model by adding a period of accelerating expansion (close to a de Sitter phase) in the very early Universe.

[5] Note that this does not mean that inflation changes the value of K, whatever there was before inflation is still the same now. However, it makes the relative energy density of curvature very small with respect to the other components.

This indicates that the kind of fluid that drives inflation must have a negative pressure, satisfying the equation of state $P < \rho/3$, and hence it cannot be regular matter or radiation. This resembles the case of a cosmological constant. However, Λ is extremely small during that period and therefore it cannot be the one driving inflation. Here we will present the dynamics of the simplest case of the inflationary models, *i.e.* the single field slow-roll inflation. The physical mechanism that produces the inflationary phase is driven by a homogeneous and isotropic scalar quantum field ϕ, called inflaton, with a "flat" potential. A scalar field, as we will see, can produce energy densities (*e.g.* vacuum state) that mimic those required by the inflationary scenario.

In the simplest case (*e.g.* neglecting coupling terms with other fields) the dynamics of a scalar field are governed by the classical Lagrangian, which is written as:

$$\mathcal{L} = \frac{1}{2}\partial_\mu\phi\partial_\nu\phi - V(\phi), \tag{2.52}$$

where $V(\phi)$ is the potential, whose form is depicted in Figure 2.1. The energy-momentum tensor of such a field is given by:

$$T^{\phi}_{\mu\nu} = -2(\partial\mathcal{L}/\partial g_{\mu\nu}) - g_{\mu\nu}\mathcal{L} \;\Rightarrow T^{\phi}_{\mu\nu} = \phi_{,\mu}\phi_{,\nu} + g_{\mu\nu}[-\frac{1}{2}g^{\alpha\beta}\phi_{,\alpha}\phi_{,\beta} - V(\phi)]. \tag{2.53}$$

In order to describe the dynamics of the scalar field, we split it into a homogeneous zero-order part ϕ_0, describing the background evolution, and a part that describes the first order quantum fluctuations of the field around ϕ_0

$$\phi(t,\mathbf{x}) = \phi_0(t) + \delta\phi(t,\mathbf{x}). \tag{2.54}$$

Considering only the background part and equating the energy-momentum tensor of the

field ϕ with that of a perfect fluid [Eq. (2.31)], we can derive:

$$T_0^0 = -\rho_\phi = -\left(\frac{\dot{\phi_0}^2}{2} + V(\phi)\right) \tag{2.55}$$

$$T_i^i = p_\phi \delta_j^i = \left(\phi = \frac{\dot{\phi_0}^2}{2} - V(\phi)\right)\delta_j^i, \tag{2.56}$$

where ρ_ϕ and p_ϕ are the density and pressure of the scalar field, interpreted as effective quantities since ϕ is not a fluid. These equations are for a particle with a kinetic energy term $\dot{\phi_0}^2/2$, moving in a potential $V(\phi)$ with a velocity $\dot{\phi}$, as shown in Figure 2.1. For a scalar field with a dominating energy density over the kinetic part we get:

$$\frac{1}{2}\dot{\phi} \ll V(\phi) \implies p_\phi \approx -\rho_\phi, \tag{2.57}$$

where the latter is the desired quasi-de Sitter phase, required for an accelerating early epoch. We could have reached to the inflationary regime even if we started from different initial condition (*e.g.* $\frac{1}{2}\dot{\phi} \gg V(\phi)$), if we waited long enough time (*i.e.* inflation is an attractor). This condition is called the *slow-roll* and is essential to get an inflationary mechanism from a scalar field. The Friedmann equation in a period dominated by ϕ can be written as:

$$H^2 = \frac{1}{3M_P^2}\left(\frac{\dot{\phi_0}^2}{2} + V(\phi)\right), \tag{2.58}$$

where the Planck mass is $M_P = 1/\sqrt{8\pi G}$. In the slow-roll case the potential must be flat (*i.e.* $V(\phi) \approx$ const.) and the Friedmann equation becomes $H^2 \approx$ const. Combining the above equation with the fluid equation we can get the EOM for the homogeneous part of the field ϕ_0

$$\ddot{\phi_0} + 3H\dot{\phi_0} = -\frac{dV}{d\phi}. \tag{2.59}$$

In the case of a flat potential the dependence of V and V' on ϕ are very mild and $\ddot{\phi}$

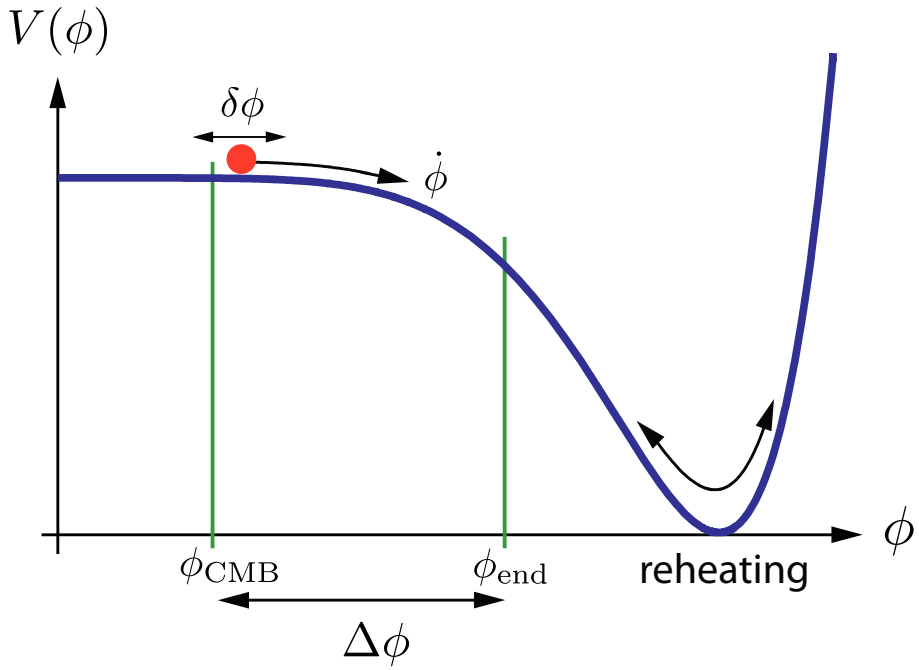

Figure 2.1 – The inflationary potential over which the scalar field slow-rolls. If it is flat enough the scalar field satisfies the slow-roll condition and can be treated as a fluid with negative energy. During this period the Universe is in the accelerating inflationary phase. The potential must be sufficiently flat so that inflation will last for an adequate amount of time, solving the problems of the standard model Inflation needs to stop at some point therefore the field moves towards the local minima where it oscillates around it; this releases the energy difference, heating the universe (*reheating*) and creating elementary particles. Source: Baumann (2009)

is negligible ($\ddot{\phi} \ll 3H\dot{\phi} \;\rightarrow\; 3H\dot{\phi} \simeq -V'$). This second condition must be also satisfied to achieve a sufficient duration of the slow-roll condition. These two conditions give the required information for the structure of the potential. They can be summarized in the form of two undimensional *slow-roll parameters*, defined as:

$$\varepsilon = \frac{M_P^2}{2}\left(\frac{V'}{V}\right)^2 \ll 1, \tag{2.60}$$

$$\eta = M_p^2 \frac{V''}{V} \ll 1. \tag{2.61}$$

The first shows the amount of deviation from the de Sitter phase, *i.e.* the level of "flatness" of the potential. While the second indicates the point that we reach the attractor phase

of inflation, where the kinetic term is smaller than the potential and the scalar field drives inflation. Measuring the values of the slow roll parameters can determine the details of the physical mechanism behind inflation.

The acceleration equation during the inflationary regime (*i.e.* $\ddot{a} = aH^2(1-\varepsilon)$) gives that, the accelerating phase lasts as long as $\ddot{a} > 0 \longleftrightarrow \varepsilon < 1$. For $\varepsilon = 1$ we have the exact definition for the end of inflation. At this point, the potential stops to be flat enough and the de Sitter phase ends. Inflaton moves further towards the local minima of the potential, where it oscillates. Coupling with other fields becomes import at this stage and hence it decays into elementary particles (*reheating*). The Universe now moves into an era of radiation domination and the HBB standard cosmological framework description.

2.4.3 Primordial fluctuations from inflation

Inflation after 35 years is still the most popular paradigm that describes the early universe; not only does it solve major cosmological problems (Sec. 2.4.1), but it also explains the production of the primordial density fluctuations that seed the LSS and the temperature anisotropies we observe in the CMB spectrum. Initially, one of the problems that inflation tried to solve is that of the unwanted relics of Grand Unified Theories (GUT). According to the modern theories of Grand Unification, the Universe underwent many phase transitions, during which spontaneous symmetry breaking occurred. As a result, unwanted relics can be created. Nevertheless, the existence of an accelerated expansion period can dilute every topological inhomogeneity.

Inflation, however, can produce perturbations in the primordial density field, through the quantum fluctuations of the scalar field itself. Quantum fluctuations cannot be wiped away because new ones will always be generated via Heisenberg's uncertainty relation. The cosmological horizon at the time of inflation was very small, therefore the wavelength of the quantum fluctuations of the scalar field dominating the Universe will exceed it soon, due to the inflationary expansion, and become classical. Quantum fluctuations will grow

due to gravitational effects outside the horizon. These perturbations will re-enter the horizon at later times giving rise to galaxies and the large structures we observe today in the Universe.

During inflation, the energy density of the inflaton is the dominant one. Therefore, a fluctuation $\delta\phi$ in the scalar field implies a perturbation in the energy density field. Moreover, through Einstein's field equations [Eq. (2.22)] inflaton fluctuations are coupled to metric perturbations. Thus, curvature perturbations can be generated and hence a gravitational potential, which create fluctuations in the density field. To derive the EOM for the full space-time scalar field of Eq. (2.54), we solve the Einstein equations with the *FLRW* during inflation, where the scalar field is the dominant component, and we get:

$$\ddot{\phi}+3H\dot{\phi}-\frac{\nabla^2\phi}{a^2}=-V'(\phi), \tag{2.62}$$

which after substituting the EOM of the background part gives the equations for the spatial fluctuations of the scalar field:

$$\ddot{\delta\phi}+3H\dot{\delta\phi}+\frac{k^2}{a^2}\delta\phi=0. \tag{2.63}$$

We can express the fluctuations in Fourier space by following the standard way of quantization of a scalar field, by promoting them to a rescaled operator ($\widehat{\delta\phi}=a\delta\phi$) and decomposing them into creation and annihilation operators as

$$\widehat{\delta\phi}(\mathbf{x},\tau)=\int\frac{d^3k}{(2\pi)^{3/2}}\left(u_k(\tau)a_k e^{i\mathbf{kx}}+u_k^*(\tau)a_k^\dagger e^{-i\mathbf{kx}}\right), \tag{2.64}$$

where $u_k(\tau)$ is the mode function of the scalar fluctuations (*i.e.* $u_k(\tau)=a\delta\phi_k$). The annihilation and creation operators follow the commutator relations

$$[a_k,a_{k'}]=[a_k^\dagger,a_{k'}^\dagger]=0,\ [a_k,a_{k'}^\dagger]=\delta^{(3)}(\mathbf{k}-\mathbf{k}'). \tag{2.65}$$

The EOM for the modes $u_k(\tau)$, after using Eq. (2.63), are

$$u_k''(\tau) + \left(k^2 - \frac{a''}{a} + \frac{\partial^2 V(\phi)}{\partial \phi^2}\right) u_k(\tau) = 0, \tag{2.66}$$

where for simplicity we can assume a massless scalar field, *i.e.* $m_\phi^2 = \frac{V(\phi)}{\phi} = 0$, and the primes denote partial derivation with respect to τ. The size of the horizon is proportional to the time t; thus, for $t \to 0$ the size will decrease very fast. Eventually the modes, which depend on the scale factor, will have superhorizon size. Therefore, we can divide the solutions of the above equation into two cases, superhorizon and subhorizon regimes. The horizon crossing is for scales $k = \alpha H$, which are simply the modes with a size of the comoving horizon at that time. For subhorizon scales, $k \gg aH \longleftrightarrow k^2 \gg a''/a$, the mass of the field is negligible; thus the fluctuations are described by ordinary plane waves. In the case of superhorizon scales $k^2 \ll a''/a$, we have a growing and decreasing solution with respect to the scale factor. After matching the two at horizon crossing, we can get the amplitude of the quantum fluctuations as:

$$|\delta\phi_k| = \frac{\widehat{\delta\phi}}{a} = \frac{H}{\sqrt{2k^3}}, \tag{2.67}$$

which is a constant. For subhorizon scales, the amplitude of the fluctuations is oscillatory and decreasing due to the presence of the scale factor, while for superhorizon scales, the amplitude is constant ("frozen"). Knowing the amplitude of the fluctuations of the scalar field on superhorizon scales, we can define their power spectrum (see Sec. 3.5.2) as

$$\langle \delta\phi_k \delta\phi_{k'}^* \rangle = \frac{|u_k|^2}{a^2} \delta^{(3)}(\mathbf{k} - \mathbf{k}'). \tag{2.68}$$

During the quasi-de Sitter phase of inflation, the scalar fluctuations are related to the energy density fluctuations of the field through the Friedmann equation ($H^2 = 8\pi G/3\phi_\phi \simeq 8\pi G V(\phi)$), as

$$\delta\rho_\phi \simeq V'(\phi)\delta\phi = -3H\dot{\phi}\delta\phi. \tag{2.69}$$

Each patch of the Universe of size H^{-1} will expand during the acceleration phase of inflation with a slightly different rate from one an other. This is due to the fact that, quantum fluctuations of the scalar field affect H and therefore the friction term in the EOM [Eq. (2.63)]. This means that, each patch will go through the same history of expansion but at different times. This time shift ($\delta t = -\frac{\delta\phi}{\dot{\phi}}$) can be linked to the difference of the e-fold numbers through the Friedmann and continuity equations as:

$$\delta N \equiv \zeta = H\delta t = -H\frac{\delta\phi}{\dot{\phi}_0} = -\Psi - H\frac{\delta\rho}{\dot{\rho}}, \tag{2.70}$$

where ζ is the curvature *adiabatic* perturbations [6] on a uniform energy density hypersurface and ρ is the energy density of the cosmic fluid. The last equality comes from the perturbed *FLRW* metric, where the field Ψ is the scalar fluctuations of the spatial part. In the absence of anisotropic stress it plays the role of the gravitational potential. Since ζ is a gauge invariant quantity, we can always choose a gauge where the field Ψ disappears (*e.g.* in the spatially flat gauge, $\Psi = 0$). The curvature perturbations follow the behaviour of the inflaton fluctuations, meaning that they will be constant at superhorizon scales. When they enter again inside the horizon, they keep memory from their inflationary period, seeding the density fluctuations that will eventually create the observed LSS and the CMB anisotropies. A proper derivation of the above equation would require to take into account the perturbed cosmological geometry, since the scalar fluctuation must coexist with the metric perturbations (see (Langlois, 2010) for a review).

The amplitude of the scalar fluctuations can be characterized in a statistical way through their two point second moment (see Sec. 3.5.2 for a definition), which is defined in Fourier space as:

$$\langle \delta\phi_{k_1}\delta\phi^*_{k_2}\rangle = (2\pi)^3|\delta\phi_{k_1}|^2\delta_D(\mathbf{k}_1 - \mathbf{k}_2), \tag{2.71}$$

[6] Adiabatic perturbations are induced by a common local time shift of all the background quantities (Langlois, 2010).

where the diagonal part of the correlator has the only non-zero terms, due to the annihilation operators. The dimension-less power spectrum (*i.e.* $\mathcal{P}_\phi(k) = P_\phi(k)(k^3/2\pi^2)$) of the scalar perturbations will be given by:

$$\mathcal{P}_\phi(k) = |\delta\phi_k|^2 = \left(\frac{H}{2\pi}\right)^2, \tag{2.72}$$

which is a scale independent spectrum. Linking this result to the the curvature perturbations, we can get their power spectrum at horizon exit as:

$$\mathcal{P}_\zeta(k) = \left(\frac{H^2}{2\pi\dot{\phi}}\right)\Bigg|_{t_H(k)}. \tag{2.73}$$

For a pure de Sitter phase ($H = \text{const.}$) this is again a scale invariant power spectrum. Note that, during the acceleration phase of inflation, the Universe is in a quasi-de Sitter phase which means that H is almost constant. Thus, the primordial curvature power spectrum will exhibit a scale dependence originating from the time of horizon exit. We can quantify the dimensionless curvature power spectrum in the following way to incorporate this effect:

$$\mathcal{P}_\zeta(k) = \Delta^2_\zeta \left(\frac{k}{k_{\rm piv}}\right)^{n_s - 1}, \tag{2.74}$$

where $k_{\rm piv}$ is a scale of reference called the *pivot* scale. In this thesis we consider $k_{\rm piv} = 0.002\,{\rm Mpc}^{-1}$. Moreover, $\Delta^2_\zeta \equiv \frac{H^2}{2\pi\dot{\phi}}$ is the amplitude of the perturbations and its value, as measured by (Planck Collaboration et al, 2016b), is:

$$10^9\Delta^2_\zeta = \ 2.142 \ \pm \ 0.049, \tag{2.75}$$

at 68% confidence level. The scalar *spectral index* n_s is defined as:

$$n_s - 1 = \frac{d\ln\mathcal{P}_\zeta(k)}{d\ln k}. \tag{2.76}$$

The scale invariance of the power spectrum can be now translated into the case where $n_s = 1$ (the Harrison-Zeldovich power spectrum), which refers to a purely de Sitter phase. Nevertheless, since during inflation we are close to de Sitter, we expect that the generated power spectrum will have a spectral index close to unity, but not exact. The results from *Planck* (Planck Collaboration et al, 2016b) on n_s, which will be used here through out, verify this prediction,

$$n_s = 0.9667 \ \pm \ 0.004, \tag{2.77}$$

at 68% confidence level. The deviation from unity is due to the dynamical process of inflation. Even if a kind of "symmetry" demanded $n_s = 1$, due to the dynamical nature the value would have deviated from unity at some point. The amount of departure from unity can be related to the slow-roll parameters, and hence to the shape of the inflationary potential, through (Bartolo et al, 2004a):

$$n_s - 1 = 2\eta - 6\varepsilon. \tag{2.78}$$

Therefore, measuring the scalar spectral index can give us information on the dynamical details during the inflationary epoch.

2.4.4 Primordial non-Gaussianity

In the simplest inflationary scenarios, *i.e.* single field slow-roll inflation with canonic kinetic terms and vacuum initial states, the predicted primordial curvature fluctuations are Gaussian (or at least very close to that) because of the quadratic nature of the action. To be more precise, the standard inflation predicts a small amount of primordial non-Gaussianity (PNG) in order to be detectable (Acquaviva et al, 2003; Maldacena, 2003; Creminelli, 2003). Violating at least one of the conditions of the standard inflationary model, will generate a deviation from the Gaussian initial conditions (Komatsu et al,

2009). The presence of primordial non-Gaussianity generates a non-zero initial bispectrum (*i.e.* a three-point correlator, see Sec. 3.5.3), which has a maximum signal in a distinct triangle configuration for a different violating condition.

Models that violate the single-field condition, *e.g.* multi-field inflation (Polarski and Starobinsky, 1994; Mukhanov and Steinhardt, 1998) or the curvaton scenario (Lyth and Wands, 2002), have been shown to generate large primordial non-Gaussinaity (Bartolo et al, 2004b; Sasaki et al, 2006; Rigopoulos et al, 2006; Byrnes et al, 2008, 2009; Byrnes and Tasinato, 2009; Byrnes and Choi, 2010). The generated bispectrum [Eq. (2.84)] takes a maximum value in the squeezed configuration ($k_3 \ll k_2 \approx k_1$). Scenarios with non-canonical kinetic terms (*i.e.* higher derivative kinetic terms) or additional field interactions condition produce a significant amount of non-Gaussianity (Linde and Mukhanov, 1997; Zaldarriaga, 2004; Dvali et al, 2004; Chen et al, 2007). Primordial matter bispectrum, from these kind of inflationary models [Eq. (2.86)], is maximized for wave vectors of approximately the same scale (*i.e.* *equilateral* configurations $k_1 \approx k_2 \approx k_3$). A detection would imply enhancement of the field interactions at horizon exit.

In the standard inflation models, as long as field theory applies, the initial quantum state of the scalar fields has to be specified, which will also be the initial state of their perturbations. In quantum field theory in curved space-time these states on the the background de Sitter space are called *Bunch-Davies vacuum*. Besides the use of the adiabatic Bunch-Davies ground state, other excitations can exist due to boundary conditions or low scales of new physics. Violating this condition for the initial state of the quantum fluctuations generated during inflation, can produce PNG (Alishahiha et al, 2004) and a bispectrum with a maximum signal in the folded shapes ($k_3 \approx k_2 \approx 2k_3$). A detection would show that, the initial quantum state of the scalar field is not the vacuum state. More complex shapes of PNG can be generated during inflation, if the slow-roll condition is not satisfied. Models like the ekpyrotic inflation (Khoury et al, 2001; Buchbinder et al, 2008; Lehners and Steinhardt, 2008; Lehners and Steinhardt, 2008; Lehners, 2010)

and vector field populated inflation (Yokoyama and Soda, 2008; Karciauskas et al, 2009; Dimastrogiovanni et al, 2010) have been shown to also produce PNG. For a review on the different inflationary models and the production of PNG from them, can be found in (Martin et al, 2014) and (Bartolo et al, 2004a) respectively.

All these different types of inflation models violate one of the previous conditions and generate large PNG. Therefore, in order to distinguish between all these different mechanisms, we have to gain additional information encompassed in the non-Gaussian part of the primordial perturbations. For a Gaussian random field (see Sec. 3.5.1), all the information for the primordial density field is hold by the power spectrum. This is true due to Wick's theorem (Sec. 3.5.1), which states that all higher moments of a Gaussian random field are just products of the two point correlator. This is not the case, though, for a general random fields. In this thesis, we will manly focus on the first higher order moment, the *bispectrum*, which is the Fourier transformation of the three point correlation function, and is defined as:

$$\langle \zeta_{\mathbf{k}_1} \zeta_{\mathbf{k}_2} \zeta_{\mathbf{k}_3} \rangle = (2\pi)^3 \delta_D (\mathbf{k}_1 + \mathbf{k}_2 + \mathbf{k}_3) B_\zeta(k_1, k_2, k_3), \tag{2.79}$$

where the Dirac delta is present to ensure the conservation of momentum, coming from the translation invariance. Bispectrum, therefore, correlates fluctuations at three points in Fourier space forming a triangle with the three wavevector[7]. It is clear that, the amount of information the bispectrum holds is far greater than that of the power spectrum, which correlates only two points. The number of shapes for the forming triangle is large and the different inflation models predict PNG that picks at different configurations. The Fourier representation of the curvature fluctuations, in the above equation, follow the convention:

$$\zeta_{\mathbf{k}} = \int \frac{d^3x}{(2\pi)^3} \zeta(\mathbf{x}) e^{-i\mathbf{kx}}, \tag{2.80}$$

[7]Throughout this work we will use $k_3 \leq k_2 \leq k_1$ between the modulus of modes in the triangle condition.

which will be the one used through out here. The curvature perturbations can be related to the gravitational potential of the perturbed *FLRW* metric, for components with a barotropic equation of state, as:

$$\Phi_{\mathbf{k}} = \frac{3+3w}{5+3w}\zeta_{\mathbf{k}}, \tag{2.81}$$

where Φ is the Bardeen gravitational potential, which is a gauge-invariant quantity. The Bardeen potential can be reduced to the usual Newtonian gravitational potential in the conformal Newtonian gauge (*i.e.* absence of anisotropic stress) for sub-Hubble scales, up to a minus sign. The choice of Newtonian gauge is ideal for the study of LSS, since it is unique for perturbations decaying at spatial infinity. For a mode that re-enters the horizon at matter domination era ($w = 0$), the above equation reduces to $\Phi_{\mathbf{k}} = 3/5\zeta_{\mathbf{k}}$. In this case, the primordial gravitational potential power spectrum will be:

$$P_{\Phi}(k) = \frac{9}{25}2\pi^2\frac{\Delta^2_{\zeta}}{k^3}\left(\frac{k}{k_{piv}}\right)^{n_s-1}, \tag{2.82}$$

The most studied model of PNG is the *local* (Salopek and Bond, 1990; Gangui et al, 1994; Verde et al, 2000; Komatsu and Spergel, 2001), where as we discussed before has a bispectrum with a maximum signal in the squeezed configurations. The importance of this shape lies in the fact that, for a single field inflation, regardless of whether or not the remaining conditions of standard inflation are satisfied, the predicted primordial bispectrum is the one in the squeezed limit (Creminelli and Zaldarriaga, 2004; Chen et al, 2007; Cheung et al, 2008; Ganc and Komatsu, 2010). Therefore, a detection of a PNG signal of this kind would rule out all single field models (Creminelli and Zaldarriaga, 2004). In the squeezed configuration we can write the primordial gravitational potential in terms of an auxiliary Gaussian random field as a Taylor expansion in real space

$$\Phi(\mathbf{x}) = \Phi_G(\mathbf{x}) + f^{\rm local}_{\rm NL}(\Phi^2_G(\mathbf{x}) - \langle\Phi^2_G(\mathbf{x})\rangle) + \ldots, \tag{2.83}$$

where Φ_G is the Gaussian part and the dimensionless constant $f_{\rm NL}^{\rm loc}$ quantifies the amount of departure from primordial Gaussianity at this first order. The one-point correlator $\langle \Phi_G^2(\mathbf{x})\rangle$ ensures a zero mean value for the field Φ_G, as it is demanded by the relation between curvature and potential. The series can be truncated at a finite order N, introducing additional terms of even momenta (odd moments vanish due to the Gaussianity of Φ_G) of the field Φ_G.

The form of Eq. (2.83) implies that, the primordial potential $\Phi(\mathbf{x})$ random field obeys non-Gaussian statistics for $f_{\rm NL}^{\rm loc} \neq 0$, even if the primordial scalar fluctuations are Gaussian. This can be seen by deriving its higher order correlators, which will be now non-zero [*e.g.* Eq. (2.84)]. The Fourier space version of Eq. (2.83) can be formulated as $\Phi(\mathbf{k}) = \Phi^{(1)}(\mathbf{k}) + f_{\rm NL}^{\rm loc}\Phi^{(2)}(\mathbf{k})$, where the first term is the Gaussian part of the field and $\Phi^{(2)}(\mathbf{k})$ is the second-order non-Gaussian part. The bispectrum of the primordial gravitational potential can be written as

$$\begin{aligned} B_\Phi^{\rm loc}(\mathbf{k}_1,\mathbf{k}_2,\mathbf{k}_3) =& 2 f_{\rm NL}^{\rm loc}(P_\Phi(k_1)P_\Phi(k_2) + P_\Phi(k_2)P_\Phi(k_3) \\ &+ P_\Phi(k_3)P_\Phi(k_1)). \end{aligned} \tag{2.84}$$

Ref. (Creminelli and Zaldarriaga, 2004) proposed the so called *consistency relation*, which gives the primordial bispectrum of the curvature perturbations of all single field inflationary models in the squeezed limit, regardless of whether or not the rest of the conditions are satisfied, as:

$$B_\zeta(k_1,k_2,k_3 \to 0) \to (1-n_s)P_\zeta(k_1)P_\zeta(k_2). \tag{2.85}$$

Taking into account the values of the spectral index shown in the previous section, we see that the primordial non-Gaussian signal of the local type predicted by single field models is very small. Any detection of this kind of bispectrum, larger than what is predicted from the above, would rule out all single field inflationary models.

The primordial bispectrum of the equilateral type, as produced by inflation, has the form (Creminelli et al, 2006)

$$\begin{aligned} B_{\Phi}^{\rm equil}(\mathbf{k}_1,\mathbf{k}_2,\mathbf{k}_3) = 6 f_{\rm NL}^{\rm eq}(&-(P_{\Phi}(k_1)P_{\Phi}(k_2)+2cyc.) \\ &-2(P_{\Phi}(k_1)P_{\Phi}(k_2)P_{\Phi}(k_3))^{2/3} \\ &+(P_{\Phi}^{1/3}(k_1)P_{\Phi}^{2/3}(k_2)P_{\Phi}(k_3)+5{\rm perm})). \end{aligned} \tag{2.86}$$

It is easy to see that, the signal of B_{Φ}^{equil} is maximum for the equilateral template (*i.e.* $k_1 \approx k_2 \approx k_3$). An additional shape that we would like to test here is the one nearly *orthogonal* to the local and equilateral cases. Its initial bispectrum is given by (Senatore et al, 2010)

$$\begin{aligned} B_{\Phi}^{\rm orth}(\mathbf{k}_1,\mathbf{k}_2,\mathbf{k}_3) = 6 f_{\rm NL}^{\rm orth}(&-3(P_{\Phi}(k_1)P_{\Phi}(k_2)+2cyc.) \\ &-8(P_{\Phi}(k_1)P_{\Phi}(k_2)P_{\Phi}(k_3))^{2/3} \\ &+3(P_{\Phi}^{1/3}(k_1)P_{\Phi}^{2/3}(k_2)P_{\Phi}(k_3)+5{\rm perm})). \end{aligned} \tag{2.87}$$

Higher moments to the bispectrum can exist, in the case of PNG, although the complexity of their numerical evaluation increases dramatically. The first one beyond the three point correlator is the *trispectrum*, which correlates four points and its values depends on the closed quadrilateral formed by the modes. For the gravitational potential it is defined as follows:

$$\langle \Phi(\mathbf{k}_1)\Phi(\mathbf{k}_2)\Phi(\mathbf{k}_3)\Phi(\mathbf{k}_4)\rangle = (2\pi)^3 \delta_D(\mathbf{k}_{1234}) T_{\Phi}(\mathbf{k}_1,\mathbf{k}_2,\mathbf{k}_3,\mathbf{k}_4), \tag{2.88}$$

In order to use non-Gaussianities as a probe of the early Universe, and more precisely for the aspects of inflation, we need to measure the shape of the primordial bispectrum and the magnitude of its signal (*i.e.* constraining the $f_{\rm NL}$ parameter). Mainly, there are two ways to get information about the perturbations in the early universe, from the CMB anisotropies and from the abundance and clustering of the LSS. The tightest constraints

up to now come from CMB, where Planck Collaboration et al (2016a) measured for the three shapes considered here at 68% confidence level:

$$f_{\rm NL}^{\rm loc} = 0.8 \ \pm \ 5, \tag{2.89}$$

$$f_{\rm NL}^{\rm eq} = -4 \ \pm \ 43, \tag{2.90}$$

$$f_{\rm NL}^{\rm orth} = -26 \ \pm \ 21, \tag{2.91}$$

while for the higher order parameter in the local tripsectrum the 68% confidence level constraints are:

$$g_{NL}{}^{\rm loc} = (-9 \ \pm \ 7.7) \times 10^4. \tag{2.92}$$

The constraints seem tight, especially in the local case, however they are far from excluding PNG.

The importance of determining and measuring primordial non-Gaussianities is tremendous. Inflation is the dominant theory that describes this period, but the variety of models is quite large. The detection of non-Gaussianities can provide a way to distinguish between the different classes of inflationary models and eliminate those that don't predict such amount of deviation from the exact Gaussian distribution. Each inflationary model leaves a unique imprint, determining the shape of the bispectrum and trispectrum. The detection of a non-Gaussian signal through the CMB anisotropies, LSS clustering, gravitational lensing, the abundance of galaxies and the Lyman-a forest can give the information needed, in order to understand the physics of the early Universe.

Chapter 3

Cosmological Perturbation Theory

3.1 Introduction

One of the most important quests of cosmology is to understand the large scale structures seen in the Universe. The current prevailing explanation of their origin is that they are created from small fluctuations of the density field, which in turn exhibit a growth in amplitude due to gravitational instabilities. These initial perturbations can be generated naturally, from within the framework of inflation (Sec. 2.4.3), from quantum fluctuations that grow to super-horizon scales. On their re-entrance, they are induced in the *dark matter* field, which dominates the Universe during the period of LSS formation. Regular matter, *i.e. baryons*, is trapped inside the gravitational potential wells of the dark matter density fluctuations. In turn due to gravitational instabilities, they collapse and cool in order to form the observed galaxies.

Understanding the dynamical evolution of the density and velocity fields of matter fluctuations, is the purpose of standard cosmological *Perturbation Theory* (PT). A perturbative approach is well suited to describe the dynamics of the gravitational instabilities at large scales, where the density fluctuations are small enough. In the PT framework a valid assumption is made, that gravity is the sole source of structure formation in the large scale regime. This is no longer true at smaller scales, where non-gravitational effects can affect the distribution of luminous matter. Furthermore, the non-linear nature of gravitational evolution will eventually bring an end to the predictive power of perturbation

theory. In the small scale regime ($k_{NL}(z=0) \lesssim 0.24\,\mathrm{h/Mpc}$ for the reference cosmology), where non-linearities are strong and non-perturbative effects dominate the dynamics, any kind of perturbative approach would breaks down. There is though a regime, *i.e.* quasi non-linear scales, where higher-order corrections to the linear PT can adequately describe the non-linear evolution of matter. The main assumption under which PT operates are:

- In the regime of large scales (valid regime of PT) baryonic pressure is neglected, *i.e.* matter is cold. Cold dark matter (CDM) and baryons are treated as a presureless single field.

- The description is restrained in scales much smaller than Hubble radius ($k \gg aH$). Since matter is non relativistic ($v_{pec} \ll c$), the Newtonian fluid equations can be used to describe the evolution of the matter field.

In this chapter we will present the main results of *Standard Perturbation Theory* (SPT) (Eulerian and Lagrangian framework), up to the scales it is valid, as well as outline the predictions of Renormalized Perturbation theory (RPT) (Crocce and Scoccimarro, 2006b) and in particular the MPTbreeze formalism (Bernardeau et al, 2008; Crocce et al, 2012). For the SPT framework, the reader is referred to the classic review of (Bernardeau et al, 2002) and references within. In addition, we will describe the statistical tools needed to match the theoretical description with observations, that swarm modern cosmology.

3.2 Eulerian Perturbation Theory

The dynamics of a single component Newtonian fluid, as is the one assumed in SPT, can be characterized only by its over-density ($\delta \equiv \rho/\overline{\rho} - 1$) and its peculiar velocity fields ($\mathbf{u} = d\mathbf{x}/d\tau$). It is just a matter of redefining these quantities to incorporate the expansion of the Universe. The position of the particles will be set in the comoving coordinates ($\mathbf{r} = a(t)\mathbf{x}$) and the evolution will be described with respect to the conformal time τ. In

the pressureless fluid approximation the continuity, Euler[1] and Poisson equations are in comoving coordinates:

$$\frac{\partial\delta(\mathbf{x},\tau)}{\partial\tau}+\boldsymbol{\nabla}[(1+\delta(\mathbf{x},\tau))\mathbf{u}]=0, \tag{3.1}$$

$$\frac{\partial\mathbf{u}(\mathbf{x},\tau)}{\partial\tau}+\mathcal{H}\mathbf{u}+(\mathbf{u}\boldsymbol{\nabla})\mathbf{u}=\boldsymbol{\nabla}\Phi, \tag{3.2}$$

$$\boldsymbol{\nabla}^2\Phi=4\pi a^2\overline{\rho}(\tau)\delta(\mathbf{x},\tau), \tag{3.3}$$

where the conformal Hubble rate is given as $\mathcal{H}=aH$ and Φ is the gravitational potential. These equations are non-linear, since all the above quantities are non-linear fluctuations. In addition, it is a closed system of equations, since we have used the perfect fluid approximation. This implies that, the form of these equations is only valid in the ΛCDM model or any other model that is build under the perfect fluid assumption. The price to pay for this choice is that we assume perfect knowledge of the density and velocity fields. Nevertheless, the prefect fluid approximation breaks down on small scales and with it the SPT description. Furthermore, we have made the assumption that the vorticity (*i.e.* $\boldsymbol{\nabla}\times\mathbf{u}$) can be neglected. This is valid at linear scales, where expansion prevents irrotational characteristics in the fluid, as long as the stress tensor $\sigma_{ij}\approx 0$. In general this does not hold in small scales, where multi-streaming and shocks generate vorticity. Moreover, we assume that the fluid is irrotational (*i.e.* spherical symmetry). By combining the above equations and transforming the fields in Fourier space, we get the EOM for the gravitational instability, which is characterised solely by the overdensity and velocity divergence fields, as:

$$\frac{\partial\delta(\mathbf{k},\tau)}{\partial\tau}+\theta(\mathbf{k},\tau)=-\int\frac{d^3k_1}{(2\pi)^3}\int\frac{d^3k_2}{(2\pi)^3}(2\pi)^3\delta_D(\mathbf{k}-\mathbf{k}_{12})\alpha(\mathbf{k}_1,\mathbf{k}_2)\theta(\mathbf{k}_1,\tau)\delta(\mathbf{k}_2,\tau), \tag{3.4}$$

$$\frac{\partial\theta(\mathbf{k},\tau)}{\partial\tau}+\mathcal{H}(\tau)\theta(\mathbf{k},\tau)+\frac{3}{2}\mathcal{H}^2(\tau)\Omega_m(\tau)\delta(\mathbf{k},\tau)=-\int_{\mathbf{k}_1}\int_{\mathbf{k}_2}(2\pi)^3\delta_D(\mathbf{k}_{12}-\mathbf{k})\beta(\mathbf{k}_1,\mathbf{k}_2)\theta(\mathbf{k}_1,\tau)\theta(\mathbf{k}_2,\tau), \tag{3.5}$$

[1]Continuity and Euler equation can be derived as the zero and first moments of the Vlasov equation.

where $\mathbf{k}_{ij\ldots} \equiv \mathbf{k}_i + \mathbf{k}_j + \cdots$. The above are just the Euler and continuity equations in Fourier space, while the field $\theta \equiv \boldsymbol{\nabla}\mathbf{u}(\mathbf{x},\tau)$ is the velocity divergence. The left hand side of Eqs. (3.4) and (3.5) is the linear part, while the right hand side encodes the non-linear evolution that generates mode couplings, imprinted in functions $\alpha(\mathbf{k}_1,\mathbf{k}_2)$ and $\beta(\mathbf{k}_1,\mathbf{k}_2)$. They are given by:

$$\alpha(\mathbf{k}_1,\mathbf{k}_2) = \frac{\mathbf{k}_{12}\cdot\mathbf{k}_1}{k_1^2}, \quad \beta(\mathbf{k}_1,\mathbf{k}_2) = \frac{k_{12}^2(\mathbf{k}_1\cdot\mathbf{k}_2)}{2k_1^2k_2^2}. \tag{3.6}$$

In the SPT framework the solution of the Euler and continuity equations can be found perturbatively with respect to the linear solution, under the assumption of small linear fluctuations, as:

$$\delta(\mathbf{k},\tau) = \sum_{n=1}^{\infty}\delta^{(n)}(\mathbf{k},\tau), \quad \theta(\mathbf{k},\tau) = \sum_{n=1}^{\infty}\theta^{(n)}(\mathbf{k},\tau), \tag{3.7}$$

where the superscript (n) denoted the term of the Taylor expansion.

3.2.1 Linear solution

The first term of the expansion in Eq. (3.2) is the linear solution. At this first order, the density and velocity fields are small enough, such that any non-linear couplings between the modes can be neglected (*i.e.* each mode evolves independently). The Euler and continuity equations [Eqs. (3.4) and (3.5)] will be now:

$$\frac{\partial^2\delta^{(1)}(\mathbf{k},\tau)}{\partial\tau^2} + \mathcal{H}(\tau)\frac{\partial\delta^{(1)}(\mathbf{k},\tau)}{\partial\tau} - \frac{3}{2}\Omega_m(\tau)\mathcal{H}^2(\tau)\delta^{(1)}(\mathbf{k},\tau) = 0. \tag{3.8}$$

The second term is the friction term, coming from the Hubble flow, while the third is the force term. To derive this equation, we have used the linear part of the continuity equation ($\frac{\partial\delta_{\mathbf{k}}^{(1)}(\tau)}{\partial\tau} = -\theta_{\mathbf{k}}(\tau)$). The solution of the density field is now a second-order differential

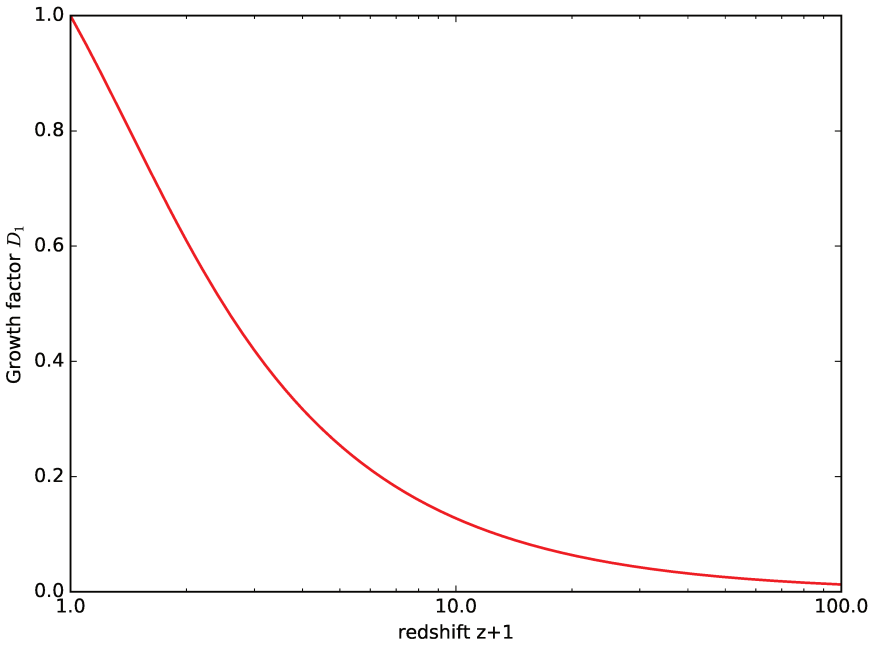

Figure 3.1 – The normalized linear growth factor $D(z)$ with respect to redshift z for the cosmology considered here.

equation, *i.e.* two independent solutions splitted into a growing $D_1^{(+)}$ and a decaying mode $D_1^{(-)}$, given by:

$$\delta_{\mathbf{k}}(\tau)^{(1)} = D_1^{(+)}(\tau)A_{\mathbf{k}} + D_1^{(-)}(\tau)B_{\mathbf{k}}, \theta_{\mathbf{k}}(\tau)^{(1)} = -\frac{\partial\delta_{\mathbf{k}}(\tau)}{\partial\tau} = -[\frac{d\ln D_1^{(+)}}{d\tau}A_{\mathbf{k}} + -\frac{d\ln D_1^{(-)}}{d\tau}(\tau)B_{\mathbf{k}}], \tag{3.9}$$

where $A_{\mathbf{k}}$ and $B_{\mathbf{k}}$ are spatial functions that describe the initial density field. Plugging the solution for the density field back in Eq. (3.2.1), we get for an Einstein-de Sitter (EdS) Universe (*i.e.* $\Omega_m = 1$ and $\Omega_\Lambda = 0$):

$$D_1^{(+)} = a, \quad D_1^{(-)} = a^{-3/2}. \tag{3.10}$$

The decaying mode dies very fast and hence holds no interest. The growing mode shows that, the density perturbations on large scales evolve independent of each other (*i.e.*

without any mixing). Therefore, we define the *linear growth factor* as $D(\tau) \equiv D_1^{(+)}(\tau)$. It describes the growth of the overdensity field from some reference time τ_0 to some later time τ, *i.e.* $\delta_{\mathbf{k}}(\tau)^{(1)} = D(\tau)\delta_{\mathbf{k}}^{(1)}(\tau_0)$. Usually, this time is taken to be the present, implying a normalization of $D(\tau_0)$ to unity (*i.e.* $D(z) = D(z)/D(0)$). One can easily see that during matter domination era, which is the epoch SPT assumes LSS formation takes place, the gravitational potential is constant. The linear velocity divergence field will be:

$$\theta^{(1)}(\tau) = -f\mathcal{H}(\tau)\delta^{(1)}\delta_{\mathbf{k}}^{(1)}(\tau), \tag{3.11}$$

where $f = d\ln D(\tau)/d\ln a$ is the *linear growth rate*. In the case of a Universe populated by only matter and cosmological constant, the growth factor is given by:

$$D(a) = H(a)\frac{5\Omega_m}{2}\int_0^a \frac{da}{a^3 H(a)}. \tag{3.12}$$

The growth factor and the growth rate, for the cosmology considered here, are plotted in Figures 3.1 and 3.2 respectively.

From the Poisson equation [Eq. (3.3)] we can relate the linear density contrast with the linearly evolved Bardeen gravitational potential fluctuations, inside the horizon, as:

$$k^2\Phi_k(a) = 4\pi G\overline{\rho}(a)\delta_{\mathbf{k}}^{(1)}(a) = \frac{3}{2}H_0^2\Omega_m(a)\delta_{\mathbf{k}}^{(1)}(a). \tag{3.13}$$

Due to pressure, modes that enter during the radiation domination era are suppressed with respect to those at superhorizon scales. The latter remain frozen, as we have already shown in Sec. 2.4.3. In addition, the strong coupling of baryons with photons refrain the former from contributing to the growth of matter fluctuations. This leads to a suppression in the growth (logarithmic growth) of the gravitational potential for small wavelength modes. In order to take into account this effect, the perturbed Einstein and Boltzmann equations should be solved for a coupled baryon-photon fluid. This task is performed numerically, by algorithms such as CAMB (Lewis et al, 2000), which is the one used

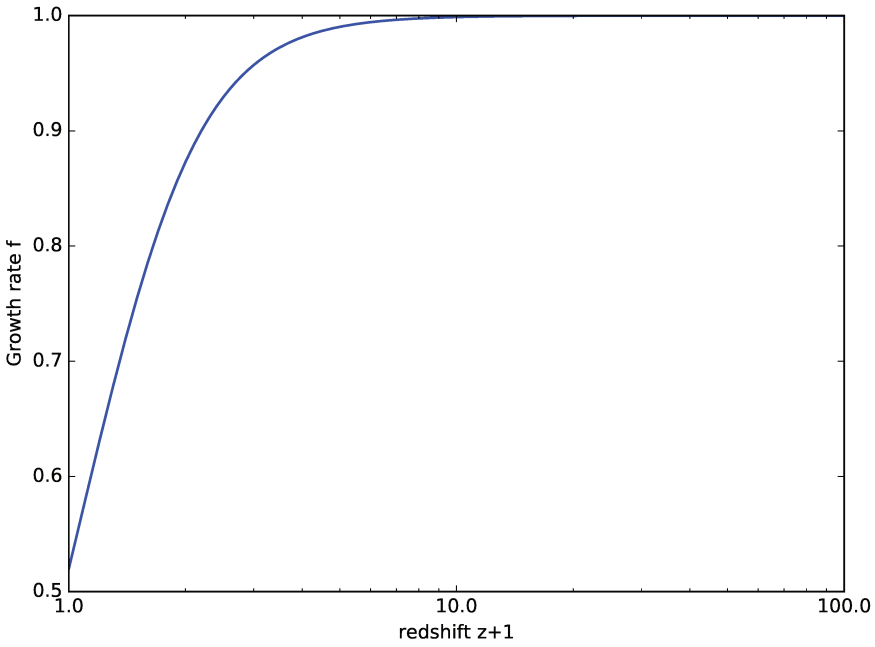

Figure 3.2 – The growth rate f with respect to redshift for the cosmology considered here.

throughout this thesis. The output of these codes is in the form of the *tranfer function* $T(k)$, which describes the delayed growth of small wavelength fluctuations, as they evolve from the radiation to matter domination era. This function does not affect the large scale modes, since they do not suffer from the effect of pressure suppression (*i.e.* $T(k \to 0) = 1$). Multiplying this function with the above equation, gives the final relation between the linear overdensity field and the gravitational potential fluctuations as:

$$\delta^{(1)}(\mathbf{k}, z) = \frac{2k^2 c^2 T(k) D(z)}{3\Omega_{m,0} H_0^2} \Phi(\mathbf{k}) = M(k, z)\Phi(\mathbf{k}), \tag{3.14}$$

which is written with respect to redshift, in order to make the connection with the following chapters.

3.2.2 Non-linear solution

Up to now, we have considered that we are on large enough scales, such that we can safely neglect the mode coupling term of Eqs. (3.4) and (3.5). Including this part and solving the EOM, we can acquire the non-linear solution for the density contrast and the velocity gradient fields. Using the Taylor expansion of Eq. (3.2) and the linear solution of the fields (Sec. 3.2.1), we can get the n-th order solution for the overdensity and velocity divergence fields with respect to the linear density as:

$$\delta(\mathbf{k},\tau) = \sum_{n=1}^{\infty} D_n(\tau) \int \frac{d^3k_1}{(2\pi)^3} \dots \int \frac{d^3k_n}{(2\pi)^3} \delta_D(\mathbf{k}-\mathbf{k}_{1\dots n}) F_n(\mathbf{k}_1,\dots,\mathbf{k}_n) \delta^{(1)}_{\mathbf{k}_1} \dots \delta^{(1)}_{\mathbf{k}_n}, \tag{3.15}$$

$$\theta(\mathbf{k},\tau) = -f\mathcal{H} \sum_{n=1}^{\infty} D_n(\tau) \int \frac{d^3k_1}{(2\pi)^3} \dots \int \frac{d^3k_n}{(2\pi)^3} \delta_D(\mathbf{k}-\mathbf{k}_{1\dots n}) G_n(\mathbf{k}_1,\dots,\mathbf{k}_n) \delta^{(1)}(\mathbf{k}_1) \dots \delta^{(1)}(\mathbf{k}_n). \tag{3.16}$$

The kernels F_n and G_n incorporate the non-linear mode coupling induced by gravity. The first order is just the linear solution and hence $F_1 = 1$ and $G_n = 1$. In an EdS Universe ($f = 1$), the n-th order growth factor is $D_n = D_1^n$. The difference in the above equations between ΛCDM and EdS cosmologies, is a factor of Ω_m/f^2. Luckily enough its value is close to unity, since the growth rate in ΛCDM has been found to be $f \simeq \Omega_m^{0.59}$. Therefore, we can safely take all the higher order growth factors in ΛCDM to be $D_n \simeq D_1^n$ and use the kernel results of an EdS Universe. The higher order kernels can be found from the following recursion relation (Goroff et al, 1986; Jain and Bertschinger, 1994):

$$\begin{aligned} F_n(\mathbf{q}_1,\dots,\mathbf{q}_n) &= \sum_{m=1}^{n-1} \frac{G_m(\mathbf{q}_1,\dots,\mathbf{q}_m)}{(2n+3)(n-1)} \Big[(2n+1)\alpha(\mathbf{k}_1,\mathbf{k}_2) F_{n-m}(\mathbf{q}_{m+1},\dots,\mathbf{q}_n) \\ &\quad + 2\beta(\mathbf{k}_1,\mathbf{k}_2) G_{n-m}(\mathbf{q}_{m+1},\dots,\mathbf{q}_n) \Big], \end{aligned} \tag{3.17}$$

$$\begin{aligned} G_n(\mathbf{q}_1,\dots,\mathbf{q}_n) &= \sum_{m=1}^{n-1} \frac{G_m(\mathbf{q}_1,\dots,\mathbf{q}_m)}{(2n+3)(n-1)} \Big[3\alpha(\mathbf{k}_1,\mathbf{k}_2) F_{n-m}(\mathbf{q}_{m+1},\dots,\mathbf{q}_n) \\ &\quad + 2n\beta(\mathbf{k}_1,\mathbf{k}_2) G_{n-m}(\mathbf{q}_{m+1},\dots,\mathbf{q}_n) \Big], \end{aligned} \tag{3.18}$$

where $\mathbf{k}_1 \equiv \mathbf{q}_1 + \ldots + \mathbf{q}_m,\ \mathbf{k}_2 \equiv \mathbf{q}_{m+1} + \ldots + \mathbf{q}_n,\ \mathbf{k} \equiv \mathbf{k}_1 + \mathbf{k}_2$. Up to third order, the symmetrized kernels (*i.e.* sum of the n-th order kernels over all possible permutations of the modes) for the density field are:

$$F_1(\mathbf{k}) = 1, \tag{3.19}$$

$$F_2^{(s)}(\mathbf{k}_1, \mathbf{k}_2) = \frac{5}{7} + \frac{1}{2}\frac{\mathbf{k}_1 \cdot \mathbf{k}_2}{k_1 k_2}\left(\frac{k_1}{k_2} + \frac{k_2}{k_1}\right) + \frac{2}{7}\left(\frac{\mathbf{k}_1 \cdot \mathbf{k}_2}{k_1 k_2}\right)^2, \tag{3.20}$$

$$\begin{aligned} F_3^{(s)}(\mathbf{k}_1, \mathbf{k}_2, \mathbf{k}_3) = {} & \frac{7}{54}\Big[F_2^{(s)}(\mathbf{k}_1, \mathbf{k}_2)\alpha(\mathbf{k}_3, \mathbf{k}_{12}) + F_2^{(s)}(\mathbf{k}_2, \mathbf{k}_3)\alpha(\mathbf{k}_1, \mathbf{k}_{23}) + F_2^{(s)}(\mathbf{k}_3, \mathbf{k}_1)\alpha(\mathbf{k}_2, \mathbf{k}_{31}) \\ & + G_2^{(s)}(\mathbf{k}_1, \mathbf{k}_2)\alpha(\mathbf{k}_{12}, \mathbf{k}_3) + G_2^{(s)}(\mathbf{k}_2, \mathbf{k}_3)\alpha(\mathbf{k}_{23}, \mathbf{k}_1) + G_2^{(s)}(\mathbf{k}_3, \mathbf{k}_1)\alpha(\mathbf{k}_{31}, \mathbf{k}_2)\Big] \\ & + \frac{2}{27}\Big[G_2^{(s)}(\mathbf{k}_1, \mathbf{k}_2)\beta(\mathbf{k}_{12}, \mathbf{k}_3) + G_2^{(s)}(\mathbf{k}_2, \mathbf{k}_3)\beta(\mathbf{k}_{23}, \mathbf{k}_1) + G_2^{(s)}(\mathbf{k}_3, \mathbf{k}_1)\beta(\mathbf{k}_{31}, \mathbf{k}_2)\Big], \end{aligned} \tag{3.21}$$

$$\begin{aligned} F_4^{(s)}(\mathbf{k}_1, \mathbf{k}_2, \mathbf{k}_3, \mathbf{k}_4) = {} & \frac{1}{792}\big[2G_2^{(s)}(\mathbf{k}_1, \mathbf{k}_4) \\ & (18F_2^{(s)}(\mathbf{k}_2, \mathbf{k}_3)\alpha(\mathbf{k}_1 + \mathbf{k}_4, \mathbf{k}_2 + \mathbf{k}_3) + 8G_2^{(s)}(\mathbf{k}_2, \mathbf{k}_3)\beta(\mathbf{k}_2 + \mathbf{k}_3, \mathbf{k}_1 + \mathbf{k}_4)) \\ & + 2G_2^{(s)}(\mathbf{k}_1, \mathbf{k}_3)(18F_2^{(s)}(\mathbf{k}_2, \mathbf{k}_4)\alpha(\mathbf{k}_1 + \mathbf{k}_3, \mathbf{k}_2 + \mathbf{k}_4) + 8G_2^{(s)}(\mathbf{k}_2, \mathbf{k}_4)\beta(\mathbf{k}_1 + \mathbf{k}_3, \mathbf{k}_2 + \mathbf{k}_4)) \\ & + 2G_2^{(s)}(\mathbf{k}_1, \mathbf{k}_2)(18F_2^{(s)}(\mathbf{k}_3, \mathbf{k}_4)\alpha(\mathbf{k}_1 + \mathbf{k}_2, \mathbf{k}_3 + \mathbf{k}_4) + 8G_2^{(s)}(\mathbf{k}_3, \mathbf{k}_4)\beta(\mathbf{k}_1 + \mathbf{k}_2, \mathbf{k}_3 + \mathbf{k}_4)) \\ & + 6G_3^{(s)}(\mathbf{k}_1, \mathbf{k}_2, \mathbf{k}_3)(9\alpha(\mathbf{k}_1 + \mathbf{k}_2 + \mathbf{k}_3, \mathbf{k}_4) + 4\beta(\mathbf{k}_1 + \mathbf{k}_2 + \mathbf{k}_3, \mathbf{k}_4)) \\ & + 6G_3^{(s)}(\mathbf{k}_1, \mathbf{k}_2, \mathbf{k}_4)(9\alpha(\mathbf{k}_1 + \mathbf{k}_2 + \mathbf{k}_4, \mathbf{k}_3) + 4\beta(\mathbf{k}_3, \mathbf{k}_1 + \mathbf{k}_2 + \mathbf{k}_4)) \\ & + 6G_3^{(s)}(\mathbf{k}_1, \mathbf{k}_3, \mathbf{k}_4)(9\alpha(\mathbf{k}_1 + \mathbf{k}_3 + \mathbf{k}_4, \mathbf{k}_2) + 4\beta(\mathbf{k}_2, \mathbf{k}_1 + \mathbf{k}_3 + \mathbf{k}_4)) \\ & + 6G_3^{(s)}(\mathbf{k}_2, \mathbf{k}_3, \mathbf{k}_4)(9\alpha(\mathbf{k}_2 + \mathbf{k}_3 + \mathbf{k}_4, \mathbf{k}_1) + 4\beta(\mathbf{k}_1, \mathbf{k}_2 + \mathbf{k}_3 + \mathbf{k}_4)) \\ & + 36F_2^{(s)}(\mathbf{k}_1, \mathbf{k}_4)G_2^{(s)}(\mathbf{k}_2, \mathbf{k}_3)\alpha(\mathbf{k}_2 + \mathbf{k}_3, \mathbf{k}_1 + \mathbf{k}_4) \\ & + 36F_2^{(s)}(\mathbf{k}_1, \mathbf{k}_3)G_2^{(s)}(\mathbf{k}_2, \mathbf{k}_4)\alpha(\mathbf{k}_2 + \mathbf{k}_4, \mathbf{k}_1 + \mathbf{k}_3) \\ & + 36F_2^{(s)}(\mathbf{k}_1, \mathbf{k}_2)G_2^{(s)}(\mathbf{k}_3, \mathbf{k}_4)\alpha(\mathbf{k}_3 + \mathbf{k}_4, \mathbf{k}_1 + \mathbf{k}_2) \\ & + 54F_3^{(s)}(\mathbf{k}_1, \mathbf{k}_2, \mathbf{k}_3)\alpha(\mathbf{k}_4, \mathbf{k}_1 + \mathbf{k}_2 + \mathbf{k}_3) + 54F_3^{(s)}(\mathbf{k}_1, \mathbf{k}_2, \mathbf{k}_4)\alpha(\mathbf{k}_3, \mathbf{k}_1 + \mathbf{k}_2 + \mathbf{k}_4) \\ & + 54F_3^{(s)}(\mathbf{k}_1, \mathbf{k}_3, \mathbf{k}_4)\alpha(\mathbf{k}_2, \mathbf{k}_1 + \mathbf{k}_3 + \mathbf{k}_4) + 54F_3^{(s)}(\mathbf{k}_2, \mathbf{k}_3, \mathbf{k}_4)\alpha(\mathbf{k}_1, \mathbf{k}_2 + \mathbf{k}_3 + \mathbf{k}_4)\big] \end{aligned} \tag{3.22}$$

while for the velocity divergence field they are:

$$G_1(\mathbf{k}) = 1, \tag{3.23}$$

$$G_2^{(s)}(\mathbf{k}_1, \mathbf{k}_2) = \frac{3}{7} + \frac{1}{2}\frac{\mathbf{k}_1 \cdot \mathbf{k}_2}{k_1 k_2}\left(\frac{k_1}{k_2} + \frac{k_2}{k_1}\right) + \frac{4}{7}\left(\frac{\mathbf{k}_1 \cdot \mathbf{k}_2}{k_1 k_2}\right)^2, \tag{3.24}$$

$$\begin{aligned} G_3^{(s)}(\mathbf{k}_1, \mathbf{k}_2, \mathbf{k}_3) = \frac{1}{18}\Big[& F_2^{(s)}(\mathbf{k}_1, \mathbf{k}_2)\alpha(\mathbf{k}_3, \mathbf{k}_{12}) + F_2^{(s)}(\mathbf{k}_2, \mathbf{k}_3)\alpha(\mathbf{k}_1, \mathbf{k}_{23}) + F_2^{(s)}(\mathbf{k}_3, \mathbf{k}_1)\alpha(\mathbf{k}_2, \mathbf{k}_{31}) \\ & + G_2^{(s)}(\mathbf{k}_1, \mathbf{k}_2)\alpha(\mathbf{k}_{12}, \mathbf{k}_3) + G_2^{(s)}(\mathbf{k}_2, \mathbf{k}_3)\alpha(\mathbf{k}_{23}, \mathbf{k}_1) + G_2^{(s)}(\mathbf{k}_3, \mathbf{k}_1)\alpha(\mathbf{k}_{31}, \mathbf{k}_2)\Big] \\ & + \frac{2}{9}\Big[G_2^{(s)}(\mathbf{k}_1, \mathbf{k}_2)\beta(\mathbf{k}_{12}, \mathbf{k}_3) + G_2^{(s)}(\mathbf{k}_2, \mathbf{k}_3)\beta(\mathbf{k}_{23}, \mathbf{k}_1) + G_2^{(s)}(\mathbf{k}_3, \mathbf{k}_1)\beta(\mathbf{k}_{31}, \mathbf{k}_2)\Big], \end{aligned} \tag{3.25}$$

$$\begin{aligned} G_4^{(s)}(\mathbf{k}_1, \mathbf{k}_2, \mathbf{k}_3, \mathbf{k}_4) = \frac{1}{792}\big[& 2G_2^{(s)}(\mathbf{k}_1, \mathbf{k}_4) \\ & (6F_2^{(s)}(\mathbf{k}_2, \mathbf{k}_3)\alpha(\mathbf{k}_1 + \mathbf{k}_4, \mathbf{k}_2 + \mathbf{k}_3) + 32G_2^{(s)}(\mathbf{k}_2, \mathbf{k}_3)\beta(\mathbf{k}_2 + \mathbf{k}_3, \mathbf{k}_1 + \mathbf{k}_4)) \\ & + 2G_2^{(s)}(\mathbf{k}_1, \mathbf{k}_3)(6F_2^{(s)}(\mathbf{k}_2, \mathbf{k}_4)\alpha(\mathbf{k}_1 + \mathbf{k}_3, \mathbf{k}_2 + \mathbf{k}_4) + 32G_2^{(s)}(\mathbf{k}_2, \mathbf{k}_4)\beta(\mathbf{k}_1 + \mathbf{k}_3, \mathbf{k}_2 + \mathbf{k}_4)) \\ & + 2G_2^{(s)}(\mathbf{k}_1, \mathbf{k}_2)(6F_2^{(s)}(\mathbf{k}_3, \mathbf{k}_4)\alpha(\mathbf{k}_1 + \mathbf{k}_2, \mathbf{k}_3 + \mathbf{k}_4) + 32G_2^{(s)}(\mathbf{k}_3, \mathbf{k}_4)\beta(\mathbf{k}_1 + \mathbf{k}_2, \mathbf{k}_3 + \mathbf{k}_4)) \\ & + 6G_3^{(s)}(\mathbf{k}_1, \mathbf{k}_2, \mathbf{k}_3)(3\alpha(\mathbf{k}_1 + \mathbf{k}_2 + \mathbf{k}_3, \mathbf{k}_4) + 16\beta(\mathbf{k}_1 + \mathbf{k}_2 + \mathbf{k}_3, \mathbf{k}_4)) \\ & + 6G_3^{(s)}(\mathbf{k}_1, \mathbf{k}_2, \mathbf{k}_4)(3\alpha(\mathbf{k}_1 + \mathbf{k}_2 + \mathbf{k}_4, \mathbf{k}_3) + 16\beta(\mathbf{k}_3, \mathbf{k}_1 + \mathbf{k}_2 + \mathbf{k}_4)) \\ & + 6G_3^{(s)}(\mathbf{k}_1, \mathbf{k}_3, \mathbf{k}_4)(3\alpha(\mathbf{k}_1 + \mathbf{k}_3 + \mathbf{k}_4, \mathbf{k}_2) + 16\beta(\mathbf{k}_2, \mathbf{k}_1 + \mathbf{k}_3 + \mathbf{k}_4)) \\ & + 6G_3^{(s)}(\mathbf{k}_2, \mathbf{k}_3, \mathbf{k}_4)(3\alpha(\mathbf{k}_2 + \mathbf{k}_3 + \mathbf{k}_4, \mathbf{k}_1) + 16\beta(\mathbf{k}_1, \mathbf{k}_2 + \mathbf{k}_3 + \mathbf{k}_4)) \\ & + 12F_2^{(s)}(\mathbf{k}_1, \mathbf{k}_4)G_2^{(s)}(\mathbf{k}_2, \mathbf{k}_3)\alpha(\mathbf{k}_2 + \mathbf{k}_3, \mathbf{k}_1 + \mathbf{k}_4) \\ & + 12F_2^{(s)}(\mathbf{k}_1, \mathbf{k}_3)G_2^{(s)}(\mathbf{k}_2, \mathbf{k}_4)\alpha(\mathbf{k}_2 + \mathbf{k}_4, \mathbf{k}_1 + \mathbf{k}_3) \\ & + 12F_2^{(s)}(\mathbf{k}_1, \mathbf{k}_2)G_2^{(s)}(\mathbf{k}_3, \mathbf{k}_4)\alpha(\mathbf{k}_3 + \mathbf{k}_4, \mathbf{k}_1 + \mathbf{k}_2) \\ & + 18F_3^{(s)}(\mathbf{k}_1, \mathbf{k}_2, \mathbf{k}_3)\alpha(\mathbf{k}_4, \mathbf{k}_1 + \mathbf{k}_2 + \mathbf{k}_3) + 18F_3^{(s)}(\mathbf{k}_1, \mathbf{k}_2, \mathbf{k}_4)\alpha(\mathbf{k}_3, \mathbf{k}_1 + \mathbf{k}_2 + \mathbf{k}_4) \\ & + 18F_3^{(s)}(\mathbf{k}_1, \mathbf{k}_3, \mathbf{k}_4)\alpha(\mathbf{k}_2, \mathbf{k}_1 + \mathbf{k}_3 + \mathbf{k}_4) + 18F_3^{(s)}(\mathbf{k}_2, \mathbf{k}_3, \mathbf{k}_4)\alpha(\mathbf{k}_1, \mathbf{k}_2 + \mathbf{k}_3 + \mathbf{k}_4)\big] \end{aligned} \tag{3.26}$$

The second order solution for the density and velocity fields in real space, can be

derived after Fourier transforming Eqs. (3.15) and (3.16) respectively (Fry, 1984):

$$\delta^{(2)}(\mathbf{x},\tau) = \frac{17}{21}[\delta^{(1)}(\mathbf{x},\tau)]^2 + \frac{2}{7}s^2_{ij}(\mathbf{x},\tau) - [\Psi^{(1)}(\mathbf{x},\tau)]^i\partial_i\delta^{(1)}(\mathbf{x},\tau), \tag{3.27}$$

$$\theta^{(2)}(\mathbf{x},\tau) = -\mathcal{H}(\tau)f(\tau)\left[\frac{13}{21}[\delta^{(1)}(\mathbf{x},\tau)]^2 + \frac{4}{7}s^2_{ij}(\mathbf{x},\tau) - [\Psi^{(1)}(\mathbf{x},\tau)]^i\partial_i\delta^{(1)}(\mathbf{x},\tau)\right], \tag{3.28}$$

where $\Psi^{(1)}(\mathbf{x},\tau) = \boldsymbol{\nabla}^{-1}_{\mathbf{q}}\delta^{(1)}(\mathbf{x},\tau)$ [Eq. (3.39)] is the linear solution of the displacement field in Lagrangian formalism (see Sec. 3.3.1) and s_{ij} is the linear tidal field tensor [Eq. (4.32)]. The multiplication factors in front of the quadratic fields come from the monopole (*i.e.* integration over all angles) of the kernels $F_2^{(s)}$ and $G_2^{(s)}$, for the density and velocity field respectively (Fosalba and Gaztanaga, 1998).

3.3 Lagrangian Perturbation theory

Eulerian perturbation theory (EPT) describes the evolution of the density and velocity fields from a fixed comoving coordinate system. An other possibility is to formulate a non-linear perturbation theory on a frame that follows the trajectories of the fluid elements, the so called *Lagrangian Perturbation Theory* (LPT) (Zel'dovich, 1970; Buchert, 1989). For a complete review the reader is advised on reading (Bouchet, 1996; Bernardeau et al, 2002). The main idea is that, instead of taking the Lagrangian of all the particles in the cosmic fluid, we parametrise instead each particle with its position. The displacement field $\boldsymbol{\Psi}(\mathbf{q})$ is the dynamical parameter in this formalism. It connects the initial Lagrangian positions $\mathbf{q}$ of the fluid elements, with the final Eulerian positions $\mathbf{x}$. It is defined as:

$$\mathbf{x}(\tau) = \mathbf{q} + \boldsymbol{\Psi}(\mathbf{q},\tau), \tag{3.29}$$

The equation of motion for the particle's trajectory will be given by

$$\frac{d^2\mathbf{x}(\tau)}{d\tau^2} + \mathcal{H}\frac{d\mathbf{x}}{d\tau} = \boldsymbol{\nabla}_{\mathbf{x}}\Phi(\mathbf{x}), \tag{3.30}$$

where again Φ is the gravitational potential fluctuations. The subscript in the gradient denotes the Eulerian position. The divergence of the above equation will give

$$J(\mathbf{q},\tau)\boldsymbol{\nabla}_{\mathbf{x}}\left[\frac{d^2\boldsymbol{\Psi}}{d\tau^2}+\mathcal{H}\frac{d\boldsymbol{\Psi}}{d\tau}\right]=\frac{3}{2}\Omega_m\mathcal{H}^2(J-1). \tag{3.31}$$

To derive the above we have used the conservation of particles in an infinitesimal volume between the two frames, *i.e.* $\overline{\rho}d^3q=\rho(\mathbf{x},\tau)d^x=\overline{\rho}[1+\delta(\mathbf{x})]d^3x$, as well as the Poisson equation [Eq. (3.3)]. The Jacobian transformation that connects the two frames is then

$$Jd^3q=d^3x \;\;\Rightarrow\;\; J=\det|\frac{\partial x_i}{\partial q_i}|=\det|\delta_{ij}+\frac{\partial\Psi_i}{\partial q_j}|, \tag{3.32}$$

which gives

$$1+\delta(\mathbf{x},\tau)=\frac{1}{J(\mathbf{q},\tau)}. \tag{3.33}$$

Using the chain rule on the divergence in Eulerian space, *i.e.* $\frac{\partial}{\partial x_i}=\frac{\partial q_i}{\partial x_i}\frac{\partial}{\partial q_i}=(\delta_{ij}+\frac{\partial\Psi_i}{\partial q_j})^{-1}\frac{\partial}{\partial q_j}$, we can get the final equation of the displacement field as

$$[\delta_{ij}+\Psi_{i,j}(\mathbf{q},\tau)]^{-1}\left[\frac{d^2\Psi_{i,j(\mathbf{q},\tau)}}{d\tau^2}+\mathcal{H}\frac{d\Psi_{i,j}(\mathbf{q},\tau)}{d\tau}\right]=\frac{3}{2}\Omega_m\mathcal{H}^2\frac{J(\mathbf{q},\tau)-1}{J(\mathbf{q},\tau)}, \tag{3.34}$$

where $\Psi_{i,j}=\partial\Psi_i/\partial\Psi_j$. The approach described in the above equation breaks down at *shell crossing*. This is due to the fact that, particles come very close to each other, acquiring after enough time the same Eulerian coordinate $\mathbf{x}$. This can happen even if they started at different Lagrangian points $\mathbf{q}$, due to the time relation between the two [Eq. (3.29)]. The Jacobian can be expanded as

$$\begin{aligned}J&=\det|\delta_{ij}+\frac{\partial\Psi_i}{\partial q_i}|=1+\boldsymbol{\nabla}_{\mathbf{q}}\cdot\boldsymbol{\Psi}(\mathbf{q},\tau)\\&+\frac{1}{2}[(\boldsymbol{\nabla}_{\mathbf{q}}\cdot\boldsymbol{\Psi}(\mathbf{q},\tau))^2-\sum_{i,j}\Psi_{i,j}\Psi_{j,i}]+\frac{1}{6}[(\boldsymbol{\nabla}_{\mathbf{q}}\cdot\boldsymbol{\Psi}(\mathbf{q},\tau))^3-3\boldsymbol{\nabla}_{\mathbf{q}}\cdot\boldsymbol{\Psi}(\mathbf{q},\tau)\sum_{i,j}\Psi_{i,j}\Psi_{j,i}\end{aligned}$$

$$+2\sum_{i,l,k}\Psi_{i,j}\Psi_{j,k}\Psi_{k,i}]+\dots\,, \tag{3.35}$$

while the EOM of the fluid trajectory can be solved perturbatively as

$$\mathbf{\Psi}(\mathbf{q},\tau)=\mathbf{\Psi}^{(1)}(\mathbf{q},\tau)+\mathbf{\Psi}^{(2)}(\mathbf{q},\tau)+\dots\,. \tag{3.36}$$

3.3.1 Linear Solution

The linear part of the Jacobian, *i.e.* the first two terms of Eq. (3.35), are used in this first approximation. The inverse of the Jacobian transformation matrix will be now

$$[\delta_{ij}+\Psi_{i,j}(\mathbf{q},\tau)]^{-1}\simeq\delta_{ij}-\Psi_{i,i}, \tag{3.37}$$

which is derived after using $\det(I+A)=1+tr(A)+\mathcal{O}(A^2)I$. Using Eq. (3.33) and the linear part of the Jacobian expansion, we can derive the linear solution as:

$$\begin{aligned}&1+\delta^{(1)}(\mathbf{x},\tau)=\frac{1}{J(\mathbf{q},\tau)}\simeq 1-\boldsymbol{\nabla}_{\mathbf{q}}\cdot\Psi(\mathbf{q},\tau)\;\;\Rightarrow\\&\boldsymbol{\nabla}_{\mathbf{q}}\cdot\Psi^{(1)}(\mathbf{q},\tau)=-D^{(+)}(\tau)\delta^{(1)}(\mathbf{q}),\end{aligned} \tag{3.38}$$

where here we have splitted, as in EPT, the time part from the spatial part in the growing linear solution. The linear density field $\delta^{(1)}(\mathbf{q})$ is the initial condition field, which evolves with the linear growth factor under the divergence of the displacement field. The linear growth factor in LPT is the same as in EPT. Therefore, at first order the position of the particle in Eulerian space will be:

$$\mathbf{x}(\tau)=\mathbf{q}-\boldsymbol{\nabla}_{\mathbf{q}}^{-1}\delta^{(1)}(\mathbf{x},\tau), \tag{3.39}$$

while the velocity field is given by

$$\mathbf{u}(\tau)\frac{d\mathbf{x}}{d\tau} = -f\mathcal{H}\boldsymbol{\nabla}_{\mathbf{q}}^{-1}\delta^{(1)}(\mathbf{x},\tau), \tag{3.40}$$

where f is the linear growth rate (same as in EPT). In the case of the Poisson equation, we can relate the displacement field divergence with the gravitational potential in Lagrangian space, under the assumption of an irrotational gravity field, as

$$\boldsymbol{\nabla}_{\mathbf{q}} \cdot \Psi^{(1)}(\mathbf{q},\tau) = -\nabla_{\mathbf{q}}^2\Phi^{(1)}(\mathbf{q},\tau) = -\delta^{(1)}(\mathbf{x},\tau), \tag{3.41}$$

which leads to $\Psi^{(1)}(\mathbf{q},\tau) = -\nabla_{\mathbf{q}}\Phi(\mathbf{q},\tau)$. Using the linear solution Zel'dovich (1970), tried to approximate (*Zel'dovich approximation* (ZA)) the dynamical equation by extrapolating it into the non-linear regime. This was done by exchanging the divergence of the displacement field with the tidal tensor (traceless part). From Eq. (3.33) we get

$$\rho(\mathbf{x},\tau) = \frac{\overline{\rho}(\tau)}{\det|\delta_{ij} + \frac{\partial\Psi_i}{\partial q_j}|} = \frac{\overline{\rho}}{|(1-\lambda_1 D(\tau))(1-\lambda_2 D(\tau))(1-\lambda_3 D(\tau))|}, \tag{3.42}$$

where the variables λ_i are the eigenvalues of the tidal tensor field $\Psi_{i,j}$. The power of this result lies on the fact that, we can predict the future of a collapsing region (*i.e.* $(1-\lambda D(\tau)) = 0$) and determine the structure this point belongs to. If the eigenvalues are all positive, while one of them is larger than the rest (*i.e.* $\lambda_1 > \lambda_2,\ \lambda_3$), we get a *pancake* shape. This indicates that the element collapses in one direction. However, the ZA breaks down before the point reaches the final steps of collapse. A spherical collapse occurs in the case where all eigenvalues are positive, but now equal in size. If two of them are positive and one negative (*i.e.* $\lambda_1,\ \lambda_2 > 0,\ 0 < \lambda_3$), then the collapse happens in 2 dimensions and therefore the point belongs to a filament. In the case where two of them are negative and only one is positive (*i.e.* $\lambda_1,\ \lambda_2 < 0,\ \lambda_3 > 0$) the element belongs to a wall. Finally, negative eigenvalues correspond to a growing mode, which indicates that the point belong to a void.

3.3.2 Second-order solution

A recursion relation does not exist in the formalism of LPT, in order to generate the higher order terms of the perturbative expansion. The solution must be performed order by order. The second-order Lagrangian PT (2LPT) can improve significantly the predictions, for the density and velocity fields, over the linear solution (Buchert et al, 1994; Melott et al, 1995; Bouchet et al, 1995). Considering up to second order terms in Eq. (3.35) and substituting them in the equation of motion [Eq. (3.34)], we get

$$\frac{d^2\Psi^{(2)}_{i,i}}{d\tau^2}+\mathcal{H}\frac{d\Psi^{(2)}_{i,i}}{d\tau}-\frac{3}{2}\mathcal{H}^2\Omega_m\Psi^{(2)}_{i,i}=-\frac{3}{4}\left[(\Psi^{(2)}_{k,k})^2-\Psi^{(2)}_{i,j}\Psi^{(2)}_{j,i}\right], \tag{3.43}$$

where the linear solution of the displacement field has be also used in the above derivation. Separating, as before, the second order solution into a time and a spatial part, we get

$$\Psi^{(2)}_{k,k}(\mathbf{q},\tau)=\frac{D_2(\tau)}{2D_1^2(\tau)}\sum_{i\neq j}\left(\Psi^{(1)}_{i,i}(\mathbf{q},\tau)\Psi^{(1)}_{j,j}(\mathbf{q},\tau)-\Psi^{(1)}_{i,j}(\mathbf{q},\tau)\Psi^{(1)}_{j,i}(\mathbf{q},\tau)\right), \tag{3.44}$$

where the time dependent part of $\Psi^{(2)}$ is denoted as $D_2(\tau)$ (*i.e.* second order growth factor) and has been show to be in ΛCDM cosmology, approximately, $D_2(\tau)\simeq -3D_1^2(\tau)\Omega_m^{-1/143}/7$ (Bouchet et al, 1995). The second-order result can be simplified, by using the Poisson equation together with the displacement field relation at second order (*i.e.* $\mathbf{\Psi}^{(2)}(\mathbf{q},\tau)=\boldsymbol{\nabla}_{\mathbf{q}}\Phi^{(2)}(\mathbf{q},\tau)$), as

$$\boldsymbol{\nabla}_{\mathbf{q}}\Phi^{(2)}(\mathbf{q},\tau)\simeq-\frac{3}{7}\Omega_m^{-1/143}\sum_{i>j}\left(\Phi^{(1)}_{,ii}(\mathbf{q},\tau)\Phi^{(1)}_{,jj}(\mathbf{q},\tau)-[\Phi^{(1)}_{,ij}(\mathbf{q},\tau)]^2\right). \tag{3.45}$$

Expanding the linear results for the position and velocity of a fluid element we get

$$\mathbf{x}(\mathbf{q},\tau)=\mathbf{q}-D_1\nabla_{\mathbf{q}}\Phi^{(1)}(\mathbf{q},\tau)+D_2\nabla_{\mathbf{q}}\Phi^{(2)}(\mathbf{q},\tau), \tag{3.46}$$

$$\mathbf{u}(\mathbf{q},\tau) = -f_1\mathcal{H}\boldsymbol{\nabla}_{\mathbf{q}}^{-1}\Phi^{(1)}(\mathbf{q},\tau) + f_2\mathcal{H}\boldsymbol{\nabla}_{\mathbf{q}}^{-1}\Phi^{(2)}(\mathbf{q},\tau), \tag{3.47}$$

The second order growth rate is approximately, $f_2 \approx 2\Omega_m^{6/11}$ (Bouchet et al, 1995). Extending the solution to the third order, although describes better the behaviour of under-dense regions (Bouchet et al, 1995), has a minimal improvement over 2LPT (Buchert et al, 1994; Melott et al, 1995).

Lagrangian perturbation theory can be used to generate initial conditions for N-body numerical simulations. One starts by generating random Gaussian density fluctuations in Fourier space, by using the definition of power spectrum (*i.e.* $\delta_{\mathbf{k}} = \sqrt{P_m^L}A\exp(i\phi)$) with a random amplitude (*i.e.* fluctuation around $\sqrt{P_m^L}$) and phase. Connecting that to the linear part of the gravitational potential $\Phi_{\mathbf{k}}^1$ is an easy task [Eq. (3.41)]. If one desires to go to second order, Eq. (3.45) must be solved. These relations can be easily linked, in Fourier space, to the displacement field at each order. The final step is to inverse-Fourier transform these results, in order to get the linear and second order perturbative solutions of the displacement field. We can use now these displacements [Eq. (3.46)] to move the particles from their starting grid points and assign to them an initial velocity [Eq. (3.47)].

3.4 MPTbreeze

In this section we discuss briefly how the MPTbreeze formalism works. We start by introducing a more general perturbation theory, the Renormalised Pertrubation Theory (RPT) (Crocce and Scoccimarro, 2006a,b). By defining $\eta = \log a$ and then a vector

$$\Psi(\mathbf{k},\eta) = \left(\delta(\mathbf{k},\eta), -\theta(\mathbf{k},\eta)/\mathcal{H}\right), \tag{3.48}$$

the usual fluid equations for can be recast in matrix notation as

$$\partial_\eta \Psi_a(\mathbf{k},\eta) + \Omega_{ab}(\mathbf{k},\eta) = \gamma^{(s)}_{abc}(\mathbf{k},\mathbf{k}_1,\mathbf{k}_2)\,\Psi_b(\mathbf{k}_1,\eta)\,\Psi_c(\mathbf{k},\eta)\,, \tag{3.49}$$

where $\gamma^{(s)}_{abc}$ is a symmetrised vertex matrix and:

$$\Omega_{ab} = \begin{pmatrix} 0 & -1/2 \\ -3/2 & 1/2 \end{pmatrix}. \tag{3.50}$$

The above equation has solutions

$$\Psi_a(\mathbf{k},\eta) = g_{ab}(\eta)\,\phi(\mathbf{k}) + \int_0^\eta d\eta' g_{ab}\left(\eta-\eta'\right)\gamma^{(s)}_{bcd}(\mathbf{k},\mathbf{k}_1,\mathbf{k}_2)\,\Psi_c\left(\mathbf{k}_1,\eta'\right)\Psi_d\left(\mathbf{k},\eta'\right), \tag{3.51}$$

where g_{ab} is the linear propagator, which is non-zero only for for positive η:

$$g_{ab}(\eta) = \frac{e^\eta}{5}\begin{pmatrix} 3 & 2 \\ 3 & 2 \end{pmatrix} - \frac{e^{-3\eta/2}}{5}\begin{pmatrix} -2 & -2 \\ 3 & -3 \end{pmatrix} \tag{3.52}$$

Analogously to SPT, Eq. (3.51) can be solved by a series expansion:

$$\Psi_a(\mathbf{k},\eta) = \sum_{n=1}^{\infty}\Psi^{(n)}_a(\mathbf{k},\eta)\,, \tag{3.53}$$

where

$$\Psi^{(n)}_a(\mathbf{k},\eta) = \int \delta_D(\mathbf{k}-\mathbf{k}_{1\cdots n})\,\mathcal{F}^{(n)}_{aa_1\cdots a_n}(\mathbf{k}_1,\cdots,\mathbf{k}_n;\eta)\,\phi(\mathbf{k}_1)\cdots\phi(\mathbf{k}_n) \tag{3.54}$$

where $\mathcal{F}^{(n)}$ are kernels and $\mathbf{k}_{1\cdots n} = \mathbf{k}_1 + \cdots \mathbf{k}_n$. Non-linearities modify both the propagator and the vertex functions. The non-linear propagator is defined by

$$G_{ab}(k,\eta)\,\delta_D\left(\mathbf{k}-\mathbf{k}'\right) = \left\langle \frac{\delta\Psi_a(\mathbf{k},\eta)}{\delta\phi_b(\mathbf{k}')}\right\rangle \tag{3.55}$$

and it can be expressed as an infinite series using Eq. (3.53),

$$G_{ab}(k,\eta) = g_{ab}(k,\eta) + \sum_{n=2}^{\infty} \left\langle \frac{\delta\Psi_a^{(n)}(\mathbf{k},\eta)}{\delta\phi_b(\mathbf{k}')} \right\rangle . \tag{3.56}$$

The full vertex functions Γ are defined in terms of the fully non-linear propagator,

$$\left\langle \frac{\delta^2\Psi_a(\mathbf{k},\eta)}{\delta\phi_e(\mathbf{k}_1)\delta\phi_f(\mathbf{k}_2)} \right\rangle = 2\int_0^\eta ds \int_0^s ds_1 \int_0^s ds_2 G_{ab}(\eta - s) \times \Gamma^{(s)}_{bcd}(\mathbf{k}, s; \mathbf{k}_1, s_1; \mathbf{k}_2, s_2)\, G_{ce}(s_1) G_{df}(s_2) . \tag{3.57}$$

By using the Feynman diagram formalism, one can see that the non-linear propagator satisfies Dyson's formula:

$$G_{ab}(\mathbf{k},\eta) = g_{ab}(\eta) + \int_0^\eta ds_1 \int_0^{s_1} ds_2 g_a c(\eta - s_1)\, \Sigma_{cd}(\mathbf{k}, s_1, s_2)\, G_{db}\left(\mathbf{k}, s_2, \eta'\right) , \tag{3.58}$$

where Σ represents the sum of the principal path irreducible diagrams.

With this formalism, one can calculate the n-point correlation function in RPT for an arbitrary number of loops, but the actual computations are difficult because they involve solving numerically a set of integro-differential equations Nevertheless, this method provides a well-defined perturbative expansion in the non-linear regime, which is not the case in SPT.

A simplification of this model,MPTbreeze, was developed in the work of (Bernardeau et al, 2008; Crocce et al, 2012) that only requires the late-time propagator. Hence, in this new theory no time integrations are required. First, the non-linear propagator is generalised to an arbitrary number of points. By defining the $(p+1)$-point propagator $\Gamma^{(p)}$ as

$$\frac{1}{p!}\left\langle \frac{\delta\Psi_a^p(\mathbf{k},a)}{\delta\phi_{b_1}(\mathbf{k}_1)\cdots\delta\phi_{b_p}(\mathbf{k}_p)} \right\rangle = \delta_D(\mathbf{k} - \mathbf{k}_{1\cdots p})\, \Gamma^{(p)}_{ab_1\cdots b_p}(\mathbf{k}_1, \cdots, \mathbf{k}_p, a) , \tag{3.59}$$

the power spectrum becomes

$$P(k,z) = \sum_{r\geq 1} r! \int \delta_D(\mathbf{k} - \mathbf{q}_{1\cdots r}) \left[\Gamma^{(r)}(\mathbf{q}_1, \cdots, \mathbf{q}_r, z)\right]^2 P_m^L(q_1) \cdots P_m^L(q_r) d^3q_1 \cdots d^3q_r \,. \tag{3.60}$$

where the propagator takes the following simple form:

$$\Gamma_\delta^{(n)}(\mathbf{k}_1, \cdots, \mathbf{k}_n; z) = D^n(z) F_n^{(s)}(\mathbf{k}_1, \cdots, \mathbf{k}_n) \exp\left[f(k) D^2(z)\right] . \tag{3.61}$$

where $D(z)$ is the standard linear growth factor of SPT. The function f can be expressed in terms of an integral over the power spectrum today

$$f(k) = \int \frac{d^3q}{(2\pi)^3} \frac{P_m^L(q, z=0)}{504 k^3 q^5} \left[6k^7 q - 79k^5 q^3 + 50 q^5 k^3 - 21 k q^7 + \frac{3}{4}\left(k^2 - q^2\right)^3 \left(2k^2 + 7q^2\right) \log \frac{|k-q|^2}{|k+q|^2}\right] . \tag{3.62}$$

Up to one loop, the power spectrum and bispectrum take the form:

$$P_{\text{linear}}^{\text{MPTbreeze}}(k,z) = \exp\left[2f(k)D^2(z)\right] P_m^L(k) \,, \tag{3.63}$$

$$P_{\text{1-loop}}^{\text{MPTbreeze}}(k,z) = \exp\left[2f(k)D^2(z)\right] P_{22}^{\text{SPT}}(k) P_m^L(|\mathbf{k}-\mathbf{q}|) P_m^L(q) \,, \tag{3.64}$$

$$B_{\text{tree-level}}^{\text{MPTbreeze}}(k_1,k_2,k_3,z) = B_{\text{tree}}^{\text{SPT}}(k_1,k_2,k_3,z) \exp\left[\left(f(k_1)+f(k_2)+f(k_3)\right) D^2(z)\right] , \tag{3.65}$$

$$B_{\text{1-loop}}^{\text{MPTbreeze}}(k_1,k_2,k_3,z) = \left(B_{222} + B_{321}^I\right)(k_1,k_2,k_3,z) \exp\left[\left(f(k_1)+f(k_2)+f(k_3)\right) D^2(z)\right] , \tag{3.66}$$

where Eq. (97) from Ref. Bernardeau et al (2012) has been used for the expansion.

3.5 Statistical description of the cosmic fields

Density perturbation lack of direct observations, hence we have to rely on the statistics of the observed objects, which have different characteristics and span across various time scales, in order to test the various cosmological theories. The density perturbations can

be described as a uniform mean field (*i.e.* background) with positive and negative fluctuations superimposed on it. More specifically, we can consider them as spatial *stochastic* or *random* fields, where the latter is just a generalization of a stochastic process. The galaxy and CMBanisotropy distributions share the same characteristic. Therefore, the entire observable Universe can be treated as a stochastic realization, coming from the statistical ensemble (*i.e.* "virtual copies") of all possible Universes.

The statistical tools available, to permit such a statistical analysis, are under the so called theory of *stationary stochastic processes*. Density fluctuations are a subclass system, described by these theories, with the additional characteristics of a continuous fluctuating spatial signal and a constant spatial average, coming from its large volume. Depending on the inflationary mechanism, the stochastic initial perturbations can have different distributions (*e.g.* Gaussian, non-Gaussian), and as discussed in Sec. 2.4.4, this can give valuable information on the physical processes that take place in the early Universe. The subject of this section is to present the statistical formalism needed to describe the initial density fluctuations and their time evolution.

3.5.1 Random fields

The density quantity $\rho(\mathbf{x})$, as generated from inflation and evolves into matter domination, is the realisation of a random field $\hat{\rho}(\mathbf{x})$. The latter can be seen as a continuous set of random numbers, where each of them is identified from its spatial coordinates. It is completely characterized by its *probability density function* (PDF) $\mathcal{P}[\rho(\mathbf{x})]$, which describes the probability of having the realisation $\rho(\mathbf{x})$ with a value ρ at a position $\mathbf{x}$. In other words, it is the joint probability of $\hat{\rho}(\mathbf{x})$ at every point. The average density in a cell of volume ΔV around a point $\mathbf{x}$ is

$$\overline{\rho}(\mathbf{x}) = \frac{1}{\Delta V}\int_{\Delta V(\mathbf{x}_i)} d^3x\rho(\mathbf{x}), \tag{3.67}$$

where the Universe is divided into cells of equal volume, with $\Delta V(\mathbf{x}_i)$ being the volume

around position $\mathbf{x}_i$. The probability density $p[\overline{\rho}(\mathbf{x}_1), \overline{\rho}(\mathbf{x}_2), \ldots]$ is defined as the joint probability of local density, for every cell. In the limit of $\Delta V \to 0$, it approached the function $\mathcal{P}[\rho(\mathbf{x})]$. In the case of a discrete stochastic process, like in the case of galaxies, the mean density at position $\mathbf{x}_i$ (*i.e.* $\overline{\rho}(\mathbf{x}_i)$) can take values, either $1/\Delta V$ or 0, in the i-th cell. Again, in the limit $\Delta V \to 0$, the point process for each realisation is completely described by the joint probability $p[\overline{\rho}(\mathbf{x}_1), \overline{\rho}(\mathbf{x}_2), \ldots]$ over all cells.

The homogeneity and isotropy of the Universe, as assumed by the cosmological principle, impose similar characteristic in the statistics of the density field. The random field $\rho(\mathbf{x})$ is *statistically homogeneous* and *statistically isotropic*. The first condition implies that the probability density at a point $\mathbf{x}_0$, inside a volume V, does not depend on the values of position $\mathbf{x}_0$. In other words, the probability of having N numbers of particles in that specific volume, depends only on the size of V and its shape. The condition of statistical isotropy dictates that $\mathcal{P}[\rho(\mathbf{x})]$ is independent under spatial rotations. The *ensemble* average of the density stochastic field is defined as

$$\langle \hat{\rho}(\mathbf{x}) \rangle = \rho_0. \tag{3.68}$$

It is the average over all possible realizations (*i.e.* ensemble) of the random field, *i.e.* the average over $\mathcal{P}[\rho(\mathbf{x})]$. The framework of a continuous stochastic process, described here, can be applied only for positive values (*i.e.* $\rho_0 > 0$). In order to measure the average of a quantity that depends on the density field, we need to invoke the *ergodicity* assumption. This is due to the fact that, we only observe one realization of the Universe. It implies that, the ensemble average of an observable $B(\rho_1, \rho_2, \ldots)$, where $\rho_i = \rho(\mathbf{x}_i)$, over all the realization is equal to the spatial average $\overline{B}$

$$\overline{B} = \lim_{V \to \infty} \frac{1}{V} \int_V B(\rho(\mathbf{x}_1 + \mathbf{x}_0), \rho(\mathbf{x}_2 + \mathbf{x}_0), \ldots), \tag{3.69}$$

where the integration is over all space V. The convergence of this integral over the infinite volume is guaranteed in the case of a random field with a well defined average

value (Birkhoff-Khinchin theorem). Due to the uniformity condition, the density average must be well defined and satisfy, for every position $\mathbf{x}_0$, the following

$$\lim_{r\to\infty} \frac{1}{|S^3(r;\mathbf{x}_0)|} \int_{S^3(r;\mathbf{x}_0)} \rho(\mathbf{x}) d^3x = \rho_0 > 0, \tag{3.70}$$

where $S^3(r;\mathbf{x}_0)$ is the volume of a sphere around point $\mathbf{x}_0$. The final inequality originates by the fact that the density field is a strictly positive field. The above implies that, in the case of a limited volume (*e.g.* the observable Universe) we can define the *homogeneity scale* λ_0 as (Gabrielli and Sylos Labini, 2001):

$$\left| \frac{1}{S^3(r;\mathbf{x}_0)} \int_{S^3(r;\mathbf{x}_0)} \rho(\mathbf{x}) d^3x - \rho_0 \right| < \rho_0. \quad \forall\, r > \lambda_0. \tag{3.71}$$

This scale quantifies the limit at which we can consider fluctuations to be small compared to the average density of the observed volume, therefore it exhibits a dependence of the size of the observed patch. Beyond these scales the perturbative approach described in the previous section breaks down and fluctuations can be large with an irregular behaviour. As was proposed in (Gaite et al, 1999; Gabrielli et al, 2000), in this regime we have to use a different statistical framework than the one reviewed here, *e.g.* a fractal. For the latter, the reader is advised to check (Gabrielli, 2005) for a detailed analysis on the argument. Nonetheless, for galaxy statistics it has been shown that $\lambda_0 \simeq 70 - 80\,\mathrm{Mpc/h}$ (Hogg et al, 2005; Sarkar et al, 2009; Scrimgeour et al, 2012) and hence a fractal distribution is excluded beyond these scales. This implies that, the Universe becomes smooth and the standard statistical tools are valid.

For a cosmic random field, such as matter density, the infinite volume condition of the ergodic hypothesis is not satisfied, due to the limited size of the observable Universe. In this case the integration in Eq. (3.69) is only over a finite sub-volume of the wholes space. This means that, the ensemble average of any cosmological quantity will be an *estimator* of its true value. The expectation value of the n-point correlation function (*i.e.* the n^{th} central moment for a multivariate joint probability density distribution) of the density

field $\rho(\mathbf{x})$ is defined as (Gnedenko, 1998)

$$\langle (\rho(\mathbf{x}_1)-\rho_0)(\rho(\mathbf{x}_2)-\rho_0)\dots(\rho(\mathbf{x}_n)-\rho_0)\rangle = \int_V (\rho(\mathbf{x}_1)-\rho_0)(\rho(\mathbf{x}_2)-\rho_0)\dots(\rho(\mathbf{x}_n)-\rho_0) \times p[\rho(\mathbf{x}_1),\rho(\mathbf{x}_2),\dots,\rho(\mathbf{x}_n)], \tag{3.72}$$

where ρ is the expectation value of the average density field and the integration is over the infinite volume. The Fourier transformation of the joint probability density function is given by:

$$M(t) = \langle \exp -t\rho \rangle = \int p[\rho] e^{t\rho} d\rho = \sum_{n=0}^{\infty} \frac{t^n}{n!} \langle \rho^n \rangle, \tag{3.73}$$

where $\rho = \rho_1, \rho_2, \dots, \rho_n$ is a vector, while $M(t)$ is called the *characteristic function*. The expectation value of $\langle \rho^n \rangle$ is the raw moment, *i.e.* the expectation value for $\rho_0 = 0$, and it is related to the central moments through the binomial transformation. The logarithm of Eq. (3.73) give the n-th *cumulants* as:

$$\ln M(t) = \sum_{n=1} \frac{t^n}{n!} \langle \rho^n \rangle_c. \tag{3.74}$$

Equating the two, after expanding the Maclaurin series of $\ln M(t)$, we can get the relationship between cumulants and central moments of the density random field. Here we present only the one-point results for the first four:

$$\begin{aligned}
\langle \rho \rangle_c &= \langle \rho \rangle, \\
\langle \rho^2 \rangle_c &= \langle \rho^2 \rangle - \langle \rho \rangle_c^2, \\
\langle \rho^3 \rangle_c &= \langle \rho^3 \rangle - 3\langle \rho^2 \rangle_c \langle \rho \rangle_c - \langle \rho \rangle_c^3, \\
\langle \rho^4 \rangle_c &= \langle \rho^4 \rangle - 4\langle \rho^3 \rangle_c \langle \rho \rangle_c - 3\langle \rho^2 \rangle_c^2 - 6\langle \rho^2 \rangle_c \langle \rho \rangle_c^2 - \langle \rho \rangle_c^4,
\end{aligned} \tag{3.75}$$

The relations for the overdensity field, $\delta(\mathbf{x})$, can be derived after dividing the above with the average density. By construction, the first central moment of the random overdensity

fluctuations is zero (*i.e.* $\langle \delta \rangle = 0$). This simplifies considerably the above relations. In the case of a multipoint correlation function, one has to additionally take into account all the permutations of the random field between the different position. The statistical quantity of interest is the cumulants, because they represent a set of independent quantities that characterize fully the PDF of the perturbations. Cumulants are also referred in the literature as connected correlation function, a name that comes from quantum field theory and the Feynman diagrams. The second, two-point, cumulant is also called *covariance*, while the one-point is the *variance* (*i.e.* diagonal part).

Up to now we have made no assumption on the distribution of the density contrast field. Most inflationary models predict a Gaussian distribution for the initial density fluctuations (see for a discussion Sec. 2.4.4). In the multivariant case we have

$$p[\delta(\mathbf{x}_1), \delta(\mathbf{x}_2), \ldots, \delta(\mathbf{x}_n)] = \frac{1}{\sqrt{2\pi}\det(C)} \exp\left[\frac{1}{2}\delta_i C_{ij}^{-1} \delta_j\right], \tag{3.76}$$

where $Cij = \langle \delta_i \delta_j \rangle_c$ is the covariance and $\delta_i \equiv \delta(\mathbf{x}_i)$. Substituting the Gaussian PDF in Eq. (3.73), all the odd cumulants vanish while the even are obtained by the sum of the product of the ensemble averages of two point correlators, with all possible combinations between the different positions. This is encoded in the *Wick's theorem* of quantum and classical field theories as

$$\langle \delta_1 \delta_2 \ldots \rangle = \sum_{\text{pairings}} \prod_{\text{pairs } (i,j)} \langle \delta_i \delta_j \rangle_c. \tag{3.77}$$

In the case of a non-Gaussian primordial perturbation field, even order cumulants will be non-zero. This means that, the measurement of these higher order correlators is a direct indication of the departure from Gaussianity. In the case of LSS, however, we expect non-zero higher order cumulants due to the non-linear nature of gravity, which induces couplings between different modes. Disentangling the primordial from the late time evolution signal is a challenging task. On the other hand, CMBprobes fluctuations

directly after the decoupling and hence it is clean from such non-linear contributions.

3.5.2 Two-point correlation function and power spectrum

The two point correlation function of the density field is the ensemble average of δ at two different points. It is given by

$$\langle \delta(\mathbf{x}_1)\delta(\mathbf{x}_2)\rangle = \langle \delta(\mathbf{x}_1)\delta(\mathbf{x}_2)\rangle_c = \xi(r). \tag{3.78}$$

Due to statistical isotropy, two point correlation function depends only in the modulus of the distance between the two points (*i.e.* $r = |\mathbf{x}_1 - \mathbf{x}_2|$) and is characterized by the spatial memory of the fluctuations. Taking the Fourier transform of $\xi(r)$ we get

$$\delta(\mathbf{x}) = \int \frac{d^3k}{(2\pi)^3}\delta(\mathbf{k})e^{i\mathbf{k}\cdot\mathbf{x}}. \tag{3.79}$$

Plugging the above in the definition of the two point correlators, we can define

$$\left\langle \delta(\mathbf{k})\delta(\mathbf{k}')\right\rangle_c = (2\pi)^3\delta_D\left(\mathbf{k}-\mathbf{k}'\right)P(k), \tag{3.80}$$

where the quantity $P(k)$ is the Fourier coefficient of the two point correlation function, called the *power spectrum*. This quantity is strictly positive for a continuous random field. To derive the above, the condition of $\delta(\mathbf{x})$ being a real quantity is used, which gives $\delta(\mathbf{k}) = \delta^*(-\mathbf{k})$. As in the case of correlation function, power spectrum does not depend either on the mode direction, *i.e.* it is non zero only for equal and opposite wavenumbers. The relation between the real and Fourier space quantities is simply (*Wiener-Khinchin* theorem)

$$\begin{aligned}
&\xi(\mathbf{r}) = \int \frac{d^3\mathbf{k}}{(2\pi)^3}P(\mathbf{k})e^{i\mathbf{k}\cdot\mathbf{x}} \;\Rightarrow \\
&\xi(\mathbf{r}) = \xi(r) = \int \frac{dk}{2\pi^2}k^2\frac{\sin(kr)}{kr}P(k), \quad P(\mathbf{k}) = P(k) = 4\pi\int dr r^2\frac{\sin(kr)}{kr}\xi(r).
\end{aligned} \tag{3.81}$$

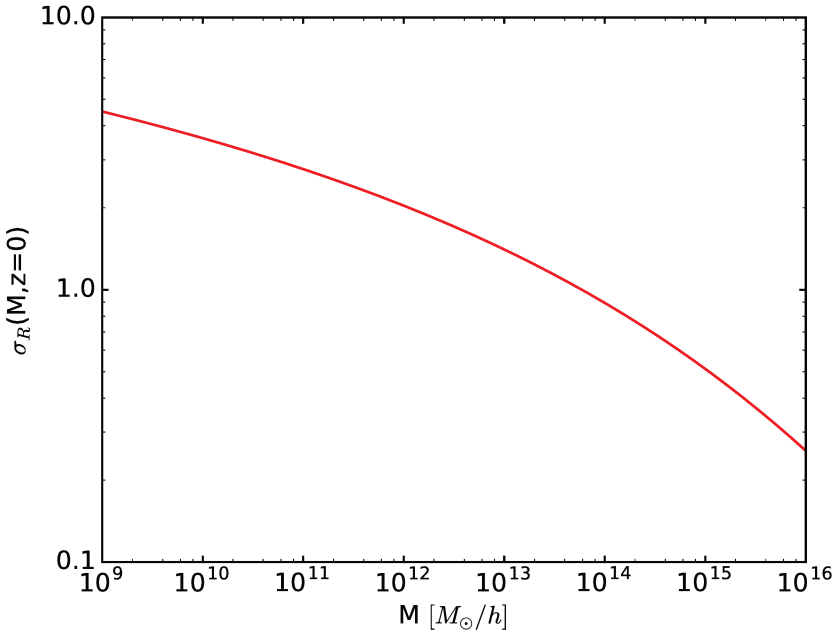

Figure 3.3 – The smoothed variance of the linear over density field at redshift $z = 0$, for the cosmology assumed here.

In order to have a more clear picture on what the power spectrum actually measures, we present the one-point second cumulant $(\xi(0))$ of the linear overdensity field

$$\sigma^2 = \left\langle \delta^2(\mathbf{k}) \right\rangle_c = \int \frac{dk}{2\pi^2} k^2 P(k). \tag{3.82}$$

Therefore, power spectrum characterizes the amplitude of the density fluctuations around the mean background value. At this point we can define the smoothed linear matter density contrast δ_R, over a radius $R(M) = (3M/4\pi\overline{\rho}_m)^{1/3}$, as

$$\delta_R(\mathbf{k}, z) = W_R(k)\delta(\mathbf{k}, z), \tag{3.83}$$

where M is the mass originating from the matter inside the region of size $R(M)$ and $\overline{\rho}_m$ is the average density of the Universe at present time. A popular choice for the filter is $W_R(k) = 3(\sin kR - kR\cos(kR))/(kR)^3$, which is the Fourier transform of the spherical

top-hat window function. Hence, we can write a smoothed linear power spectrum $P_R(k)$ as in Eq. (3.14), where now $M(k,z)$ is replaced by $M_R(k,z) = W_R(k)M(k,z)$. The smoothed mass variance of the density field, at mass scale M, is defined as

$$\sigma_R^2(z) = \left\langle \delta_R^2(\mathbf{k}) \right\rangle_c = \frac{1}{2\pi^2} \int k^2 P_R(k,z) dk. \tag{3.84}$$

The variance is plotted in Figure 3.3 as a function of the smoothing mass M. It is easy to show that, for a density random field with a well defined average ($\rho > 0$) the mass variance must go to zero for very large radii (*i.e.* $\lim_{R\to\infty} \sigma^2(R) = 0$). A direct consequence of this is that, the two-point correlation function must also go to zero for large separations (*i.e.* $\xi(r \to \infty) \to 0$). This indicates that

$$\int d^3 r \xi(\mathbf{r}) = 0, \tag{3.85}$$

where the integral is over all space. A consequence of the above is that for some values of r, we must have $\xi(r) < 0$. An other important property of the two-point correlation function, originating from the ergodicity of the density random field, is that it has a maximum at zero separation (*i.e.* $\xi(0) > |\xi(\mathbf{r})|$). Finally, from Eq. (3.85), one can define the *correlation length* as

$$r_c^2 = \frac{\int dr r^2 \, |\xi(r)|}{\int dr \, |\xi(r)|}, \tag{3.86}$$

which characterizes the endurance of the correlations in the density fluctuation field. It indicates, therefore, the region up to which a localised perturbation is felt in the system.

For a discrete stochastic density field, such as in the case of galaxies, each cell of infinitesimal volume dV has a probability $P = n_g dV$ to be occupied with n_g galaxies and $1 - n_g dV$ to be empty, where $n_g = M^{-1}\rho(\mathbf{x})dV$ is the mean number of galaxies in dV and M the mean mass. Here we have assumed a Poisson process, where the occupation probability of each cell is independent from the rest. The probability of finding one galaxy

at a point inside the volume dV_1 and an other in volume dV_2, separated by a distance r, is

$$\begin{aligned}\delta P &= \frac{\langle \rho(\mathbf{x})\rho(\mathbf{y})\rangle}{m^2} dV_1 dV_2 \\ &= \overline{n}_g^2 \frac{\langle (\rho(\mathbf{x})-\rho_0)(\rho(\mathbf{y})-\rho_0)\rangle}{\rho_0^2} dV_1 dV_1 \\ &= \overline{n}_g^2 (1+\langle \delta(\mathbf{x})\delta(\mathbf{x}+\mathbf{r})\rangle dV_1 dV_2 \\ &= \overline{n}_g^2 (1+\xi(r)) dV_1 dV_2. \end{aligned} \tag{3.87}$$

Therefore, the correlation function of galaxies characterizes the amount of clustering, where for $\xi(r) > 0$ we have clustering while for $\xi(r) < 0$ we have anti-correlated objects. In the discrete density field the two-point correlation function is just, $\xi_g(r) = 1 + \xi(r)$, which gives for the variance

$$\sigma_g^2(R) = \sigma_{PN}^2 + \sigma^2(R). \tag{3.88}$$

The subscript g denotes that we are considering a discrete random field (*e.g.* galaxies, particles) and $\sigma_{PN}^2 = 1/\overline{n}_g$ is the Poisson shot noise, with $\overline{n}_g$ being the mean number density of galaxies. In a Poisson distribution, as the one followed by galaxies (discrete tracers of dark matter), the shot noise refers to the contribution in the statistics from the self-correlation of the object.

3.5.2.1 Perturbative Expansion: up to one-loop

The density and velocity fields have a perturbative solution, depending on the PT scheme, with respect to the first order (linear) fields. Using the linear part of such an expansion, one can derive the linear matter power spectrum as:

$$\begin{aligned}&\left\langle \delta_m^{(1)}(\mathbf{k}_1)\delta_m^{(1)}(\mathbf{k}_2)\right\rangle_c = M(k_1,z)M(k_2,z)\langle \Phi(\mathbf{k}_1)\Phi(\mathbf{k}_2)\rangle_c \quad \Rightarrow \\ &P_m^L(k,z) = M^2(k,z)P_\Phi(k), \end{aligned} \tag{3.89}$$

where Φ is the primordial Bardeen gravitational potential, with a power spectrum given by Eq. (2.82), while the transition between the two equations uses the reality condition of the density field in real space. Here we have used in the perturbative solution the transfer function, incorporated through the Poisson relation of the linear density field with the primordial gravitational potential [Eq. (3.14)]. Since we are mainly interested in the matter statistics in this chapter, we will drop the m subscript in the density field and we will always denote with δ the matter density fluctuation field. The linear matter power spectrum is derived throughout this thesis from the numerical Boltzmann solver CAMB (Lewis et al, 2000).

One can proceed in deriving higher order corrections to the linear power spectrum, from the perturbative solution of the matter and velocity fields. This is done by using the perturbative expansion of a field and substituting it in the two-point correlation function [Eq. (3.80)]. Keeping only the non zero combinations, after taking into account the cumulant relation, results in a series of terms with an increasing power of the linear field. The terms that have power of the linear solution to the n-th order denote the *nth-loop* correction to the linear order, which is also called tree-level order. The above process leads to:

$$\begin{aligned}
&\langle X(\mathbf{k},z)X(\mathbf{k}',z)\rangle_c = \left\langle X^{(1)}_{\mathbf{k}}(z)X^{(1)}_{\mathbf{k}'}(z)\right\rangle_c + 2\left\langle X^{(1)}_{\mathbf{k}}(z)X^{(2)}_{\mathbf{k}'}(z)\right\rangle_c \\
&+\left\langle X^{(2)}_{\mathbf{k}}(z)X^{(2)}_{\mathbf{k}'}(z)\right\rangle_c + 2\left\langle X^{(1)}_{\mathbf{k}}(z)X^{(3)}_{\mathbf{k}'}(z)\right\rangle_c + \ldots \quad \Rightarrow \\
&P(k,z) = P^{(0)}(k,z) + P^{(1)}(k,z) + \ldots,
\end{aligned} \tag{3.90}$$

where the zero loop term is just the linear power spectrum (*i.e.* $P^{(0)}(k,z) \equiv P^L_m(k,z)$) and $P^{(1)}(k,z)$ is the 1-loop correction. The field X denotes a quantity that can have a perturbative solution, *e.g.* matter overdensity and velocity fields. In the case of Gaussian initial conditions all the odd terms in each loop order are zero, due to Wick's theorem. In the Eulerian PT, the higher order perturbative terms are given in Eq. (3.15)eq:thetapt for the density and velocity fields respectively. For the matter density field, assuming

Gaussian initial conditions, the 1-loop results in SPT are

$$P^{(1)}(k,z) = P_{22}(k,z) + P_{13}(k,z), \tag{3.91}$$

where

$$P_{22}(k,z) \equiv 2\int [F_2^{(s)}(\mathbf{k}-\mathbf{q},\mathbf{q})]^2 P_m^L(|\mathbf{k}-\mathbf{q}|,z) P_m^L(q,z)\mathrm{d}^3\mathbf{q}, \tag{3.92}$$

$$P_{13}(k,z) \equiv 6P_m^L(k,z)\int F_3^{(s)}(\mathbf{k},\mathbf{q},-\mathbf{q}) P_m^L(q,z)\mathrm{d}^3\mathbf{q}. \tag{3.93}$$

One-loop corrections describe the primal effects of mode coupling and can give a quantitative estimation on the break down scales of SPT. The first part of the 1-loop contribution (*i.e.* $P_{22}(k,z)$) is positive and describes the mode coupling between $\mathbf{k}-\mathbf{q}$ and $\mathbf{q}$, coming from the presence of the second order SPT kernel. On the other hand, P_{13} term is negative and does not exhibit any mode coupling, *i.e.* it is just a term proportional to the linear power spectrum. However, due to terms of $\alpha(\mathbf{q}-\mathbf{q},\mathbf{k})$ and $\beta(\mathbf{q}-\mathbf{q},\mathbf{k})$, in the third order density kernel [Eq. (3.21)], it becomes infinite. Note that, the nature of this infinity is numerical and does not represent any fundamental pole divergence of the third order kernel. In order to remove the infinities, we calculate the limit $\lim_{\mathbf{p}->-\mathbf{q}} F_3^{(s)}(\mathbf{k},\mathbf{q},\mathbf{p})$, which gives

$$\begin{aligned} F_3^{(s)}(\mathbf{k},\mathbf{q},-\mathbf{q}) = \frac{1}{54}(&7\alpha(\mathbf{q},\mathbf{k}-\mathbf{q})F_2^{(s)}(\mathbf{k},-\mathbf{q}) + 7\alpha(-\mathbf{q},\mathbf{k}+\mathbf{q})F_2^{(s)}(\mathbf{k},\mathbf{q}) \\ &+ 7\alpha(\mathbf{k}-\mathbf{q},\mathbf{q})G_2^{(s)}(\mathbf{k},-\mathbf{q}) + 7\alpha(\mathbf{k}+\mathbf{q},-\mathbf{q})G_2^{(s)}(\mathbf{k},\mathbf{q}) + 4\beta(\mathbf{k}-\mathbf{q},\mathbf{q})G_2^{(s)}(\mathbf{k},-\mathbf{q}) \\ &+ 4\beta(-\mathbf{q},\mathbf{k}+\mathbf{q})G_2^{(s)}(\mathbf{k},\mathbf{q})). \end{aligned} \tag{3.94}$$

For completeness, the third order velocity kernel will be

$$\begin{aligned} G_3^{(s)}(\mathbf{k},\mathbf{q},-\mathbf{q}) = \frac{1}{18}(&G_2^{(s)}(\mathbf{k},-\mathbf{q})(\alpha(\mathbf{k}-\mathbf{q},\mathbf{q}) + 4\beta(\mathbf{k}-\mathbf{q},\mathbf{q})) \\ &+ G_2^{(s)}(\mathbf{k},\mathbf{q})(\alpha(\mathbf{k}+\mathbf{q},-\mathbf{q}) + 4\beta(-\mathbf{q},\mathbf{k}+\mathbf{q})) \\ &+ \alpha(\mathbf{q},\mathbf{k}-\mathbf{q})F_2^{(s)}(\mathbf{k},-\mathbf{q}) + \alpha(-\mathbf{q},\mathbf{k}+\mathbf{q})F_2^{(s)}(\mathbf{k},\mathbf{q})). \end{aligned} \tag{3.95}$$

Note that, the expressions presented in (Makino et al, 1992; Jeong and Komatsu, 2006) for $P_{13}(k,z)$, integrate also over the azimuthal angle of the dummy vector $\mathbf{q}$, as well as absorbing the square magnitude of the radial coordinate (*i.e.* q^2 factor from $\mathrm{d}^3\mathbf{q}$), while they do not show the exact vector form of the $F_3^{(s)}(\mathbf{k},\mathbf{q},-\mathbf{q})$ kernel.

The 1-loop correction has been extensively studied and tested with simulations (Coles, 1990; Suto and Sasaki, 1991; Makino et al, 1992; Jain and Bertschinger, 1994; Scoccimarro, 1997; Jeong and Komatsu, 2006). As was shown in Jeong and Komatsu (2006), the power spectrum up to 1-loop agrees, with better than 1% accuracy, with simulations in the range of $1 < z < 6$, and in the quasi non-linear scales. Beyond a scale, 1-loop corrections are inadequate to describe the power spectrum of simulations and therefore we must reside in higher loop corrections, *e.g.* 2-loop. A way to characterize the non-linear scales in rel space, R_0, is through the variance, after requiring $\sigma^2(R_0) = 1$. Additionally, one can use the dimensionless power spectrum and define the non-linear scales k_{NL}, as those where $\Delta^2(k_N L) = k_{NL}^3 P(k_{NL})/(2\pi^2) \sim \delta\rho/\overline{\rho} = 1$.

In the case of non-Gaussian initial conditions, an additional term appears in the sum of the 1-loop corrections, which is given by

$$P_{13} = 2\int \mathrm{d}^3 q F_2(\mathbf{q},\mathbf{k}-\mathbf{q}) B_I(k,q,|\mathbf{k}-\mathbf{q}|), \tag{3.96}$$

where an analytical form was derived in (Taruya et al, 2008). The quantity B_I is the initial bispectrum linearly evolved to the present [Eq. (3.105)]. This term is expected to be a small correction, mainly due to the damping of the bispectrum from the second order density kernel.

3.5.3 Three-point correlation function and bispectrum

The first and simplest higher order correlator, beyond the two-point correlation function, is the three-point correlation function. It is defined as

$$\langle \delta(\mathbf{x}_1)\delta(\mathbf{x}_2)\delta(\mathbf{x}_3)\rangle = \langle \delta(\mathbf{x}_1)\delta(\mathbf{x}_2)\delta(\mathbf{x}_3)\rangle_c = \zeta(\mathbf{x}_1,\mathbf{x}_2,\mathbf{x}_3). \tag{3.97}$$

In an analogy to the power spectrum, we take the Fourier transformation of the three-point correlator and we define a quantity called the *bispectrum* as

$$\langle \delta(\mathbf{k}_1)\delta(\mathbf{k}_2)\delta(\mathbf{k}_3)\rangle_c = (2\pi)^3\delta_D(\mathbf{k}_1+\mathbf{k}_2+\mathbf{k}_3)\,B(\mathbf{k}_1,\mathbf{k}_2,\mathbf{k}_3), \tag{3.98}$$

where the Dirac delta is imposed by the translation invariance dictated from the statistical homogeneity. It ensures that the wavenumbers $\mathbf{k}_i$ must be three sides of a closed triangle in order to contribute to the bispectrum (*i.e.* $\mathbf{k}_1+\mathbf{k}_2+\mathbf{k}_3=0$). Both quantities, due to statistical isotropy, depend only on the moduli of the vectors, *i.e.* $k_i=|\mathbf{k}_i|$ and $r_{ij}=|\mathbf{r}_{ij}|$. This quantity measures directly the non-linear evolution of the density and velocity fields and therefore is rich on information from the non-linear regime. The relation between the real and Fourier space three-point correlator is given by

$$\zeta(\mathbf{x}_1,\mathbf{x}_2,\mathbf{x}_3) = \int \frac{d^3k_1}{(2\pi)^3}\int \frac{d^3k_2}{(2\pi)^3}\frac{d^3k_3}{(2\pi)^3}\delta_D(\mathbf{k}_1+\mathbf{k}_2+\mathbf{k}_3)\,B(\mathbf{k}_1,\mathbf{k}_2,\mathbf{k}_3)e^{i(\mathbf{k}_1\cdot\mathbf{x}_1+\mathbf{k}_2\cdot\mathbf{x}_2+\mathbf{k}_3\cdot\mathbf{x}_3)}. \tag{3.99}$$

In the case of a galaxy field the probability of finding three objects inside infinitesimal volumes dV_1, dV_2 and dV_3 is given by (Peebles, 1980):

$$P(\mathbf{x}_1,\mathbf{x}_2,\mathbf{x}_3) = \overline{n}_g^3[1+\xi(r_{12})+\xi(r_{23})+\xi(r_{31})+\zeta(r_{12},r_{23},r_{31})]dV_1dV_2dV_3. \tag{3.100}$$

After taking the perturbative expansion of the quantity X we get:

$$\begin{aligned}\langle X(k_1,z)X(k_2,z)X(k_3,z)\rangle_c &= \left\langle X^{(1)}(k_1,z)X^{(1)}(k_2,z)X^{(1)}(k_3,z)\right\rangle_c \\ &+\left\langle X^{(1)}(k_1,z)X^{(1)}(k_2,z)X^{(2)}(k_3,z)\right\rangle_c + \left\langle X^{(1)}(k_1,z)X^{(2)}(k_2,z)X^{(1)}(k_3,z)\right\rangle_c\end{aligned}$$

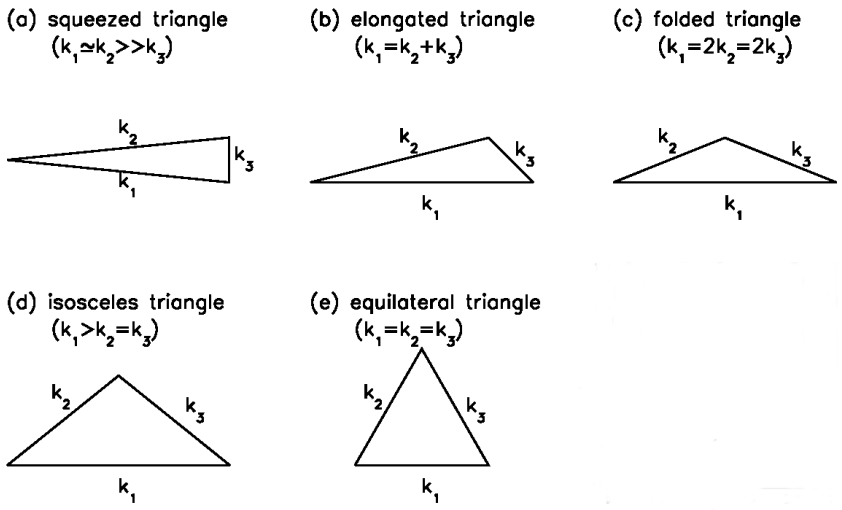

Figure 3.4 – Illustration of different triangle configurations for the bispectrum $B(k_1, k_2, k_3)$. Source: modified from (Jeong and Komatsu, 2009).

$$+\left\langle X^{(2)}(k_1,z)X^{(1)}(k_2,z)X^{(1)}(k_3,z)\right\rangle_c + \ldots \quad \Rightarrow \tag{3.101}$$

$$B(k_1,k_2,k_3,z) = B_{111}(k_1,k_2,k_3,z) + B_{112}(k_1,k_2,k_3,z) + 2 \text{ perm} + \ldots . \tag{3.102}$$

For a Gaussian random field, Wick's theorem implies that the first term is zero. Substituting the solution for the second order density field, gives $\left\langle X^{(1)}X^{(1)}X^{(2)}\right\rangle_c \propto \left\langle X^{(1)}X^{(1)}X^{(1)}X^{(1)}\right\rangle_c$, which is a four-point correlator. For the Gaussian case, it is given by pairs of the product of two-point correlators. Now we can write the tree-level bispectrum of matter field as :

$$\begin{aligned} B_G(k_1,k_2,k_3,z) \equiv B_{112} = 2[&F_2(\mathbf{k}_1,\mathbf{k}_2)P_m^L(k_1,z)P_m^L(k_2,z) + F_2(\mathbf{k}_2,\mathbf{k}_3)P_m^L(k_2,z)P_m^L(k_3,z) \\ &+ F_2(\mathbf{k}_3,\mathbf{k}_1)P_m^L(k_3,z)P_m^L(k_1,z)]. \end{aligned} \tag{3.103}$$

The configuration dependence of B_G originates from the kernel F_2, which has terms (*i.e.* $\alpha(\mathbf{k}_1,\mathbf{k}_2)$) that come from the gradient of the density with the velocity field (*i.e.* $\mathbf{u}\nabla\delta$

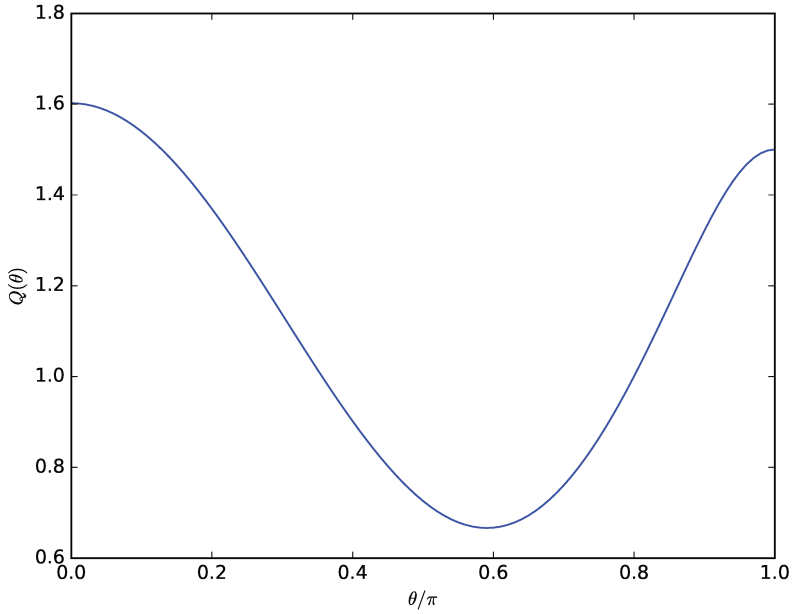

Figure 3.5 – The reduced tree-level bispectrum at redshift $z = 0$, for the cosmology assumed here, as a function of the angle θ ($\hat{k}_1 \cdot \hat{k}_2 = \cos\theta$) for a fixed $k_2/k_1 = 2$ and $k_1 = 0.02\,\mathrm{h/Mpc}$.

term in continuous equation), as well as contributions from the $(\mathbf{u}\nabla)\cdot\mathbf{u}$ term of the Euler equation. Therefore, the tree-level bispectrum is highly sensitive to the the non-linear nature of gravity, which enhances the amplitude of the three-point correlator. The scale dependence originates from the linear power spectrum, which increases the anisotropic nature of bispectrum in the large scales. In Figure 3.4 we plot a set of different triangle configurations for illustration purposes.

In order to be able to study the shape of the tree-level bispectrum we introduce the reduced bispectrum quantity as (Fry, 1984):

$$Q \equiv \frac{B(k_1, k_2, k_3, z)}{P_m^L(k_1, z)P_m^L(k_2, z) + P_m^L(k_2, z)P_m^L(k_3, z) + P_m^L(k_1, z)P_m^L(k_3, z)}, \tag{3.104}$$

which at tree-level is almost independent from cosmology (Fry, 1994) and redshift (Fry,

1984). We plot the reduced bispectrum as a function of the angle [2] in Figure 3.5 between $\mathbf{k}_1$ and $\mathbf{k}_2$, while we generate all the triangle configurations that have $k_2/k_1 = 2$ for $k_1 = 0.02\,\mathrm{h/Mpc}$. It is easy to see that, for equilateral triangles ($\theta = -1/2$) the reduce bispectrum has a constant value. In the case of collapsed triangle configurations ($k_3 = k_1 + k_2$), which correspond to $\theta = 0$, as well as for squeezed configurations ($\theta = \pi$; $k_2 \approx k_2 \gg k_3$), we get the largest values. This is not the case though for equilateral triangles, where Q takes the minimum value. Having in mind that the bispectrum is the Fourier coefficient of the three-point correlation function, which in turn is linked to the probability of having three galaxies in a triangle configuration, we can draw some additional conclusions from the shape of bispectrum. The minimum of Q in the equilateral configurations show that they are less probable to occur than squeezed or collapsed. This can be understood from the filament nature of galaxy clustering, which in the end will favour these kind of configurations. This implies that equilateral triangles should be less frequent, at least up to the tree-level we consider here.

Lets consider now the case of primordial non-Gaussianity, where additional terms will appear in the bispectrum already at tree-level. Bispectrum is the perfect candidate to study PNG, since it is very sensitive to any kind of non-linearities. The drawback is though in this statement; we need to carefully remove any contribution coming from gravity in order to achieve any significant conclusions on the primordial Universe. The first non-zero term will be B_{111}, which is just the linearly extrapolated primordial bispectrum of the gravitational potential, as generated by the models of inflation. It is given by

$$B_I(k_1, k_2, k_3, z) \equiv B_{111}(k_1, k_2, k_3, z) = M(k_1, z)M(k_2, z)M(k_3, z)B_\Phi(k_1, k_2, k_3). \quad (3.105)$$

In the case of the local primordial non-Gaussianity, the primordial gravitational field

[2] The angle θ is not the internal angle of the triangle formed by k_1, k_2 and k_3, but the angle that satisfy the translation invariance condition $\mathbf{k}_1 + \mathbf{k}_2 + \mathbf{k}_3 = 0$.

is written as a Taylor expansion around the Gaussian part, as in Eq. (2.83), where we write it here again for convenience

$$\Phi(\mathbf{x}) = \Phi_G(\mathbf{x}) + f_{\rm NL}^{\rm local}(\Phi_G^2(\mathbf{x}) - \langle\Phi_G^2(\mathbf{x})\rangle) + \dots . \tag{3.106}$$

Plugging this expansion in Eq. (3.101), where now $X = \Phi$, we get a similar expression to that of the tree-level bispectrum. Note that the kernel F_2 will not be present, due to the primordial nature of Φ. taking into account the Poisson equation, as well as by using the local expansion of Φ, we get up to second order:

$$\begin{aligned}
&\delta_{lin}(\mathbf{k},z) = M(k,z)\Phi(\mathbf{k}) \\
&= M(k,z)\Phi^{(1)}(\mathbf{k}) + f_{\rm NL}^{\rm loc} M(k,z)\Phi^{(2)}(\mathbf{k}) \\
&= M(k,z)\Phi_G(\mathbf{k}) + M(k,z) f_{\rm NL}^{\rm loc} \int \frac{d^3q_1}{(2\pi)^3}\frac{d^3q_2}{(2\pi)^3}\delta_D(\mathbf{k}-\mathbf{q}_{12})\Phi_G(\mathbf{q}_1)\Phi_G(\mathbf{q}_2) \\
&= \delta_{lin}^{(1)}(\mathbf{k},z) + f_{\rm NL}^{\rm loc}\delta_{lin}^{(2)}(\mathbf{k},z).
\end{aligned} \tag{3.107}$$

The first order results, which coincide with the Gaussian case, are given by $\delta^{(1)}(\mathbf{k},z) \equiv \delta_{lin}^{(1)}(\mathbf{k},z) = M(k,z)\Phi_G(\mathbf{k})$. Plugging this in B_{111}, we get Eq. (2.84). The signal coming from primordial bispectrum is much smaller than the tree-level gravitational bispectrum ($\mathcal{O}(10^3)$; see (Sefusatti and Komatsu, 2007) for a quantitatively comparison).

3.5.3.1 One-loop matter bispectrum

The 1-loop corrections to the tree-level bispectrum is given in an analogous way to the power spectrum ($B = B^{(0)} + B^{(1)}$), *i.e.* by adding higher order solutions of the density field in the connected correlator and keeping terms up to some power of the linear density field. For Gaussian initial conditions, we get four terms that constitute the bispectrum 1-loop, involving up to fourth order perturbative solution, *i.e.* $B^{(1)} = B_{222} + B_{321}^I + B_{321}^I + B_{411}$.

Each term is given as follows (Scoccimarro, 1997; Scoccimarro et al, 1998) :

$$B_{222} \equiv 8\int \frac{d^3q}{(2\pi)^3} P_m^L(q,z) F_2^{(s)}(-\mathbf{q},\mathbf{q}+\mathbf{k}_1) P_m^L(|\mathbf{q}+\mathbf{k}_1|,z) \times F_2^{(s)}(-\mathbf{q}-\mathbf{k}_1,\mathbf{q}-\mathbf{k}_2) P_m^L(|\mathbf{q}-\mathbf{k}_2|,z) F_2^{(s)}(\mathbf{k}_2-\mathbf{q},\mathbf{q}), \tag{3.108}$$

$$B_{321}^I \equiv 6P_m^L(k_3,z)\int \frac{d^3q}{(2\pi)^3} P_m^L(q,z) F_3^{(s)}(-\mathbf{q},\mathbf{q}-\mathbf{k}_2,-\mathbf{k}_3) P_m^L(|\mathbf{q}-\mathbf{k}_2|,z) \times F_2^{(s)}(\mathbf{q},\mathbf{k}_2-\mathbf{q}) + 5 \text{ perm}, \tag{3.109}$$

$$B_{321}^{II} \equiv 6P_m^L(k_2,z) P_m^L(k_3,z) F_2^{(s)}(\mathbf{k}_2,\mathbf{k}_3)\int \frac{d^3q}{(2\pi)^3} P_m^L(q,z) F_3^{(s)}(\mathbf{k}_3,\mathbf{q},-\mathbf{q}) + 5 \text{ perm}, \tag{3.110}$$

$$B_{411} \equiv 12P_m^L(k_2,z) P_m^L(k_3,z)\int \frac{d^3q}{(2\pi)^3} P_m^L(q,z) F_4^{(s)}(\mathbf{q},-\mathbf{q},-\mathbf{k}_2,-\mathbf{k}_3) + 2 \text{ perm}. \tag{3.111}$$

The kernel $F_3^{(s)}(\mathbf{k}_3,\mathbf{q},-\mathbf{q})$ and $F_4^{(s)}(\mathbf{q},-\mathbf{q},-\mathbf{k}_2,-\mathbf{k}_3)$ will exhibit infinities for the same reason as in 1-loop power spectrum (Sec. 3.5.2.1). The expression for the third order density kernel is given in Eq. (3.94), while for the fourth order kernel we follow the same procedure, described in Sec. 3.5.2.1, and we get

$$\begin{aligned}
F_4^{(s)}(\mathbf{q},-\mathbf{q},\mathbf{q}_1,\mathbf{q}_2) = \\
&\frac{1}{792}\big[4G_2^{(s)}(\mathbf{q}_1,\mathbf{q})(9F_2^{(s)}(\mathbf{q}_2,-\mathbf{q})\alpha(\mathbf{q}_1+\mathbf{q},\mathbf{q}_2-\mathbf{q}) + 4G_2^{(s)}(\mathbf{q}_2,-\mathbf{q})\beta(\mathbf{q}_2-\mathbf{q},\mathbf{q}_1+\mathbf{q})) \\
&+4G_2^{(s)}(\mathbf{q}_2,\mathbf{q})(9F_2^{(s)}(\mathbf{q}_1,-\mathbf{q})\alpha(\mathbf{q}_2+\mathbf{q},\mathbf{q}_1-\mathbf{q}) + 4G_2^{(s)}(\mathbf{q}_1,-\mathbf{q})\beta(\mathbf{q}_1-\mathbf{q},\mathbf{q}_2+\mathbf{q})) \\
&+6G_3^{(s)}(\mathbf{q}_1,\mathbf{q}_2,-\mathbf{q})(9\alpha(\mathbf{q}_1+\mathbf{q}_2-\mathbf{q},\mathbf{q}) + 4\beta(\mathbf{q}_1+\mathbf{q}_2-\mathbf{q},\mathbf{q})) \\
&+6G_3^{(s)}(\mathbf{q}_1,\mathbf{q}_2,\mathbf{q})(9\alpha(\mathbf{q}_1+\mathbf{q}_2+\mathbf{q},-\mathbf{q}) + 4\beta(-\mathbf{q},\mathbf{q}_1+\mathbf{q}_2+\mathbf{q})) \\
&+6G_3^{(s)}(\mathbf{q}_1,-\mathbf{q},\mathbf{q})(9\alpha(\mathbf{q}_1,\mathbf{q}_2) + 4\beta(\mathbf{q}_1,\mathbf{q}_2)) + 6G_3^{(s)}(\mathbf{q}_2,-\mathbf{q},\mathbf{q})(9\alpha(\mathbf{q}_2,\mathbf{q}_1) + 4\beta(\mathbf{q}_1,\mathbf{q}_2)) \\
&+36F_2^{(s)}(\mathbf{q}_2,\mathbf{q})G_2^{(s)}(\mathbf{q}_1,-\mathbf{q})\alpha(\mathbf{q}_1-\mathbf{q},\mathbf{q}_2+\mathbf{q}) + 36F_2^{(s)}(\mathbf{q}_1,\mathbf{q})G_2^{(s)}(\mathbf{q}_2,-\mathbf{q})\alpha(\mathbf{q}_2-\mathbf{q},\mathbf{q}_1+\mathbf{q}) \\
&+54\alpha(\mathbf{q},\mathbf{q}_1+\mathbf{q}_2-\mathbf{q})F_3^{(s)}(\mathbf{q}_1,\mathbf{q}_2,-\mathbf{q}) + 54\alpha(-\mathbf{q},\mathbf{q}_1+\mathbf{q}_2+\mathbf{q})F_3^{(s)}(\mathbf{q}_1,\mathbf{q}_2,\mathbf{q})
\end{aligned}$$

$$+54\alpha(\mathbf{q}_2,\mathbf{q}_1)F_3^{(s)}(\mathbf{q}_1,-\mathbf{q},\mathbf{q})+54\alpha(\mathbf{q}_1,\mathbf{q}_2)F_3^{(s)}(\mathbf{q}_2,-\mathbf{q},\mathbf{q})], \tag{3.112}$$

while for completeness we present the result for the fourth order velocity kernel

$$\begin{aligned}
&G_4^{(s)}(\mathbf{q},-\mathbf{q},\mathbf{q}_1,\mathbf{q}_2)= \\
&\quad\frac{1}{396}[G_2^{(s)}(\mathbf{q}_1,\mathbf{q})(6F_2^{(s)}(\mathbf{q}_2,-\mathbf{q})\alpha(\mathbf{q}_1+\mathbf{q},\mathbf{q}_2-\mathbf{q})+32G_2^{(s)}(\mathbf{q}_2,-\mathbf{q})\beta(\mathbf{q}_2-\mathbf{q},\mathbf{q}_1+\mathbf{q})) \\
&\quad+G_2^{(s)}(\mathbf{q}_2,\mathbf{q})(6F_2^{(s)}(\mathbf{q}_1,-\mathbf{q})\alpha(\mathbf{q}_2+\mathbf{q},\mathbf{q}_1-\mathbf{q})+32G_2^{(s)}(\mathbf{q}_1,-\mathbf{q})\beta(\mathbf{q}_1-\mathbf{q},\mathbf{q}_2+\mathbf{q})) \\
&\quad+3G_3^{(s)}(\mathbf{q}_1,\mathbf{q}_2,-\mathbf{q})(3\alpha(\mathbf{q}_1+\mathbf{q}_2-\mathbf{q},\mathbf{q})+16\beta(\mathbf{q}_1+\mathbf{q}_2-\mathbf{q},\mathbf{q})) \\
&\quad+3G_3^{(s)}(\mathbf{q}_1,\mathbf{q}_2,\mathbf{q})(3\alpha(\mathbf{q}_1+\mathbf{q}_2+\mathbf{q},-\mathbf{q})+16\beta(-\mathbf{q},\mathbf{q}_1+\mathbf{q}_2+\mathbf{q})) \\
&\quad+3G_3^{(s)}(\mathbf{q}_1,-\mathbf{q},\mathbf{q})(3\alpha(\mathbf{q}_1,\mathbf{q}_2)+16\beta(\mathbf{q}_1,\mathbf{q}_2))+3G_3^{(s)}(\mathbf{q}_2,-\mathbf{q},\mathbf{q})(3\alpha(\mathbf{q}_2,\mathbf{q}_1)+16\beta(\mathbf{q}_1,\mathbf{q}_2)) \\
&\quad+6F_2^{(s)}(\mathbf{q}_2,\mathbf{q})G_2^{(s)}(\mathbf{q}_1,-\mathbf{q})\alpha(\mathbf{q}_1-\mathbf{q},\mathbf{q}_2+\mathbf{q})+6F_2^{(s)}(\mathbf{q}_1,\mathbf{q})G_2^{(s)}(\mathbf{q}_2,-\mathbf{q})\alpha(\mathbf{q}_2-\mathbf{q},\mathbf{q}_1+\mathbf{q}) \\
&\quad+9\alpha(\mathbf{q},\mathbf{q}_1+\mathbf{q}_2-\mathbf{q})F_3^{(s)}(\mathbf{q}_1,\mathbf{q}_2,-\mathbf{q})+9\alpha(-\mathbf{q},\mathbf{q}_1+\mathbf{q}_2+\mathbf{q})F_3^{(s)}(\mathbf{q}_1,\mathbf{q}_2,\mathbf{q}) \\
&\quad+9\alpha(\mathbf{q}_2,\mathbf{q}_1)F_3^{(s)}(\mathbf{q}_1,-\mathbf{q},\mathbf{q})+9\alpha(\mathbf{q}_1,\mathbf{q}_2)F_3^{(s)}(\mathbf{q}_2,-\mathbf{q},\mathbf{q})],
\end{aligned} \tag{3.113}$$

where the dummy vectors $\mathbf{q}_1$ and $\mathbf{q}_2$ represent a side on the closed triangle, imposed by the momentum conservation.

For non-Gaussian initial conditions there are additional terms introduced in the above, contributing at each order with up to $\mathcal{O}(\delta^6)$. They are given by (Sefusatti, 2009):

$$B_{NG}^{(1)}=B_{112}^{II}+B_{122}^{I}+B_{122}^{II}+B_{113}^{I}+B_{113}^{II}, \tag{3.114}$$

The first non trivial term, involving up to second order solutions of the density field, is

$$B_{112}^{II}\equiv \quad = \quad \int\frac{d^3q}{(2\pi)^3}\;F_2^{(s)}(\mathbf{q},\mathbf{k}_3-\mathbf{q})\;T_I(\mathbf{k}_1,\mathbf{k}_2,\mathbf{q},\mathbf{k}_3-\mathbf{q})+2\;\text{perm}\,. \tag{3.115}$$

This correction to the $\mathcal{O}(\delta^4)$ terms of the matter bispectrum [Eq. (3.102)] is negligibly small, as it was shown in Scoccimarro et al (2004), due to the kernel suppression. The

remaining terms of the 1-loop correction are listed bellow (Sefusatti, 2009):

$$
\begin{aligned}
B^{I}_{122} &= 2\, P^{L}_{m}(k_1,z)\left[F^{(s)}_{2}(\mathbf{k}_1,\mathbf{k}_3)\int\frac{d^3q}{(2\pi)^3}\, F^{(s)}_{2}(\mathbf{q},\mathbf{k}_3-\mathbf{q})\; B_I(k_3,q,|\mathbf{k}_3-\mathbf{q}|)+(k_3\leftrightarrow k_2)\right]+2 \text{ perm.} \\
&= F^{(s)}_{2}(\mathbf{k}_1,\mathbf{k}_2)\left[P^{L}_{m}(k_1,z)\; P_{12}(k_2)+P^{L}_{m}(k_2,z)\; P_{12}(k_1)\right]+2 \text{ perm.}, \qquad (3.116)\\
B^{II}_{122} &= 4\int\frac{d^3q}{(2\pi)^3}\, F^{(s)}_{2}(\mathbf{q},\mathbf{k}_2-\mathbf{q})\; F^{(s)}_{2}(\mathbf{k}_1+\mathbf{q},\mathbf{k}_2-\mathbf{q})\; B_I(k_1,q,|\mathbf{k}_1+\mathbf{q}|) \\
&\times\; P^{L}_{m}(|\mathbf{k}_2-\mathbf{q}|,z)+2 \text{ perm.}, \qquad (3.117)\\
B^{I}_{113} &= 3B_I(k_1,k_2,k_3)\int\frac{d^3q}{(2\pi)^3}\, F^{(s)}_{3}(\mathbf{k}_3,\mathbf{q},-\mathbf{q})P^{L}_{m}(q,z)+2 \text{ perm.}, \qquad (3.118)\\
B^{II}_{113} &= 3P^{L}_{m}(k_1,z)\int\frac{d^3q}{(2\pi)^3}\, F^{(s)}_{3}(\mathbf{k}_1,\mathbf{q},\mathbf{k}_2-\mathbf{q})B_I(k_2,q,|\mathbf{k}_2-\mathbf{q}|)+(k_1\leftrightarrow k_2)+2 \text{ perm.}\,. \qquad (3.119)
\end{aligned}
$$

3.5.4 Tree-level trispectrum

Beyond bispectrum there is an increasing complexity, both in deriving the perturbative corrections, as well as in the numerical calculations of the correlators. Here we will present the results of the four-point correlation function, up to tree-level, since these results are going to be used in Chapter 5. The four-point correlator is defined from Eq. (3.75) as:

$$
\langle\,\delta(\mathbf{x}_1)\delta(\mathbf{x}_2)\delta(\mathbf{x}_3)\delta(\mathbf{x}_1)\,\rangle=\xi^{(4)}(\mathbf{x}_1,\mathbf{x}_2,\mathbf{x}_3,\mathbf{x}_4)+\xi(r_{12})\xi(r_{34})+2\;\text{perm}, \qquad (3.120)
$$

where $\xi^{(4)}(\mathbf{x}_1,\mathbf{x}_2,\mathbf{x}_3,\mathbf{x}_4)$ is the four-point cumulant. The Fourier transformation of the connected four-point correlator is called the *trispectrum* and is given by:

$$
\langle\,\delta(\mathbf{k}_1)\delta(\mathbf{k}_2)\delta(\mathbf{k}_3)\delta(\mathbf{k}_4)\,\rangle_c=(2\pi)^3\delta_D\,(\mathbf{k}_1+\mathbf{k}_2+\mathbf{k}_3+\mathbf{k}_4)\,T(\mathbf{k}_1,\mathbf{k}_2,\mathbf{k}_3.\mathbf{k}_4). \qquad (3.121)
$$

It quantifies the amount of correlation of the density fluctuation field between four points forming a rectangular, where each side is a wavevector as its is ensured by the translation invariance. This quantity depends on six variable, *e.g.* the magnitude of the four vectors

forming the rectangular and of the two diagonals. For a discrete stochastic process, the resulting probability of finding four galaxies inside four infinitesimal volumes, forming a rectangular, is :

$$P(\mathbf{x}_1,\mathbf{x}_2,\mathbf{x}_3,\mathbf{x}_4)=\overline{n}_g^2[1+\xi(r_{12})+\text{ perm}+\zeta(\mathbf{x}_1,\mathbf{x}_2,\mathbf{x}_3)+\xi(r_{12})\xi(r_{34})+\text{ perm}+\xi^{(4)}(\mathbf{x}_1,\mathbf{x}_2,\mathbf{x}_3,\mathbf{x}_4)]. \tag{3.122}$$

The tree-level results for the trispectrum are obtained after substituting the perturbative expansion in the connected correlator. For a general quantity X we get as before:

$$\begin{aligned}
&\langle X(k_1,z)X(k_2,z)X(k_3,z)X(k_4,z)\rangle_c=\left\langle X^{(1)}(k_1,z)X^{(1)}(k_2,z)X^{(1)}(k_3,z)X^{(1)}(k_4,z)\right\rangle_c\\
&+\left\langle X^{(1)}(k_1,z)X^{(1)}(k_2,z)X^{(1)}(k_3,z)X^{(2)}(k_4,z)\right\rangle_c+3\text{ perm}\\
&+\left\langle X^{(1)}(k_1,z)X^{(1)}(k_2,z)X^{(2)}(k_3,z)X^{(2)}(k_4,z)\right\rangle_c+5\text{ perm}\\
&\left\langle X^{(1)}(k_1,z)X^{(1)}(k_2,z)X^{(1)}(k_3,z)X^{(3)}(k_4,z)\right\rangle_c+3\text{ perm}+\ldots\quad\Rightarrow
\end{aligned}$$

$$\begin{aligned}
&T(k_1,k_2,k_3,z)=T_{1111}(k_1,k_2,k_3,k_4,z)+T_{1112}(k_1,k_2,k_3,k_4,z)+3\text{ perm}\\
&+T_{1122}(k_1,k_2,k_3,k_4,z)+5\text{ perm}+T_{1113}(k_1,k_2,k_3,k_4,z)+3\text{ perm}+\ldots.
\end{aligned} \tag{3.123}$$

The tree-level results for Gaussian initial conditions are given by:

$$T_{1122}(\mathbf{k}_1,\mathbf{k}_2,\mathbf{k}_3,\mathbf{k}_4)=4F_2^{(s)}(\mathbf{k}_{13},-\mathbf{k}_1)F_2^{(s)}(\mathbf{k}_{13},\mathbf{k}_2)P_m^L(k_1)P_m^L(k_2)P_m^L(k_{13})+11\text{ perm} \tag{3.124}$$

$$T_{1113}(\mathbf{k}_1,\mathbf{k}_2,\mathbf{k}_3,\mathbf{k}_4)=6F_3^{(s)}(\mathbf{k}_1,\mathbf{k}_2,\mathbf{k}_3)P_m^L(k_1)P_m^L(k_2)P_m^L(k_3)+3\text{ perm}. \tag{3.125}$$

The primordial trispectrum term is non-zero only in the case of a non-Gaussian primordial field. For the local shape, it can be derived, by going to the next order in the local expansion of the primordial potential [Eq. (3.106)], as

$$\Phi(\mathbf{x})=\Phi_G(\mathbf{x})+f_{\rm NL}^{\rm loc}\left[\Phi_G^2(\mathbf{x})-\langle\Phi_G^2(\mathbf{x})\rangle\right]+\frac{9}{25}g_{NL}\Phi_G^3(\mathbf{x}). \tag{3.126}$$

The parameter g_{NL} measures the amplitude of this additional non-Gaussian term. The term $\mathcal{O}(\delta^4)$ in Eq. (3.123) is the linearly evolved primordial trispectrum given by:

$$T_{1111}(k_1,k_2,k_3,k_4,z) \equiv T_I(k_1,k_2,k_3,k_4,z) = M(k_1,z)M(k_2,z)M(k_3,z)M(k_4,z)T_\Phi^{\rm loc}(k_1,k_2,k_3,k_4), \tag{3.127}$$

where the primordial potential trispectrum is given for the local PNG by

$$\begin{aligned} T_\Phi^{\rm loc}(k_1,k_2,k_3,k_4) = f_{\rm NL}^2 \,(P_\Phi(k_1)P_\Phi(k_3)P_\Phi(k_4) + 11 \ \ \text{perm}) + \\ \frac{56}{25} g_{NL}\,(P_\Phi(k_2)P_\Phi(k_3)P_\Phi(k_4) + 3 \ \ \text{perm}). \end{aligned} \tag{3.128}$$

The primordial trispectrum for the local type was found to have sub-dominant contribution compared to bispectrum (Verde and Matarrese, 2009).

Finally, for non-Gaussian initial conditions there is an additional term introduced ($\mathcal{O}([\delta^{(1)}]^5)$) at the tree-level result, which is given by

$$\begin{aligned} T_{1112}(\mathbf{k}_1,\mathbf{k}_2,\mathbf{k}_3,\mathbf{k}_4) = 2[B_I(k_1,k_2,k_{12})F_2^{(s)}(\mathbf{k}_{12},\mathbf{k}_3)P_m^L(k_3) + B_I(k_2,k_3,k_{23})F_2^{(s)}(\mathbf{k}_{23},\mathbf{k}_2)P_m^L(k_1) \\ + B_I(k_3,k_1,k_{31})F_2^{(s)}(\mathbf{k}_{31},\mathbf{k}_2)P_m^L(k_2)] + 3 \ \text{perm}, \end{aligned} \tag{3.129}$$

It is a linear term with respect to $f_{\rm NL}$ and as it was shown in (Sefusatti, 2009; Jeong and Komatsu, 2009) exhibits a scale dependence coming from the linearly extrapolated bispectrum. Its importance, in improving PNG constraints of any type, will be extensively discussed in Chapter 5.

Chapter 4

Structure formation and bias

4.1 Introduction

The distribution of LSS hold a rich amount of cosmological information and has been one of the pillars of our understanding of the evolution of the Universe. A key ingredient for extracting this wealth of information is to understand how the statistics of tracers (*e.g.* galaxies, cluster of galaxies, Lyman-α forest, *etc.*) is related to the distribution of the underlying matter. The connection between the two is incorporated in the concept of *bias*. LSS surveys observe only the distribution of luminous objects, which are the products of a highly non-linear and complex formation process. The task of quantifying the relationship between the two distributions is very challenging and there is still progress to be made.

Nevertheless, there is a well established picture on the formation of galaxies, or in general any other dark matter tracer. The distribution of matter originates from the growth of initial perturbations, generated during inflation (see Sec. 2.4.3) under gravitational collapse. This process leads to massive, gravitationally bound, virialized objects called *halos*, which form on the overdense regions of the initial matter density distribution. In standard cosmology, dark matter density overweights by a large amount the density of baryons. It makes up to almost 80% of the total matter in the Universe. Therefore, the potential wells of the halos, which are dominated by dark matter, trap baryons which later on cool and concentrate to create galaxies.

In order to retrieve cosmological information from the distribution of LSS, one needs to construct reliable models for each step of this formation process. The evolution of matter perturbations, as it was reviewed in the previous chapter, can be described by a perturbation theory. However, such an approach is destined to fail in the regime where the perturbations are highly non-linear, *i.e.* the small scales. The size of this regime depends on the time scale of the Universe, *e.g.* at low redshifts gravitational evolution makes the Universe more non-linear than at large redshifts. Still, we can be confident enough on the theoretical description provided by PT, up to the quasi non-linear regime. Down to these scales, where the structure formation is governed only by gravity (corrections from astrophysical and other effects is negligible), the relation between the distribution of luminous objects and dark matter can be parametrized at each order in perturbation theory into a finite set of bias parameters. On small scales, the description for the formation of LSS and the clustering of halos must rely on simulations.

In this Chapter we will review shortly the methods used to describe the bias relation between matter and halos, as well as some simple models for the population of halos by galaxies. Further on, we will discuss the implications of a non-Gaussian distribution in the initial conditions on the formation process of dark matter tracers. This can prove to be an important tool for probing the initial perturbations through LSS. Here we will mainly follow the notation of (Desjacques et al, 2016). The reader is advised to check the reviews of (Zentner, 2007; Desjacques et al, 2016), for a detailed description on the subjects of bias and excursion set formalism.

4.2 Mass function

Halos are assumed to form on the peaks of the smoothed underlying matter overdensity field, when its value exceeds some threshold value δ_c. Therefore, the number of created objects depend on the distribution of points that exceed such a threshold. In the early work of (Press and Schechter, 1974), it was found that the mass function can be expressed

in terms of the height of the peaks, by using the *spherical collapse model*. It states that in a smoothed linear contrast field in Lagrangian space ($\delta_R^{(1)}(\mathbf{q})$), a spherical region of radius R with uniform density and enclosed mass $M = (4\pi/3)\overline{\rho}_m R^3$, where $\overline{\rho}_m$ is the mean co-moving density at time t, will collapse to form a bound object when $\delta_R^{(1)}$ exceeds a threshold δ_c (spherical collapse threshold). Assuming Gaussian statistics for the smoothed overdensity field, one can write the probability of having a halo with mass greater than M as a fraction of a Lagrangian volume by

$$p_G(\delta_R^{(1)} > \delta_c) = \frac{1}{\sqrt{2\pi}\sigma(R)} \int_{\delta_c}^{\infty} d\delta \, \exp\left[-\frac{1}{2}\frac{\delta^2}{\sigma^2(R)}\right], \tag{4.1}$$

where $\sigma(R)$ is the smoothed variance of the density field over a radius R [Eq. (3.84)]. The Lagrangian volume fraction that encloses the halo with mass greater than M is given by:

$$F(>M) = \frac{1}{\overline{\rho}_m} \int_M^{\infty} d\ln M' \, M' n_h(M') = p_G(\delta_R^{(1)} > \delta_c), \tag{4.2}$$

where $n_h(M)$ is the co-moving number density of halos above mass M. Differentiating over the halo mass M gives

$$f(M) \equiv -\frac{dF(>M)}{dM}, \tag{4.3}$$

which leads to the *mass function* of halos

$$\begin{aligned} \frac{dF}{dM} &= -n_h(M)M = \frac{1}{\sqrt{2\pi}\sigma(R)} \exp\left[-\frac{1}{2}\frac{\delta^2}{\sigma^2(R)}\right] \frac{d}{dM}\left(\frac{\delta_c}{\sigma_R}\right) \quad \Rightarrow \\ n_h(M) &= -\frac{2\overline{\rho}_m}{\sqrt{2\pi}} \frac{\delta_c}{\sigma_R^2} \frac{1}{M} \frac{d\sigma_R}{dM} \exp\left[-\frac{1}{2}\frac{\delta^2}{\sigma^2(R)}\right]. \end{aligned} \tag{4.4}$$

The factor 2 in front of the mean density is introduced to recover the proper normalisation and to get the total mass after the integration over the whole range of M, *i.e.* $\int_0^{\infty} dM M n_h(M) = \overline{\rho}_m/2$. It is convenient to parametrize the mass function with a multi-

plicity function $f(\nu)$ as:

$$n_h(M,z) = \frac{d\mathcal{N}}{\mathrm{dln}M} = \frac{\overline{\rho}_m}{M} f(\nu) \left| \frac{\mathrm{dln}\nu}{\mathrm{dln}M} \right|, \tag{4.5}$$

where $\nu(M,z) = \delta_c/\sigma_R(M,z)$ is the height of the peak. In the Press-Schechter (PS) formalism this function is simply:

$$f_{PS}(\nu) = \sqrt{\frac{2}{\pi}} \nu e^{-\nu^2/2}. \tag{4.6}$$

The PS mass function has a dependence on redshift and cosmological parameters, as well as on the primordial power spectrum, therefore it has a universal character (Sheth and Tormen, 1999). The mass function shows that an increasing halo mass (decreasing σ_R; see Figure 3.3), leads to high-peaks ($\nu \gg 1$) and therefore to more rare objects. The opposite happens for low mass halos, which seem to be a common case during the process of halo formation. In the work of (Sheth and Tormen, 1999) (ST hereafter) a modified version of the PS mass function is proposed to improve the agreement with simulations

$$f_{ST}(\nu) = A\sqrt{\frac{2q}{\pi}} \left(1 + \frac{1}{(q\nu^2)^p} \right) \nu e^{-\frac{q\nu^2}{2}}, \tag{4.7}$$

where $A = 1/(1+2^{-p}\Gamma(0.5-p)/\sqrt{\pi}) \approx 0.322184$, $q = 0.707$ and $p = 0.3$.

Although, the PS formalism predictions on the form of the mass function is in agreement with simulations, it does not treat properly the small overdensities that might exist inside the Lagrangian radius. This is due to the fact that the PS formalism considers the whole smoothed region as one halo. In other words, all the points inside the halo exceed the threshold value, which is not generally true for realistic cases. This is known as the *cloud-in-cloud* problem and excursion set formalism was introduced (Bond et al, 1991) to solve it. The latter approach adds the *first-crossing* condition, where it states that a region belongs to a bound structure only if the smoothing radius R has the maximum value, in order for $\delta_R^{(1)}$ to reach the threshold δ_c.

4.3 Large-Scale halo bias

The main idea of bias is to describe the relation between the statistics of halos and the underlying dark matter with respect to a finite number of terms per perturbative order, up to some minimum scale. This perturbative approach, however, is destined to collapse towards the small scales (see Sec. 4.3.2 for a discussion). Throughout this section, we will refer to halos, but the formalism can be applied to any kind of tracer. We start with the spherical collapse approach, by taking $\delta_R^{(1)}$ at a radius R ($R(M) = (3M/4\pi\overline{\rho}_m)^{1/3}$) in Lagrangian space and at the initial time $\tau = 0$, which is the formation time of halos. During this early period the density field is close to uniform, hence we can assume that halos correspond to the overdense regions, defined by the Lagrangian radius $R(M)$, above the threshold of collapse. The co-moving number density of halos, in the initial Lagrangian frame, is given by

$$n^L(\mathbf{q}) = \Theta(\delta_R^{(1)}(\mathbf{q}) - \delta_c), \tag{4.8}$$

where Θ is the Heaviside function. Following the previous section, we assume again that the initial smoothed field is Gaussian and therefore described completely by the two-point correlator $\xi_R^L(r)$ [Eq. (3.78)]. It is related to the probability of finding two halos at a separation r [Eq. (3.87)] as (Kaiser, 1984):

$$1 + \xi_h^L(r) = \frac{p_2(\mathbf{q}, \mathbf{q}+\mathbf{r})}{p_1^2} = \sqrt{\frac{2}{\pi}} \left[\mathrm{erfc}(\nu/\sqrt{2})\right]^{-2} \int_\nu^\infty e^{-\nu'^2/2} \mathrm{erfc}\left[\frac{\nu - \nu'\hat{\xi}(r)}{\sqrt{2\{1-\hat{\xi}^2(r)\}}}\right] d\nu', \tag{4.9}$$

where $\xi_h^L(r)$ is the two-point correlation function of the initial density fluctuation field, in Lagrangian space, extrapolated to the present time and $\hat{\xi}(r) = \xi_R^L(r)/\sigma^2(R)$. Here we used the expectation value of the number density one-point statistics, for a Gaussian PDF, (*i.e.* $\langle n^L(\mathbf{q}) \rangle = \mathrm{erfc}[\nu/2]/2$). Inside the regime of small fluctuations we can Taylor expand the

extrapolated two point correlation function in terms of the initial two-point correlator, as

$$\xi_h^L(r) = \sum_{N=1}^{\infty} \frac{1}{N!} (b_N^L)^2 \left[\xi_R^L(r)\right]^N , \tag{4.10}$$

where each coefficient is given by (Kaiser, 1984; Szalay, 1988):

$$b_N^L = \sqrt{\frac{2}{\pi}} \left[\mathrm{erfc}\left(\frac{\nu}{\sqrt{2}}\right)\right]^{-1} \frac{e^{-\nu^2/2}}{\sigma^N(R)} H_{N-1}(\nu) . \tag{4.11}$$

These coefficients are the bias parameters. In the case of high-peaks (*i.e.* $\nu \gg 1$) they reduce to

$$b_N^L \approx \frac{\nu^N}{\sigma^N(R)}. \tag{4.12}$$

Since the two-point correlation function goes to zero for large separations (see Eq. (3.5.2)), we need to take only the first few terms of the bias expansion into account, in the larger scale regime. The first term gives the well known linear bias relation in Lagrangian space:

$$\xi_h^L(r) = (b_1^L)^2 \xi_R^L(r). \tag{4.13}$$

This indicates that on large scales the statistics of halos are related to those of the underlying matter field by just a multiplicative factor (Kaiser, 1984). This means that high-mass peaks, which correspond to rare massive halos, will have larger bias parameter [Eq. (4.12)]. In other words on large scales, the distribution of galaxies is more responsive to the rare regions than underlying matter, which leads to more biased and clustered halos (Kaiser, 1984). This holds also for high redshifts, where the Universe is more dense, leading to an increase in the background density by a factor of δ. This is equivalent to a change in the threshold by, $\delta_c - \delta$. The occurrence of high peaks and massive halos will increase this way, leading again to a high biased population and therefore to more clustered objects [Eq. (4.13)].

The expansion of Eq. (4.10) motivates us to write the overdensity field of halos as a

local bias perturbative expansion over the linear field as (Fry and Gaztanaga, 1993):

$$\delta_h^L(\mathbf{q}) = b_0^L + b_1^L \delta_R^{(1)}(\mathbf{q}) + \frac{b_2^L}{2!}[\delta_R^{(1)}(\mathbf{q})]^2 + \frac{b_3^L}{3!}[\delta_R^{(1)}(\mathbf{q})]^3 + \dots \,, \tag{4.14}$$

where the zero-order bias term is just a constant offset that guarantees $\langle \delta_h \rangle = 0$. Here, following (Desjacques et al, 2016), we will call it *local-in-matter* bias expansion to distinguish it from the general case discussed in Sec. 4.3.2. This expansion accurately describes the effect of bias on large scales and converges to the correct result by using a minimum set of free parameters. Since the analysis, up to now, is restricted to the spherical collapse approximation, we don't expect the local-in-matter relation to describe correctly the bias of low mass objects ($R \to 0$ then $\nu \to 0$), due to the cloud-in-cloud problem. In addition, the convergence to the correct result is not guaranteed beyond the non-linear scales (*i.e.* k_{NL}), where higher order terms can be larger than the lower. This indicates the break down of the expansion, not only for bias, but also for the perturbative approach of the underlying matter field. Therefore, the restriction of the analysis up to the mildly non-linear regime is necessary. In this chapter, from this point on, we drop the subscript R denoting the smoothed density field over a Lagrangian radius and we implicitly assume it.

The local-in-matter bias expansion, as we have already discussed, does not capture sufficiently the complicated process of halo formation. Additional non-local terms (*i.e.* terms that are not proportional to the linear matter density field) are expected to be present due to the non-local nature of gravity. It was pointed out in (Fry and Gaztanaga, 1993) that there is no need to limit ourselves strictly on local terms, in order to make the local-in-matter bias expansion efficient, as long as these non-local contributions become important at small scales. The local-in-matter expansion is deterministic by construction. However, this characteristic is not realistic, due to the presence of small scale fluctuations and the discrete nature galaxies [Eq. (3.88)]. Therefore, additional *stochastic bias* terms must be introduced in the expansion (Sec. 4.3.2).

4.3.1 Bias evolution

Now we proceed to describe the evolution of the bias relation from a Lagrangian initial frame to an evolved Eulerian space. Following (Mo and White, 1996) we can write a similar expansion for the overdensity field to Eq. (4.14) at a given redshift as:

$$\delta_h(\mathbf{x},\tau) = b_1^E(\tau)\delta^{(1)}(\mathbf{x}) + \frac{b_2^E(\tau)}{2!}[\delta^{(1)}(\mathbf{x})]^2 + \frac{b_3^E(\tau)}{3!}[\delta^{(1)}(\mathbf{x})]^3 + \dots . \tag{4.15}$$

The superscript E denotes the bias parameters in the Eulerian framework. The bias parameters between the two frames are related through the conservation of mass in each cell. The following relation emerges (Catelan et al, 1998):

$$1 + \delta_h(\mathbf{x},\tau) = [1 + \delta(\mathbf{x},\tau)][1 + \delta_h^L(\mathbf{q})]\,. \tag{4.16}$$

This yields immediately the relation for the linear bias term between the two frames,*i.e.* $b_1^E = 1 + b_1^L$. This expression is non-local in general, but for a local approximation (*i.e.* $\mathbf{x} \equiv \mathbf{q}$) we can derive a mapping between the initial linear Lagrangian density field $\delta^{(1)}$ and the non-linear evolved field $\delta(\tau)$ in Eulerian frame. In the spherical collapse approximation, after integrating over all angles (*i.e.* the monopole) of the second order density kernel in Fourier space [Eq. (3.20)], we get (Bernardeau, 1992; Fosalba and Gaztanaga, 1998)

$$\delta^{(1)} = \sum_{i=1}^{\infty} a_i \delta^i = \alpha_1\delta + \alpha_2\delta^2 + \alpha_3\delta^3 + \dots\,, \tag{4.17}$$

where the first four coefficient are, $\alpha_1 = 1$, $\alpha_2 = -17/21$, $\alpha_3 = 2815/3969$ and $\alpha_4 = -590725/916839$. The coefficients α_3 and α_4 in Eq. (4.17) are taken from Wagner et al (2015), where they correct the results of Mo et al (1996). Finally the relations for the the first four bias factors between the two frames are (Mo and White, 1996; Mo et al, 1996)

$$b_1^E = 1 + b_1^L, \tag{4.18}$$

$$b_2^E = b_2^L + 2(\alpha_1 + \alpha_2)b_1^L = \frac{8}{21}(b_1^E - 1) + b_2^L, \tag{4.19}$$

$$b_3^E = 6(\alpha_2+\alpha_3)b_1^L + 3(1+2\alpha_2)b_2^L + b_3^L = \frac{20}{198}(b_1^E-1) - \frac{13}{7}b_2^E + b_3^L, \tag{4.20}$$

$$\begin{aligned} b_4^E &= 24(\alpha_3+\alpha_4)b_1^L + 12(\alpha_2^2+2(\alpha_2+\alpha_3))b_2^L + 4(1+3\alpha_2)b_3^L + b_4^L \\ &= \frac{3680}{43659}(b_1^E-1) - \frac{6820}{1323}b_2^E - \frac{40}{7}b_3^E + b_4^L. \end{aligned} \tag{4.21}$$

Having found the relation between the bias parameters in the two frames, we continue the derivation of the gravitational evolution of bias by assuming that the number of halos is conserved from the initial time $\tau = \tau_*$ to the evolved τ. Obviously this is an approximation, since as they evolve small mass halos merge and form larger ones (*i.e.* hierarchical clustering of galaxies). Additionally, we assume that halos form instantaneous in the initial time τ_*. Up to now, we have used the spherical collapse model, which is in fact the case with neglected tidal effects, therefore the evolved field will be a local non-linear expansion of the initial field (Fosalba and Gaztanaga, 1998). Dropping this assumption, introduces additional non-local terms originating from the non-local nature of gravity. This means that even though we are in the Newtonian approximation, tidal forces are present (Kofman and Pogosyan, 1995; Fosalba and Gaztanaga, 1998). A final point to make is that there is no velocity bias. This can be justified by the fact that, for a sufficiently large radius the peculiar velocity of halos is regulated by the physics inside the patch (mainly of non-gravitational nature) and hence at large scales, where non-gravitational forces are absent, all bodies free fall in an external gravitational field, as dictated by the equivalence principle. Thus, we can safely consider halos to comove with matter.

We start from a local expansion, similar to Eq. (4.15), at the initial time slice τ_* and we let it evolve under gravity, to a late time τ (*i.e.* passive evolution). Gravity will move away the fluid element, which contains the halo, from the initial Lagrangian coordinate $\mathbf{q}$ to a late-time Eulerian position $\mathbf{x}(\tau) = \mathbf{q} + \mathbf{s}(\mathbf{q},\tau)$, where $\mathbf{s}(\mathbf{q},\tau)$ is the Lagrangian displacement field. Here we use a different notation from the usual (see *e.g.* (Desjacques et al, 2016)), in order to avoid confusion with the general quadratic potential field, defined

in the next section. The displacement field is the same as in LPT [Eq. (3.29)] and its Lagrangian coordinate coincides with $\mathbf{q} = \mathbf{x}(0)$. Following (Catelan et al, 1998; Tegmark and Peebles, 1998), we write the continuity equation of halos [Eq. (3.1)] in the following form:

$$\frac{\mathrm{d}}{\mathrm{d}\tau}\delta_h = -\theta(1+\delta_h)\,, \tag{4.22}$$

where

$$\mathrm{d}/\mathrm{d}\tau = \frac{\partial}{\partial\tau} + \mathbf{u}\cdot\boldsymbol{\nabla} \tag{4.23}$$

is the connective derivative. The continuity equation of matter will be :

$$\frac{\mathrm{d}}{\mathrm{d}\tau}\delta = -\theta(1+\delta)\,. \tag{4.24}$$

Equating the two we get

$$\frac{1}{1+\delta_h}\frac{\mathrm{d}}{\mathrm{d}\tau}\delta_h = -\theta = \frac{1}{1+\delta}\frac{\mathrm{d}}{\mathrm{d}\tau}\delta\,, \tag{4.25}$$

which leads, after integrating, to:

$$1+\delta_h(\mathbf{x},\tau) = \frac{1+\delta(\mathbf{x},\tau)}{1+\delta(\mathbf{x}_*,\tau_*)}(1+\delta(\mathbf{x}_*,\tau_*))\,, \tag{4.26}$$

where the Eulerian coordinates of the fluid element, at formation time, are given by $\mathbf{x}_* = \mathbf{x}(\tau_*)$. The above equation states that, conserved halos free fall with the same rate, and along the same trajectory, as matter[1]. This solution is reduced to the one in Eq. (4.16), if we take $\tau_* \to 0$. If we take the solution of the fields up to second order, we can get

$$1+\delta_h^{(1)}(\mathbf{x},\tau)+\delta_h^{(2)}(\mathbf{x},\tau) = 1+\delta^{(1)}(\mathbf{x},\tau)-\delta^{(1)}(\mathbf{x}_*,\tau_*)+\delta_h^{(1)}(\mathbf{x}_*,\tau_*)+\delta^{(2)}(\mathbf{x},\tau)-\delta^{(2)}(\mathbf{x}_*,\tau_*)$$

[1] This is also imposed by the equivalence principle.

$$+\delta_h^{(2)}(\mathbf{x}_*,\tau_*)+[\delta^{(1)}(\mathbf{x}_*,\tau_*)]^2-\delta^{(1)}(\mathbf{x},\tau)\delta^{(1)}(\mathbf{x}_*,\tau_*)+\delta^{(1)}(\mathbf{x},\tau)\delta_h^{(1)}(\mathbf{x}_*,\tau_*)-\delta^{(1)}(\mathbf{x}_*,\tau_*)\delta_h^{(1)}(\mathbf{x}_*,\tau_*)\,. \tag{4.27}$$

The next step is to take the bias expansion at the formation time slice. We use the the most general expansion up to second order written as (Chan et al, 2012):

$$\delta_h(\mathbf{x}_*,\tau_*)=b_1^*[\delta^{(1)}(\mathbf{x}_*,\tau_*)+\delta^{(2)}(\mathbf{x}_*,\tau_*)]+\varepsilon^*(\mathbf{x}_*,\tau_*)+\frac{1}{2}b_2^*[\delta^{(1)}(\mathbf{x}_*,\tau_*)]^2+b_{s^2}^*[s_{ij}(\mathbf{x}_*,\tau_*)]^2, \tag{4.28}$$

where we have introduced the linear tidal field term [Eq. (4.32)], following (Chan et al, 2012). In general there is no reason for the formation of galaxies not to depend on the tidal field (Catelan et al, 1998; Heavens et al, 1998; Smith et al, 2007; McDonald and Roy, 2009; Baldauf et al, 2012; Chan et al, 2012). The term ε is the stochastic term at first order, which is assumed to capture the perturbations that are uncorrelated with fluctuations at large scales (Mirbabayi et al, 2015). In the following section we will discuss in greater detail the tidal and the stochastic terms. After using the above expansion in Eq. (4.27) and rearranging the terms, we can get the final evolved bias relation up to second order:

$$\begin{aligned}\delta_h(\mathbf{x},\tau)&=b_1^E(\tau)[\delta^{(1)}(\mathbf{x},\tau)+\delta^{(2)}(\mathbf{x},\tau)]+\varepsilon(\mathbf{x}_*,\tau_*)+\frac{1}{2}b_2^E(\tau)[\delta^{(1)}(\mathbf{x},\tau)]^2+b_{s^2}^E(\tau)s_{ij}^2(\mathbf{x},\tau)\\&-(D(\tau_*)-1)\varepsilon(\mathbf{x}_*,\tau_*)\delta^{(1)}(\mathbf{x},\tau)+[D(\tau_*)-1]\mathbf{s}^i\partial_i\varepsilon(\mathbf{x}_*,\tau_*).\end{aligned} \tag{4.29}$$

The quadratic bias parameters are (Sheth et al, 2013):

$$\begin{aligned}b_2^E(\tau)&=b_2(\tau_*)D^2(\tau_*)+\frac{8}{21}\left(1-D(\tau_*)\right)\left[b_1^E(\tau)-1\right]\\b_{s^2}^E(\tau)&=b_{K^2}(\tau_*)D^2(\tau_*)-\frac{2}{7}\left(1-D(\tau_*)\right)\left[b_1^E(\tau)-1\right].\end{aligned} \tag{4.30}$$

Now, if we take $\tau\to 0$, while substituting the quantities $D^n(\tau_*)b_n(\tau_*)$ to the corresponding Lagrangian biases, we can get the result for the Lagrangian initial frame. If we

don't consider a tidal field in the initial slice ($b_{s^2}^L = 0$) and we follow the evolution of the bias expansion, we notice that a tidal term appears in the evolved Eulerian frame. This was first noticed by (Catelan et al, 1998, 2000), where they studied the difference of the three-point correlation function in the two frames.

4.3.2 General bias expansion

In order to determine the set of bias terms needed for describing the statistics of LSS tracers up to the scales of validity of PT, one needs to investigate the interplay of bias with gravity. This can be done by defining a mapping for the tracer's field, from an initial formation time τ_* to that of a later time $\tau > \tau_*$. Here we will expand the argument of locality, reviewed in the previous section, to the more general and physically motivated formalism of *local* expansion[2]. A complete set of terms was presented in (Senatore, 2015; Mirbabayi et al, 2015), where they argue that the most general bias expansion is constructed out of all possible *local gravitational observables* along the fluid trajectory. The general deterministic bias expansion for the halos is given by

$$\delta_h(\mathbf{x},\tau) = \sum_O b_O(\tau) O(\mathbf{x},\tau), \tag{4.31}$$

where $O(\mathbf{x},\tau)$ is the set of all relevant operators in Eulerian co-moving coordinates $\mathbf{x}$, which describe the properties that can affect the density of halos, at a given order in PT. The bias parameters can be seen as coefficients of such a basis, which for a fixed time they are just numbers. The well known large-scale linear bias result can be easily derived for $O = \delta$ and $b_O = b_1$. Such an expansion, is only useful if there is a finite set of parameters at a given order in PT.

This set of operators contain all the leading local gravitational observables. From the equivalence principle, they are constructed only from powers of the tensor $\partial_i \partial_j \phi$ (the derivatives here are over the spatial dimension), in the case of non-relativistic tracers

[2]Do not confuse this with the standard local bias expansion that is used in the literature.

(Mirbabayi et al, 2015). The field ϕ is the gravitational potential of the time-time component of the metric, in the conformal Newtonian gauge (*i.e.* absence of anisotropic stress), and is equal to the Bardeen potential Φ up to a minus sign. This tensor can be decomposed into its trace (*i.e.* $\nabla^2\phi$), which is equal to the non-linear density field through Poisson equation, and its traceless part s_{ij}. The latter is defined as (Catelan et al, 2000):

$$\begin{aligned} s_{ij}(\mathbf{x},\tau) &= (\frac{\partial_i\partial_j}{\nabla^2} - \frac{1}{3}\delta_{ij})\delta(\mathbf{x},\tau) \\ &= \frac{2}{3\Omega_m(\tau)\mathcal{H}^2}\partial_i\partial_j\phi - \frac{1}{3}\delta_{ij}\delta(\mathbf{x},\tau). \end{aligned} \tag{4.32}$$

This quantity, as we discussed before, is the tidal field and it was introduced in the bias expansion (together with higher-order derivatives) in the work of (McDonald and Roy, 2009; Chan et al, 2012; Baldauf et al, 2012) in order to address the issue of non-equivalence between Lagrangian and Eulerian bias at first order. Note that, since it is traceless (*i.e.* $s_{ij}\delta^{ij} = 0$) , it cannot appear at linear order in the bias expansion. In Fourier space the tidal field is written as

$$s_{ij}(\mathbf{k},\tau) = \left(\frac{k_i k_j}{k^2} - \frac{1}{3}\delta_{ij}\right)\delta(\mathbf{k},\tau). \tag{4.33}$$

The local bias coefficients, in this general bias expansion, will be all the terms constructed from powers of the density and the tidal fields, as well as the combinations of the two, along the fluid trajectory. Terms containing ϕ or its first derivative are not included in the expansion, since they cannot be measured by a free-falling observer co-moving with the trajectory of the fluid, due to the equivalence principle. Therefore, the operator O includes only powers of the density and the tidal field. Note that, in this general bias formalism the assumption of conserved tracers can be abandoned, since gravitational interactions on large scales depend only on the local density and tidal fields. To acquire a complete basis, one needs to consider also the connective time derivatives of the operators O [Eq. (4.23)], *i.e.* $\mathrm{d}(\partial_i\partial_j\phi)/\mathrm{d}\tau$. However, this would suggest that an infinite amount of time derivative

terms is needed in the expansion, since the formation of galaxies occurs over a long time range (Desjacques et al, 2016). Nevertheless, up to the fixed PT order, such terms are finite. This is due to the fact that, up to the scales of validity of PT, the time evolution of perturbations is governed by the linear growth factor, which is scale independent, and hence the evolution will proceed at the same rate. Any deviation from the linear time evolution should be observed at higher orders (Desjacques et al, 2016). In fact, already at third order, connective time derivative terms appear (Mirbabayi et al, 2015). Such a third order term cannot be expressed locally with respect to density and tidal fields, however it can be included in the local operators basis, since it can be measured from an observer co-moving with the fluid element, in the case of conserved tracers (Mirbabayi et al, 2015).

Higher-derivative bias terms include operators that have more than two spatial derivatives on ϕ. Each operator O has higher-derivative terms of the form $b_{\nabla^2 O}\nabla^2 O$, as well as others (see (Desjacques et al, 2016) for an extensive discussion). They introduce a spatial scale R_*, which is the characteristic dimension around a position $\mathbf{x}$, denoting the region from which matter, that forms halos, originates. At scales comparable to R_* ($k \sim 1/R_*$), higher-derivative terms become important, indicating the limit of validity of the perturbative bias expansion (Desjacques et al, 2016). Such terms incorporate all the non-gravitational contributions during the halo formation process (*e.g.* gas heating, feedback processes) and in fact indicate that halo formation is not a perfectly local process. The contribution of these terms in the bias relation depend on the limiting scales R_*, which in the case of dark matter halos is of the size of the Lagrangian radius $R(M)$.

The bias relation of Eq. (4.31) is deterministic, since it does not take into account the dependence of the halo formation process on small scale perturbations. These fluctuations must be treated stochastically, since their initial conditions are uncorrelated with the density perturbations. In order to take this effect into account, an introduction of a leading stochastic field $\varepsilon(\mathbf{x}, \tau)$ in the bias expansion is necessary (*stochastic* bias terms) (Dekel and Lahav, 1999; Taruya and Soda, 1999; Matsubara, 1999). The stochastic field

couples to the gravitational evolution, introducing additional stochastic terms ε_O, which can be seen as a scatter in the deterministic bias coefficient b_O, for each operator O. These fields have zero mean and they are characterised fully by their one-point PDF, since they are uncorrelated with large scale fluctuations ($\langle \varepsilon_O \delta \rangle = 0$). Due to that, only correlators between themselves survive (*e.g.* $\langle \varepsilon\varepsilon \rangle$, $\langle \varepsilon\varepsilon_\delta \rangle$, *etc.*). They are expected to be important at scalesof $\mathcal{O}(R_*)$. A consequence of this is the presence of higher-derivative stochastic counterparts (Desjacques et al, 2016). Taking account this randomness, the bias expansion at any given order in SPT will be

$$\delta_h(\mathbf{x},\tau) = \sum_O [b_O(\tau) + \varepsilon_O(\mathbf{x},\tau)] O(\mathbf{x},\tau) + \varepsilon(\mathbf{x},\tau). \tag{4.34}$$

The results of the expansion up to second order in Eulerian coordinates and Gaussian initial conditions are

$$\delta_h^{E,(G)}(\mathbf{x},\tau) = b_1^E(\tau)\delta(\mathbf{x},\tau) + \varepsilon^E(\mathbf{x},\tau) + \frac{b_2^E(\tau)}{2}\delta^2(\mathbf{x},\tau) + b_{s^2}^E(\tau)s^2(\mathbf{x},\tau) + \varepsilon_\delta^E(\mathbf{x},\tau)\delta(\mathbf{x},\tau), \tag{4.35}$$

where $s^2 = s_{ij}s^{ij}$ is the simplest scalar that can be formed from the tidal field. A factor $1/2$ in the tidal term has been absorbed here in the bias parameter. Following the definition of (Baldauf et al, 2012) the second order tidal bias term in Eulerian frame is given by:

$$b_{s^2}^E(M,z) = -\frac{2}{7}b_1^L(M,z) = -\frac{2}{7}(b_1^E(M,z) - 1), \tag{4.36}$$

where the above is derived from Eq. (4.30), for $\tau_* \to 0$. Although the subscript R is missing from the fields in the bias expansion, they are all assumed smoothed at a radius R_*. In the above expansion we have excluded one higher-derivative term of the form $b_{\nabla^2\delta}\nabla^2\delta$, where the coefficient is $b_{\nabla^2\delta} \sim R_*^2$ (Desjacques et al, 2016). If sufficiently large scales ($k \ll 1/R_*$) are considered, the contribution of such term, in the bias relation, is suppressed.

4.3.3 Peak-background split

The main idea of the *peak-background split* formalism (Kaiser, 1984; Bardeen et al, 1986; Cole and Kaiser, 1989) is to give the bias parameters, in the general expansion [Eq. (4.31)], a physical interpretation, while providing a link to observables. The mapping is achieved by identifying the change of the halo number density to the perturbations induced by a long-wavelength mode. The density fluctuation field is decomposed into a low-amplitude, long-wavelength, linear fluctuation and a noisy short-wavelength, as:

$$\delta_h(\mathbf{x}) = \delta_{h,l}(\mathbf{x}) + \delta_{h,s}(\mathbf{x}). \tag{4.37}$$

The short-wavelength fluctuations ride on top of the linear long-wavelength modes (*i.e.* $\delta_l = \delta^{(1)}$), where the matter perturbations are treated as a superposition of small and long modes, separated by a cut-off wavenumber. The short-wavelength modes are the source of the dark matter halos, while the long-wavelength modes increase or decrease the background density in large patches of the sky. In other words, large modes act as a modification of the background density, altering the threshold of collapse. In this picture, the peaks of the small modes, that are located over peaks of long-wavelength modes, will be more clustered than the average and they will be the first to collapse, forming galaxy clusters. This explains why galaxy clusters are more clustered than the galaxies themselves.

The presence of the long-wavelength mode will modulate the background density and eventually alter the height of the peaks to an effective value, given by:

$$\nu \to \nu_{eff} = \frac{\delta_c - \delta_l}{\sigma_R}. \tag{4.38}$$

To show the reasoning behind the PBS argument, we write the expression for the number

of mass M halos, located inside a cell of volume V, in the Eulerian frame as

$$\delta_h^E(M|M_1,V) = \frac{\mathcal{N}(M|M_1,V,z)}{n_h(M,z)V} - 1\,, \tag{4.39}$$

where $\mathcal{N}(M|M_1,V,z)$ is the number of subhalos of mass M, corresponding to the short-wavelength peaks, which are ready to collapse, on top of the long modes and above some mass M_1. The latter is defined by the "background" (*i.e.* long wavelength) mode, while $n_h(M,z)$ is the mean number of halos above mass M (*i.e.* the halo mass function). Using the relationship $M/V = \overline{\rho}_m(1+\delta) \Rightarrow V_0 = M/\overline{\rho}_m = V(1+\delta)$, together with the mapping between the Eulerian and Lagrangian frames in the case of conserved tracers [Eq. (4.16)], we get the overdensity field in Lagrangian coordinates as (Mo and White, 1996):

$$\delta_h^L(M|M_1,V_0) = \frac{n_h(M|M_1,V_0,z_0)}{n_h(M_1,z_0)} - 1, \tag{4.40}$$

where now $n_h(M|M_1,V_0,z_0)$ is a Lagrangian quantity. The Lagrangian bias can be identified from a matching between a Taylor expansion of the above equation and the Lagrangian local-in-matter bias relation [Eq. (4.14)] as:

$$\begin{aligned}\delta_h^L &= \sum_{n=0}^{\infty} \frac{1}{n!} b_n^L(M)[\delta^{(1)}]^n = b_1^h(M)\delta^{(1)} + \frac{b_2^h(M)}{2}[\delta^{(1)}]^2 + \ldots \\ &= \frac{1}{n_h(M,z)} \sum_{N=0}^{\infty} \frac{1}{N!} \frac{\partial^N n_h(M|M_1,V_0,z)}{\partial \delta_l^N}\bigg|_{\delta_l=0} \delta_l^N,\end{aligned} \tag{4.41}$$

which gives eventually:

$$b_N^L(M,z) = \frac{1}{n_h(M,z)} \frac{\partial^N n_h(M,z)}{\partial \delta_l^N}\bigg|_{\delta_l=0}. \tag{4.42}$$

Although,this approach was introduced to model the local-in-matter bias terms b_N^L (Kaiser, 1984; Cole and Kaiser, 1989; Mo and White, 1996; Mo et al, 1996), we can use it to derive the bias coefficients of the tidal field and the higher-derivative terms, as well as for terms induced by primordial non-Gaussianity (see Sec. 4.4). Since we are interested in

the statistics of the evolved halo field (Eulerian frame), a mapping between Lagrangian and Eulerian bias can be build. For the local-in-matter bias terms one can assume spherical symmetry (*i.e.* no tidal field term is induced in the late-time field) and derive an exact relation between the two. Therefore, the knowledge of the bias parameters (excluding higher-derivative terms; for a discussion see (Desjacques et al, 2016)) in one frame determines the set in the other, at each order in PT.

For a universal mass function, as the one in Eq. (4.5), the PBS argument [Eq. (4.42)] can become

$$b_N^L(M,z) = \frac{(-\nu)^N}{\delta_c^N f(\nu)} \frac{d^N f(\nu)}{d\nu^N}. \tag{4.43}$$

This result is general enough to derive the Lagrangian halo bias for any type of universal mass function. Here we will present the Lagrangian bias in the case of ST mass function. For the first four local-in-matter halo bias parameters we have (Mo and White, 1996; Mo et al, 1996; Scoccimarro et al, 2001b)

$$b_1^L(M,z) = \frac{q\nu^2-1}{\delta_c} + \frac{2p}{\delta_c(1+(q\nu^2)^p)}, \tag{4.44}$$

$$b_2^L(M,z) = \frac{q\nu^2(q\nu^2-3)}{\delta_c^2} + \left(\frac{1+2p}{\delta_c} + \frac{2(q\nu^2-1)}{\delta_c}\right)\frac{2p}{\delta_c(1+(q\nu^2)^p)}, \tag{4.45}$$

$$b_3^L(M,z) = \frac{q\nu^2}{\delta_c^3}(q^2\nu^4 - 6q\nu^2 + 3) + \left[\frac{4(p^2-1)+6pq\nu^2}{\delta_c^2} + 3\left(\frac{q\nu^2-1}{\delta_c}\right)^2\right]\frac{2p}{\delta_c(1+(q\nu^2)^p)}, \tag{4.46}$$

$$b_4^L(M,z) = \left(\frac{q\nu^2}{\delta_c^2}\right)^2 (q^2\nu^4 - 10q\nu^2 + 15) + \frac{2p}{\delta_c(1+(q\nu^2)^p)}\left[\frac{2q\nu^2}{\delta_c^2}\left(2\frac{q^2\nu^4}{\delta_c} - 15\frac{q\nu^2-1}{\delta_c}\right)\right.$$
$$\left. + 2\frac{(1+p)}{\delta_c^2}\left(\frac{4(p^2-1)+8(p-1)q\nu^2+3}{\delta_c} + 6q\nu^2\frac{q\nu^2-1}{\delta_c}\right)\right], \tag{4.47}$$

where $q = 0.707$ and $p = 0.3$.

The halo density field in Eq. (4.41) needs to be transformed into the Eulerian frame, in order to take into account the halos' dynamics. Therefore, we use the transformation rule, presented Eq. (4.18)-(4.21), to achieve the mapping between the two frames. The

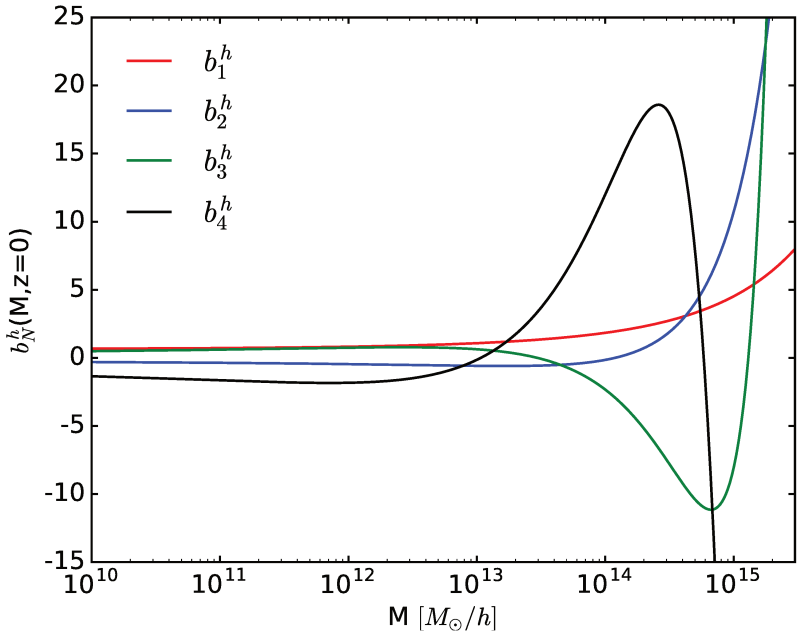

Figure 4.1 – The Eulerian halo bias parameters up to fourth order redshift $z = 0$ as a function of the halo mass.

Eulerian bias parameters, listed above, are plotted in Figure 4.1 as a function of the halo mass.

4.4 Effects of primordial Non-Gaussianity

4.4.1 Non-Gasusian mass function

Primordial non-Gaussianity affects the high-peak tail of the smoothed matter density probability distribution function. Hence, the Gaussian assumption of the Press-Schechter formalism is no longer valid. Here we follow (LoVerde et al, 2008) (later on LV), where the authors approximate the unknown non-Gaussian PDF with an Edgeworth expansion. By expanding the ST formula up the the third order, we have

$$f_{LV}(\nu, z, f_{NL}) = f_{ST}(\nu) R_{NG}(\nu, z, f_{NL})$$

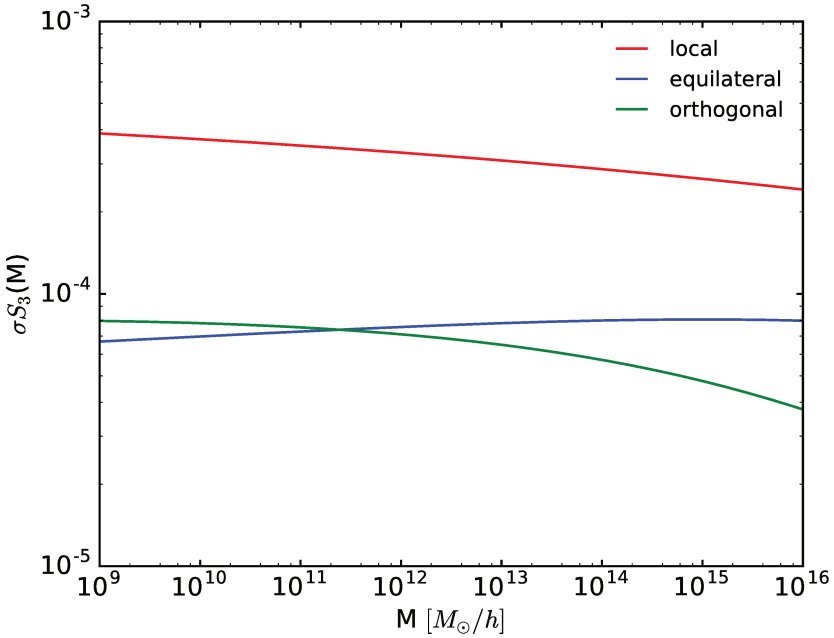

Figure 4.2 – The third one-point cumulant $\sigma_R S_3$ with $f_{NL} = 1$ for the three shapes considered here. For the orthogonal case the absolute value is plotted here since it is negative.

$$= f_{ST}(1 + \frac{1}{6}\sigma_R S_3(\nu^3 - 3\nu) - \frac{1}{6}\frac{\mathrm{d}(\sigma_R S_3)}{\mathrm{dln}\nu}), \tag{4.48}$$

where $S_3(M, z, f_{NL}) = \langle\delta^3(M, z)\rangle/\sigma_R^4(M, z)$ is the skewness. Cumulants beyond skewness are not included in the expansion, although, as mentioned in LoVerde et al (2008) they become important for high mass halos ($M \gtrsim 10^{15}\, h^{-1} M_\odot$). This indicates that we should trust the LV mass function only for the low and intermediate mass scales. Such mass function has a better agreement with N-body simulations, after correcting the collapse threshold by $\delta_c \to \sqrt{0.8}\delta_c(z)$ (Pillepich et al, 2010; Grossi et al, 2009). This change in δ_c will be incorporated in our calculations throughout this thesis[3]. The skewness S_3 can be

[3]The value of the correction parameter, $\sqrt{q}\delta_c$, depends on the halo finding algorithm, *i.e.* friends-of-friends (FOF) or the spherical overdensity method. The first one is used in the work of (Pillepich et al, 2010; Grossi et al, 2009), whose results we use here.

measured from

$$S_3(M,z,f_{NL}) = \frac{(2\pi)^3}{\sigma_R^4(M,z)} \int \frac{d^3\mathbf{k}_1}{(2\pi)^3}\frac{d^3\mathbf{k}_2}{(2\pi)^3}\frac{d^3\mathbf{k}_3}{(2\pi)^3}\delta_D(\mathbf{k}_{123}) \times M_R(k_1,z)M_R(k_2,z)M_R(k_3,z)B_\Phi(k_1,k_2,k_3). \quad (4.49)$$

Such 3D integral can be factorized into three 1D integrals, after expressing the Dirac delta as a plane wave and taking advantage of the spherical symmetry. In the case of a separable primordial bispectrum, such as those considered here, we can separate the integrals by grouping the relevant terms with the same wave number, resulting in a sequence of 1D integrals (see Appendix of LoVerde and Smith (2011), which can be easily calculated numerically by using an FFT code.

A fitting function for $\sigma_R S_3$, which depends weakly on the mass, is presented in (LoVerde and Smith, 2011). Although the fitting function agrees with our results, it is provided only for the local case. Since our interest lies also in additional shapes, we will compute the skewness directly from Eq. (4.49). The results for $\sigma_R S_3$, in the case of the three shapes considered here, are plotted in Figure 4.2 as a function of the smoothing mass M.

4.4.2 Non-Gaussian bias

In the presence of primordial non-Gaussianity of the local type [Eq. (2.84)], and in the spirit of PBS, long-wavelength fluctuations of the primordial gravitational potential modulate the small scale initial perturbations, due to the induced coupling between the two. This will lead to an analogous modulation in the abundance of halos and eventually to a scale-dependant bias correction on large scales (Dalal et al, 2008; Slosar et al, 2008). Following a different approach, (Matarrese and Verde, 2008; Afshordi and Tolley, 2008) derived the same result. In the work of Verde and Matarrese (2009), the impact in two-point statistics from a general three-point function was considered. A generalisation of

the scale-dependent bias results in the local case was made by (Desjacques and Seljak, 2010; Schmidt and Kamionkowski, 2010; Desjacques et al, 2011b; Schmidt et al, 2013), in order to derive the leading scale-dependent contribution in the squeezed-limit of a generic quadratic primordial non-Gaussianity.

Following the general local bias philosophy [Eq. (4.31)], additional operators involving the primordial Bardeen potential Φ (without any derivatives) must be added, in order to model the scale-dependent corrections (in the same spirit as in (McDonald, 2008; Giannantonio and Porciani, 2010; Baldauf et al, 2011)). Due to the equivalence principle, such operators are not local gravitational observables and cannot be included in the local part of the expansion. The non-Gaussian set of terms that is introduced, up to linear order in $f_{\rm NL}$ and at lowest order in higher-derivatives, are all the combination between $f_{\rm NL}\Phi$ and the Gaussian operators. These include terms proportional to $\Phi\delta^m$, as introduced in Giannantonio and Porciani (2010), as well as non-Gaussian counterparts of the tidal terms (Φs^N_{ij}) and higher-derivative terms (Assassi et al, 2015). Non-Gaussian corrections to the stochastic bias terms are also expected to be present, due to their dependence on small scale perturbations.

In the case of an arbitrary isotropic quadratic primordial non-Gaussianity, the full set of operators was derived in (Assassi et al, 2015). Up to second-order in terms and linear in $f_{\rm NL}$, we have in the Eulerian frame

$$\delta_h^{E,(NG)}(\mathbf{x},\tau) = b^E_\Psi(\tau)\Psi(\mathbf{q}) + b^E_{\Psi\delta}(\tau)\Psi(\mathbf{q})\delta(\mathbf{x},\tau) + \varepsilon^E_\Psi(\mathbf{x},\tau)\Psi(\mathbf{q}), \tag{4.50}$$

where the field Ψ is a non-local transformation of the primordial Bardeen potential, defined as:

$$\Psi(\mathbf{q}) = \int \frac{d^3\mathbf{k}}{(2\pi)^3} k^\alpha \Phi_G(\mathbf{k}) e^{i\mathbf{kq}}, \tag{4.51}$$

where α can take real values, which depend on the shape of the primordial bispectrum. This field originates from the generalization of the local ansatz [Eq. (2.83)] in the case of

general quadratic primordial non-Gaussianity, where a kernel is introduced in the Fourier version of Eq. (2.83) in the convolved term (Schmidt and Kamionkowski, 2010; Scoccimarro et al, 2012). Such kernel cannot be uniquely defined by the primordial bispectrum. For the large scales considered here ($k \ll 1/R_*$), only the squeezed limit is relevant for the bias expansion, which can be expressed as an expansion over the Legendre polynomials (Schmidt and Hui, 2013; Assassi et al, 2015). Throughout this thesis we consider only terms of $\mathcal{O}(f_{\rm NL})$ in the bias expansion, since higher order non-Gaussian contributions (*e.g.* $\mathcal{O}(f_{\rm NL}^2)$,$\mathcal{O}(g_{NL})$) have an extremely small observable effect in the statistics of LSS (Assassi et al, 2015).

The primordial non-local field Ψ is evaluated at the Lagrangian position $\mathbf{q}$ (initial slice), which is related to the Eulerian coordinates through $\mathbf{q} = \mathbf{x}(\tau) - \mathbf{s}(\mathbf{q}, \tau)$. The latter introduces additional terms, through couplings to other fields (starting from second-order), in the bias expansion due to gravitational evolution. In the Gaussian case they cancel out, since they generate a deviation from the fluid trajectory, which in fact is forbidden by the equivalence principle when non-gravitational forces are neglected. However, this is not the case for primordial non-Gaussianity, where the coupling is not induced by gravitational evolution, but is present in the initial conditions. Hence, the corresponding Eulerian position of the primordial potential field is related to the Lagrangian, up to second order, through $\Phi_G(\mathbf{q}) = \Phi_G(\mathbf{x}) - s^i(\mathbf{x}, \tau)\partial_i \Phi_G(\mathbf{x})$ (Giannantonio and Porciani, 2010; Baldauf et al, 2011). Such an expansion must be taken into account when the statistics of tracers is evaluated at observation time (Tellarini et al, 2015), since it introduces displacement terms whose amplitude is regulated by the corresponding bias term[4] (*e.g.* b_Ψ for tree-level). Finally, higher-derivative terms, present already at the linear order of Eq. (4.50) (*i.e.* $b_{\nabla^2\Psi}\nabla_q^2\Psi(\mathbf{q})$ and $b_{\nabla^2\Psi} \sim R_*^2$; see (Desjacques et al, 2016) for a discussion), are excluded. This follows the same argument as in the Gaussian case (see Sec. 4.3.2).

The presence of primordial non-Gaussianity will affect the halo number density, as

[4]Up to second order a term of the form, $-b_\Psi^L s^i(\mathbf{x}, \tau)\partial_i \Psi(\mathbf{x})$, is introduced for general non-Gaussianity in Eq. (4.50).

shown in Sec. 4.4.1. More specifically, for the non-Gaussian mass function considered here (LV mass function), the fractional correction R_{NG} will introduce a scale-independent offset in the bias parameters originating from the partial derivative in Eq. (4.61). These terms will depend on f_{NL}, due to the presence of a non zero skewness S_3 in the Edgeworth expansion of the LV mass function. These corrections will be (Desjacques et al, 2009; Sefusatti et al, 2012):

$$\delta b^E_{1,NG}(f_{NL}) = \delta b^L_{1,NG} = -\frac{1}{\delta_c}\frac{\nu}{R_{NG}}\frac{\partial R_{NG}}{\partial \nu} = -\frac{\nu}{6\delta_c}\frac{f(\nu,0)}{f(\nu,f_{NL})}\left(3\sigma_R S_3(\nu^2-1) - \frac{d^2S_3}{d\ln\nu^2}\left(1-\frac{1}{\nu^2}\right) + \frac{dS_3}{d\ln\nu}\left(\nu^2-4-\frac{1}{\nu^2}\right)\right), \tag{4.52}$$

and

$$\delta b^E_{2,NG}(f_{NL}) = \delta b^L_{2,NG} + \frac{8}{21}\delta b^E_{1,NG} = \frac{\nu^2}{\delta_c^2 R_{NG}}\frac{\partial^2 R_{NG}}{\partial \nu^2} + 2\nu(b^E_1 - \frac{17}{21})\delta b^E_{1,NG}$$
$$= \frac{\nu^2}{6\delta_c}\frac{f(\nu,0)}{f(\nu,f_{NL})}\left(6\sigma_R S_3\nu + \frac{dS_3}{d\ln\nu}\left(5\nu - \frac{3}{\nu} + \frac{2}{\nu^3}\right) + \frac{d^2S_3}{d\ln\nu^2}\left(\nu - \frac{4}{\nu} - \frac{3}{\nu^3}\right) - \frac{d^3S_3}{d\ln\nu^3}\left(\frac{1}{\nu} - \frac{1}{\nu^3}\right)\right)$$
$$+ 2\nu(b^E_1 - \frac{17}{21})\delta b^E_{1,NG}. \tag{4.53}$$

Throughout this thesis we will consider only first order f_{NL} corrections, and therefore we can set $f(\nu,0) = f(\nu,f_{NL})$ in the above expressions. The Eulerian halo bias will be then:

$$b^E_1 = b^E_{1,G} + f_{NL}\delta b^E_{1,NG}, \tag{4.54}$$
$$b^E_2 = b^E_{2,G} + f_{NL}\delta b^E_{2,NG}, \tag{4.55}$$

where we have taken out from $\delta b_{i,NG}$ the f_{NL} dependence introduced by σS_3 for clarity. These are the values we will use for the linear and quadratic bias parameters, in all the expressions of this thesis, independently of the non-Gaussian shape. Similar scale-independent corrections are expected for all the bias parameters, derived through the PBS approach. However, for the non-Gaussian terms considered here in the bias expansion, the corrections are of percent level (for a LV mass function) and hence can be neglected

(Baldauf et al, 2011).

The peak-background split treatment of the halo bias should be generalized, in order to consider the response of the number density sourced by non-Gaussian initial conditions. What changes from the Gaussian case is that the long and short wavelength modes are coupled to each other. For the local case, after splitting the Gaussian part of the primordial gravitational potential into long and short wavelength fluctuations (*i.e.* $\Phi_G = \phi_l + \phi_s$) and substituting it into the local expansion of the non-Gaussian potential field Φ [Eq. (2.83)] we get (Giannantonio and Porciani, 2010; Baldauf et al, 2011)

$$\Phi = \phi_l + f_{NL}\phi_l^2 + (1 + 2f_{NL}\phi_l)\phi_s + f_{NL}\phi_s. \tag{4.56}$$

The most important term here is the coupling term, $(1 + 2f_{NL}\phi_l)\phi_s$, between long and short modes, since the long wavelength linear fluctuations will introduce a scale dependence rescaling in the amplitude of the short modes. In the case of a general non-local non-Gaussianity, this rescaling can be parametrized through (Desjacques et al, 2011b)

$$\delta_l(\mathbf{k}) \to [1 + 2\epsilon k^{-\alpha}]\delta_l(\mathbf{k}), \tag{4.57}$$

where the ϵ is an infinitesimal parameter, which becomes $\epsilon = f_{\rm NL}\phi_l$ for the local PNG. The modulation in the primordial large wavelength density mode will affect the variance of the small scale modes, introducing additional dependences in the number of collapsed objects. The short wavelength variance will transform at the lowest order to

$$\sigma_R \to \sigma_R \left[1 + 2\epsilon \frac{\sigma^2_{R,-\alpha}}{\sigma^2_R}\right], \tag{4.58}$$

where we define:

$$\sigma^2_{R,n} = \frac{1}{2\pi^2}\int k^{2+n} P^L_R(k,z) dk. \tag{4.59}$$

The Jacobian $J \equiv \left|\frac{{\rm dln}\nu}{{\rm dln}M}\right|$, for a universal mass function, will also be transformed into

(Desjacques et al, 2011b,a)

$$J \to J\left[1+4\epsilon\frac{\sigma^2_{R,-\alpha}}{\sigma^2_R}\left(\frac{d\ln\sigma^2_{R,-\alpha}}{d\ln\sigma^2_R}-1\right)\right]. \tag{4.60}$$

The PBS argument of Eq. (4.42) can be easily generalized now to

$$b^L_{\Psi\delta^N} = \frac{1}{n_h(M,z)}\frac{\partial^{N+1}n_h(M,z)}{\partial\delta_l^N\partial\epsilon}\bigg|_{\delta_l=0,\epsilon=0}, \tag{4.61}$$

where the average halo number density n_h is given by Eq. (4.5), after substituting Eq. (4.38), (4.58) and (4.60). The leading non-Gaussian bias b_Ψ can be derived from the above relation, as a special case (*i.e.* $N=0$):

$$b^L_\Psi = \frac{1}{n_h(M,z)}\frac{\partial n_h(M,z)}{\partial\epsilon}\bigg|_{\epsilon=0}. \tag{4.62}$$

while the first higher order non-Gaussian bias parameter $b_{\Psi\delta}$ can be derived through (*i.e.* $N=1$)

$$\begin{aligned} b^L_{\Psi\delta}(M,z) &= \frac{1}{n_h(M,z)}\frac{\partial^2 n_h(M,z)}{\partial\delta_l\partial\epsilon}\bigg|_{\delta_l=0,\epsilon=0} \\ &= Af^X_{\rm NL}\left[2\delta_c b^L_2 + b^L_1\left(4\frac{d\ln\sigma^2_{R,-\alpha}}{d\ln\sigma^2_R}-6\right)\frac{\sigma^2_{R,-\alpha}}{\sigma^2_R}\right]. \end{aligned} \tag{4.63}$$

Following the same steps as for the local-in-matter bias parameters, we relate Lagrangian bias to the desired Eulerian one through Eq. (4.17)), following (Giannantonio and Porciani, 2010; Baldauf et al, 2011)

$$b^E_\Psi = b^L_\Psi, \tag{4.64}$$

$$b^E_{\Psi\delta} = b^L_{\Psi\delta} + b^L_\Psi. \tag{4.65}$$

Combining the above equations with Eq. (4.63) and the Eulerian results for the local-in-matter bias parameters, we can derive the non-Gaussian leading bias term in the squeezed

limit , for a general non-local PNG, as (Desjacques et al, 2011b; Schmidt et al, 2013):

$$b_\Psi^E(M,z) = A f_{\rm NL}^X \left[2\delta_c b_1^L + 4\left(\frac{d\ln\sigma^2_{R,-\alpha}}{d\ln\sigma^2_R} - 1\right)\right]\frac{\sigma^2_{R,-\alpha}}{\sigma^2_R}, \tag{4.66}$$

where $A = 1$ for the local primordial non-Gaussianity. For the other types two types considered throughout this thesis, the relevant parameters are $\alpha = 2$, $A = 3$ for the equilateral case and $\alpha = 1$, $A = -3$ for the orthogonal type. In the case of the higher order bias parameters, we have in the Eulerian framework

$$b_{\Psi\delta}^E(M,z) = 2A f_{\rm NL}^X \left[\delta_c\left(b_2^E + \frac{13}{21}(b_1^E - 1)\right) + b_1^E\left(2\frac{d\ln\sigma^2_{R,-\alpha}}{d\ln\sigma^2_R} - 3\right) + 1\right]\frac{\sigma^2_{R,-\alpha}}{\sigma^2_R}. \tag{4.67}$$

The superscript X in $f_{\rm NL}$ denotes one of the three non-Gaussian shape considered here.

The local non-Gaussian result can be calculated from the above for $\alpha = 0$, where for a mass function with a universal form like in Eq. (4.5), we get (Dalal et al, 2008; Slosar et al, 2008; Giannantonio and Porciani, 2010):

$$b_\Phi^L(M,z) = b_\Psi^L(\alpha=0) = \frac{1}{n_h(M,z)}\frac{\partial n_h(M,z)}{\partial\epsilon}\bigg|_{\epsilon=0} = -2\frac{\nu}{\delta_c f(\nu)}\frac{df(\nu)}{d\nu} = 2f_{\rm NL}^{\rm loc}\delta_c b_1^L, \tag{4.68}$$

which eventually results in the well-known formula for the scale-dependent bias of the local case, derived by (Matarrese and Verde, 2008; Afshordi and Tolley, 2008; Matarrese and Verde, 2008; Dalal et al, 2008; Slosar et al, 2008; Taruya et al, 2008; Schmidt and Kamionkowski, 2010) using different frameworks. It is given by

$$\Delta b(k, f_{\rm NL}, z) \equiv \frac{b_\Psi k^\alpha}{M(k,z)} \overset{\text{local NG}}{=} \frac{2f_{\rm NL}^{\rm loc}\delta_c(b_1^E - 1)}{M(k,z)}. \tag{4.69}$$

The first higher order term reduces for the local case to the results of (Giannantonio and Porciani, 2010)

$$b_{\Phi\delta}^L(M,z) = 2f_{\rm NL}^{\rm loc}(\delta_c b_2^L - b_1^L). \tag{4.70}$$

The scale-dependence of $\Delta b(k)$ on large scales ($\propto k^{\alpha-2}$), approaches a constant value in the equilateral case and turns into a scale-independent one. Therefore, it becomes degenerate with the linear bias parameter, excluding the possibility of constraining equilateral non-Gaussianity through this formalism. On the other hand a scale dependence is introduced towards the small scales ($k \gtrsim k_{eq} \approx 0.01$ h/Mpc), due to the presence of the transfer function in $M(k)$, which can break, in principle, such degeneracies. However on these scales, the transfer function is no longer constant, while for adiabatic perturbations its inverse can be expanded as $T^{-1}(k) = 1 + t_1(k/k_{eq})^2 + t_2(k/k_{eq})^4 + \ldots$, where factors t_i are of $\mathcal{O}(1)$. Eventually, this leads to a scale dependence of the form, $\Delta b(k, f_{\rm NL}^{\rm eq}) \sim \text{const} + f_{\rm NL}^{\rm eq} R_*^2 (k^2/k_{eq}^2 + k^4/k_{eq}^4 + \ldots)$. However, its amplitude is smaller than the Gaussian higher-derivative terms (*e.g.* $b_{\nabla^2\delta} k^2 \delta \propto R_*^2 k^2 \delta$) and therefore degenerate with them (Assassi et al, 2015; Desjacques et al, 2016). Probing primordial non-Gaussianity of the equilateral type through scale-dependent bias correction is not feasible, except if $f_{\rm NL}^{\rm eq} \gtrsim 10^3$ (Assassi et al, 2015). In order to break this small scale degeneracy the measurements of the bias scale dependence must be measured with sufficient precision for $k \gtrsim k_{eq}$ (Desjacques et al, 2016). This is the reason why we will not use the scale dependent bias corrections in the two and three-point statistics of the equilateral PNG in our Fisher forecast analysis (Chapter 5). The only non-Gaussian terms present in the galaxy bispectrum, will be the primordial bispectrum and the scale-dependent corrections, originating from the trispectrum one loop bias (see Sec. 5.2).

Chapter 5

Fisher matrix predictions from LSS surveys

5.1 Introduction

So far, cosmological analyses of Large Scale Structure (LSS) surveys have relied nearly exclusively on matter and galaxy power spectrum estimation. It is however well-known that important extra-information can be extracted via higher-order correlation functions, such as the matter and galaxy bispectrum (see Sec. 3.5.3 for details), which allow both probing the non-linear regime of structure growth and setting constraints on primordial non-Gaussianity (NG) (see *e.g.*, Bernardeau et al (2002); Bartolo et al (2004a); Liguori et al (2010) and references therein). Three very important shapes, encompassing a large amount of scenarios, are the so called *local* shape, *equilateral* shape or *folded* shape (see Sec. 2.4.4 for details).

Currently, the tightest experimental $f_{\rm NL}$ bounds, including a large number of different shapes, come from *Planck* CMB bispectrum measurements (Planck Collaboration et al, 2016a). Bispectrum measurements of LSS data have been already obtained (Scoccimarro et al, 2001a; Feldman et al, 2001; Verde et al, 2002; Marín et al, 2013; Gil-Marín et al, 2014, 2017), but the current level of sensitivity is not enough to generate useful primordial NG bounds (current LSS power spectrum constraints on local $f_{\rm NL}$ are more interesting (Padmanabhan et al, 2007; Slosar et al, 2008; Xia et al, 2010b, 2011; Nikoloudakis et al,

2013; Agarwal et al, 2014; Karagiannis et al, 2014; Leistedt et al, 2014), albeit still not competitive with the CMB). On the other hand, bispectrum estimates of $f_{\rm NL}$ with future LSS data do have in principle great potential to improve over CMB bounds, at least for specific shapes. This is because 3D LSS surveys, covering large volumes and probing a wide range of scales, have access to a much larger amount of modes, with respect to 2D CMB maps. However, LSS measurements will also be very challenging, due to late-time non-linearities, expected to produce much larger NG signatures than the primordial component. These contributions need therefore to be understood and subtracted with exquisite accuracy.

The issue of theoretical modelling of non-linear effects and of higher order LSS correlators has indeed been long debated in the literature (see Chapter 3 for a review) and the interest in producing accurate and realistic LSS primordial bispectrum forecasts has been steadily increasing in recent times. Important contributions in this direction include the work of (Scoccimarro et al, 2004; Sefusatti and Komatsu, 2007) - where the bispectrum of galaxies is used for the first time to forecast the constraining power of LSS surveys on measuring the amplitude of primordial NG - and the study of Song et al (2015), where information from power spectrum and bispectrum of galaxies is combined - also including redshift space distortion effects (Scoccimarro et al, 1999) - in order to constrain growth parameters and galaxy bias terms. Additional contributions were then made by Tellarini et al (2016), who took into account the second order tidal bias term (McDonald and Roy, 2009; Baldauf et al, 2012; Chan et al, 2012), as well as the bivariate bias expansion (Giannantonio and Porciani, 2010) in the redshift space galaxy bispectrum, in order to constrain the amplitude of primordial local NG. Finally, the authors of Baldauf et al (2016) pointed out the importance of including uncertainties in the theoretical modelling of the signal (*theoretical errors*) and properly propagating them into the final error bar estimates.

Many more details on these issues - including a more detailed description of improve-

ments and refinements in redshift space distortion modelling - will be provided in Sec. 5.2.2. Here we point out that many of the analysis ingredients mentioned above were considered *separately* and independently in previous forecasts, with different works considering the importance of specific new terms, without accounting however for all of them at once (for example, theoretical errors are studied in detail in the real space treatment of Baldauf et al (2016), whereas redshift space distortions are accounted for in detail in Tellarini et al (2016), without including theoretical errors). Here, for the first time, we consistently include all these terms and produce as complete and realistic as possible primordial NG forecasts, in terms of $f_{\rm NL}$ parameters, combining power spectrum and bispectrum constraints. One advantage of using the bispectrum is that it opens the possibility to explore the full range of primordial shapes, including the equilateral and orthogonal ones. These shapes are very little explored in previous NG LSS studies. In addition, we will also include – for the first time in an actual forecast – trispectrum contributions to $f_{\rm NL}$ arising from the bias expansion in the galaxy bispectrum, which were originally pointed out as potentially important by (Sefusatti, 2009; Jeong and Komatsu, 2009). We note that such term could play a significant role in constraining the signal from non-local shapes.

Another important issue in a LSS primordial NG analysis is of course that of establishing which survey design and which statistical probe provide the best $f_{\rm NL}$ constraints and can improve over current *Planck* CMB bounds. Clearly, adding modes by going to smaller scales does in principle improve sensitivity. The obvious caveat is that such approach requires non-linear scales, where the non-primordial NG contribution gets very large and hard to model. Moreover, late time non-linearities couple different modes. This unavoidably produces a saturation of the available information. To estimate in detail this effect, a full calculation of the bispectrum covariance is needed in the evaluation of the signal-to-noise ratio for $f_{\rm NL}$. All these issues are still open, and they are currently under a significant amount of scrutiny in the literature (Heavens et al, 1998; Crocce and

Scoccimarro, 2006a,b; Pietroni, 2008; Bernardeau et al, 2008; Wagner et al, 2010; Crocce et al, 2012; Baumann et al, 2012; Carrasco et al, 2012; Gil-Marín et al, 2012, 2014; Lazanu et al, 2016; Lazanu et al, 2017).

In this chapter we consider the alternative approach: we look at galaxy clustering statistics at high redshift, where non-linearities become important at much smaller scales. Besides considering several forthcoming, future or proposed optical galaxy surveys – such as Euclid (Laureijs et al, 2011), DESI (Levi et al, 2013), LSST (Ivezic et al, 2008; LSST Science Collaboration et al, 2009), SPHEREx (Doré et al, 2014; Bock and SPHEREx Science Team, 2016) – we will also devote particular attention to radio continuum data. The latter seem ideally suited to this purpose and especially the forthcoming radio surveys – such as EMU (Johnston et al, 2008; Norris et al, 2011) and SKA (Jarvis et al, 2015). Besides the obvious point of probing very large volumes, *i.e.* more modes, they also allow estimation at high redshift, where a larger amount of modes is in the linear regime. The drawback with radio continuum sources is the lack of a direct determination of their redshifts. Our analysis therefore considers the possibility to extract redshift information via clustering-based estimation methods (Ménard et al, 2013). We follow the implementation for forthcoming radio surveys developed in Kovetz et al (2016). While the power spectrum of radio continuum has been already considered in the literature (Xia et al, 2010a,c, 2011; Raccanelli et al, 2012; Camera et al, 2015; Raccanelli et al, 2017), the bispectrum of radio continuum surveys has not been studied so far. We devote particular attention to it in this chapter.

5.2 Galaxy statistics

The goal of this chapter is to predict the constraining power of future LSS surveys on measuring the primordial non-Gaussian amplitude, as well as various bias parameters. In order to achieve this, the statistics we will use are the two and three point correlation functions in Fourier space (*i.e.* power spectrum and bispectrum). The halo bias expansion

discussed in Chapter 4 is not restricted to halos and can be generalized for any kind of dark matter tracer. In the case of galaxies, the bias expansion in the Eulerian framework can be expressed up to second order in Fourier space, for non-Gaussian initial conditions, by Eqs. (4.35) and (4.50) as:

$$\begin{aligned}\delta_g(\mathbf{k}) &= \delta_g^{(G)}(\mathbf{k}) + \delta_g^{(NG)}(\mathbf{k}) \\ &= b_1^E \delta(\mathbf{k}) + b_\Psi^E \Psi(\mathbf{k}) + \varepsilon^E(\mathbf{k}) \\ &+ \int \frac{d^3q_1}{(2\pi)^3}\frac{d^3q_2}{(2\pi)^3}\delta_D(\mathbf{k}-\mathbf{q}_{12})\Bigg[\left(\frac{b_2^E}{2} + b_{s^2}^E S_2(\mathbf{q}_1,\mathbf{q}_2)\right)\delta(\mathbf{q}_1)\delta(\mathbf{q}_2) + \frac{1}{2}\left(\varepsilon_\delta^E(\mathbf{q}_1)\delta(\mathbf{q}_2) + \delta(\mathbf{q}_1)\varepsilon_\delta^E(\mathbf{q}_2)\right) \\ &+ \frac{1}{2}\Bigg((b_{\Psi\delta}^E - b_\Psi^E N_2(\mathbf{q}_2,\mathbf{q}_1))\Psi(\mathbf{q}_1)\delta(\mathbf{q}_2) + (b_{\Psi\delta}^E - b_\Psi^E N_2(\mathbf{q}_1,\mathbf{q}_2))\delta(\mathbf{q}_1)\Psi(\mathbf{q}_2) \\ &+ \varepsilon_\Psi^E(\mathbf{q}_1)\Psi(\mathbf{q}_2) + \Psi(\mathbf{q}_1)\varepsilon_\Psi^E(\mathbf{q}_2)\Bigg)\Bigg],\end{aligned} \tag{5.1}$$

where we have included also all the stochastic bias terms up to the second order. The kernel $S_2(\mathbf{k}_1,\mathbf{k}_2)$ is defined from the Fourier transform of the tidal field scalar s^2 [Eq. (4.35)] and is given by (McDonald and Roy, 2009; Baldauf et al, 2012):

$$S_2(\mathbf{k}_1,\mathbf{k}_2) = \frac{(\mathbf{k}_1\cdot\mathbf{k}_2)^2}{\mathbf{k}_1^2\mathbf{k}_2^2} - \frac{1}{3}. \tag{5.2}$$

The kernel $N_2(\mathbf{k}_1,\mathbf{k}_2)$ originates from the Fourier transformation of the displacement field connecting the Eulerian and Lagrangian frames. Since the primordial gravitational potential field is defined at the initial Lagrangian frame, the two will still be coupled in the late time Eulerian frame. The coupling is given by (Tellarini et al, 2015; Angulo et al, 2015):

$$N_2(\mathbf{k}_1,\mathbf{k}_2) = \frac{\mathbf{k}_1\cdot\mathbf{k}_2}{k_1^2}. \tag{5.3}$$

Henceforth, we drop the superscript E from the bias parameters, since we consider galaxy statistics at the time of observation (Eulerian frame).

Before presenting the galaxy power spectrum and bispectrum model, we should note

that we only consider up to linear terms in $f_{\rm NL}$, since we assume an $f_{\rm NL}=0$ fiducial cosmology.In addition we would like to stress that, as we discussed in the previous chapter, the bias expansion of Eq. (5.1) is with respect to the smoothed non-linear matter field, at a smoothing radius $R > R_*$, in order to truncate the bias expansion to a finite order in a meaningful way. Here we will continue to assume an implicit smoothing, over a scale R, of the Gaussian field $\delta^{(1)}$ [Eq. (3.83)] and we will not retain $W_R(\mathbf{k})$ factors in the expressions. Following Heavens et al (1998), we can evolve the non-linear density field up to the desired order, smooth it with a filter and then apply the general bias expansion of Eq. (4.34). As long as we use modes with wavelengths larger than the smoothing radius ($k_{\rm max} << 1/R$) this is allowed. In addition at large scales, as those considered in our analysis, the smoothing kernel goes to unity and does not affect the results, *i.e.* $W_R(k \ll 1/R) \to 1$. .

5.2.1 Real space

The derivation of the galaxy power spectrum and bispectrum follows the same principles as in the case of matter (see Sec. 3.5.2 and 3.5.3). For the power spectrum we start by writing the correlation function as in Eq. (3.90) and substitute the galaxy overdensity expansion of Eq. (5.1), while keeping up to n-th order correction terms.

For a Gaussian galaxy field, the tree-level term is the linear power spectrum multiplied by the linear bias term

$$P_g(k,z) = b_1^2 P_m^L(k,z) + P_\varepsilon, \tag{5.4}$$

where P_ε is the stochastic contribution to the power spectrum, $P_\varepsilon = \langle \varepsilon(\mathbf{k})\varepsilon(\mathbf{k}')\rangle$, which for large scales is given by Poisson sampling, *i.e.* $P_\varepsilon = 1/\overline{n}_g$ with $\overline{n}_g$ being the mean number density of galaxies. To derive the 1-loop correction, terms up to third order are needed in the bias expansion. If we consider only the local-in-matter terms in Eq. (4.15),

then the 1-loop correction is written as $P_g^{(1)} = P_{g,22} + P_{g,13}$, where each term is given by

$$P_{g,22}(k,z) = \frac{b_2^2}{2}\int \frac{d^3q}{(2\pi)^3}\; P_m^L(q,z)\; P_m^L(|\mathbf{k}-\mathbf{q}|,z), \tag{5.5}$$

$$P_{g,13}(k,z) = b_1 b_3\; P_m^L(k,z)\int \frac{d^3q}{(2\pi)^3}\; P_m^L(q,z). \tag{5.6}$$

If PNG is present, an additional terms appear (Smith et al, 2007; Taruya et al, 2008)

$$P_{g,12}(k,z) = b_1 b_2 \int \frac{d^3q}{(2\pi)^3}\; B_I(k,q,|\mathbf{k}-\mathbf{q}|,z), \tag{5.7}$$

The importance of this term lies on the fact that, in the large scale limit, for local PNG, it reduces to the scale dependent bias of Eq. (4.69), for the hight density peaks ($\nu \gg 1$) (Taruya et al, 2008). The complete expression for the 1-loop power spectrum, including all terms in the general local bias expansion, is derived by (Assassi et al, 2014). For the expressions with the explicit smoothing kernel see (Sefusatti, 2009).

The final result for the tree-level galaxy power spectrum with non-Gaussian initial conditions is:

$$P_g(k,z) = (b_1 + \Delta b(k, f_{\rm NL}, z))^2 P_m^L(k,z) + P_\varepsilon, \tag{5.8}$$

where the non-Gaussian scale dependent bias term is given by

$$\Delta b(k, f_{\rm NL}, z) \equiv \frac{b_\Psi k^\alpha}{M(k,z)}. \tag{5.9}$$

Note that the scale dependent correction should not be used in order to measure equilateral primordial non-Gaussianity (see Sec. 4.4.2 for an extensive discussion), as pointed out by Assassi et al (2015), due to degeneracies with the higher-order derivative bias terms. This is the reason why we will not use the scale dependent bias corrections in the two and three-point statistics for the equilateral case.

In the case of the bispectrum, after assuming Gaussian initial conditions and consid-

ering the general bias expansion [Eq. (4.34)], we get for the tree-level expression

$$B_{ggg}^{\rm tree,G}(k_1,k_2,k_3,z) = b_1^3 B_G(k_1,k_2,k_3,z) + B_\varepsilon \\ + \left[2b_1 P_{\varepsilon\varepsilon_\delta} P_m^L(k_1,z) + 2b_1^2\left(\frac{b_2}{2} + b_{s^2} S_2(\mathbf{k}_1,\mathbf{k}_2)\right) P_m^L(k_1,z) P_m^L(k_2,z) + 2 \text{ perm}\right], \tag{5.10}$$

where the gravity induced bispectrum (B_G) is given by Eq. (3.103). For the leading stochastic contributions at large scales ($k \ll 1/R$), the fiducial values are predicted by Poisson statistics and are given by (Schmidt, 2016; Desjacques et al, 2016):

$$B_\varepsilon = \lim_{\mathbf{k},\mathbf{k}'\to 0} \langle \varepsilon(\mathbf{k})\varepsilon(\mathbf{k}')\varepsilon(\mathbf{k}'')\rangle = \frac{1}{\overline{n}_g^2}, \tag{5.11}$$

$$P_{\varepsilon\varepsilon_\delta} = \lim_{\mathbf{k}\to 0} \langle \varepsilon(\mathbf{k})\varepsilon_\delta(\mathbf{k}')\rangle = \frac{b_1}{2\overline{n}_g}, \tag{5.12}$$

where B_ε is the bispectrum of the leading stochastic field (*i.e.*, $\varepsilon(\mathbf{k})$), $P_{\varepsilon\varepsilon_\delta}$ is the cross power spectrum between ε and the next-to-leading order stochastic field (*i.e.*, $\varepsilon_\delta(\mathbf{k})$).

The tree-level Gaussian part of the galaxy bispectrum [Eq. (5.10)] is plotted in Figure 5.1, for all the triangle configurations generated after keeping k_1 fixed. The condition $k_1 \geq k_2 \geq k_3$ applies here. Three different values are chosen for k_1, *i.e.* $k_1 = 0.01\ h/\text{Mpc}$, $k_1 = 0.05\ h/\text{Mpc}$ and $k_1 = 0.1\ h/\text{Mpc}$. In addition, the highest contributing terms to $B_{ggg}^{\rm tree,G}$, are also shown in Figure 5.1. These include the tree-level gravity-induced matter bispectrum (B_G), the quadratic bias term ($P_m^L(k_1,z)P_m^L(k_2,z) + 2$ perm), denoted in the plot as P^2, and the tidal bias term ($S_2(k_1,k_2)P_m^L(k_1)P_m^L(k_2) + 2$ perm), denoted as B_{S_2}. In order to show the shape dependence on the triangle configurations, the amplitude of each term is divided by the maximum value in each panel.

In the second row of Figure 5.1 the tree-level matter bispectrum signal is plotted, as derived by SPT. We can see that this term peaks mainly at the elongated ($k_1 = k_2 + k_3$) and folded ($k_1 = 2k_2 = 2k_3$) configurations, while for the squeezed triangles ($k_1 \simeq k_2 \gg k_3$) its contribution vanishes. This is due to presence of the non-linear second order SPT kernel $F_2(\mathbf{k}_i,\mathbf{k}_j)$ [Eq. (3.20)] in B_G, which disappears at the squeezed limit and has a

maximum at the folded/elongated triangles (see (Sefusatti and Komatsu, 2007; Sefusatti, 2009; Jeong and Komatsu, 2009) for a discussion). As we approach large scales (first column in Figure 5.1) we observe that the maximum signal of the matter bispectrum is now at the equilateral triangles ($k_1 = k_2 = k_3$). This is due to the fact that in this regime the matter power spectrum increases as a function of k and therefore we can get an excess in the signal of B_G when all sides of the triangle are equally large (*i.e.* equilateral configurations). The quadratic bias term (shown in the third row of Figure 5.1) follows a similar behaviour, where the only difference from B_G is the absence of the F_2 kernel. This leads to an enhancement at the squeezed limit and a suppression for the folded/elongated triangles.

The tree-level galaxy bispectrum contribution, proportional to the tidal bias (*i.e.* B_{S_2}), peaks on elongated configurations, as we can see from the last row of Figure 5.1. Note that, due to the presence of the S_2 kernel, B_{S_2} can have an amplitude with a negative sign. In order to avoid the saturation of the colour maps in Figure 5.1, we show the absolute value of B_{S_2} and we use a white dotted line to separate negative and positive B_{S_2} regions. For most of the configurations, B_{S_2} is negative at small scales (right column of Figure 5.1), while the occurrence of positive values increases on large scales. Note here that, for all equilateral and for most isosceles triangles the tidal bispectrum term is negative, independently of the scale. This behaviour can be explained by the nature of the $S_2(\mathbf{k}_i, \mathbf{k}_j)$ kernel, which takes its maximum positive value (for simplicity $\mathbf{k}_i = \mathbf{k}_1$ and $\mathbf{k}_j = \mathbf{k}_2$) when $\mathbf{k}_1 = a\mathbf{k}_2$, where $a > 1$ (*i.e.* elongated and folded triangles), and its maximum negative value for $\mathbf{k}_1 = \mathbf{k}_2$ (*i.e.* equilateral triangles). In the folded limit we have, $B_{S_2} \propto P_m^2(k) + 2P_m(2k)P_m(k)$, and since the matter power spectrum increases towards the large scales, the peak of the signal moves towards this configuration. On the other hand, for isosceles configurations ($k_1 > k_2 = k_3$) the resulting tidal term can be positive or negative depending on the relative size of k_1 with respect to the other sides of the triangle.

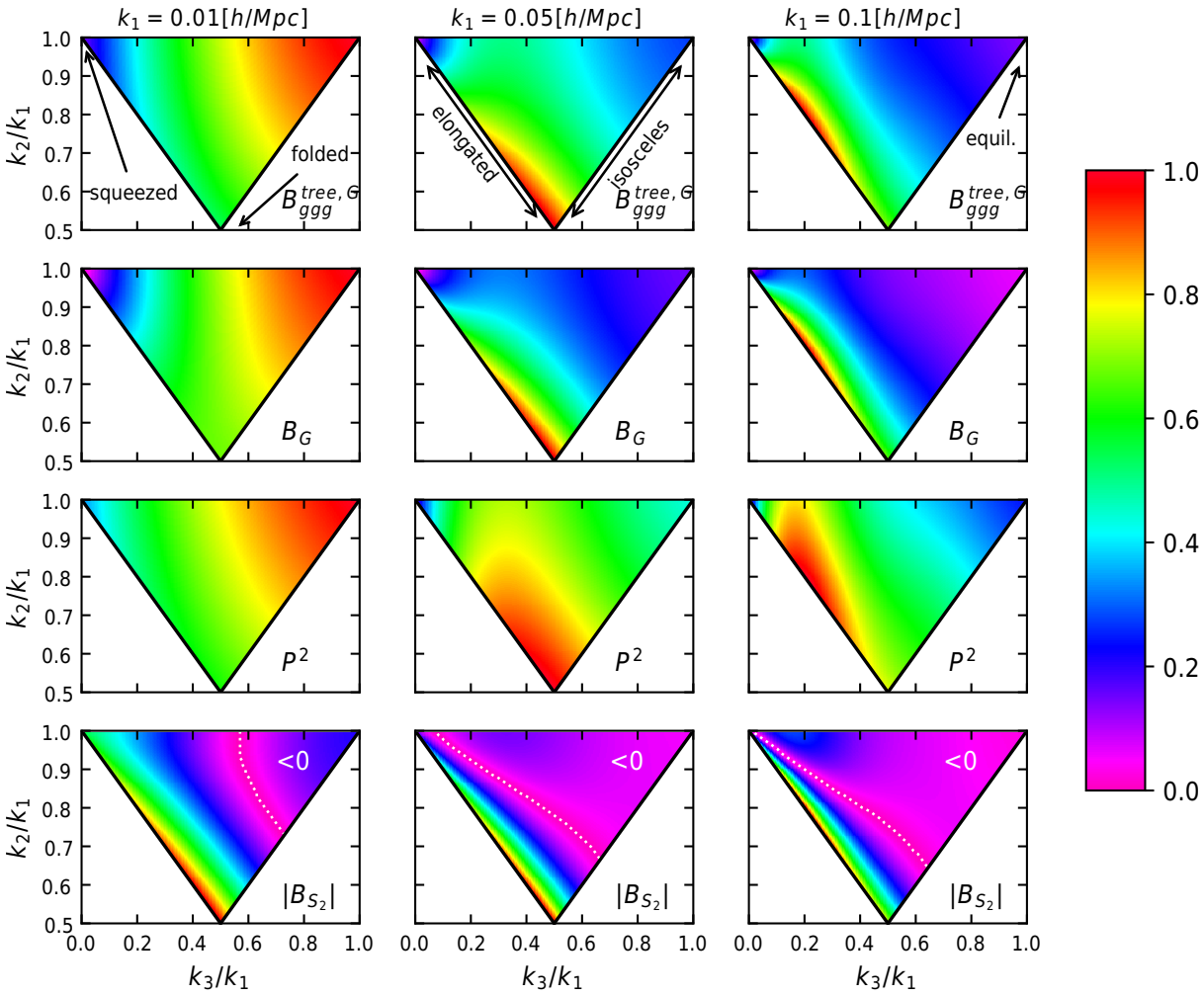

Figure 5.1 – The shape of the galaxy bispectrum for Gaussian initial conditions, together with its highest contributing terms. In each panel the bispectrum, normalized to its absolute maximum value, is plotted as a function of k_2/k_1 and k_3/k_1 for all configurations in the case of fixed k_1. We consider the following three values: $k_1 = 0.01$, 0.05, 0.1 h/Mpc, where the triangle sides follow the relation $k_3 \leq k_2 \leq k_1$. In the first row the Gaussian tree-level galaxy bispectrum $B_{ggg}^{\rm tree,G}$ is plotted [Eq. (5.10)], in the second we plot the tree-level matter bispectrum (B_G) as predicted by SPT, in the third the quadratic bias term indicated as P^2 is plotted (*i.e.* $P_m(k_1)P_m(k_2) + 2$ perm) and finally in the last row we plot the tidal bias term contribution (*i.e.* $B_{S_2} = S_2(k_1,k_2)P_m(k_1)P_m(k_2) + 2$ perm). Note that for the latter the absolute value is plotted, where a white dotted line shows the separation between the positive (left side) and negative (right side) values. For a detailed explanation, see the main text (Sec. 5.2.1).

The 1-loop Gaussian terms up to $\mathcal{O}([\delta^{(1)}]^6)$ for the local-in-matter bias expansion, are given by (McDonald, 2006; Smith et al, 2007; Taruya et al, 2008; Sefusatti, 2009)

$$B^{II}_{g,112} = \frac{b_1^2 b_2}{2}\int \frac{d^3q}{(2\pi)^3}\, T(\mathbf{k}_1,\mathbf{k}_2,\mathbf{q},\mathbf{k}_3-\mathbf{q},z) + 2 \text{ perm.}, \tag{5.13}$$

$$B^{I}_{g,222} = \frac{b_2^3}{2}\int \frac{d^3q}{(2\pi)^3} P_m^L(q,z) P_m^L(|\mathbf{k}_1+\mathbf{q}|) P_m^L(|\mathbf{k}_2-\mathbf{q}|,z), \tag{5.14}$$

$$B^{I}_{g,123} = \frac{b_1 b_2 b_3}{2} P_m^L(k_1,z)\int \frac{d^3q}{(2\pi)^3} P_m^L(q,z) + 5 \text{ perm.}, \tag{5.15}$$

$$B^{II}_{g,123} = b_1 b_2 b_3 P_m^L(k_1,z) P_m^L(k_2,z)\int \frac{d^3q}{(2\pi)^3} P_m^L(q,z) + 2 \text{ perm.}, \tag{5.16}$$

$$B^{I}_{g,114} = \frac{b_1^2 b_4}{2} P_m^L(k_1,z) P_m^L(k_2,z)\int \frac{d^3q}{(2\pi)^3} P_m^L(q,z) + 2 \text{ perm.}, \tag{5.17}$$

On the other hand, non-Gaussian 1-loop corrections have no effect on the large scales (Taruya et al, 2008; Sefusatti, 2009) and hence they will not be listed here. The terms $B^{II}_{g,123}$ and $B^{I}_{g,114}$ can be considered as a kind of re-normalization of the bias parameters (McDonald, 2006; Smith et al, 2007), while $B^{I}_{g,123}$ and $B^{I}_{g,222}$ exhibit the same functional dependence with the $P^2(k)$ term in Eq. (5.10) towards the large scales, hence they are expected to be small compared to the tree-level terms at that regime (Sefusatti, 2009). Moreover, the term $B^{II}_{g,112}$ is $\mathcal{O}(\delta^4)$ and hence will be considered additionally to the Gaussian tree-level terms of Eq. (5.10). The importance of this contribution in constraining PNG was pointed out in (Sefusatti, 2009; Jeong and Komatsu, 2009), where it was shown that in the local case it exhibits a scale dependence at large scales similar to the one provided by the scale dependent bias term in the case of the power spectrum [Eq. (5.8)].

The final galaxy bispectrum up to $\mathcal{O}(\delta^4)$ with all the relevant bias terms of the corresponding order in PT will be for Gaussian initial conditions:

$$B^{(G)}_{ggg}(k_1,k_2,k_3,z) = B^{\text{tree},G}_{ggg}(k_1,k_2,k_3,z) + b_1^2\int \frac{d^3q}{(2\pi)^3}\left(\frac{b_2}{2} + b_{s^2} S_2(\mathbf{q},\mathbf{k}_3-\mathbf{q})\right) T_\delta(\mathbf{k}_1,\mathbf{k}_2,\mathbf{q},\mathbf{k}_3-\mathbf{q},z) + 2 \text{ perm.} \tag{5.18}$$

where $T_\delta(k_1,k_2,k_3,k_4,z)$ is the trispectrum of the non-linear matter overdensity (*i.e.*, $\delta(\mathbf{k})$)

described in Sec. 3.5.4. The full result including non-Gaussian terms up to linear order in $f_{\rm NL}$ is given by

$$
\begin{aligned}
&B_{ggg}(k_1,k_2,k_3,z) = B^{(G)}_{ggg}(k_1,k_2,k_3,z) + b_1^3 B_I(k_1,k_2,k_3,z) \\
&+ b_1 b_\Psi \left(\frac{k_1^\alpha}{M(k_1,z)} + \frac{k_2^\alpha}{M(k_2,z)}\right)\left[2\left(b_1 F_2(\mathbf{k}_1,\mathbf{k}_2) + \frac{b_2}{2} + b_{s^2} S_2(\mathbf{k}_1,\mathbf{k}_2)\right) P_m^L(k_1,z) P_m^L(k_2,z)\right. \\
&\left. + \int \frac{d^3q}{(2\pi)^3}\left(\frac{b_2}{2} + b_{s^2} S_2(\mathbf{q},\mathbf{k}_3-\mathbf{q})\right) T_{\delta^{(1)}\delta}(\mathbf{k}_1,\mathbf{k}_2,\mathbf{q},\mathbf{k}_3-\mathbf{q})\right] \\
&+ b_1^2\left[\left(\frac{(b_{\Psi\delta} - b_\Psi N_2(\mathbf{k}_2,\mathbf{k}_1))k_1^\alpha}{M(k_1,z)} + \frac{(b_{\Psi\delta} - b_\Psi N_2(\mathbf{k}_1,\mathbf{k}_2))k_2^\alpha}{M(k_2,z)}\right) P_m^L(k_1,z) P_m^L(k_2,z)\right. \\
&\left. + \frac{1}{2}\int \frac{d^3q}{(2\pi)^3}\left(\frac{(b_{\Psi\delta} - b_\Psi N_2(\mathbf{k}_3-\mathbf{q},\mathbf{q}))q^\alpha}{M(q,z)} + \frac{(b_{\Psi\delta} - b_\Psi N_2(\mathbf{q},\mathbf{k}_3-\mathbf{q}))|\mathbf{k}_3-\mathbf{q}|^\alpha}{M(|\mathbf{k}_3-\mathbf{q}|,z)}\right) T_{\delta^{(1)}\delta}(\mathbf{k}_1,\mathbf{k}_2,\mathbf{q},\mathbf{k}_3-\mathbf{q})\right] \\
&+ 2 b_1 P_{\varepsilon\varepsilon_\Psi} \frac{P_m^L(k_1) k_1^\alpha}{M(k_1,z)} + 2 \text{ perm},
\end{aligned}
\tag{5.19}
$$

where the trispectrum term $\delta_D(\sum_i \mathbf{k}_i) T_{\delta^{(1)}\delta} = \langle \delta^{(1)}(\mathbf{k}_1)\delta(\mathbf{k}_2)\delta(\mathbf{k}_3)\delta(\mathbf{k}_4)\rangle$, with $\delta^{(1)}$ being the Gaussian part of the density field (i.e. the Gaussian part of the primordial curvature perturbation, linearly propagated via Poisson equation) originating from the gravitational potential in the bias expansion [Eq. (5.1)]. The cross power spectrum between ε and ε_Ψ will be (Desjacques et al, 2016)

$$
P_{\varepsilon\varepsilon_\Psi} = \frac{b_\Psi}{2\overline{n}_g}, \tag{5.20}
$$

which can be written also as, $b_1 P_{\varepsilon\varepsilon_\Psi} = b_\Psi P_{\varepsilon\varepsilon_\delta}$.

Let us now discuss in greater detail the trispectrum terms generated by the bias expansion in the galaxy bispectrum. The importance of the non-linear bias term in Eq. (5.18) was recognised in the work of (Sefusatti, 2009; Jeong and Komatsu, 2009) for increasing the sensitivity of galaxy bispectrum to the non-Gaussian initial conditions. The SPT tree-level results for the matter trispectrum T_δ include, as shown in Sec. 3.5.4, three distinct parts. The primordial term T_{1111} [Eq. (3.127)], which for the local case depends on $f_{\rm NL}^2$ and $g_{\rm NL}$ and can therefore be neglected in the Fisher analysis performed here. However, we should note that such term has a dominant large scale behaviour for

the squeezed configurations and is larger than the non-Gaussian correction to the galaxy power spectrum [Eq. (5.8)]. The part generated by the non linear gravitational coupling [Eqs. (3.124) and (3.125)] exhibits no $f_{\rm NL}$ dependence up to tree-level and therefore it can ignored in the linear regime considered here. Finally, the important contribution for PNG constraints is a coupling term between a non-zero primordial bispectrum and the tree-level gravitational contribution [Eq. (3.129)], which is linear in $f_{\rm NL}$.

This $f_{\rm NL}$-dependent term [Eq. (3.129)], generates on large scales a signal which dominates over non-linear terms, for essentially all triangle configurations in the case of local non-Gaussianity (Sefusatti, 2009; Jeong and Komatsu, 2009). Therefore, the constraints on $f_{\rm NL}$ can be significantly improved, as we will show in Sec. 5.7. When terms proportional to the primordial field Ψ are also considered in the bias expansion, the corresponding trispectrum corrections in Eq. (5.19) (*i.e.* $T_{\delta^{(1)}\delta}$) exhibits one occurrence of $\delta^{(1)}$ and therefore will be missing a permutation in Eq. (3.129). However, since we only consider T_{1112} in the tree level matter trispectrum, all the terms in Eq. (5.19) with $T_{\delta^{(1)}\delta}$ will be $\mathcal{O}(f_{\rm NL}^2)$ and hence they can be ignored. The only remaining $\mathcal{O}(f_{\rm NL})$ trispectrum contribution is the one coming from the T_δ term of Eq. (5.18). Its amplitude is shown in the colour maps of Figure 5.2, 5.3 and 5.4, for the three PNG types considered here. Moreover, the non-Gaussian part of the galaxy bispectrum [Eq. (5.19)] is also shown.

The colouring in the plots shows the shape of the non-Gaussian terms of the galaxy bispectrum, as a function of k_3/k_1 and k_2/k_1, for three different fixed values of $k_1 = 0.01, 0.05, 0.1\,h/\mathrm{Mpc}$. In the local case, both the primordial bispectrum and the trispectrum correction peak in the squeezed limit. A small difference between the two is originating from the presence of the tidal kernel S_2. The PNG contribution can be easily disentangled from the non-primordial part of the galaxy bispectrum, as already pointed out earlier. On larger scales a small increase in the signal is also observed for all configurations, due to the behaviour of the matter power spectrum and of the F_2 kernel in this regime (see Sec. 5.2.1 for a discussion).

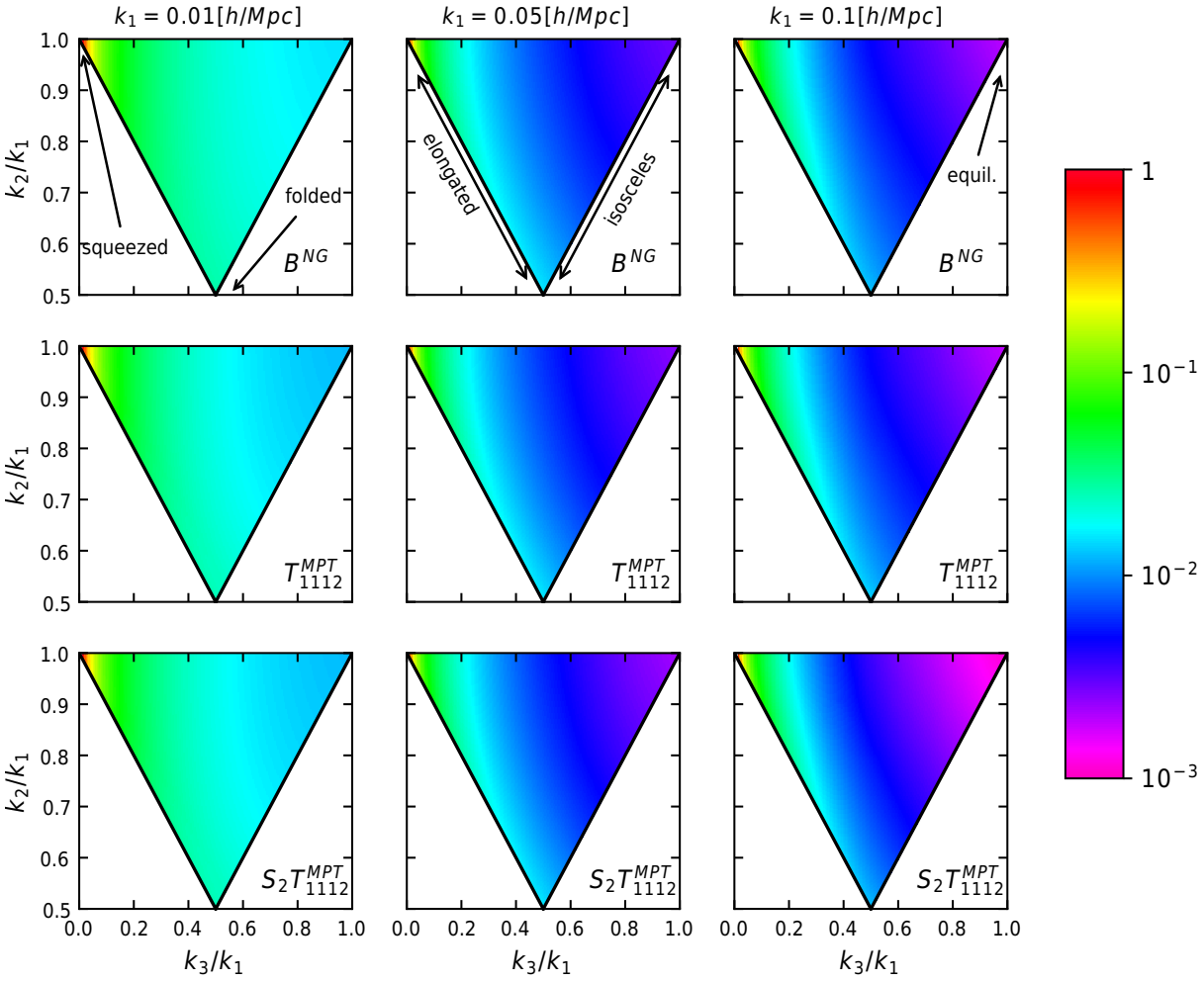

Figure 5.2 – The shape of the non-Gaussian part of the galaxy bispectrum (top panel) in Eq. (5.19), *i.e.* $B^{NG}(k_1,k_2,k_3,z) = B_{ggg}(k_1,k_2,k_3,z) - B^{(G)}_{ggg}(k_1,k_2,k_3,z)$ (cf. Figure 5.1 for the Gaussian part). The panels display the amplitude of the galaxy bispectrum, normalized to the respective maximum value (note that this implies that a direct comparison of the color scale between different panels is meaningless). The non-linear evolution of the matter field is treated here with the MPTBREEZE perturbation theory scheme (see Sec. 3.4). In the middle panel the trispectrum loop quadratic bias correction (the b_2 trispectrum term in Eq. (5.18), *i.e.* $\int \frac{d^3q}{(2\pi)^3} T_{1112}(\mathbf{k}_1,\mathbf{k}_2,\mathbf{q},\mathbf{k}_3-\mathbf{q},z) + 2$ perm), is plotted. Finally, in the bottom panel the tidal bias term trispectrum correction (*i.e.* $\int \frac{d^3q}{(2\pi)^3} S_2(\mathbf{q},\mathbf{k}_3-\mathbf{q}) T_{1112}(\mathbf{k}_1,\mathbf{k}_2,\mathbf{q},\mathbf{k}_3-\mathbf{q},z) + 2$ perm) is plotted. All the terms plotted here peak at the squeezed limit for this type of PNG.

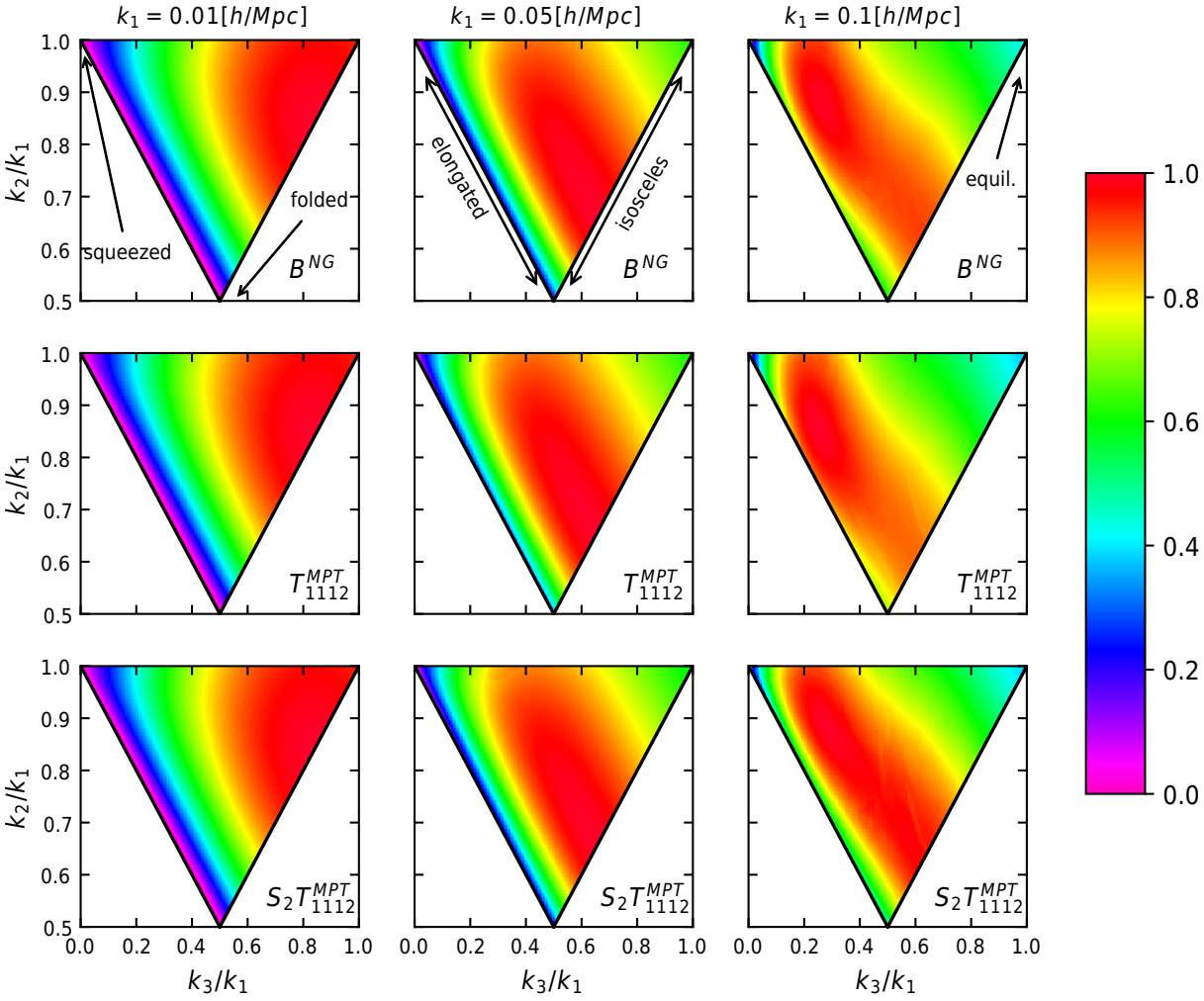

Figure 5.3 – Same as Figure 5.2 but for the equilateral type of PNG. For this type of PNG the galaxy bispectrum is taken to be that of Eq. (5.18) (*i.e.* B^{NG} is here the sum of the trispectrum bias corrections), since any term proportional to the field Ψ in Eq. (5.19) (introduced to model the scale dependent bias corrections) is excluded as we discuss in Sec. 4.4.2.

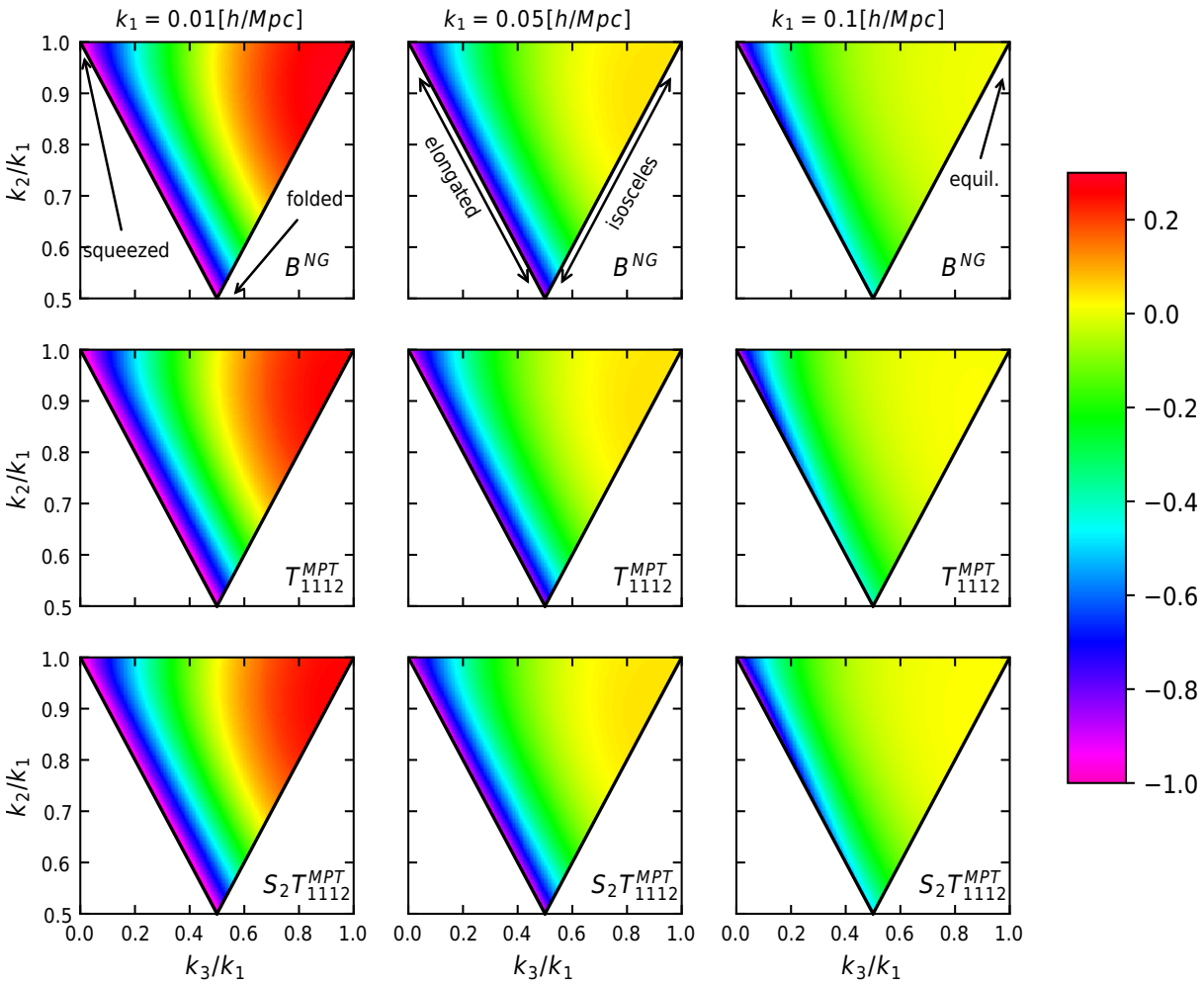

Figure 5.4 – Same as Figure 5.2 but for the orthogonal type of PNG. In this case the equations used are the same as for the local PNG.

In the equilateral case, the NG scale dependence is easily observed. The peak of the signal moves towards large scales, for equilateral configurations. The PNG contribution includes only trispectrum corrections and B_I, since the additional NG scale dependence, introduced by the terms proportional to Ψ [see Eq. (5.19)] up to the order considered here, is degenerate with bias parameters, and not included in the bias case. This explains why the panels of Figure 5.3 display a similar behaviour. Note that the observed scale dependence is stronger and more localized, in the equilateral configurations, with respect to the non-primordial bispectrum signal (see first row in Figure 5.1), in the large scale regime. This scale dependence can in principle provide a unique signature for measuring $f_{\rm NL}^{\rm eq}$. The same general scale dependent behaviour is observed also for orthogonal models and it can improve the $f_{\rm NL}$ constraints also in this case.

The trispectrum integrals present an ultraviolet divergence, which is automatically cured by adding the smoothing filter with a finite value of R. Nevertheless, this introduces a dependence on the smoothing scale in the integration of the trispectrum for the three shapes we consider here[1]. This makes the results rely upon a non-fundamental quantity, which is unsatisfactory. On large scales this dependence on the smoothing radius goes like $1/\sigma_R^2$, as was also noted in Jeong and Komatsu (2009). In order to cancel it, σ_R^2 is included explicitly in front of the trispectrum integral and later on is reabsorbed by the bias parameters. The "new" bias coefficients so obtained can be then considered free parameters in the Fisher matrix analysis.

An alternative approach it would be to use a perturbation theory that applies a renormalized technique, like renormalized perturbation theory (RPT) (Crocce and Scoccimarro, 2006a,b), time renormalized group model (Pietroni, 2008) and renormalization of bias (McDonald, 2006; Schmidt et al, 2013; Assassi et al, 2014; Senatore, 2015; Mirbabayi et al, 2015). Regardless of the approach taken, the final result for the statistics of galaxies must be the same, therefore here we will use the MPTbreeze formalism (Bernardeau

[1]This was also observed in Jeong and Komatsu (2009) for the local case.

et al, 2008; Crocce et al, 2012) which simplifies greatly the computational effort of RPT (see Sec. 3.4). The reasoning behind this choice is the exponential cut-off that is generated within this formalism and removes the UV divergence of the trispectrum integral by suppressing the small scales contribution. For the physical motivation and the details of the MPTbreeze formalism we refer the reader to (Bernardeau et al, 2008; Crocce et al, 2012). On the other hand, a reduction in the signal originating from intermediate scales is expected in this approach, due to the drop of the matter power spectrum and bispectrum beyond these scales ($k > 0.15\,h/\mathrm{Mpc}$ at $z = 0$). This is shown in Refs. (Lazanu et al, 2016; Lazanu et al, 2017), where a comparison between different perturbation theories is performed using simulations. The resulting power spectrum and bispectrum in the case of MPTbreeze are the same as those defined in Eqs. (5.8) and (5.19) respectively, but multiplied by the exponent of the function $f(k)$ [Eq. (3.62)] (see Sec. 3.4 for a quick review).

5.2.2 Redshift space

The power spectrum and bispectrum presented in the previous section, assumed perfect knowledge of the proper distances of galaxies. However, the distances measured in galaxy surveys, come from the shift in the spectrum of luminous objects, due to their motion with the Hubble flow (see Sec. 2.2.2). These measured velocities have additional contribution, independent from the Hubble expansion, originating from the peculiar velocities of the objects, which in turn arise from their dynamical motion. The map of objects generated from galaxy surveys is therefore distorted with respect to the real distribution of galaxies. This effect is known as *redshift space distortion* (RSD) and the observed coordinate system is called *redshift space*. The peculiar velocities of galaxies on large scales is due to the gravitational force of clusters. If in-fall velocities are pointing in the opposite direction from the observer, objects appear further away with respect to real space (*i.e.* their velocities are added to the Hubble expansion). On the other hand, if the velocities

point towards us the galaxies appear closer than they really are (*i.e.* their velocities are subtracted from the Hubble flow). On sub-cluster scales the peculiar velocities originate from the velocity dispersion of the objects, due to the process of virialization. In this case, the structures in redshift space appear more elongated towards the observer with respect to real space, this effect is called *Finger of God* effect (FOG).

The radial coordinate of a galaxy in redshift space, $\mathbf{s}$, is derived from the object's velocity, *i.e.* the sum between the velocities coming from the Hubble flow and the peculiar motion. Therefore we can define the mapping between the two spaces as:

$$\mathbf{s} = \mathbf{x} + (1+z)\frac{v_r(\mathbf{x})}{H(z)}\hat{\mathbf{r}} \tag{5.21}$$

where the position of the galaxy in real space is $\mathbf{x}$ and $v_r(\mathbf{x})$ is the projected part of its peculiar velocity on the line-of-sight. Note that the redshift and the Hubble parameter used in the above relation, correspond to their values after the subtraction of the peculiar velocities. In order to simplify the analysis the plane parallel approximation is adopted, where the objects are assumed to be far away and hence their radial directions are parallel to the line-of-sight, $\hat{z}$. Direction $\hat{z}$ is considered fixed and the mapping between the real space $\mathbf{x}$ and the redshift space $\mathbf{s}$ coordinates is now given by (Scoccimarro et al, 1999)

$$\mathbf{s} = \mathbf{x} - f u_z(\mathbf{x})\hat{z}, \tag{5.22}$$

where $\mathbf{u}(\mathbf{x}) = -v(\mathbf{x})\cdot\hat{z}/(f\mathcal{H}) = -i\mathbf{k}\theta_{\mathbf{k}}(\tau)/(k^2 f\mathcal{H})$ and $v(\mathbf{x})$ is the peculiar velocity field. The conservation of number density between the two frames will give the relation between the overdensity field in redshift and real space (*i.e.* $\delta_{\mathbf{s}}$ and δ_r respectively) as:

$$(1+\delta_s)d^3s = (1+\delta)d^3x. \tag{5.23}$$

The above is derived after using, $d^3s = J(\mathbf{x})d^3x$, where $J(\mathbf{x}) = 1 - f\nabla_z u_z(\mathbf{x})$ is the Jacobian of the mapping in the plane parallel approximation. The Fourier transformation of

the galaxy density field in redshift space is (Scoccimarro et al, 1999)

$$\delta_g^s(\mathbf{k}) = \int d^3x e^{-i\mathbf{k}\cdot\mathbf{x}} e^{ifk_z u_z(\mathbf{x})}(\delta(\mathbf{x}) + f\nabla_z u_z(\mathbf{x})). \tag{5.24}$$

At this point a perturbative approach can be applied, by expanding the second exponent in a power series, giving:

$$\delta_g^s(\mathbf{k}_i) = \sum_{n=1}^{\infty} \int \frac{d^3q_1}{(2\pi)^3} \dots \int \frac{d^3q_n}{(2\pi)^3} \delta_D(\mathbf{k}_i - \mathbf{q}_{1\dots n})[\delta_g(\mathbf{q}_1) + f\mu_1^2\theta(\mathbf{q}_1)] \frac{(f\mu q)^{n-1}}{(n-1)!} \frac{\mu_2}{q_2}\theta(\mathbf{q}_2)\dots\frac{\mu_n}{q_n}\theta(\mathbf{q}_n) \tag{5.25}$$

$$= \delta_g(\mathbf{k}_i) + f\mu_i^2\theta(\mathbf{k}_i) + \int \frac{d^3q_1}{(2\pi)^3} \int \frac{d^3q_2}{(2\pi)^3} [\delta_g(\mathbf{q}_1) + f\mu_1^2\theta(\mathbf{q}_1)] f\mu_{12}q_{12}\frac{\mu_2}{q_2}\theta(\mathbf{q}_2), \tag{5.26}$$

where $\mu_i = \mathbf{k}_i \cdot \hat{z}/k_i$ is the cosine of the angle between the wavevector $\mathbf{k}_i$ and the line-of-sight $\hat{z}$, $\mu_{ij} = (\mu_i k_i + \mu_j k_j)/k_{ij}$ and $k_{ij}^2 = (\mathbf{k}_i + \mathbf{k}_j)^2$. In the linear regime we retrieve the well known result of (Kaiser, 1987), $\delta_g^s(\mathbf{k}_i) = (1 + f\mu_i^2)\delta_g(\mathbf{k}_i)$. In order to model the statistics of galaxies in redshift space, the kernel formalism of SPT can be generalised to include the redshift distortions and the bias terms [Eq. (5.1)] (*i.e.* use the bias expansion in Eq. (5.1) to substitute δ_g in Eq. (5.26)). The galaxy overdensity in redshift space can be written as (Verde et al, 1998)

$$\delta_g^s(\mathbf{k}, z) = \sum_{n=1}^{\infty} D^n(z) \int \frac{d^3q_1}{(2\pi)^3} \dots \frac{d^3q_n}{(2\pi)^3} \delta_D(\mathbf{k} - \mathbf{q}_1 \dots - \mathbf{q}_n) Z_n(\mathbf{q}_1, \dots, \mathbf{q}_n)\delta^{(1)}(\mathbf{k}_1)\dots\delta^{(1)}(\mathbf{k}_n), \tag{5.27}$$

where Z_n are the n-th order redshift space galaxy kernels. Since the analysis is restricted to large scales, we only require up to the second order redshift kernel in order to derive the linear power spectrum and tree-level bispectrum in redshift space. For the general, non-local, primordial non-Gaussianity the results are:

$$P_g^s(k, z) = D_{\rm FOG}^P(\mathbf{k})[Z_1^2(\mathbf{k})P_m^L(k, z) + P_\varepsilon], \tag{5.28}$$

$$B_g^s(k_1,k_2,k_3,z) = D^B_{\rm FOG}(\mathbf{k}_1,\mathbf{k}_2,\mathbf{k}_3)\Big[Z_1(\mathbf{k}_1)Z_1(\mathbf{k}_2)Z_1(\mathbf{k}_3)B_I(k_1,k_2,k_3,z)$$
$$+\left(2Z_1(\mathbf{k}_1)Z_1(\mathbf{k}_2)Z_2(\mathbf{k}_1,\mathbf{k}_2)P_m^L(k_1,z)P_m^L(k_2,z)+\int\frac{d^3q}{(2\pi)^3}T^{RSD}_{1112}(\mathbf{k}_1,\mathbf{k}_2,\mathbf{q},\mathbf{k}_3-\mathbf{q})+2\text{ perm}\right)$$
$$+2P_{\varepsilon\varepsilon_\delta}(Z_1(\mathbf{k}_1)P_m^L(k_1)+2\text{ perm})+B_\varepsilon\Big], \tag{5.29}$$

while the redshift kernels are given by

$$Z_1(\mathbf{k}_i) = b_1+f\mu_i^2+\frac{b_\Psi k_i^\alpha}{M(k_i,z)}, \tag{5.30}$$
$$Z_2(\mathbf{k}_i,\mathbf{k}_j) = b_1F_2(\mathbf{k}_i,\mathbf{k}_j)+f\mu_{ij}^2G_2(\mathbf{k}_i,\mathbf{k}_j)+\frac{b_2}{2}+b_{s^2}S_2(\mathbf{k}_i,\mathbf{k}_j)+\frac{f\mu_{ij}k_{ij}}{2}\left[\frac{\mu_i}{k_i}Z_1(\mathbf{k}_j)+\frac{\mu_j}{k_j}Z_1(\mathbf{k}_i)\right]$$
$$+\frac{1}{2}\left(\frac{(b_{\Psi\delta}-b_\Psi N_2(\mathbf{k}_j,\mathbf{k}_i))k_i^\alpha}{M(k_i,z)}+\frac{(b_{\Psi\delta}-b_\Psi N_2(\mathbf{k}_i,\mathbf{k}_j))k_j^\alpha}{M(k_j,z)}\right), \tag{5.31}$$

where $G_2(\mathbf{k}_i,\mathbf{k}_j)$ is the second order velocity kernel of SPT [Eq. (3.24)]. Note that here, all the $\mathcal{O}(f_{\rm NL}^2)$ terms in the Z_2 kernel are excluded.

The term T_{1112} in redshift space, after excluding all $\mathcal{O}(f_{\rm NL}^2)$ contributions, derived by using standard PT formalism, the bias expansion of Eq. (5.1) and RSD up to second order, is given by

$$T^{RSD}_{1112}(\mathbf{k}_1,\mathbf{k}_2,\mathbf{k}_3,\mathbf{k}_4) = Z_1^G(\mathbf{k}_2)Z_2^{G,b}(\mathbf{k}_3,\mathbf{k}_4)[G_{P_1}\mu_1^2f+b_1F_{P_1}]+Z_1^G(\mathbf{k}_1)Z_2^{G,b}(\mathbf{k}_3,\mathbf{k}_4)[G_{P_2}\mu_2^2f+b_1F_{P_2}]$$
$$+Z_1^G(\mathbf{k}_1)Z_1^G(\mathbf{k}_2)\left[\left(\frac{b_2}{2}+S_2(\mathbf{k}_3,\mathbf{k}_4)\right)F_{P_3}+\frac{fk_{34}\mu_{34}}{2}\left(Z_1^G(\mathbf{k}_4)\frac{\mu_3}{k_3}G_{P_3}+\frac{\mu_4}{k_4}(b_1F_{P_3}+\mu_3^2fG_{P_3})\right)\right]$$
$$+Z_1^G(\mathbf{k}_1)Z_1^G(\mathbf{k}_2)\left[\left(\frac{b_2}{2}+S_2(\mathbf{k}_3,\mathbf{k}_4)\right)F_{P_4}+\frac{fk_{34}\mu_{34}}{2}\left(Z_1^G(\mathbf{k}_3)\frac{\mu_4}{k_4}G_{P_4}+\frac{\mu_3}{k_3}(b_1F_{P_4}+\mu_4^2fG_{P_4})\right)\right] \tag{5.32}$$

where $Z_1^G(\mathbf{k})$ and $Z_2^{G,b}(\mathbf{k}_1,\mathbf{k}_2)$ are the Gaussian parts of the redshift kernels Z_1 and Z_2 respectively [Eqs. (5.30) and (5.31)], while for $Z_2^{G,b}$ we exclude also the two SPT kernel contributions. The terms denoted F_{P_i} and G_{P_i} are the ith permutation of Eq. (3.129), where the letter F and G represent the SPT kernel used in the expression at hand (*e.g.* $G_{P_4} = \langle\delta^{(1)}_{\mathbf{k}_1}\delta^{(1)}_{\mathbf{k}_2}\delta^{(1)}_{\mathbf{k}_3}\theta^{(2)}_{\mathbf{k}_4}\rangle = 2G_2(\mathbf{k}_{12},\mathbf{k}_3)B_I(k_1,k_2,k_{12},z)P_m^L(k_3,z)+2$ perm). A

redshift space model similar to the one in Eq. (5.29) was used in Tellarini et al (2016) to put constraints on the primordial non-Gaussian amplitude for a list of future LSS surveys. However, in this reference, only the local case without trispectrum contributions and stochastic bias terms is considered. Besides these new terms, redshift uncertainties are also included in our redshift model, as discussed in the next paragraph.

The FOG term models the damping effect of the clustering power induced by the Finger Of God effect on linear scales. The two terms for the power spectrum and bispectrum are (Peacock and Dodds, 1994; Ballinger et al, 1996; Scoccimarro et al, 1999)

$$D^{P}_{\rm FOG}(\mathbf{k}) = e^{-(k\mu\sigma_P)^2}, \tag{5.33}$$

$$D^{B}_{\rm FOG}(\mathbf{k}_1,\mathbf{k}_2,\mathbf{k}_3) = e^{-(k_1^2\mu_1^2+k_2^2\mu_2^2+k_3^2\mu_3^2)\sigma_B^2}. \tag{5.34}$$

The amplitude of the effect is characterized by one free parameter σ, which in principle is different for these two correlators. Here we treat it as being the same in both cases and define its fiducial value as $\sigma_P = \sigma_B = \sigma_v(z)$, with σ_v being the usual linear, one dimensional velocity dispersion.

Besides the FOG effect, the redshift uncertainty of galaxy surveys must be also taken into account. The redshift error, σ_z, can be translated into a position uncertainty along the line of sight. The treatment of this effect is the same as in the case of FOG (see *e.g.* (Seo and Eisenstein, 2003)), where the only difference is the fiducial value of the σ parameter, which will be $\sigma_r = c\sigma_z(z)/H(z)$. Considering both effects gives the final form of the damping factors in Eqs. (5.28) and (5.29), with the σ parameters given by $\sigma_{\rm v}^2 = \sigma_v^2 + \sigma_r^2$. These multiplicative factors introduce a suppression of the signal for all scales with a large component along the line of sight, affecting mostly small scales. In other words, only modes k that have $k\mu\sigma_{\rm v} \lesssim 1$ are not dominated by noise and can contribute to the power spectrum and bispectrum measurements.

The redshift space bispectrum is characterized by five variables, three of them define the triangle shape (*i.e.* the magnitude of the three wavenumbers, k_1, k_2, k_3) and the

remaining two the orientation of the triangle with the line of sight $\hat{z}$, which we consider to be the polar angle $\mu = \cos\omega$ of k_1 with $\hat{z}$ and the azimuthal angle ϕ. Therefore we can define the vectors (Scoccimarro et al, 1999):

$$\mathbf{k}_1 = (0, 0, k_1), \tag{5.35}$$

$$\mathbf{k}_2 = (0, k_2 \sin\theta_{12}, k_2 \cos\theta_{12}), \tag{5.36}$$

$$\mathbf{k}_3 = (0, -k_2 \sin\theta_{12}, -k_1 - k_2 \cos\theta_{12}), \tag{5.37}$$

$$\hat{z} = (\sin\omega\cos\phi, \sin\omega\sin\phi, \cos\omega), \tag{5.38}$$

where $\cos\theta_{12} = \mathbf{k}_1 \cdot \mathbf{k}_2/(k_1 k_2)$. The cosine of the angles μ_i will be now:

$$\mu_1 = \mathbf{k}_1 \cdot \hat{z} = \mu, \tag{5.39}$$

$$\mu_2 = \mathbf{k}_2 \cdot \hat{z} = \cos\theta_{12}\mu + \sin\theta_{12}\sqrt{1-\mu_1^2}\sin\phi, \tag{5.40}$$

$$\mu_3 = \mathbf{k}_3 \cdot \hat{z} = -\mu_{12} = -\frac{k_1}{k_3}\mu_1 - \frac{k_2}{k_3}\mu_2. \tag{5.41}$$

The bispectrum will now be $B_g^s(\mathbf{k}_1, \mathbf{k}_2, \mathbf{k}_3) = B_g^s(k_1, k_2, k_3, \mu_1, \phi)$. Taking the spherical average over all possible orientations of the triangles with respect to the line of sight (*i.e.* the monopole term in the Legendre expansion) of Eq. (5.29), in a similar fashion as it was done in (Kaiser, 1987) for the power spectrum, one can obtain (Sefusatti et al, 2006; Gil-Marín et al, 2012):

$$P_g^s(k, z) = \alpha_P(\beta) P_g(k, z), \tag{5.42}$$

$$B_g^s(k_1, k_2, k_3, z) = \alpha_B(\beta) B_{ggg}(k_1, k_2, k_3, z), \tag{5.43}$$

where

$$\alpha_P(\beta) = 1 + \frac{2}{3}\beta + \frac{1}{5}\beta^2, \tag{5.44}$$

$$\alpha_B(\beta) = 1 + \frac{2}{3}\beta + \frac{1}{9}\beta^2, \tag{5.45}$$

with $\beta = f/b1$. The terms P_g and B_{ggg} are the real space galaxy power spectrum and bispectrum, given by Eqs. (5.8) and (5.19) respectively. The redshift space bispectrum presented above, as described in (Sefusatti et al, 2006), is derived after averaging over $\theta_{12} = \mathrm{acos}(\widehat{k_1 k_2})$ and dropping the dependence on the second-order PT velocity kernel [Eq. (3.24)] and the FOG effect (*i.e.* keep only Eq. (24) and (28) of (Scoccimarro et al, 1999)). This is a good approximation on large scales since these two partially cancel out.

In the cases of local and orthogonal primordial non-Gaussianity the galaxy power spectrum and bispectrum will be described by the full model of Eqs. (5.8), (5.19) and (5.28), (5.29) for real and redshift space respectively. In Eq. (5.29) we will keep only the $\mathcal{O}(f_{\rm NL})$ terms, while the full form was written down for completeness. For the equilateral case, as we discussed before, the scale dependent bias contribution is degenerate and will not be used. Nevertheless we will use the Gaussian power spectrum, excluding its signal contribution from constraining $f_{\rm NL}$, and the bispectrum without the terms proportional to the non-local primordial field Ψ. In this case, the trispectrum bias contribution can compensate for the missing large scale signal and improve the constraints on the non-Gaussian amplitude, as we will show in Sec. 5.7.

5.3 Fisher information matrix formalism

Suppose we have a random variable x with a probability that depends on a parameter θ. We can define the conditional probability $p(x;\theta)$ as the probability of having x given the parameter θ. If we make independent measurements of the parameter and obtain x_1, x_2, x_3, *etc.*, then the *joint probability*, *i.e.* the probability of having a specific sequence assuming independence of the measurements, is given by

$$L(x_1, x_2, \ldots; \theta) = \prod_i p(x_i; \theta) \tag{5.46}$$

where $L(\mathbf{x};\theta)$ is the *likelihood* probability. In the case of many parameters we can write

this as $L(\mathbf{x};\theta)$, where $\theta = \{\theta_1, \theta_2, \ldots\}$ is the parameter vector. The set of parameters θ that maximize the joint probability $L(\mathbf{x};\theta)$, *i.e.* the set that makes the occurrence of our data set the most probable, must solve

$$\frac{\partial L(\mathbf{x};\theta)}{\partial \theta_\alpha}\Big|_{\theta_\alpha} = 0 \quad \alpha = 1, \ldots, m \tag{5.47}$$

From this we can define the maximum likelihood estimator $\hat{\theta}_\alpha$ as the value of the parameter θ_α that maximised the likelihood (see Sec. 6.2 for a discussion). The estimator of the parameters is taken to be the mean, $\hat{\theta} = \int \theta P(\theta;\mathbf{x}) d\theta$, where $P(\theta,\mathbf{x})$ is the probability distribution of the parameters given the data. An assumption about the distribution of the data must be made, *e.g.* a Gaussian, in order to form the likelihood of the parameters. Once we have it though, we can derive the maximum likelihood estimator $\hat{\theta}$ by sampling the likelihood at various points in a multi-dimensional parameter space. Such a computation can be very demanding for a large number of parameters.

A faster approach, in order to avoid the parameter space sampling, is to assume that the likelihood is a multivariate Gaussian function of the parameters

$$\mathcal{L} \equiv -\ln L(\mathbf{x};\theta) = \frac{1}{\sqrt{(2\pi)^N \det C}} \exp\left[-\frac{1}{2}(\theta_\alpha - \hat{\theta}_\alpha) F_{\alpha\beta} (\theta_\beta - \hat{\theta}_\beta)\right] \tag{5.48}$$

where $F_{\alpha\beta}$ is the *Fisher information* matrix and it is the inverse of the covariance between the parameters evaluated at the expected value of the estimator. In the case of an unbiased estimator, like the maximum likelihood, the expected value equals the true, *i.e.* $\langle \hat{\theta} \rangle = \theta_0$. The Gaussian assumption is reasonable near the peak of the likelihood distribution. Therefore we can Taylor expand around the maximum likelihood value of the parameters as derived from the estimator $\hat{\theta}$, *i.e.* θ_0, to get

$$\mathcal{L}(\mathbf{x};\theta) = \mathcal{L}(\mathbf{x};\theta_0) + \frac{1}{2}(\theta_\alpha - \theta_{0\alpha}) \frac{\partial^2 \mathcal{L}(\mathbf{x};\theta)}{\partial \theta_\alpha \partial \theta_\beta} (\theta_\alpha - \theta_{0\alpha}) + \ldots \tag{5.49}$$

This gives the Fisher matrix as

$$F_{\alpha\beta} = \left\langle \frac{\partial^2 \mathcal{L}(\mathbf{x}_0;\theta)}{\partial\theta_\alpha \partial\theta_\beta} \right\rangle \Bigg|_{\theta=\theta_0} \tag{5.50}$$

where $\mathbf{x}_0$ is the dataset which corresponds to the maximum likelihood parameters. A direct consequence of the fact that a maximum likelihood estimator saturates the minimum bound in its variance, imposed by the Cramer-Rao inequality (see Sec. 6.2) in the case of a large sample, is that the minimum error of a parameter is related to the Fisher matrix [Eq. (6.9)] as

$$\sigma_\alpha = \sqrt{F^{-1}_{\alpha\alpha}} \tag{5.51}$$

Assuming that the likelihood follows a Gaussian distribution, we can write

$$2\mathcal{L} = \ln \det C + (\mathbf{x}-\mu)C^{-1}(\mathbf{x}-\mu)^T \tag{5.52}$$

where μ is the mean vector, *i.e.* the dataset that corresponds to the true values of the parameters θ_0 and hence depends on them, and $C^{-1} = \langle (\mathbf{x}-\mu)(\mathbf{x}-\mu)^T \rangle$. Using this in Eq. (5.50) we get (see *e.g.* Heavens (2009))

$$F_{\alpha\beta} = \frac{1}{2}[C^{-1}C_{,\alpha}C^{-1}C_{,\beta} + C^{-1}(\mu_{,\alpha}\mu^T_{,\beta} + \mu_{,\beta}\mu^T_{,\alpha})] \tag{5.53}$$

This is a very powerful result since we can perform predictions by assuming a theoretical model, which we treat as being the maximum likelihood dataset, without the use of any data.

In the case of the galaxy power spectrum, the Fisher matrix is given by

$$F^{Ps}_{\alpha\beta} = \sum_{\mu_1=0}^{1} \sum_{k=k_{\rm min}}^{k_{\rm max}} \frac{\partial P^s_g}{\partial p_\alpha} \frac{\partial P^s_g}{\partial p_\beta} \frac{1}{\Delta P^2} \tag{5.54}$$

while for the bispectrum we have (Scoccimarro et al, 2004)

$$F^{Bs}_{\alpha\beta} = \sum_{\mu_1=-1}^{1} \sum_{\phi=-\pi/2}^{\pi/2} \sum_{T} \frac{\partial B^s_g}{\partial p_\alpha} \frac{\partial B^s_g}{\partial p_\beta} \frac{1}{\Delta B^2}, \tag{5.55}$$

where $p_{\alpha,\beta}$ are the unknown parameters of interest and the derivatives are evaluated at the fiducial value of the parameter vector. The sum over the triangle is written as

$$\sum_{T} \equiv \sum_{k_1=k_{\rm min}}^{k_{\rm max}} \sum_{k_2=k_1}^{k_{\rm max}} \sum_{k_3=k_*}^{k_2} \tag{5.56}$$

where k modes are binned with a bin size of Δk, which is some integer multiple of the fundamental frequency of the survey $k_f = 2\pi/V^{1/3}$ (here we consider $\Delta k = k_f$), between a minimum value $k_{min} = k_f$ (largest scales probed by survey) and $k_{\rm max}$ (smallest scales considered). The mode ordering used here is $k_1 \geq k_2 \geq k_3$ and $k_* = \min(k_{\rm min}, k_1 - k_2)$. The angular bin sizes are taken here to be $\Delta\mu_1 = 0.1$ and $\Delta\phi = \pi/25$ throughout this chapter. The sum over the angle ϕ is a half cycle due to the azimuthal symmetry of $B^s_g(k_1, k_2, k_3, \mu, \phi)$, which is due to the fact that the functional dependence of the redshift space bispectrum on the azimuthal angle is $\sin\phi$. Additionally a symmetry on μ_1 is observed in the case of the power spectrum, originating from the quadratic dependence of P^s_g on the angle μ_1. Taking advantage of these symmetries significantly improves the speed of the numerical calculations, especially in the case of the bispectrum. The lower limit on the parameter of interest for a given survey, is found after marginalizing over all the other unknown parameters by using Eq. (5.51).

Note that the Fisher matrix of the power spectrum [Eq. (5.54)] is calculated from the sum over k bins, rather than using an integral (see *e.g.* (Wang, 2006)). This choice is due to the fact that the integral would assume a survey with infinite precision. Even if it is done numerically, an arbitrarily small Δk is used to achieve accurate results. For a survey with a finite volume, a Fourier mode cannot be measured more accurately than $k_f/2$ due to the uncertainty principle. In other words, there is not enough room inside a survey to tell apart two waves whose frequencies differ from each other by less than $k_f/2$.

The parameter vector considered here consists of the non-Gaussian amplitude, three bias parameters, stochastic power spectrum and bispectrum contributions, the linear growth rate and the velocity dispersion,

$$\mathbf{p} = \{f_{\rm NL}^X, b_1, b_2, b_{s^2}, P_\varepsilon, P_{\varepsilon\varepsilon_\delta}, B_\varepsilon, f, \sigma_v\}. \tag{5.57}$$

where the superscript X in $f_{\rm NL}$ denotes one of the three non-Gaussian types considered here. The amplitudes of the stochastic bias terms are considered here nuisance parameters and must be marginalized over at each redshift bin to acquire the subset of the parameters of interest $\mathbf{p}_{sub}$. This can be done by taking the inverse of the full Fisher matrix and keep the sub-matrix that corresponds to the parameters of interest (*i.e.* $\{f_{\rm NL}^X, b_1, b_2, b_{s^2}, f, \sigma_v\}$) and then invert back to get F^{sub}. To derive the constraints on the non-Gaussian amplitude we invert again the sub-matrix F^{sub}, and we keep only the matrix element that holds the information on $f_{\rm NL}$. Finally, we invert back to acquire the Fisher 1×1 matrix for the amplitude of primordial non-Gaussianity. It is this matrix that is summed over redshift bins that will give us the desired constraints on $f_{\rm NL}$. We aim for a complete and conservative analysis, therefore we will stick to the linear regime, and exclude non-linear scales. For the redshift evolution of $k_{\rm max}(z)$ we consider, $k_{\rm max}(z) = 0.1/D(z)$. $k_{\rm max}$ slowly varies with redshift while in the linear and semi-linear regime, ensuring the validity of the bias expansion, as well as SPT itself.

In our Fisher matrix analysis, only the diagonal part of the covariance matrix (*i.e.* ΔP^2 and ΔB^2) is taken into consideration, neglecting all the cross-correlations between different triangles (bispectrum) and k-bins (power spectrum). Using the estimators for the power spectrum and bispectrum, as defined in (Scoccimarro et al, 1998), we can retrieve the analytic results for the variance of the estimators as

$$\begin{aligned}
\Delta P^2(k,z) &= 2\frac{V_f}{V_P}P_{\rm tot}^2(k,z) = \frac{4\pi^2}{V_{\rm survey}k^2\Delta k\Delta\mu}P_{\rm tot}^2(k,z), \\
\Delta B^2(k_1,k_2,k_3,z) &= s_{123}\frac{V_f}{V_B}P_{\rm tot}(k_1,z)P_{\rm tot}(k_2,z)P_{\rm tot}(k_3,z)
\end{aligned} \tag{5.58}$$

$$= s_{123}\pi k_f^3 \frac{P_{\rm tot}(k_1,z)P_{\rm tot}(k_2,z)P_{\rm tot}(k_3,z)}{k_1k_2k_3\Delta k^3\Delta\mu\Delta\phi}, \tag{5.59}$$

where $s_{123} = 6, 2, 1$ for equilateral, isosceles and scalene triangle respectively. The volume of the fundamental shell in Fourier space is $V_f = k_f^3$. In addition $P_{\rm tot}(k,z) = P_g^s(k,z) + 1/\overline{n}_g$, where the stochastic contribution is excluded from P_g^s and the remaining term accounts for the shot noise. Note that for the Fisher matrix in redshift space, the normalization for the two angles, *i.e.* $N_\mu = \mu_{max} - \mu_{min}$ and $N_\phi = \phi_{max} - \phi_{min}$, must be applied. Finally, in the above expressions the normalization volumes are given by

$$V_P = \int_{k_1} \frac{d^3q_1}{(2\pi)^3} \int_{k_2} \frac{d^3q_2}{(2\pi)^3} \delta_D(\mathbf{q}_1 + \mathbf{q}_2) \approx 4\pi k_1 k_2 \Delta k, \tag{5.60}$$

$$V_B = \int_{k_1} \frac{d^3q_1}{(2\pi)^3} \int_{k_2} \frac{d^3q_2}{(2\pi)^3} \int_{k_3} \frac{d^3q_3}{(2\pi)^3} \delta_D(\mathbf{q}_1 + \mathbf{q}_2 + \mathbf{q}_3) \approx 8\pi^2 k_1 k_2 k_3 \Delta k^3. \tag{5.61}$$

The full covariance of the two estimators is outlined in (Sefusatti et al, 2006), where the off-diagonal elements are defined by higher than three point correlators. Although the above results are for redshift space statistics, the reduction to real space is straightforward. The real space Fisher matrix results are also used for the power spectrum and bispectrum monopole approximation case [Eqs. (5.42) and (5.43)].

Recently, the authors of Ref. (Chan and Blot, 2017) used dark matter N-body simulations, including four halo samples with different number densities, in order to study the full covariance of the power spectrum and bispectrum estimators. They focused on extracting an integrated signal-to-noise ratio for all bins/triangles, checking how this gets degraded when off-diagonal covariance elements and non-Gaussian contributions to the variance are accounted for. While this does not include a specific study of the degradation of error bars for primordial NG or other cosmological parameters, their results can provide useful guidelines to assess the validity of our diagonal covariance approximation and the error on the parameter forecast we introduce by employing it.

For the dark matter power spectrum, (Chan and Blot, 2017) show that the correlation coefficient between different modes never exceeds $\sim 15\%$ at $z = 0$, up to $k_j = 0.1\,h/\mathrm{Mpc}$. For $z = 1$, the correlation reaches at most $\sim 20\%$ for (*i.e.* $k_j \sim 0.15\,h/\mathrm{Mpc}$ for $z = 1$). This is due to the fact that the Universe becomes more linear and hence the effect of the non-Gaussian contributions to the covariance is less important. On the scale range considered here, the non-Gaussian corrections to the diagonal part of the covariance is negligible at $z = 0$, as well as for $z = 1$. For halos, these corrections can be up to $\sim 10\%$ for the same scale range, in the case of the small density halo samples, with the exact value depending on the redshift. Furthermore, the results agree with the covariance model predicted by PT up to $k = 1\,\mathrm{h/Mpc}$ for the abundant halo sample. Therefore we conclude that the exclusion of the off-diagonal part in the galaxy power spectrum covariance will introduce an error of the order of few to $10-15\%$ percent, for the scale range and redshifts considered here, depending on the number density of the sample. In addition, the NG corrections to the variance are negligible for the high density samples and scale range considered here.

For the dark matter bispectrum, it is shown that the non-Gaussian corrections to the diagonal Gaussian part (for equilateral configurations) is $\sim 8\%$ at $z = 0$ and $k = 0.1\,h/\mathrm{Mpc}$ and that PT predictions agree with the numerical results up to $k \sim 0.15\,h/\mathrm{Mpc}$. For higher redshifts (*i.e.* $z = 0.5,\ 1$) the corrections are at a few percent level, up to $k \sim 0.16\,\mathrm{h/Mpc}$, while the PT predictions are in good agreement with the results up to $k \sim 0.2\,\mathrm{h/Mpc}$ and $k \sim 0.3\,\mathrm{h/Mpc}$ for $z = 0.5$ and $z = 1$ respectively. In addition, it is shown show that the correlation coefficient, used to test couplings between different triangles, is consistent with zero for the large scales and for the redshift slices considered. This means that, for the chosen scale range and redshifts of this chapter, we are always in the low mode-mode correlation regime.

When, instead of dark matter, we consider halos, triangle couplings and non-Gaussian corrections strongly depend on the redshift and density of the sample. Corrections to

the diagonal Gaussian part are negligible at $z = 0$ and $k = 0.1\ h/\mathrm{Mpc}$ in the case of a high density sample ($\overline{n} \sim 10^{-3}\ [\mathrm{Mpc/h}]^{-3}$). On the other hand, for a low density case ($\overline{n} \lesssim 2 \times 10^{-5}\ [\mathrm{Mpc/h}]^{-3}$) the correction is found to be between few percent and $\sim 10\%$ at low redshift, and increasing up to $\sim 90\%$ at high redshifts.

Moreover, the S/N ratio is reported for both power spectrum and bispectrum in the case of dark matter and the small abundant halo sample. For the dark matter, the inclusion of the full covariance suppresses the bispectrum S/N almost two times at $k = 0.1$ h/Mpc and $z = 0$, while the power spectrum S/N is almost unchanged. The same behaviour is observed also in the higher redshift bins. For rare halos, the effect is more intense. The bispectrum S/N is suppressed 3-4 times at $z = 0$ and $k = 0.1$ h/Mpc, while at $z = 1$ and $k \sim 0.15$ h/Mpc an order of magnitude suppression is observed. These findings are for the rare mass groups and therefore we expect the changes to be less aggressive for more abundant samples.

The samples considered in this work have a high number density for the majority of the redshift bins (except only for some high redshift slices, where non-linearities are anyway less important), $\overline{n}_g \gtrsim 10^4\ (\mathrm{h/Mpc})^3$ (see Table 5.1, 5.2, 5.3 and 5.4). Therefore we do not expect the exclusion of the non-Gaussian part in the covariance to overestimate much the S/N ratio and have a large impact on the final PNG constraints.

A final remark to make is that the S/N, after including the full non-Gaussian covariance, is always larger for the $P(k)$ than the bispectrum case, throughout the whole scale range (up to $k_{\mathrm{max}} \sim 1$ h/Mpc) and for all redshift bins considered in (Chan and Blot, 2017). This indicates that the amount of information contained in the three-point statistics is small compared to that derived from the two-point. However, note that the general S/N analysis, performed in (Chan and Blot, 2017), reflects the capabilities of the bispectrum in measuring cosmological parameters. On the other hand, three-point statistics hold a rich amount of information to put tight constrains in the amplitude of primordial non-Gaussianities. This will be shown extensively in this chapter.

As explicitly shown in (Chan and Blot, 2017), on the large scales considered here the full NG contribution can be well approximated by including perturbative corrections to the power spectrum appearing in the bispectrum variance expression, obtaining:

$$\Delta B^2_{\rm NL}(k_1,k_2,k_3,z) = \Delta B^2(k_1,k_2,k_3,z) + \frac{s_{123}\pi V_f}{k_1 k_2 k_3 \Delta k^3 \Delta\mu \Delta\phi} \times \left(P_{\rm tot}(k_1) P_{\rm tot}(k_2) (P_g^{\rm NL}(k_3) - P_g(k_3) + \frac{1}{\overline{n}_g}) + 2 \text{ perm} \right) \tag{5.62}$$

where $P_g^{\rm NL}(k_3)$ is given by Eq. (5.8) after replacing the linear matter power spectrum with the non-linear one, as predicted by the HALOFIT algorithm (Smith et al, 2003; Takahashi et al, 2012). The reason that HALOFIT, instead of the PT one-loop matter power spectrum, is used, lies in the fact that the latter leads to overestimating the actual variance in the weakly non-linear regime. We will use this expression later on in our analysis, in order to estimate more in detail the effect of neglecting NG corrections in our forecasts.

The combined prediction coming from the power spectrum and bispectrum, neglecting the cross covariance between the two, is given by

$$F_{\alpha\beta}^{P+B} = F_{\alpha\beta}^{P} + F_{\alpha\beta}^{B}. \tag{5.63}$$

Another aspect to consider is the covariance between the power spectrum and the bispectrum when the two are used jointly. This was provided, in the Gaussian case, in the work of (Sefusatti et al, 2006) and used in (Song et al, 2015). In the work of (Chan and Blot, 2017), a comparison between the S/N ratios coming from N-body simulations is made in order to test the effect of the PB cross-covariance. In the case of dark matter they show that at $z = 0$ and $k_{\rm max} = 0.1$ h/Mpc the effect of the cross covariance is negligible, while for larger scales it can reduce the total S/N by $\sim 10\%$. On the other hand, at small scales an enhancement of $15 - 40\%$ is observed. This behaviour is less pronounced in the case of higher redshifts: for $z = 1$ and $k_{\rm max} \sim 0.15$ h/Mpc (*i.e.* the one that matches our

choice of $k_{\rm max}(z)$) the cross covariance affects S/N by a negligible to $\sim 1\%$ amount. For a sample with higher abundance, like those we consider here, the effect of cross covariance follows the behaviour of dark matter, *i.e.* a few percent effect for our chosen scale range. This justifies neglecting the cross-covariance in our forecasts, as well as the value of the adopted $k_{\rm max}$ limit.

5.4 Theoretical Errors

Theoretical errors quantify the uncertainties on the modelling of the matter perturbations and the bias expansion in the statistics of galaxies. Perturbation theory can provide an adequate description of the evolution of the density field up to the mildly non-linear scales. In the non-linear regime, the predictability of PT loses power and we are dominated by theoretical uncertainties. Even before reaching these scales, the effect of theoretical errors arising from a finite loop expansion, should be taken into account and this is especially true in the case of the Fisher matrix formalism, where a perfect theoretical description is otherwise assumed.

Here we will follow and extend the treatment of (Baldauf et al, 2016), where theoretical errors **e** are defined as the difference between the true theory and the fiducial theoretical prediction. This formalism considers the true theory to be the model which takes into account at least one more perturbative order than the fiducial one. These errors are bounded by an envelope **E** and their variation as a function of wavenumbers is characterized by Δk [Eq. (5.65)]. The value of the correlation length Δk is taken to be that of the smallest coherence length of the total power spectrum, that is the scale of the Baryon Acoustic Oscillations (BAO), $\Delta k = \Delta_{BAO} = 0.05$ h/Mpc (see (Baldauf et al, 2016) for an extensive discussion). The error covariance matrix is written as:

$$C^e_{ij} = E_i \rho_{ij} E_j \tag{5.64}$$

where i, j are the indices of the different momentum configurations (*i.e.* number of bins and triangles for the power spectrum and bispectrum respectively). The correlation coefficient ρ_{ij} accounts for the correlations between the momentum configurations, considered to follow a Gaussian distribution, and given by

$$\rho_{ij} = \begin{cases} \exp(-(k_i - k_j)^2/2\Delta k^2) & \text{P}, \\ \prod_{\alpha=1}^{3} \exp(-(k_{i,\alpha} - k_{j,\alpha})^2/2\Delta k^2) & \text{B}. \end{cases} \tag{5.65}$$

For a diagonal error covariance (*i.e.* $\rho_{ii} = 1$ and $\rho_{ij} = 0$ for $i \neq j$) and a fixed Δk, the envelope $E(k)$ would be independent of the bin size, contrary to the statistical errors. This means that, for uncorrelated bins, choosing a smaller bin size will reduce the effect of the theoretical errors. The presence of an off-diagonal ρ_{ij} ensures that this does not happen and the relative impact of errors is independent from the size of the k bins. After marginalising over the theoretical errors $\mathbf{e}$, the final covariance that will be used in the Fisher matrix analysis becomes just the sum of the variance of the power spectrum and bispectrum estimators (Eqs. (5.58) and (5.59) respectively) with the theoretical error covariance [Eq. (5.64)].

One of the goals of this work is to test the effect of theoretical errors on the parameter constraints coming from high redshift LSS surveys. The Universe is more linear at large redshifts and hence, for the scales considered in this analysis, we would not expect to see a significant impact on the constraints solely from the theoretical uncertainties attributed to PT. As we discussed in Sec. 4.3.2, bias has its own limitation towards the small scales, where the contribution of additional terms becomes important (see *e.g.* (Desjacques et al, 2016) and references therein for a discussion). In the formalism proposed by Baldauf et al (2016), the envelope is fitted up to two-loops in matter perturbations for both power spectrum and bispectrum while for the bias expansion they consider only the linear bias. Here, we proceed in extending their approach to include the theoretical uncertainties coming from the local-in-matter bias terms (*i.e.* b_1, b_2, b_3, *etc.*) that appear up to the

1-loop expression of the galaxy power spectrum and bispectrum. This set of terms has been shown to provide an accurate description by comparing with simulations and galaxy catalogues (see *e.g.* (Scoccimarro et al, 2001a; Feldman et al, 2001; Verde et al, 2002; Marín et al, 2013; Gil-Marín et al, 2014)). Note that the inclusion of all the bias terms at each order (e.g. including tidal terms and other operators, see (Desjacques et al, 2016) for a review) is potentially important and we will consider their contribution in the theoretical error formalism in the near future (see Sec. 5.7.1.1 for a discussion).

In order to quantify the theoretical uncertainties, we fit the galaxy power spectrum and bispectrum envelope after including the local-in-matter bias terms up to 1-loop, in addition to the 1-loop matter expressions originating from the description of PT, while assuming Gaussian initial conditions. More precisely, for the galaxy power spectrum we take into account all the terms originating from the bias expansion, that have a dependence on b_1, b_2 and b_3, up to 1-loop (*i.e.* Eqs. (5.4), (5.5) and (5.6)). For the galaxy bispectrum, the bias terms considered are all those with a dependence on b_1, b_2, b_3 and b_4, up to 1-loop, while we exclude those with a dependence on PNG initial conditions (*i.e.* Eqs. (5.14) – (5.17)). For the matter expansion, we consider up to 1-loop terms for both power spectrum and bispectrum in the cases of SPT (see *e.g.* (Bernardeau et al, 2002) for a review) and MPTbreeze (see Sec. 3.4 for details). The SPT fits are presented here for completeness, since, throughout this chapter the MPTbreeze description of the matter perturbations will be used. The envelope for the power spectrum for the MPTbreeze and the SPT schemes are:

$$E_P(k,z) = \begin{cases} D^2(z)P_m^L(k,z)\left[b_1^2(k/0.32)^{1.8} + b_2^2(k/0.43)^{1.1} + b_1 b_3 1.13\right] & \text{SPT}, \\ D^2(z)P_m^L(k,z)\left[b_1^2(k/0.16)^2 + b_2^2(k/0.43)^{1.1}\right] & \text{MPTbreeze}, \end{cases} \tag{5.66}$$

while the fitting results for the bispectrum are:

$$E_B(k_1,k_2,k_3,z)=\begin{cases} D^2(z)B_G(k_1,k_2,k_3,z)\Big[3b_1^3(\hat{k}/0.32)^{1.8}+b_2^3 1.8\hat{k}^{1.25} & \\ +b_1b_2b_3 3.2+b_1^2b_4\Big] & \text{SPT,} \\ D^2(z)B_G(k_1,k_2,k_3,z)\Big[3b_1^3(\hat{k}/0.15)^{1.7} & \\ +b_2^3 1.8\hat{k}^{1.25}+b_1b_2b_3 3.2\Big] & \text{MPTBREEZE.} \end{cases} \tag{5.67}$$

where $\hat{k}=(k_1+k_2+k_3)/3$. Note that the values of the fitted free parameters in the above envelopes exhibit a small dependence on the fiducial cosmology (a few percent). The numerical values shown above correspond to the cosmological parameters considered here.

A slightly different methodology to quantify the effect of theoretical errors was developed in Ref. (Audren et al, 2013). The procedure followed is similar to the one used here. The main difference is that they define theoretical uncertainties by fitting a correction function to the HALOFIT, instead of the desired loop order given by PT. Their technique is applied only to the power spectrum and the relative error to the non-linear P is added to the diagonal part of the covariance matrix. The level of correction is quantified by the precision of HALOFIT, where only the linear bias is taken into account. In order to quantify the difference between the two approaches, we tested this methodology for the power spectrum, since the fitting function is provided only for this case, while a generalisation to the halo bispectrum is not straightforward. To perform the comparison, we adjusted the envelope function of Eq. (5.66) by removing the higher order bias contributions, as well as by using only the diagonal part of the error covariance [Eq. (5.64)]. In the case of local PNG the difference on the final $f_{\rm NL}$ constraint turns out to be $\sim 2\%$, while for orthogonal PNG is $\sim 8\%$. Therefore the two approaches produce very consistent results, whenever a comparison is possible.

However, we note that the (Baldauf et al, 2016) technique used here is in a sense more complete than the one provided by Audren et al (2013), despite the fact that the latter

considers, for the description of the dark matter perturbations, a more precise model (*i.e.* they use the HALOFIT model contrary to Baldauf et al (2016) that use the explicit PT calculations up to 1-loop). This is due to the fact that theoretical errors, as defined here, take also into account higher-order bias corrections, which are important for the redshift range we consider. In addition, we have shown that using only the diagonal part of the error covariance underestimates the effect of theoretical uncertainties at low redshifts, when the Universe is more non-linear and the correlations between different modes affect the final $f_{\rm NL}$ constraints. At higher redshifts, the effect of the full error covariance converges to the one given by only the diagonal part. Therefore, we expect the difference between the two methodologies to be at the level of a few percent, in the case where we consider only the linear bias terms for the galaxy power spectrum.

5.5 Galaxy Surveys

In this Section we describe the specifications of the radio continuum and optical galaxy surveys we used in this chapter.

5.5.1 Future radio surveys

In this section we forecast measurements of the bispectrum for future radio surveys; we focus on such experiments to investigate whether the high-redshift, full sky nature of those datasets will provide better constraints on non-Gaussianity parameters, despite the lower precision in redshift information.

We forecast results for two radio continuum surveys: the forthcoming Evolutionary Map of the Universe (EMU (Johnston et al, 2008; Norris et al, 2011)) survey, that recently started their early science survey, and a possible configuration of the full Square Kilometre Array (SKA), assuming the specifications of (Jarvis et al, 2015). For the EMU case, we use a $10\mu Jy$ flux limit, while for the SKA we assume it will go down to $1\mu Jy$. In both cases

we consider $30,000\,\mathrm{deg}^2$. Given that we want to forecast the advantages of having both full sky and high-z data, we use radio continuum surveys, that are however plagued by the fact that the sources' redshift is in principle unknown. This would allow, in the standard case, only the computation of an angular projected power spectrum and bispectrum.

The knowledge of the redshift distribution allows us to perform statistics in a three dimensional space and improve significantly upon a 2D analysis. The advantage of radio continuum surveys is that they cover large volumes, by mapping the sky on large angular separations and retrieving information from high redshifts. The combination of these characteristics can increase the accessible scales, since large volumes increase the scale resolution ($k_f = 2\pi/V^{1/3}$) and hence the signal-to-noise ratio. At high redshifts the Universe is more linear, since gravity did not have enough time to heavily couple the modes, increasing the scales up to which SPT can predict the evolution of matter (Jeong and Komatsu, 2006). This indicates that we can push further into smaller scales and enhance the bispectrum signal.

Recently, some techniques have been developed in order to provide such surveys with statistical redshift information. Here we follow the Clustering-Based Redshift (CBR) estimation, developed in the work of (Schneider et al, 2006; Newman, 2008; Ménard et al, 2013), where the missing redshift information can be retrieved by using a technique that cross-correlates the unknown distribution with a sample that has a well known redshift. This technique was studied for some cosmological applications, including the SKA in (Kovetz et al, 2016). The main idea of this method is to perform the angular cross-correlation of the unknown sample with redshift slices of the reference survey with known redshift information. The cross-correlation amplitude is then related to the redshift distribution, as discussed in (Ménard et al, 2013), which is then inferred to the initial 2D sample. A disadvantage of this method is that the provided redshift information can have a large uncertainty. In fact it is safe to assume that the redshift error $\sigma_z(z)$ is equal to the width of the said bin.

EMU ($10\mu Jy$)				SKA ($1\mu Jy$)			
z	σ_z	V	$\overline{n}_g$	z	σ_z	V	$\overline{n}_g$
0.86	0.18	12.73	2.54	0.41	0.16	4.32	2.15
1.45	0.28	29.63	2.04	1.01	0.23	18.93	5.84
2.3	0.28	33.74	1.27	1.6	0.3	33.22	9.23
3.46	0.46	52.6	0.43	2.56	0.42	50.6	4.57
5.48	0.63	58.2	0.057	4.1	1.63	175.1	1.17

Table 5.1 – The basic numbers for the two surveys considered here for each redshift bin. The shell volume is in units of $(\mathrm{Gpc/h})^3$ and the mean number density in $10^{-4}(\mathrm{h/Mpc})^3$. The redshift uncertainty of an object takes the same value as the width of the bin it resides.

The resulting predicted redshift distribution and redshift errors for the radio surveys used here are presented in Table 5.1. The volume of each redshift shell is calculated in units of $(\mathrm{Mpc/h})^3$ from

$$V = (r^3_{com}(z_{max}) - r^3_{com}(z_{min}))\left(\frac{\pi}{180}\right)^2 \frac{\mathrm{area}}{3}. \tag{5.68}$$

The galaxy mean number density is derived from, $\overline{n}_g = N \cdot \mathrm{area}/V$, where N is the number of objects per square degree for each redshift bin.

In order to connect the prediction of the halo bias, as derived from the PBS formalism (see Sec. 4.3.3), with he bias of galaxies, we adopt a halo model (Cooray and Sheth, 2002), where a Halo Occupation Distribution (HOD) function is used to provide, $\langle N \rangle_M$ the mean number density of galaxies per halo of a given mass M. The galaxy bias coefficients can be obtained from a weighted average of the halo bias over the range of host halo masses corresponding to the desired galaxy type as

$$b_i(z) = \frac{\int_{M_{min}(z)} d\ln M n_h(M,z) b^h_i(M,z) \langle N(M,z) \rangle}{\overline{n}_g(z)}, \tag{5.69}$$

where $\langle N(M,z) \rangle$ is the mean number of galaxies per dark matter halo of mass M, given by the HOD model, and M_{min} is the minimum mass a halo must have to contain a central galaxy. Finally $\overline{n}_g(z)$ is the mean galaxy density given by

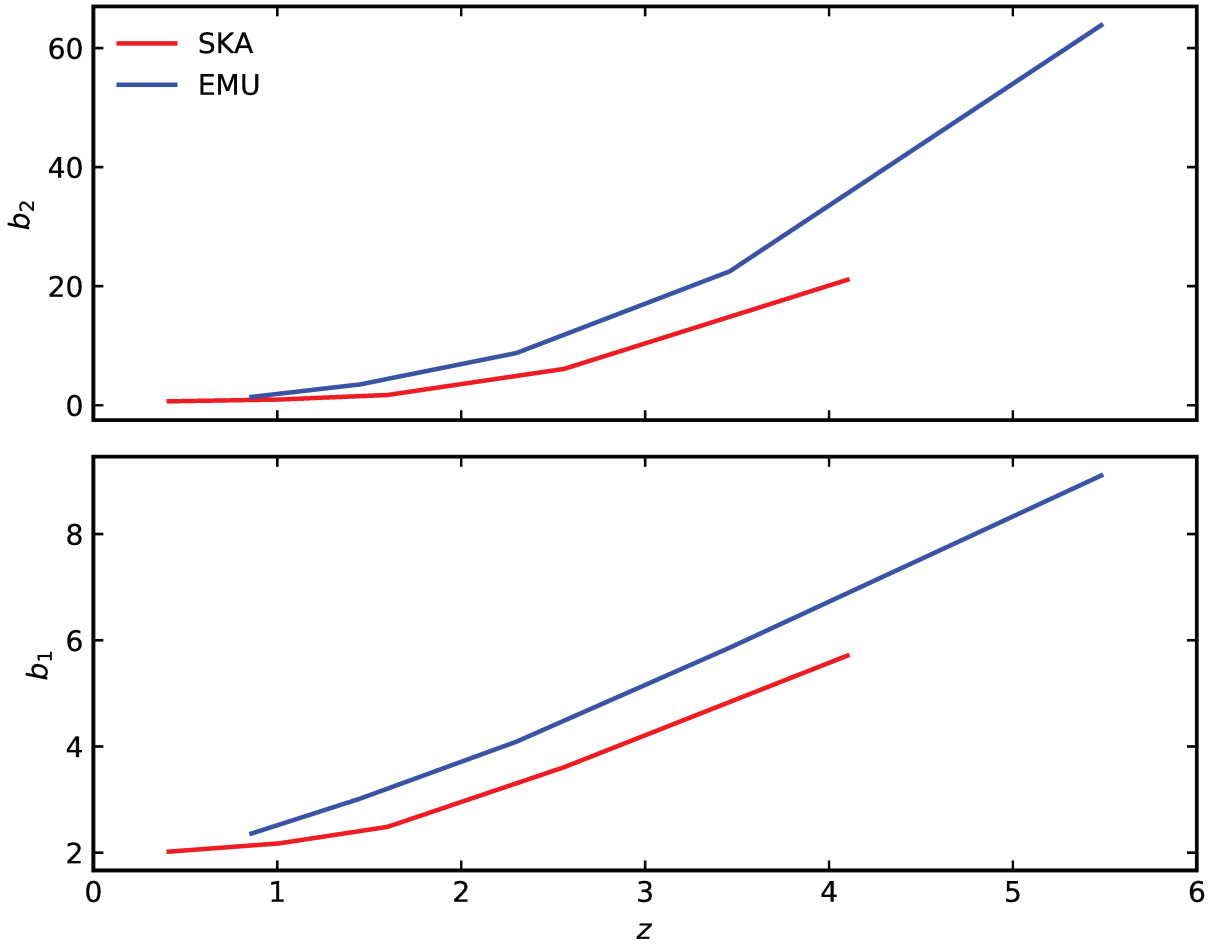

Figure 5.5 – The galaxy bias, defined from the weighted average over the halo one, as a function of redshift for the two radio surveys considered here, a EMU like survey flux limited at $10\mu Jy$ and a SKA like one with a $1\mu Jy$ flux limit. The details of the surveys are listed in Table 5.1

$$\overline{n}_g(z) = \int_{M_{min}(z)} d\ln M n_h(M,z) \langle N(M,z) \rangle \,. \tag{5.70}$$

The HOD used here is a simple three-parameter model proposed by (Tinker et al, 2005) and previously used in the literature (*e.g.*, Conroy et al 2006; Sefusatti and Komatsu

2007)

$$\langle N(M,z)\rangle = \begin{cases} 1+\dfrac{M}{M_1(z)}\exp\left(-\dfrac{M_{cut}(z)}{M}\right), & \text{if } M \geq M_{min}(z) \\ 0, & \text{otherwise,} \end{cases} \tag{5.71}$$

where M_1 is the mass required for a halo to contain a second satellite galaxy. In Conroy et al (2006), a relationship between M_1 and M_{cut} has been derived, $\log_{10}(M_{cut}) = 0.76\log_{10}(M_1) + 2.3$, by fitting the HOD free parameters on N-body simulations at different redshifts and number densities. In addition, it has been shown that the ratio $\log_{10}(M_1/M_{min}) = 1.1$ is almost redshift and mean number density independent. We will use both relationships in order to simplify the HOD model, leaving M_{min} as the only free parameter. Finally, we set M_{min} so that $\overline{n}_g$ matches the expected mean galaxy number density of the survey in each redshift bin. The resulting galaxy bias is plotted in Figure 5.5 as a function of redshift for the two radio survey examined here.

5.5.2 Future optical surveys

In the forthcoming years, a plethora of large scale structure surveys will provide accurate information on the redshifts and positions of various galaxy types, spreading over large volumes. Although this won't be the primary goal, the large number of modes and high redshifts probed by these surveys will give the possibility to produce tight constraints on the amplitude of PNG. In this section we present the details of three spectroscopic and one photometric catalogue, covering a variety of redshift ranges and volumes, namely Euclid, DESI, SPHEREx and LSST.

5.5.2.1 Euclid

Euclid (Laureijs et al, 2011) is a space mission scheduled to launch in 2020, with a primary goal of shedding light on the dark sector of the Universe and the nature of gravity. This will be achieved by using the main observables of the survey, *i.e.* galaxy clustering

z	V	$\overline{n}_g$
0.7	2.82	12.95
0.8	3.28	19.95
0.9	3.70	19.13
1.0	4.08	17.7
1.1	4.42	16.0
1.2	4.72	14.31
1.3	4.98	12.85
1.4	5.20	10.72
1.5	5.39	8.64
1.6	5.54	6.24
1.7	5.67	4.07
1.8	5.78	3.82
1.9	5.86	2.28
2.0	5.93	1.26

Table 5.2 – The basic numbers for the Euclid spectroscopic survey for each redshift bin. The shell volume is in units of $(\mathrm{Gpc/h})^3$ and the mean number density in $10^{-4}(\mathrm{h/Mpc})^3$.

and weak gravitational lensing. The former dataset consists of a photometric sample of billions of galaxies and a spectroscopic one composed of Hα emitters. The latter is the dataset that we will use in this work, which covers a redshift range of $0.7 \leq z \leq 2$ over $15,000\,\mathrm{deg}^2$. The redshift distribution is taken from the work of (Orsi et al, 2010) (see also Font-Ribera et al (2014) and references therein), and in Table 5.2 we show the main specifications for Euclid, as used in this work. The size of redshift bins is $\Delta z = 0.1$, while the spectroscopic redshift error is given by $\sigma_z(z) \approx 0.001(1+z)$, as proposed in (Amendola et al, 2013).

The galaxy sample is assumed to involve a single tracer, whose linear bias is given by $b_1(z) = 0.76/D(z)$ as proposed in Refs. (Font-Ribera et al, 2014; Tellarini et al, 2016). The higher order Eulerian bias coefficients are given from the halo bias predictions (see Sec. 4.3.3), where ν is determined by $b_1(z) = b_1^h(\nu, z)$ [see Eq. (4.44)]. The results for the linear and quadratic cases can be seen in Figure 5.7.

5.5.2.2 DESI

The *Dark Energy Spectroscopic Survey* (DESI) (Levi et al, 2013) is a ground-based $14,000\,\mathrm{deg}^2$ spectroscopic redshift survey, with the first light expected in 2019. The main goal is to study dark energy and its effects on the expansion of the Universe. This will be achieved by measuring the spectra of luminous red galaxies (LRGs), bright $[OII]$ emission line galaxies (ELGs) and quasars (QSOs) over different redshift ranges and up to $z < 2.1$, while a higher redshift ($2.1 < z < 3.5$) quasar sample will be used to measure the Lyman-α forest absorption features in their spectra. In addition DESI will perform a magnitude-limited Bright Galaxy Survey (BGS) at small redshifts ($0.05 \leq z \leq 0.4$). The specifications used here can be found in (DESI Collaboration et al, 2016) (see in particular Table 2.3 and 2.5), from where we take the baseline sample, composed by LRGs, ELGs, QSOs, as well as the BGS to construct an effective population extending from redshift $z = 0$ up to $z = 1.9$. As described in Ref. (Alonso and Ferreira, 2015), this approach approximates well the multi-tracer technique to the limit where the tracers can be considered independent. The size of the redshift bin is taken to be $\Delta z = 0.1$, while the spectroscopic redshift error is given by $\sigma_z(z) = 0.001(1+z)$ (DESI Collaboration et al, 2016). The main numbers for DESI are shown in Table 5.3.

In order to derive the bias parameters we follow the work of (Alonso and Ferreira, 2015), who define an effective bias as the weighted average over the biases of all the tracers considered in the effective sample, given by:

$$b_1^{\mathrm{eff}}(z) = \frac{\sum\limits_X \overline{n}_{\mathrm{X}}(z) b_1^{\mathrm{X}}(z)}{\sum\limits_X \overline{n}_{\mathrm{X}}(z)} \tag{5.72}$$

where $X = \{\mathrm{ELG}, \mathrm{LRG}, \mathrm{QSO}, \mathrm{BGS}\}$ and the sum is over all the different populations considered in the sample. The linear bias for each individual case is, $b_1^{\mathrm{ELG}} = 0.84/D(z)$ (Mostek et al, 2013), $b_1^{\mathrm{LRG}} = 1.7/D(z)$, $b_1^{\mathrm{QSO}} = 1.2/D(z)$ and $b_1^{\mathrm{BGS}} = 1.34/D(z)$ (DESI Collaboration et al, 2016). Equating the effective linear bias with the predictions of the

z	V	$\overline{n}_{\rm ELG}$	$\overline{n}_{\rm LRG}$	$\overline{n}_{\rm QSO}$	$\overline{n}_{\rm BGS}$
0.05	0.035	0	0	0	457.28
0.15	0.23	0	0	0	187.86
0.25	0.56	0	0	0	47.55
0.35	0.98	0	0	0	10.42
0.45	1.45	0	0	0	11.58
0.65	2.4	1.80	4.84	0.274	0
0.75	2.85	11.14	4.84	0.27	0
0.85	3.26	8.24	2.83	0.26	0
0.95	3.64	8.04	1.04	0.257	0
1.05	3.97	5.07	0.18	0.253	0
1.15	4.27	4.43	0.05	0.248	0
1.25	4.53	4.13	0	0.247	0
1.35	4.75	1.54	0	0.244	0
1.45	4.94	1.32	0	0.24	0
1.55	5.1	0.9	0	0.238	0
1.65	5.24	0.33	0	0.232	0
1.75	5.35	0	0	0.227	0
1.85	5.43	0	0	0.221	0

Table 5.3 – The basic numbers for DESI for each redshift bin. The shell volume is in units of $(\mathrm{Gpc/h})^3$ and the mean number density of each tracer in $10^{-4}(\mathrm{h/Mpc})^3$.

PBS halo bias model (*i.e.* $b_1^{\rm eff}(z) = b_1^h(\nu, z)$), gives the peak height ν which is used to derive the higher-order bias parameters. The results for the linear and quadratic bias terms are plotted in Figure 5.7.

5.5.2.3 SPHEREx

The *Spectro-Photometer for the History of the Universe, Epoch of Reionization, and Ice Explorer* (SPHEREx) (Bock and SPHEREx Science Team, 2016; Doré et al, 2014) is a proposed satellite with a primary goal of providing a full-sky ($\sim 40{,}000\,\mathrm{deg}^2$) spectro-photometric survey in the near-infrared. One of the main scientific objectives of the SPHEREx is to put tight constraints on PNG by using the spectroscopic galaxy sample, which is the one used here in order to compare the constraints with the results coming from

other large volume, deep redshift surveys (*e.g.* the radio continuum surveys of the previous section). Two different configurations of SPHEREx with a different redshift range will be used, one with a spectroscopic redshift error of $\sigma_z(z) = 0.01(1+z)$ denoted 'SPHEREx1' and another with $\sigma_z(z) = 0.2(1+z)$ named 'SPHEREx2'. The number density of galaxies for both cases can be found in (Doré et al, 2014) (in particular Fig. 10).

For the bias prescription we follow the work of (Doré et al, 2014), where the linear bias is calculated from the halo bias prediction [Eqs. (4.44) and (4.18)] for a minimum halo mass $M_{\rm min}$, *i.e.* $b_1(z) = b_1^h(M_{\rm min}, z)$. The mass $M_{\rm min}$ in each redshift bin is found by equating the mean number of halos, as derived by the halo mass function, with the mean number density of the sample. However, the number density of galaxies is not the same as the halo number density, since the presence of satellite galaxies must be taken into account. Therefore, we assume that only 80% of the galaxies in the sample are central galaxies (Doré et al, 2014), matching the number predicted by the halo mass function, *i.e.* $n_h(M > M_{\rm min}), z) = 0.8\overline{n}_g(z)$. Once the minimum halo mass is found, it is also used to derive all the higher-order bias parameters. The results of the first two bias coefficients for the two SPHEREx configurations are plotted in Figure 5.7.

5.5.2.4 LSST

The *Large Synoptic Survey Telescope* (LSST) (Ivezic et al, 2008; LSST Science Collaboration et al, 2009) is a ground-based facility, which is planned to receive first light around 2022. LSST is a photometric survey planed to scan an area $18,000\,{\rm deg}^2$ multiple times in six bands, *ugrizy*. This deep-wide-fast multi-band survey will provide a variety of different probes simultaneously, making it ideal for cosmological studies. In this work we are interested in the galaxy clustering dataset of the survey, in order to test its capabilities in constraining the amplitude of PNG. In order to derive the redshift distribution of galaxies in LSST, we split the photometric galaxy sample in 8 equally spaced tomographic redshift bins covering the range $0 \leq z_{\rm ph} \leq 3$ (LSST Science Collaboration et al, 2009), with $z_{\rm ph}$

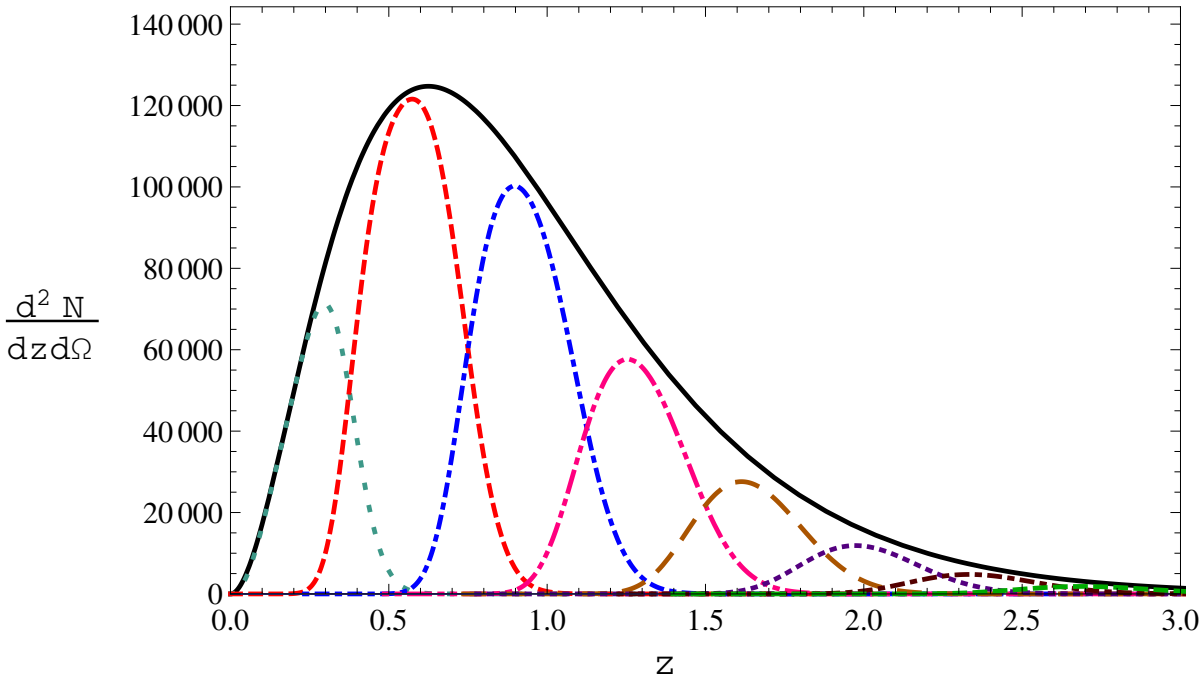

Figure 5.6 – The overall true redshift distribution $n(z)$ (solid black line) is plotted over the redshift range considered for LSST. The redshift distribution for each tomographic bin, given by Eq. (5.73), is also shown (dashed, dotted, *etc.* lines).

being the photometric redshift. The distribution of the true (or spectroscopic) redshifts of galaxies inside each photometric bin i is given by (Ma et al, 2006; Zhan, 2006):

$$n_i(z) = n(z) \int_{z_{\rm ph}^{(i)}}^{z_{\rm ph}^{(i+1)}} dz_{\rm ph} P(z_{\rm ph}|z), \tag{5.73}$$

where the integration limits define the extent of the bin i. Following the work of (Ma et al, 2006), we model the photometric redshift error at each redshift by a Gaussian, given by:

$$P(z_{\rm ph}|z) = \frac{1}{\sqrt{2\pi}\sigma_z} \exp[-\frac{(z - z_{\rm ph} - z_{\rm bias})^2}{2\sigma_z^2}], \tag{5.74}$$

where the photometric redshift bias $z_{\rm bias}$ and the photometric rms error σ_z are functions of the true redshift. The latter is chosen here to be $\sigma_z(z) = 0.05(1+z)$ (LSST Science

z	V	$\overline{n}_g$
0.1875	1.95	166.64
0.5625	9.57	82.84
0.9375	17.24	39.62
1.3125	22.46	18.37
1.6875	25.41	8.26
2.0625	26.78	3.60
2.4375	27.14	1.53
2.8125	26.89	0.63

Table 5.4 – The basic numbers for the LSST photometric survey for each redshift bin. The derivation of these values is described in Sec. 5.5.2.4. The shell volume is in units of $(\mathrm{Gpc/h})^3$ and the mean number density in $10^{-3}(\mathrm{h/Mpc})^3$.

Collaboration et al, 2009; Zhan and Tyson, 2017). The fiducial value of the redshift bias is chosen to be $z_{\rm bias}(z) = 0$. Note that the above probability must be normalised with $\int_0^\infty dz_{\rm ph} P(z_{\rm ph}|z)$ in order to ensure the positiveness on the photometric redshifts.

The overall galaxy true redshift distribution $n(z) = d^2N/dzd\Omega$ is given by the following functional form, $n(z) \propto z^\alpha \exp[-(z/z_0)^\beta]$ (Wittman et al, 2000), where the adopted free parameters are $\alpha = 2$, $\beta = 1$ and $z_0 = 0.3125$ (LSST Science Collaboration et al, 2009; Zhan and Tyson, 2017). The normalization of the overall galaxy redshift distribution is fixed by requiring the total number of galaxies per steradian (*i.e.* $n_{\rm tot} = \int_0^\infty dz n(z)$) to be equal to the cumulative galaxy counts of the survey. Here we use the so called "gold" sample of LSST, corresponding to the galaxies with i-band magnitude of $i_{\rm AB} < 25.3$ mag, which has a surface number density of $n_{\rm tot} = 40$ gal/arcmin^2 (see section 3.7 of LSST Science Collaboration et al (2009) for details). The total number of galaxies per steradian is given in each photometric bin by $n_{{\rm tot},i} = \int_0^\infty dz n_i(z)$. The overall normalized redshift distribution $n(z)$ is plotted together with the true redshift distribution in each photometric bin in Figure 5.6. The final number densities for each photometric redshift bin are listed in Table 5.4. The fiducial value for the linear bias is chosen to be $b_1(z) = 1/D(z)$ (LSST Science Collaboration et al, 2009; Passaglia et al, 2017), where the derivation of the

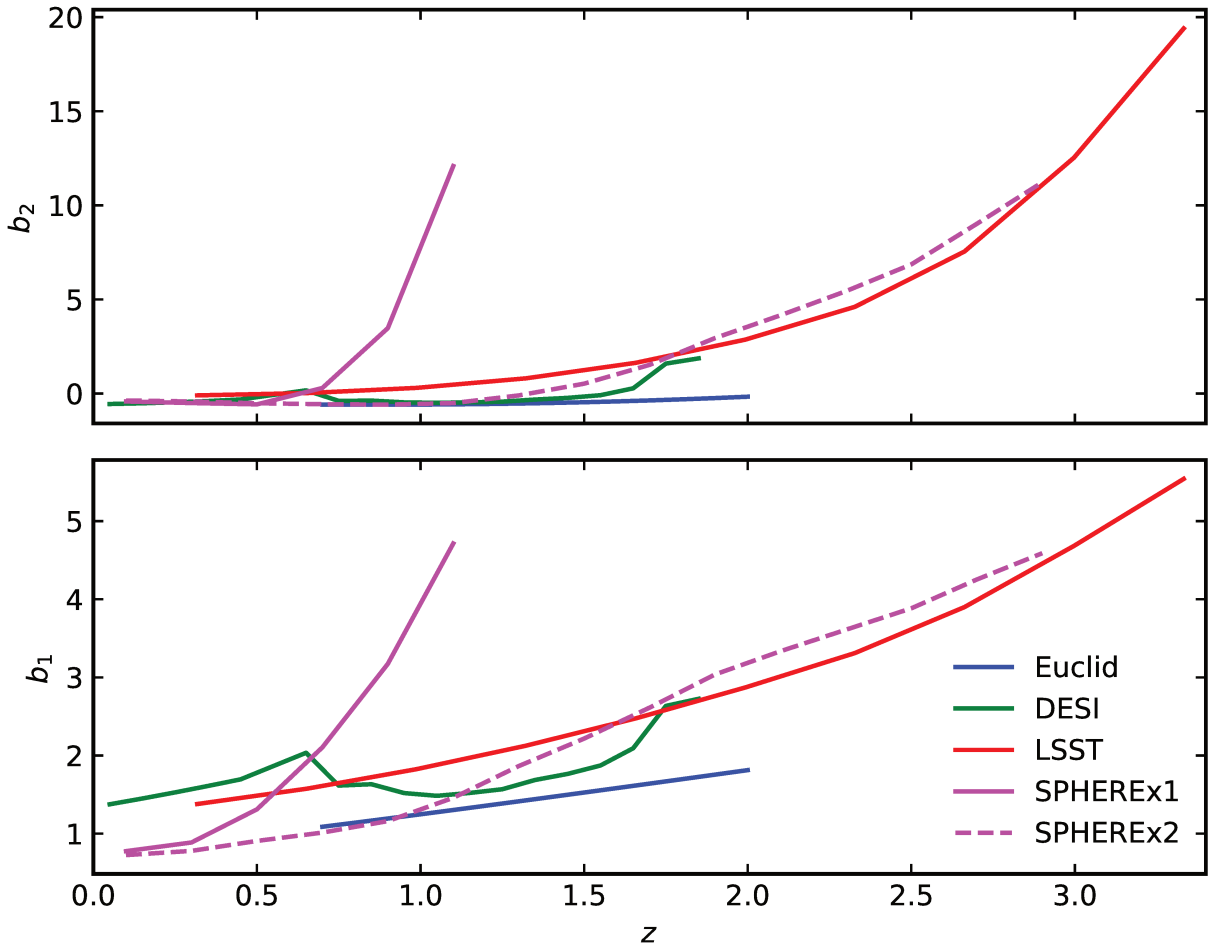

Figure 5.7 – The linear and quadratic galaxy bias for the optical surveys considered here. The details for the derivation are described in Sec. 5.5.2 for each individual survey.

higher-order bias parameters follows the prescription in Sec. 5.5.2.1. The final results for the linear and quadratic biases are plotted in Figure 5.7.

5.6 Summary of the analysis method

Here we summarize the modelling used for the galaxy power spectrum and bispectrum, as well as all the steps followed in the next section in order to test the various effects that have an effect on the $f_{\rm NL}$ forecasts.

(i) For the matter power spectrum and bispectrum, the MPTbreeze tree-level description is used throughout. In order to cross-validate our results, we have also considered the scenario of using SPT. The forecast results are in agreement between SPT and MPTbreeze (see Sec. 5.7.1.1).

(ii) Non-Gaussian initial conditions are assumed and the bias expansion up to second order is used [Eq. (5.1)].

(iii) The forecasts are performed by following the Fisher matrix formalism (see Sec. 5.3), where a diagonal covariance is used for both power spectrum and bispectrum as described in Eqs. (5.58) and (5.59) respectively. The analysis is restricted up to scales $k_{\rm max} = 0.1/D(z)$ h/Mpc.

(iv) We start by working in real space. Our model is in this case defined by equations Eqs. (5.8) and (5.19) for the galaxy power spectrum and bispectrum. The monopole approximation of Eqs. (5.42) and (5.43) is in this case used to approximate the RSD effect. Note that, at this initial stage, the trispectrum term shown in Eq. (5.19) is always excluded. We refer to this as the "monopole approximation" model, throughout the rest of this work. The reason to start with this simplified scenario is threefold. First, a non-trivial amount of previous literature includes only real space forecasts, so that showing our monopole approximation results can facilitate comparisons. Second, by proceeding step-by-step we are able to better isolate the impact of different effects, such as theoretical and redshift errors. Third, as explained more in detail in the following, off-diagonal terms in the theoretical error covariance are

often neglected in our full redshift space analysis, due to computational limitations. On the other hand, they can be in most cases included in the monopole approximation forecast. The real space analysis therefore provides useful guidelines to assess the accuracy of the diagonal covariance approximation, used for theoretical errors in redshift space, at high z (we anticipate here that we find such approximation to be quite good).

(v) The second step is to add the theoretical error covariance given in Eq. (5.64) to the variance of Fisher matrix, in order to account for the uncertainties in the theoretical model (see Sec. 5.4 for a discussion). Here we account only for the exclusion of 1-loop corrections in the matter perturbations for both power spectrum and bispectrum. For the bias expansion we only quantify the error in excluding the 1-loop contributions that are related to the local-in-matter bias coefficients, *i.e.* b_1, b_2, b_3, *etc.*

(vi) The effect of the theoretical errors on forecasts is shown as a function of redshift in Figure 5.8 for the two radio continuum surveys considered here. The effect on the forecasts coming from the summed signal over all redshift bins is shown in Tables 5.5 and 5.9 for the radio and optical surveys respectively.

(vii) The third step is to move to redshift space and include the full RSD treatment up to second order. The galaxy power spectrum and bispectrum model in redshift space is given by Eqs. (5.28) and (5.29) respectively. Note that the trispectrum term in Eq. (5.29) is still excluded for now. Only the diagonal part of the theoretical error covariance is used in the redshift space models. As also mentioned just above, we argue in Sec. 5.7.1.1 that the effect of the off-diagonal part on the final $f_{\rm NL}$ forecasts is small.

(viii) In addition to the RSD effect, we consider redshift uncertainties which are modelled like Eqs. (5.33) and (5.34) for the power spectrum and bispectrum respectively

(see Sec. 5.2.2 for a discussion). The effect of RSD, theoretical errors and redshift uncertainties to the $f_{\rm NL}$ forecasts is shown in Tables 5.6 and 5.11 for the radio and optical surveys respectively.

(ix) Finally, we take into account the trispectrum term in the galaxy bispectrum for both the monopole approximation and for the full RSD model (*i.e.* Eqs. (5.19) and (5.29)). The effect of this trispectrum correction to the final PNG forecasts is shown, for the monopole approximation model, in Tables 5.7 and 5.10 for the radio and optical surveys respectively. For the RSD model, the $f_{\rm NL}$ forecast are shown in Tables 5.8 and 5.11 for the radio continuum and optical surveys respectively.

(x) We summarize our final forecast results on the amplitude of PNG coming from future LSS surveys in Table 5.12.

5.7 Results

In this section we present the results of our forecasts for radio continuum and optical surveys, obtained with the procedure summarized in Sec. 5.6. For the local and orthogonal PNG, we consider the power spectrum and bispectrum model that was described in detail in Sec. 5.2.1 and Sec. 5.2.2, for real and redshift spaces respectively [by Eqs. (5.8), (5.19), (5.42) and (5.43)]. In the case of the equilateral type of non-Gaussianity, we use the same expressions, but without the corrections from the primordial local gravitational potential Ψ due to degeneracies with the bias parameters (see Sec. 4.4.2). The final constraints are derived after marginalizing over the nuisance stochastic bias parameters (see Sec. 5.3). The linear matter power spectrum is computed with CAMB (Lewis et al, 2000), while the cosmological parameters are those determined by (Planck Collaboration et al, 2016b): $h = 0.6774$, $\Omega_c h^2 = 0.1188$, $\Omega_b h^2 = 0.0223$, $n_s = 0.9667$, $\Delta^2_\zeta = 2.142 \times 10^{-9}$, $\tau = 0.066$.

5.7.1 Radio continuum surveys forecasts

In this section we present the results of our forecasts for the parameter vector [Eq. (5.57)], considering the two high redshift radio continuum surveys, SKA and EMU. The modelling used is described in the previous sections.

5.7.1.1 Theoretical errors effect

Our main goal at this stage will be quantifying the effect of theoretical errors, by testing their impact on our "monopole model" forecasts. Due to the demanding computational effort needed to perform the inversion of the bispectrum covariance matrix (a $10^6 \times 10^6$ size matrix for the final redshift bins), which is no longer diagonal when the theoretical errors are included [Eq. (5.64)], we use the full covariance matrix only for the three lowest redshift bins (that's the largest computationally affordable amount; we choose the lowest three redshifts because the effect of off-diagonal terms is largest there), while for the rest we consider only the diagonal contribution. This means that cross-correlations between modes are excluded. This can in principle affect the impact of the theoretical errors. However, we performed tests to check the effects of these off-diagonal components, up to the redshift bin allowed by the computational resources available, and we observed that the effect of the off-diagonal terms becomes actually negligible at high-z. This is reasonable: the Universe is more linear at higher redshifts, therefore the loop corrections, up to the scales we consider, are expected to be suppressed. Our approximations work therefore very well. Let us note that, in the case of the power spectrum, we always use the full covariance matrix, since no computational issues arise in this case. Let us also note here again that the theoretical modelling was performed using MPTbreeze, which has an embedded cut-off function at high-k. This means that higher order contributions, as well as the theoretical error effect will be suppressed on small scales. In order to check whether this has a significant effect, we have performed a similar analysis using SPT. The results were consistent with those presented here, throughout the range of scales chosen

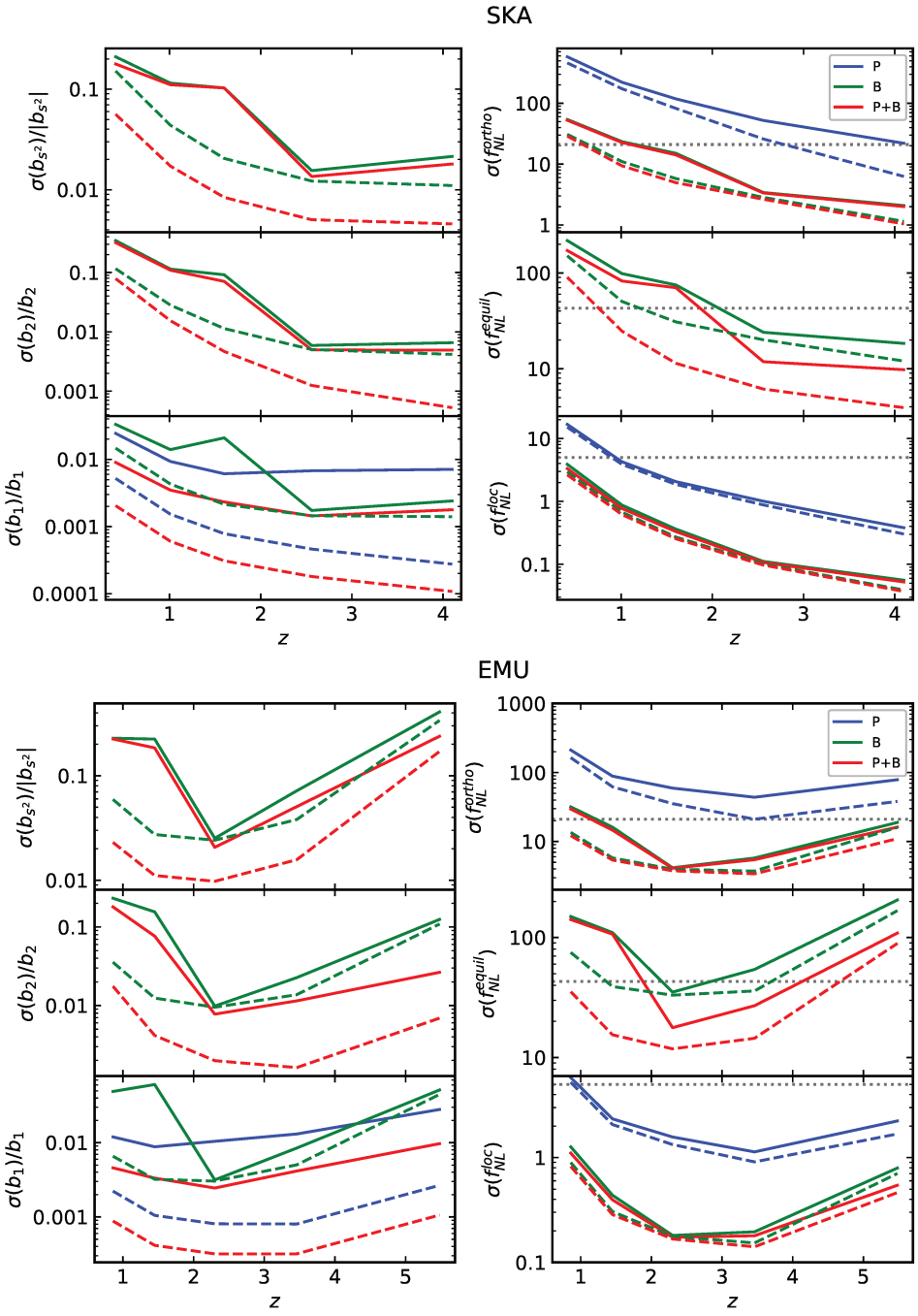

Figure 5.8 – The effect of theoretical errors on the bias parameters and on the three f_{NL} parameters with respect to the redshift bins for the two surveys considered: SKA (up) and EMU (down). The dashed lines represent our "monopole approximation model", without theoretical errors (*i.e.* our starting step, as explained in the main text); for the power spectrum we used the linear predictions with PNG [Eq. (5.42)], while for the bispectrum of galaxies we used Eq. (5.43). The solid lines represent the same model, but including theoretical errors, as described in Sec. 5.4. The constraints from the power spectrum are plotted in blue, from the bispectrum in green and from both power spectrum and bispectrum in red, without taking into account their cross term in the covariance. The bias constraints are derived after assuming local PNG, while non-linear evolution is treated within the formalism of MPTbreeze. The dotted grey line indicates the best constraints on the primordial non-Gaussian amplitude, as given by (Planck Collaboration et al, 2016a).

	SKA		EMU	
	Monopole approximation	Theoretical errors	Monopole approximation	Theoretical errors
P(loc)	0.283	0.35	0.646	0.792
B(loc)	0.036	0.049	0.106	0.125
P+B(loc)	0.034	0.046	0.098	0.116
P(equil)	-	-	-	-
B(equil)	9.6	14.16	19.75	27.68
P+B(equil)	3.15	7.46	7.65	14.47
P(ortho)	6.81	19.91	15.73	29.93
B(ortho)	1.2	1.76	2.39	3.24
P+B(ortho)	1.08	1.7	2.2	3.12

Table 5.5 – The constraints on the non-Gaussian amplitude $f_{\rm NL}$ for the three shapes (local, equilateral and orthogonal) over all redshift bins, from the two surveys considered here (SKA – left and EMU – right), in the monopole approximation case and the case including theoretical errors. The constraints were derived from the power spectrum (P), bispectrum (B) and by combining the two (P + B).

for our analysis.

The comparison is shown in Figure 5.8 and the forecasts for $f_{\rm NL}$ are quantitatively reported in Table 5.5. The latter are derived after summing the signal over all the available redshift bins in each survey. A similar behaviour is observed for the two radio surveys. The bias constraints are significantly affected by the presence of the theoretical systematics, due to the fact that, for the envelope fitting, the one-loop bias corrections are here taken into account. For the PNG amplitudes, we note that, for local PNG, the effect is modest (as was also noted by (Baldauf et al, 2016)). This can be attributed to the fact that this shape has very little correlation to the gravitational contribution. This is not the case, though, for the equilateral and orthogonal shapes, which show a stronger dependence for all redshift bins.

In addition, the ratio of the marginal 1σ error is presented for the two radio continuum surveys in Figure 5.9, for the cases where theoretical errors are taken into account and when they are omitted. Note that the effect of theoretical errors doesn't get smaller at high redshifts in all cases, as seen in Figure 5.8, and in particular this is evident for the

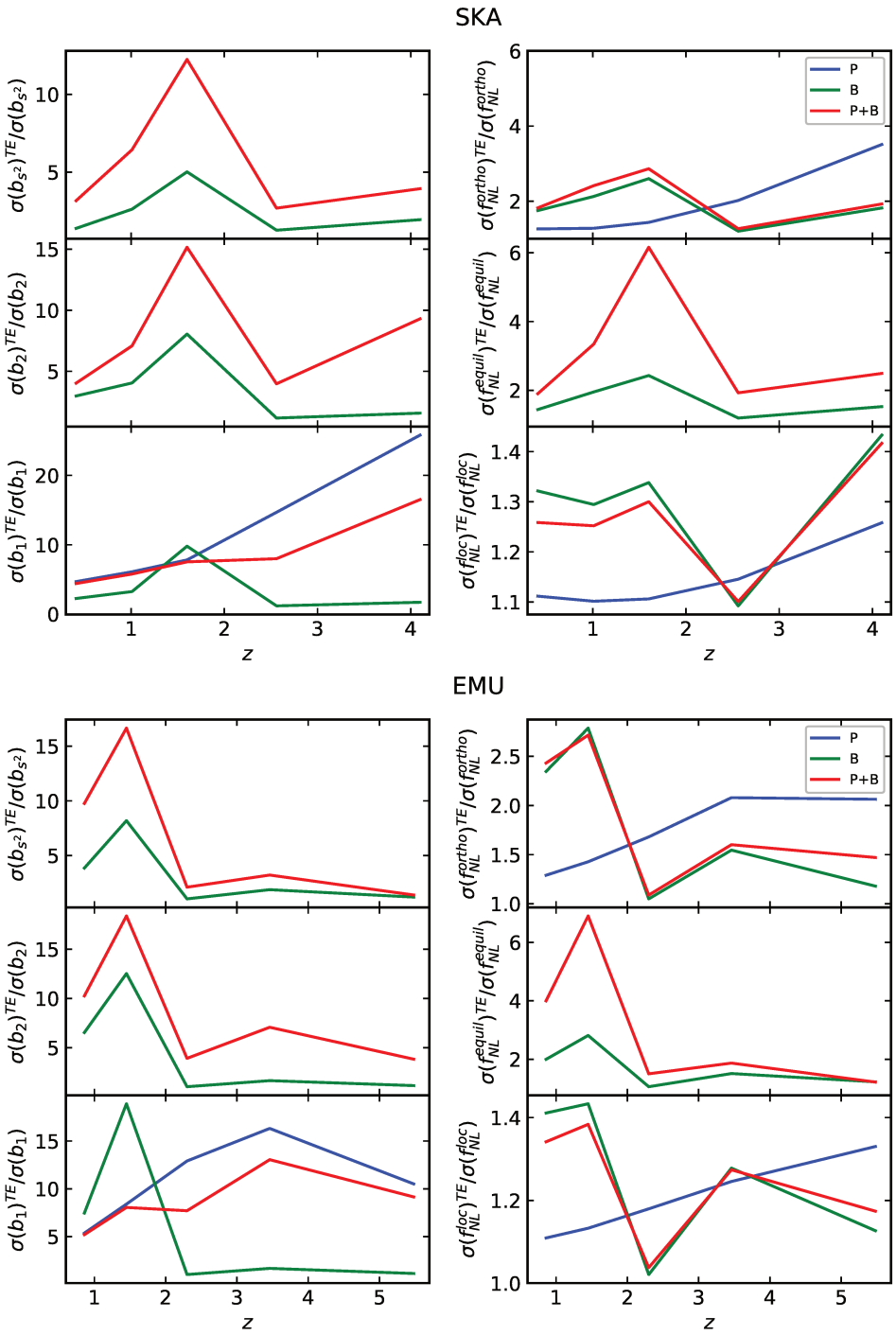

Figure 5.9 – Same as Figure 5.8, where here the ratio of the 1σ errors between the case with theoretical errors (denoted in the plots with the upper index TE) and without is shown.

power spectrum case. The argument of a more linear Universe at high redshifts, which leads to a reduction in the contribution of the higher loop corrections, holds for the case of matter and it is not generally true for the biased tracers. The reason is that at large redshifts, and in the scale range considered here, galaxies become more biased, while the matter loop corrections become less important. Hence, there is a trade off between the two. This indicates that, depending on the redshift evolution of the bias parameters, the depth of the survey and its volume, a different behaviour of the impact of the theoretical errors can be observed, when bias loop corrections are taken into account in the envelope fitting (see Sec. 5.4 for details). This shows the importance of extending the formalism of (Baldauf et al, 2016), to include theoretical errors attributed to the bias expansion, as we did.

At this stage of the analysis (*i.e.* before accounting for RSD and redshift errors, which will be included in the next section), it seems that the combined information from the power spectrum and bispectrum of galaxies can provide very tight constraints on the amplitude of local PNG. For a SKA radio continuum survey, an error of $\sigma(f_{\rm NL}^{\rm loc}) < 0.13$ can be achieved after using the total signal from all redshift bins. In the orthogonal case, SKA can provide $\sigma(f_{\rm NL}^{\rm orth}) \sim 3$, while for the equilateral PNG, already at this stage the constraints are weaker, compared to the other shapes, as we can see from Table 5.5. It is important however to keep in mind that these constraints will deteriorate when considering realistic redshift space measurements and accounting for errors in the determination of the redshift of radio sources (see next section). At this point in the analysis, the most important aspect is therefore not the absolute value of the constraint, but the assessment of the effect of theoretical errors.

Real space constraints on bias parameters are shown in the left panels of Figure 5.8 for each of the surveys considered here. Again, rather than on quantitative assessments, which will be refined in the redshift space section later on, it is useful at this level to focus on qualitative behaviours. We see, as expected, that the power spectrum provides

the main signal for constraining b_1 (blue lines in Figure 5.8), while the contribution from the bispectrum (green lines) is minimal as we can also see in the results coming from the combination of the two (red lines). For the quadratic bias parameter, as well as the tidal bias, the constraints are weaker. For both these bias coefficients, the constraining signal originates solely from the bispectrum, since these terms appear in loop corrections of the linear galaxy power spectrum, which we do not consider here, and therefore this reduction in the constraining power is justified. In the combined power spectrum and bispectrum case, an improvement is observed in the statistical error of b_2 and b_{s^2}, due to the tight constraint on the linear bias provided by the power spectrum. In addition, the presence of the tidal bias term breaks the degeneracy between the linear and quadratic terms, improving the predicted errors on b_2. For both bias parameters, radio continuum surveys (mainly the high redshift bins) contribute enough signal in order to achieve a few per-cent precision measurements. However the introduction of theoretical errors deteriorates the constraints to a $10-20\%$ precision at high redshift, mainly due to the uncertainty introduced by the exclusion of higher bias terms in the power spectrum and bispectrum of galaxies.

5.7.1.2 Redshift Space Distortions and redshift uncertainties

Both the effect of RSD and of uncertainties in the determination of redshifts must be fully taken into account in any realistic galaxy forecast, since galaxies are observed in this coordinate system. In the second step of our analysis, we start by comparing the monopole approximation model (see Sec. 5.2.2), which is always our starting analysis step, with the results derived from including RSD, up to second order (*i.e.* for the galaxy power spectrum and bispectrum we use Eqs. (5.28) and (5.29) respectively).

We consider separately the effect of adding RSD and theoretical errors, in order to quantitatively check the impact of RSD alone. The final constraints use the signal coming from the power spectrum, bispectrum and their combination. Results for bias and PNG

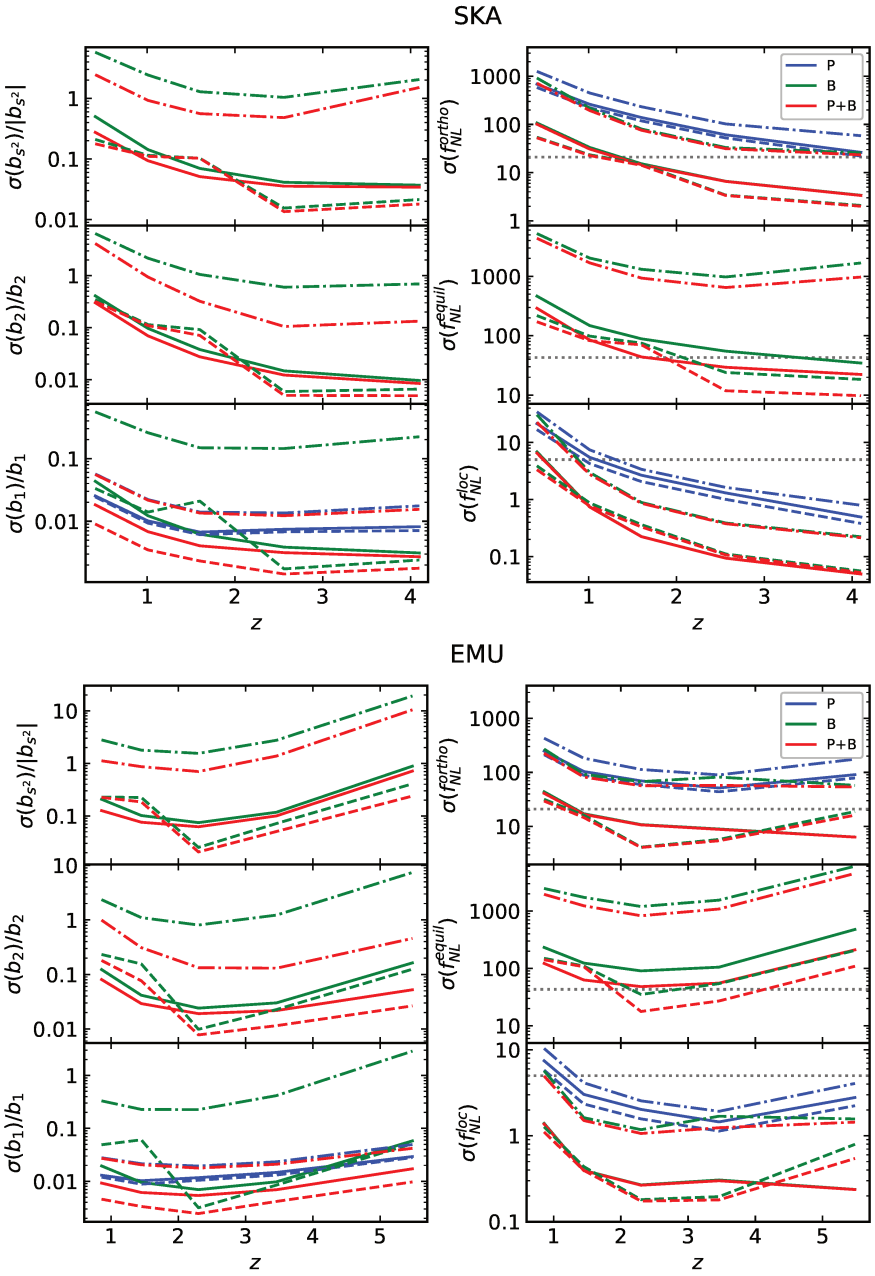

Figure 5.10 – Constraints on the linear and on the two quadratic bias parameters from the tree-level bias expansion and on the amplitudes of the PNG parameter $f_{\rm NL}$ with respect to redshift for the two radio surveys considered [SKA (up) and EMU (down)] when including RSD and FOG effects. The dashed lines represent the monopole approximation model, including theoretical errors as described in Sec. 5.7.1.1. The solid lines represent the model which accounts for RSD and FOG effects, while the dashed-dotted lines results take also into account the redshift uncertainties. The constraints from the power spectrum are plotted in blue, from the bispectrum in green and from both power spectrum and bispectrum in red, without taking into account their cross term in the covariance. The expressions used for the modelling of the power spectrum and bispectrum are given, in Eqs. (5.28) and (5.29) respectively, while for the latter the trispectrum term is excluded. These results consider only the diagonal part of theoretical error covariance [Eq. (5.64)]. MPTbreeze has been used to derive the matter two- and three-point correlators. For the bias forecasts we assume Gaussian initial conditions (*i.e.* $f_{\rm NL}^{\rm loc}=0$).

	SKA				EMU			
	Monopole approximation	RSD[$\sigma_z(z)=0$]	RSD[$\sigma_z(z)=0$] +Theoretical errors	RSD +Theoretical errors	Monopole approximation	RSD[$\sigma_z(z)=0$]	RSD[$\sigma_z(z)=0$] +Theoretical errors	RSD +Theoretical errors
P(loc)	0.283	0.38	0.471	0.695	0.646	0.869	1.066	1.345
B(loc)	0.036	0.039	0.053	0.188	0.106	0.131	0.154	0.727
P+B(loc)	0.034	0.039	0.052	0.181	0.098	0.13	0.153	0.632
P(equil)	-	-	-	-	-	-	-	-
B(equil)	9.6	24.52	36.19	663.98	19.75	54.72	76.67	779.99
P+B(equil)	3.15	8.3	19.66	447.52	7.65	20.04	37.89	551.22
P(ortho)	6.81	7.82	22.85	49.09	15.73	20.61	39.2	60.85
B(ortho)	1.2	2.23	3.26	19.58	2.39	3.92	5.31	35.31
P+B(ortho)	1.08	2.03	3.2	18.08	2.2	3.8	5.38	29.78

Table 5.6 – The forecast results on the amplitude of PNG ($f_{\rm NL}$) in the case of three different primordial shapes (local, equilateral and orthogonal), when considering respectively the monopole approximation model, the model taking into account RSD and FOG effects and the redshift space model with theoretical errors, for the two radio surveys: SKA (left half) and EMU (right half). The redshift uncertainties are considered separately and added on top of all the previous effects under the column denoted "RSD+Theoretical errors". The constraints on the bias parameters, up to quadratic order [Eq. (5.1)], are also presented. The results are derived after marginalising over the unknown parameters. Note that the observed improvement in the P+B(equil) results, with respect to B(equil), originate from the tighter forecasts on b_1 provided by P(equil).

parameters, as a function of redshift, are displayed in Figure 5.10. The constraints on $f_{\rm NL}$, coming from the summed signal over all redshift bins, are reported in Table 5.6 (column marked by "RSD[$\sigma_z(z)=0$]").

The difference between the model including RSD and theoretical errors, and the monopole approximation results is evident for the bias constraints, especially the bispectrum derived ones. As we can see in Figure 5.10, the effect of RSD is instead overall small for PNG, with the bispectrum again being affected the most.

As a further step, in addition to RSD, we include theoretical errors in order to test the combined effect on the $f_{\rm NL}$ constraints for the local, equilateral and orthogonal shapes. A comparison of the 68% error bars on the non-Gaussian amplitude obtained from the monopole approximation model, the RSD model only and the RSD + theoretical errors model is displayed in Table 5.6. Here the off-diagonal part of the theoretical error covariance matrix is ignored in the case of the bispectrum, due to the significant computational cost of inverting this matrix; this task should now be undertaken for each orientation of the triangles [see Eq. (5.55)]. Excluding the off-diagonal terms underestimates the mode

coupling and the overall effect of theoretical errors. In order to quantify this effect, we compare forecasts with and without off-diagonal terms, for the computationally affordable monopole approximation case. Since we do not consider any RSD corrections in the theoretical error treatment, the effect of the off-diagonal terms in the constraints can be truncated for the present forecasts. The marginal error provided by the bispectrum for the PNG amplitude, in the local case, increases in this test by $\sim 1\%$, if we include the full theoretical error covariance matrix for the initial redshift bins (see Sec. 5.7.1.1), instead of only the diagonal part. For the equilateral and orthogonal cases, we observe $\sim 10\%$ and $\sim 5\%$ enhancement, respectively. Moreover, the predicted errors on the bias parameters degrade by a factor of $1.5-8$, depending on the bias type (*i.e.* linear, quadratic, *etc.*) and the redshift. Note that these quantitative results are valid only for the radio surveys we consider here, since the effect of theoretical errors depends on redshift as well as the fiducial values of the bias parameters. With these caveats in mind, we see that the effect of theoretical errors follows a similar pattern to the one already discussed in the previous section, as expected. In the case of local non-Gaussianity, the impact of theoretical errors is small, while it is very large for the equilateral shape

Having considered RSD, we now include redshift uncertainties, modelled like in Eqs. (5.33) and (5.34) with $\sigma = \sigma_r(z)$. Before discussing the consequences on $f_{\rm NL}$ and bias constraints, we would like to mention some details on the redshift errors and galaxy statistics modelling. Note that the dumping factor, containing the redshift uncertainties, should be multiplied to the power spectrum and bispectrum as shown in Eqs. (5.28) and (5.29) respectively, including the stochastic bias terms which at large scales resembles the Poisson shot noise. This is important in the noise dominated regime, *i.e.* scales with $k\mu\sigma_{\rm v} > 1$, where the redshift error dumps the signal together with the shot noise terms in the numerator of the Fisher matrix while the shot noise part of the denominator is unaffected [Eqs. (5.58) and (5.59)]. In the case where this dumping is not applied to the shot noise terms of the signal in the S/N ratio, we observed an improvement in

the final constraints when we increased the redshift errors, which is unnatural. This is due to the fact that the denominator of the Fisher matrix becomes larger than the numerator in the noise dominated regime. This effect is stronger in the case where the redshift errors are large, like in the radio continuum surveys considered here. Therefore one should be careful and apply the dumping factor on every term of the power spectrum and bispectrum, including the stochastic elements which should be considered part of the signal.

The constraints on PNG amplitudes and bias, after including the redshift errors, are presented as a function of redshift in Figure 5.10. The final 68% error bars on $f_{\rm NL}$ are displayed in Table 5.6 under the column named "RSD+Theoretical errors". In the case of local primordial non-Gaussianity the effect of redshift uncertainties is small and the constraints from both radio surveys are still tighter than those originating from *Planck* , for more or less the whole redshift range. The final error on $f_{\rm NL}^{\rm loc}$ is degraded by a factor of ~ 1.5 for a SKA survey with respect to the case with a perfect redshift determination. This shows that future radio surveys can tightly constrain PNG of the local type, even with large redshift errors like those derived by the methodology used here. For the SKA case an error of ~ 0.18 can be achieved from the combined P + B signal, *i.e.* a ~ 30 times improvement from the constraints of *Planck* . In the case of orthogonal PNG the degradation due to redshift uncertainties is much larger, as seen in Figure 5.10. The final power spectrum + bispectrum constraints on the orthogonal PNG amplitude, adding contributions from all redshift bins, show a ~ 7 times deterioration, compared to the case with no z-errors, and is slightly worse than the current *Planck* constraint. The degradation is even larger for PNG of the equilateral type. In this case, constraints provided by both radio surveys are far weaker than those coming from *Planck* , for the whole redshift range (dashed-dotted lines in Figure 5.10). The predictions on the $f_{\rm NL}^{\rm eq}$ parameter coming from all redshifts and the combined P and B signal get degraded by a factor ~ 29, as seen in Table 5.6.

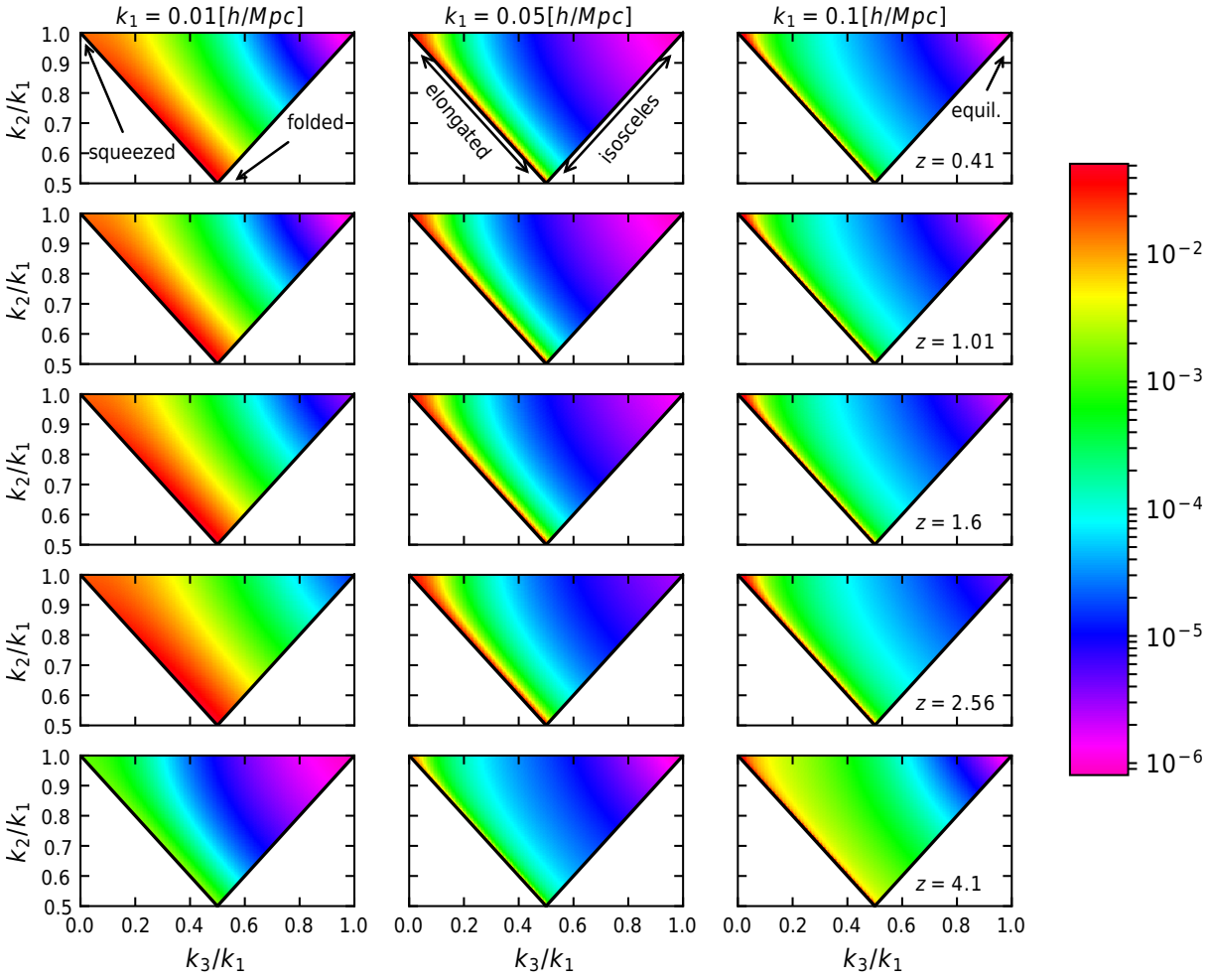

Figure 5.11 – The dumping factor, in the case of bispectrum [Eq. (5.34)] and for the SKA survey, including the FOG effect and redshift errors as a function of k_2/k_1 and k_3/k_1 for three constant values of k_1. The results are not normalised to their individual maximum values for each redshift bin, while we sum over all the positional angles of the triangles around the line of sight and normalise with the angle's bin size (see Sec. 5.2.1 for more details on these type of plots and in the main text of this subsection).

In order to study further the effect of the redshift uncertainties, we show the bispectrum dumping factor [Eq. (5.34)] for the SKA survey (Figure 5.11) and for all triangles formed after fixing one side (*e.g.* k_1, see Sec. 5.2.1 for more details on the colour map plots). The results are not normalised to their maximum value, since we are not interested only in the shape dependence of the $D_{\rm FOG}$ term, but also in its amplitude. Furthermore, a sum over all angles around the line of sight (*i.e.* θ and ϕ) is performed, where the final outcome is normalised over their bin size (see Sec. 5.2.2 for a discussion). An immediate observation is that the dumping factor takes the smallest value, and hence has the maximum effect on the galaxy bispectrum, in correspondence to equilateral configurations, for all redshift bins and scales. The reason behind this is the functional form of the dumping factor, which takes a minimum value in the case where $k_1 \approx k_2 \approx k_3$, giving $D_{\rm FOG} = \exp -3(k\mu\sigma_{\rm v})^2$. On the other hand, the results peak on squeezed triangles in the intermediate scales, while at large scales the maximum shifts towards folded configurations. This means that these configurations will be affected the least from the dumping factor over redshift bins and scale range considered. The redshift errors increase towards the larger redshifts and, as seen in the last row of Figure 5.11, a growing number of configurations is affected towards the equilateral limit. These results agree with the observed behaviour of the $f_{\rm NL}$ constraints discussed before.

Therefore we can conclude that radio continuum samples, in combination with clustering-based redshift estimation, can provide tight constraints for the local PNG amplitude, with an important contribution from bispectrum measurements. In order to achieve tight constraints for other shapes, though, the precision in the determination of redshift should at least match the one achieved by photometric surveys (it is currently estimated to be about an order of magnitude worse). Theoretical errors, as seen in Table 5.6, are less relevant for the $f_{\rm NL}$ predictions coming from surveys with large redshift uncertainties (*e.g.* SKA), since the effect of the latter overshadows completely the impact of the former.

The power spectrum redshift space forecasts presented here (*i.e.* column under the

name "RSD+Theoretical errors" in Table 5.6) for the two radio continuum surveys are consistent with those presented in (Raccanelli et al, 2017), after taking into account the different flux limits used in the latter. More precisely, here we use $10\mu Jy$ and $1\mu Jy$ flux limits, while the optimistic forecasts of (Raccanelli et al, 2017) assume 50 μJy and 100 nJy.

The relative errors on bias parameters, shown in Figure 5.10, coming from joint power spectrum and bispectrum estimation, increases by a factor of two when redshift errors are included. For linear bias, the increase originates mainly from the deterioration of the power spectrum results. For the two quadratic bias terms, the relative errors become larger than unity, since the signal comes only from the bispectrum which is more affected by redshift errors.

It is interesting to compare the power spectrum-only $f_{\rm NL}^{\rm loc}$ constraints presented in Table 5.6 (in particular those under the column named "RSD+Theoretical errors") with the forecasts shown in Ref. (Camera et al, 2015). They use the HI galaxy sample of SKA, which allows for a very accurate redshift measurements from the 21 cm line of neutral hydrogen. Of course, this approach has also its drawbacks, such as the need for sophisticated techniques for the identification of unresolved galaxies, as well as issues arising from foreground cleaning and unknown systematics (see (Camera et al, 2013, 2015) and references therein for a discussion). Nevertheless, leaving such issues aside at this stage, the precise redshift information provided by 21 cm intensity mapping can in principle provide tight constraints on the PNG amplitude. The specifications for SKA used in (Camera et al, 2015), that most closely match those presented here, consider a redshift range of $0 < z <= 3$ and a sensitivity of 3 μJy. For that case, (Camera et al, 2015) obtain comparable forecasts to those achieved here using power spectrum information. The bispectrum, in our study, improves the bounds on $f_{\rm NL}$ by a factor ~ 4 when redshift errors are neglected. Therefore, measurements of the angular bispectrum of HI galaxies might be able to achieve a similar enhancement of the PNG amplitude constraints. We leave the study of this angular bispectrum signal for forthcoming work.

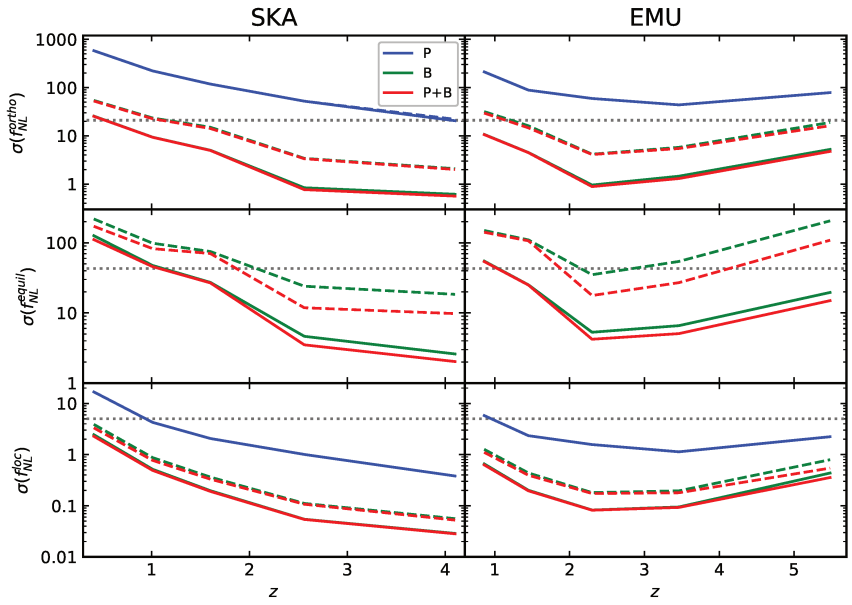

Figure 5.12 – Fisher forecasts on $f_{\rm NL}$ for local, equilateral and orthogonal shapes in the case of a SKA survey (left) and an EMU on (right). The dashed lines represent the starting monopole approximation model, while the solid lines represent the same model when the trispectrum correction is considered [*i.e.* Eq. (5.8) for the power spectrum and Eq. (5.19) for the bispectrum]. The constraints from the power spectrum are plotted in blue, from the bispectrum in green and from both power spectrum and bispectrum in red, without taking into account their cross term in the covariance. The full theoretical errors covariance is considered here.

5.7.1.3 The effect of the trispectrum term

In our final step, we include the trispectrum contribution in the galaxy bispectrum (*i.e.* Eq. (5.19) and Eq. (5.29) for the monopole approximation and the full redshift space models respectively), together with theoretical errors (see Sections 5.7.1.1 and 5.7.1.2 for details). The trispectrum term is present only for non-Gaussian initial conditions and exhibits a scale dependence, coming from the primordial bispectrum [Eq. (3.129)]. It can then be used to tighten the constraints on PNG amplitudes. Interestingly, this is limited no only to the local case, but it also includes the equilateral shape. The importance of the trispectrum contribution was originally investigated by (Sefusatti, 2009; Jeong and Komatsu, 2009) for local non-Gaussianity, but the term is included in an actual forecast

	SKA		EMU	
	Monopole approximation	Monopole approximation + Trispectrum	Monopole approximation	Monopole approximation + Trispectrum
P(loc)	0.35	0.35	0.792	0.792
B(loc)	0.049	0.025	0.125	0.059
P+B(loc)	0.046	0.025	0.116	0.057
P(equil)	-	-	-	-
B(equil)	14.16	2.26	27.68	3.98
P+B(equil)	7.46	1.75	14.47	3.14
P(ortho)	18.79	18.79	29.93	29.93
B(ortho)	1.76	0.49	3.24	0.78
P+B(ortho)	1.7	0.45	3.12	0.71

Table 5.7 – Forecast 1σ results for the local, equilateral and orthogonal PNG. The modelling used is for the power spectrum Eq. (5.8) and for the bispectrum is given by Eq. (5.19), where for the latter the trispectrum bias term is taken into account. The full effect of the theoretical errors is taken into account here. The calculations are performed by using the approximated monopole [Eqs. (5.42) and (5.43)]. The monopole approximation model is shown for comparison purposes.

here for the first time. The scale dependence induced in the galaxy bispectrum by the quadratic bias trispectrum correction is analogous to the scale dependent bias of the power spectrum. It can be calculated exactly for any type of PNG, without the need of using any kind of squeezed limit approximation, and it goes like $1/M(k) \propto k^{-2}$. Due to this, the degeneracy of $f_{\rm NL}^{\rm eq}$ with the bias parameters on large scales can now be broken (see the discussion in Sec. 4.4.2).

The results for the primordial non-Gaussianity amplitude, after including the trispectrum contribution, as well as theoretical errors, are presented in Figure 5.12, where we compare them to the constraints coming from the monopole approximation model. An improvement is observed for all PNG amplitudes and especially the constraints for the equilateral shape show an impressive enhancement. We have checked that the theoretical errors do not affect significantly $\sigma(f_{\rm NL}^{\rm eq})$ in this case, since the scale dependent signal contribution compensates for the theoretical uncertainties. The bias constraints are un-

affected, since the trispectrum correction disappears for chosen $f_{\rm NL} = 0$ fiducial value. The final predicted errors on the PNG amplitudes for the three cases considered here are presented in Table 5.7, after including the trispectrum term from the bias expansion. We see that, in principle, the inclusion of trispectrum corrections allows for significant improvements for all shapes, including equilateral.

One concern is that the two trispectrum corrections, *i.e.* T^{MPT}_{1112} and $S_2 T^{MPT}_{1112}$, depend both on $f_{\rm NL}$ and on bias parameters b_1, b_2 and b_{s_2}. Therefore, they could generate degeneracies between primordial NG and bias terms, which indeed is the case. However, we explicitly checked that, for large volume surveys such as the SKA radio continuum survey considered here, where very large scales are included, such degeneracies are broken.

The extension of this formalism to redshift space, by using the derived expression in Eq. (5.29) with the trispectrum correction [Eq. (5.32)], is performed here for the SKA and EMU radio continuum surveys. The resulting forecasts of the PNG amplitude are presented as a function of redshift in Figure 5.13. The forecast constraints from the summed signal over the whole redshift range are presented in Table 5.8. The modelling for both correlators is described in detail in Sec. 5.7.1.2 (*i.e.* Eqs. (5.28) and (5.29) for power spectrum and bispectrum respectively), where the effects of redshift errors and FOG are taken into account. Note that, only the diagonal part of theoretical error covariance is used in these redshift space forecasts (see Sec. 5.7.1.2 for a discussion).

As seen in Figure 5.13 and Table 5.8, the improvement provided by the trispectrum term in the forecasts of $f^{\rm loc}_{\rm NL}$ is negligible, while for the orthogonal PNG type the contribution is minimal. The constraining power of the trispectrum term reduces when the RSD effect is taken into account, contrary to the monopole approximation modelling (Table 5.7). This can be mainly attributed to the presence of redshift errors included in the redshift space modelling, which damp the signal. On the other hand, the scale dependence provided by the trispectrum term significantly improves the final forecast constraints for the equilateral PNG type, in combination with clustering-based redshift estimation. More

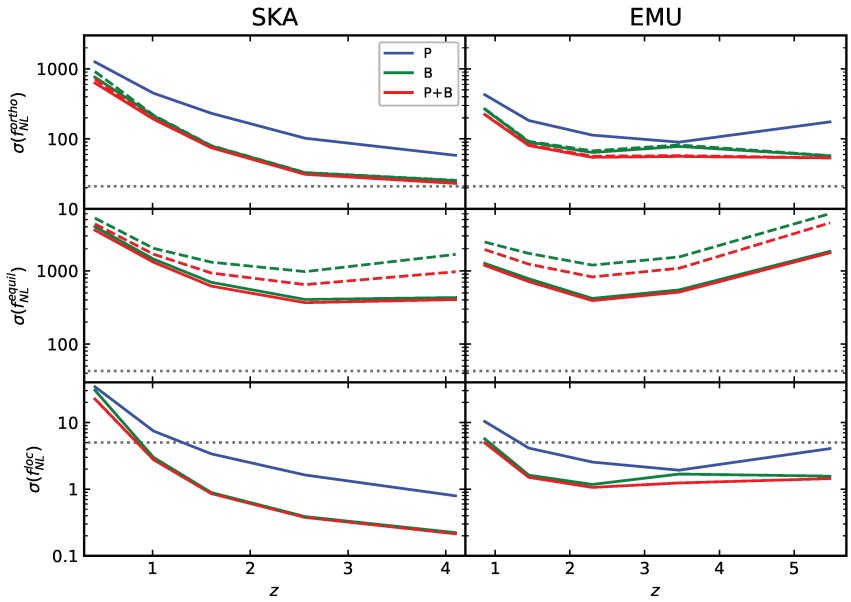

Figure 5.13 – Fisher forecasts on $f_{\rm NL}$ for local, equilateral and orthogonal shapes in the case of a SKA survey (left) and an EMU on (right). The dashed lines represent the model for the power spectrum and bispectrum in redshift space, given by Eqs. (5.28) and (5.29) respectively, while for the latter the trispectrum term is excluded. The solid lines represent the same model when the trispectrum correction [Eq. (5.32)] is taken into account. Redshift errors and FOG effects are considered for both cases. The constraints from the power spectrum are plotted in blue, from the bispectrum in green and from both power spectrum and bispectrum in red, without taking into account their cross term in the covariance. These results consider only the diagonal part of theoretical error covariance [Eq. (5.64)].

precisely, the forecasts coming from the redshift space bispectrum are tighter by a factor of ~ 2.5, while for the combined signal from the two correlators the improvement can reach up to a factor of ~ 2. This observation is in agreement with the improvement recognized before for the monopole approximation modelling.

Nevertheless, the final redshift space forecast constraints provided by the radio continuum samples, show a significant improvement with respect to the measured $f_{\rm NL}^{\rm loc}$ *Planck* constraints, while for the orthogonal PNG the 1σ forecast results are on the same level to those measured by *Planck* . For the equilateral type, the forecasts are still weaker, although we demonstrated the importance of the trispectrum bias term in improving the constraints provided by large volume LSS surveys (*e.g.* SKA), even in the case of large

	SKA		EMU	
	RSD	RSD + Trispectrum	RSD	RSD + Trispectrum
P(loc)	0.695	0.695	1.345	1.345
B(loc)	0.188	0.188	0.727	0.727
P+B(loc)	0.181	0.181	0.632	0.632
P(equil)	-	-	-	-
B(equil)	663.98	267.05	779.99	294.03
P+B(equil)	447.52	244.06	551.22	273.78
P(ortho)	49.09	49.09	60.85	60.85
B(ortho)	19.58	19.4	35.31	34.25
P+B(ortho)	18.08	17.94	29.78	29.11

Table 5.8 – Forecast 1σ results for the local, equilateral and orthogonal PNG in redshift space. The modelling used is for the power spectrum Eq. (5.28) and for the bispectrum is given by Eq. (5.29), where for the latter the trispectrum bias term [Eq. (5.32)] is taken into account. Only the diagonal part of theoretical error covariance is taken into account here. In addition FOG effects and redshift errors are considered. The RSD model without the trispectrum contribution (*i.e.* "RSD") is shown for comparison purposes.

redshift uncertainties. If large volume surveys (either optical or radio) will allow accurate redshift measurement at some stage, not only local models will be measured with high sensitivity, but also all other shapes. This will be further discussed in the optical survey forecasts to follow (Sec. 5.7.2).

5.7.1.4 Non-Gaussian corrections to the bispectrum variance.

In this work, as discussed in Sec. 5.3, only the diagonal part of the bispectrum covariance is used in the Fisher matrix formalism. In addition, for the variance we use the predictions of PT up to tree-level. Therefore, at this point, we would like to test the effect of excluding higher-order corrections. Using Eq. (5.62), we test the effect on the $f_{\rm NL}$ constraints coming from the 1 μJy radio continuum, and in particular those originating from the real-space model [Eq. (5.19)] as well as the redshift space bispectrum [Eq. (5.29)], following the procedure outlined at the end of section Sec. 5.3. For local PNG, constraints in real space deteriorate by $\sim 39\%$, while in redshift space the deterioration increases to $\sim 67\%$. For equilateral PNG, the effect seems to be smaller, a degradation of $\sim 12\%$

and $\sim 17\%$ is observed for the real and redshift space case, respectively. This should be kept in mind when quoting final constraints. A full Fisher matrix analysis, including full covariances, rather than the simplified estimates provided here, will be object of a future study.

5.7.2 Optical surveys forecasts

In this section we show forecasts for five optical surveys, which are the following: Euclid, DESI, LSST, SPHEREx1 and SPHEREx2 (see Sec. 5.5.2 for details on the specifications used). These will be ultimately compared with those originating from the two radio continuum surveys (see Sec. 5.5.1), presented in the previous section. Additionally, these surveys will allow us to test the full effect of theoretical uncertainties, mainly because their smaller volumes reduces significantly the computational time. We will in particular include off-diagonal theoretical error terms in real space (monopole approximation), up to the highest redshift bins (for nearly all scenarios; few exceptions will be pointed out case by case).

The optical survey analysis will broadly follow the same scheme as adopted in the previous section, based on adding realistic features and higher order corrections step by step, on top of the initial monopole approximation model, in order to check separately their impact.

5.7.2.1 Monopole approximation

As usual, we start with the monopole approximation and show the effect of adding theoretical errors. The full theoretical error covariance is used in the bispectrum Fisher matrix for the total redshift range in the cases of Euclid, DESI and SPHEREx1 surveys. For the rest, the full covariance is used up to the 6th bin for LSST and up to the 7th for the SPHEREx2 configuration. For the remaining bins, only the diagonal contribution is considered, since for the high redshift bins the off-diagonal terms have a minimum effect

	Monopole approximation					Monopole approximation + Theoretical Errors				
	Euclid	DESI	LSST	SPHEREx1	SPHEREx2	Euclid	DESI	LSST	SPHEREx1	SPHEREx2
P(loc)	3.985	4.432	0.808	3.741	0.575	4.394	4.856	0.9	4.244	0.66
B(loc)	1.487	1.644	0.127	1.108	0.112	1.858	2.072	0.14	1.463	0.12
P+B(loc)	1.086	1.204	0.118	0.89	0.1	1.275	1.415	0.13	1.1	0.109
P(equil)	-	-	-	-	-	-	-	-	-	-
B(equil)	30.65	42.4	12.28	55.52	11.91	42.01	57.24	16.68	80.98	14.47
P+B(equil)	18.68	26.55	4.58	35.4	5.36	33.59	46.15	7.84	60.68	7.46
P(ortho)	128.36	249.01	42.91	75.15	19.41	146.82	275.5	73.72	101.64	29.64
B(ortho)	9.35	12.66	3.11	12.49	2.43	9.74	18.19	4.25	22.04	2.78
P+B(ortho)	6.28	9.58	2.26	10.4	2.06	6.82	15.62	3.61	17.75	2.48

Table 5.9 – Forecast 1σ results for the three PNG type considered here, originating from a spectroscopic and a photometric survey. The monopole approximation model is as usual given by Eqs. (5.42) and (5.43), and we show the full effect of including theoretical errors.

on the final PNG amplitude forecasts, as discussed extensively in Sec. 5.7.1.1. The full theoretical error covariance will instead always be used over the whole redshift range for the power spectrum, as done before. Besides discussing theoretical errors, we also show the effect of the inclusion of trispectrum corrections. The marginalised $f_{\rm NL}$ constraints in both cases are shown as a function of redshift for Euclid and DESI surveys in Figure 5.14 and for the rest in Figure 5.15.

The effect of the full theoretical error covariance is presented in Table 5.9 for each optical survey. As done also for the radio continuum surveys, the practicality of using the monopole approximation lies in the fact that a quantification of the effect of the full theoretical error covariance is needed in order to propagate it to the RSD treatment (next section), where the computational effort is large. It is evident that the behaviour follows the same pattern as in the case of radio continuum. A degradation in the final PNG forecasts is observed ranging between $25-50\%$ depending on the PNG type, as well as the size and redshift range of the survey (see Table 5.9), where for the equilateral case the effect is maximum. Excluding the off-diagonal elements of the theoretical error covariance introduces an almost negligible error for local PNG for all optical surveys, while for the equilateral and orthogonal forecasts an underestimation of the theoretical uncertainties by 9% and 4% is observed respectively.

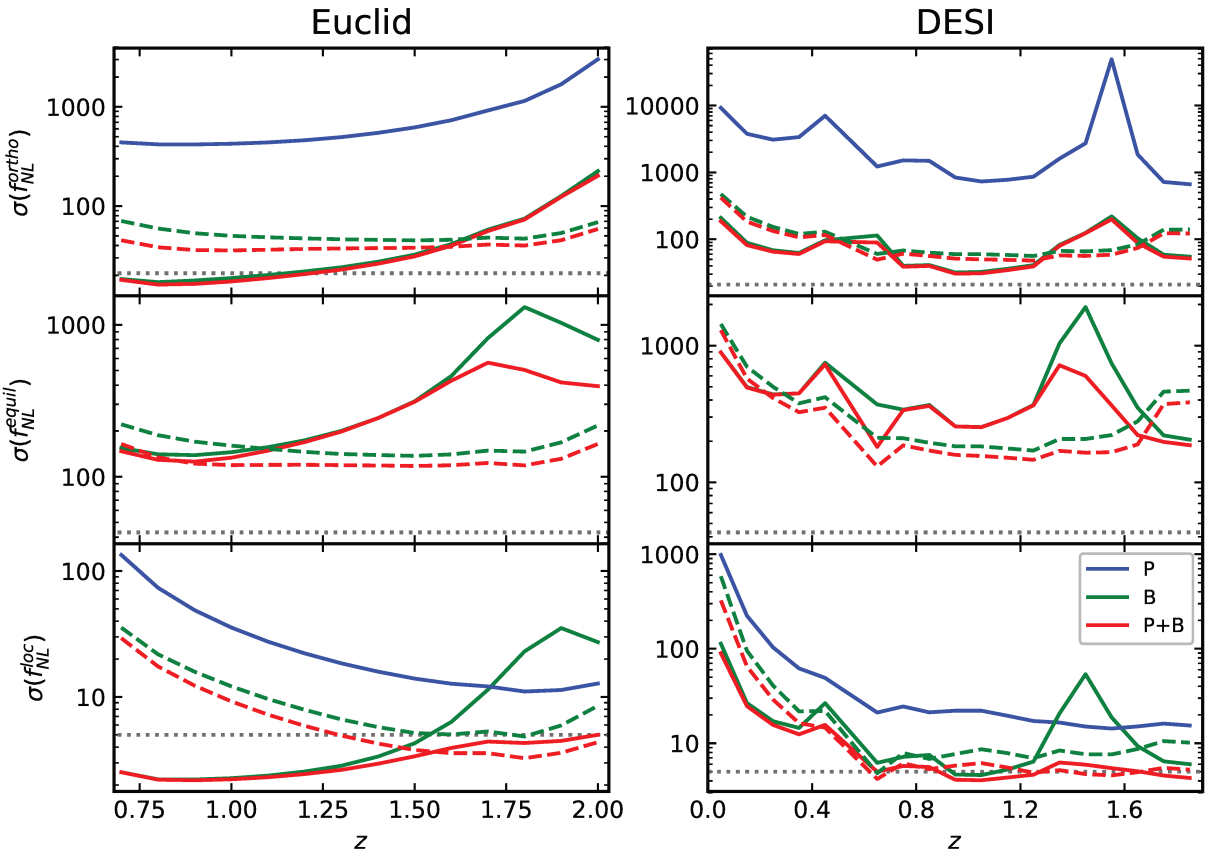

Figure 5.14 – Fisher forecasts on $f_{\rm NL}$ for local, equilateral and orthogonal shapes in the case of a Euclid survey (left) and a DESI on (right). The dashed lines represent the minimum monopole approximation model of this section, while the solid lines represent the same model when the trispectrum correction is considered (*i.e.* Eq. (5.8) for the power spectrum and Eq. (5.19) for the bispectrum). The constraints from the power spectrum are plotted in blue, from the bispectrum in green and from both power spectrum and bispectrum in red, without taking into account their cross term in the covariance. The full theoretical errors covariance for the whole redshift range is considered here.

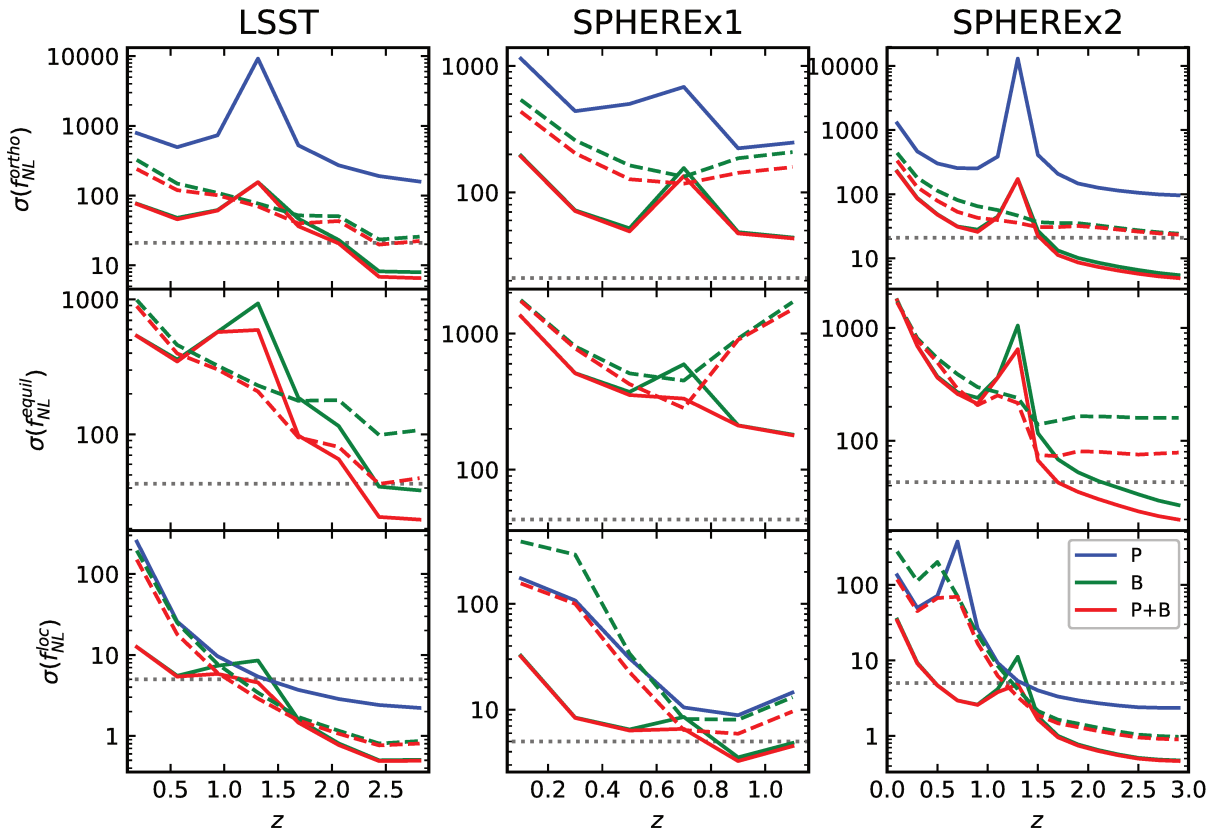

Figure 5.15 – Same as in Figure 5.14, but for the LSST (left) and the two configurations of a SPHEREx surveys (middle and right). The specifications used are presented in Sec. 5.5.2.3 and 5.5.2.4.

An immediate observation for the cases of the Euclid and the DESI surveys (Figure 5.14) is that the constraints coming from the monopole approximation model on equilateral and orthogonal PNG types are worse than current *Planck* bounds (plotted as grey dotted lines in Figure 5.14 and 5.15) for the whole redshift range. For the local shape, the forecasts are tighter for the majority of the cases and mainly for the larger redshift bins. This holds for both power spectrum and bispectrum, as well as for the sum of their signal. The constraints on the equilateral PNG shape are the most affected (see Sec. 5.7.1 for a discussion).

Adding trispectrum corrections produce some improvements, in the case of these two surveys. For local PNG, low redshift bins produce an order of magnitude improvement,

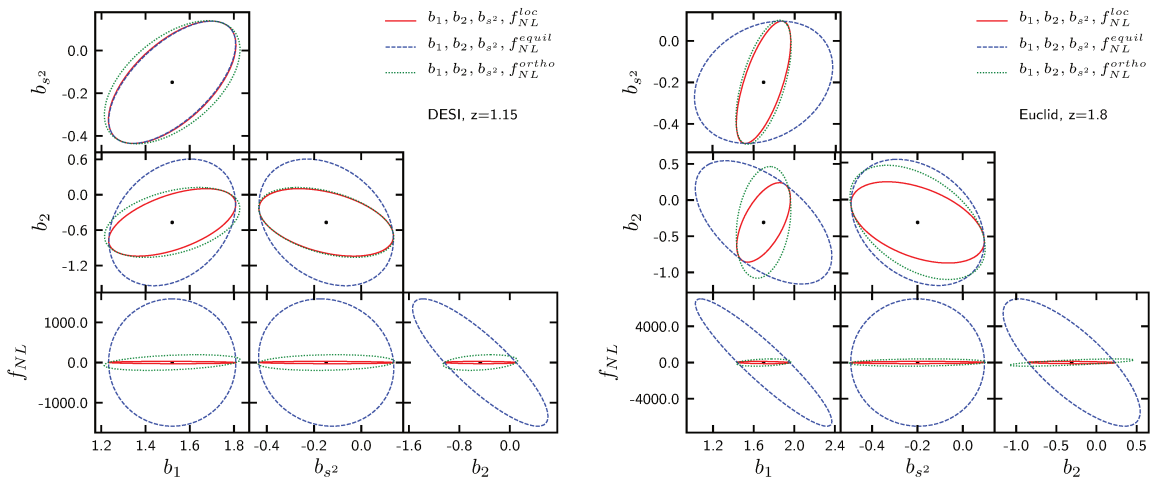

Figure 5.16 – The joint 68% C.L. forecasts on the three galaxy bias parameters (*i.e.* b_1, b_2 and b_{s^2}) and primordial non-Gaussianity from the $z = 1.15$ redshift bin of the DESI survey (left) and the $z = 1.8$ bin of the Euclid survey (right). In each panel the two-dimensional joint forecast constraints are shown for all the combinations between the parameters, after marginalising over the remaining. The model used is the approximating monopole for both power spectrum and bispectrum (Eqs. (5.42) and (5.43)), after considering in the galaxy bispectrum the trispectrum bias term shown in Eq. (5.19)

while high redshifts have a much smaller effect. The same behaviour is also observed for the orthogonal shape, but in this case the improvement is much smaller (~ 2.5 times). For equilateral PNG, a small improvement is observed only for the very low redshift bins, while for the large redshifts the constraints become even worse. The lack of improvement observed in the small volume surveys (*e.g.* Euclid, DESI) is due to degeneracies between $f_{\rm NL}$ and bias parameters, which are enhanced by the presence of the trispectrum term. As seen in Figure 5.16, $f_{\rm NL}^{\rm loc}$ and $f_{\rm NL}^{\rm orth}$ do not show any degeneracies with the three bias terms (*i.e.* b_1, b_2 and b_{s^2}), considered here as free parameters. On the other hand, $f_{\rm NL}^{\rm eq}$ shows strong degeneracies with all three of them and hence this explains the observed degradation in results (see Figure 5.14 and Table 5.10) after the inclusion of the trispectrum term. Such degeneracies can be broken if large enough scales are available in the survey (see Figure 5.12 for the radio continuum cases), due to the scale dependent nature of the trispectrum corrections in the galaxy bispectrum.

The Euclid survey has a slightly overall better performance that the DESI for all three PNG types. This is more or less expected, since Euclid is designed to probe marginally larger volume than DESI, as we can see in Table 5.2 and 5.3. Therefore a larger number of modes is available to the first, which is what mainly matters for the forecasts coming from the Fisher matrix formalism (see Sec. 5.3 for a discussion). Even thought theoretical errors are treated in both surveys using the same methodology, they can have different impact on the results. The reason for this can be tracked down to the different redshift ranges of the two surveys. Despite the fact that DESI has a wider redshift range than Euclid, half of its bins are in the low redshift regime. This means that the constraints originating from them are highly affected by theoretical errors (as discussed in Sec. 5.7.1) and therefore will have a minor contribution to the final constraints. These reasons can mainly explain the observed difference in the forecasts coming from the two surveys.

An overall gain can be observed when considering LSST and SPHEREx can be observed (Figure 5.15) with respect to Euclid and DESI, since they probe a larger part of the sky and hence grant access to larger scale modes. More specifically, the forecasts of the monopole approximation model in the case of local PNG are tighter than the *Planck* measurements for the majority of the redshift bins (see Figure 5.15), which holds for both power spectrum and bispectrum. For the SPHEREx1 configuration, the bispectrum results approach those of *Planck* only in the largest redshift bins. In the case of equilateral-type PNG, the bispectrum constraints generally are worst than those of *Planck* ; however they approach the latter in large redshift bins for the LSST and SPHEREx2 cases. Moreover, the results for the orthogonal PNG type follow roughly the same trend as for the equilateral case. Note that the improvement, after the inclusion of the power spectrum signal to the bispectrum, is minimal for all PNG types.

Adding the trispectrum scale dependent bias corrections to the galaxy bispectrum produces an overall gain in the constraints provided by LSST and SPHEREx. As described before, these surveys will probe a larger part of the sky and hence grant access to large

scale modes. This fact will break the degeneracy of $f_{\rm NL}$ with bias parameters, providing the observed improvement over the results of the monopole approximation model. More specifically, for the local-type PNG, the trispectrum corrections reduce the 1σ constraints on $f_{\rm NL}^{\rm loc}$ originating from LSST beyond unity for the high redshift bins. While for the two SPHEREx configurations, a significant improvement in the bispectrum forecasts is observed for the whole redshift range. For the equilateral PNG case, a compelling improvement is observed for all surveys. Note that although SPHEREx has been proposed with a primary goal of studying primordial non-Gaussianity, the second configuration used here offers a clear advantage over the first in constraining all the three PNG type considered here.

Here we would like to point out the importance of the bispectrum for the PNG amplitude forecasts coming from LSS surveys. As we can see in Figure 5.14 and 5.15, the gain in the final $f_{\rm NL}$ constraints of the local type is small when the signal from the bispectrum is added on top of the one generated by the power spectrum. However, this changes dramatically for the equilateral and orthogonal types, where the bispectrum is the main source of signal while it can improve up to an order of magnitude the forecasts originating from the power spectrum.

After marginalising appropriately over the free parameters and sum the signal from each redshift bin for each optical surveys considered here, we present the 1σ forecasts for the PNG amplitude in Table 5.10. The forecasts of the monopole approximation model coming from Euclid and DESI are tight enough in order to provide compelling constraints. The addition of the trispectrum corrections in the galaxy bispectrum improves approximately by a factor of two the local and orthogonal PNG forecasts, while for the equilateral PNG type the enhancement of the forecasts can be up to a factor of four (in the case of the large volume surveys). More precisely, for the local PNG type, LSST and the SPHEREx2 configuration may give for the combined power spectrum and bispectrum signal $\sigma(f_{\rm NL}^{\rm loc}) < 1$, where the latter can have a better performance due to its

	Monopole approximation					Monopole approximation + trispectrum				
	Euclid	DESI	LSST	SPHEREx1	SPHEREx2	Euclid	DESI	LSST	SPHEREx1	SPHEREx2
P(loc)	4.394	4.856	0.9	4.244	0.66	4.394	4.856	0.9	4.244	0.66
B(loc)	1.858	2.072	0.14	1.463	0.12	0.847	1.837	0.09	0.674	0.061
P+B(loc)	1.275	1.415	0.13	1.1	0.109	0.759	1.328	0.087	0.622	0.059
P(equil)	-	-	-	-	-	-	-	-	-	-
B(equil)	42.01	57.24	16.68	80.98	14.47	55.27	82.87	7.56	34.42	3.86
P+B(equil)	33.59	46.15	7.84	60.68	7.46	51.08	70.55	4.54	32.57	2.74
P(ortho)	146.82	275.5	73.72	101.64	29.64	146.82	275.5	73.72	101.64	29.64
B(ortho)	9.74	18.19	4.25	22.04	2.78	6.72	12.63	1.53	7.12	0.76
P+B(ortho)	6.82	15.62	3.61	17.75	2.48	6.35	12.03	1.28	6.9	0.67

Table 5.10 – Forecast 1σ results for the three PNG type considered here, originating from Euclid, DESI, LSST and SPHEREx. The monopole approximation model is given by the approximating monopole in Eqs. (5.42) and (5.43), while the same model is used with the additional trispectrum corrections whose results are under the column named "Monopole approximation+trispectrum". The full effect of the theoretical errors is taken into account here.

larger volume.

All the previous results, assume a Gaussian and diagonal bispectrum covariance matrix. By using Eq. (5.62), proposed in Ref. (Chan and Blot, 2017), we can effectively resum the contributions to the diagonal coming from higher order terms. Doing so will degrade the results presented in Table 5.10. In the case of Euclid, a $\sim 35\%$ and $\sim 16\%$ increase is observed for the 1σ forecast errors in the case of local and equilateral PNG type respectively. For the LSST the deterioration of the constraints on local and equilateral PNG is $\sim 29\%$ and $\sim 10\%$ respectively, while for the SPHEREx2 configuration we observe a $\sim 47\%$ and $\sim 18\%$ increase in the 1σ results. The same trend seen for the radio continuum surveys is also observed here, *i.e.* the local constraints are highly affected by the higher order corrections in the bispectrum variance, while a minimum effect is observed for the equilateral PNG case.

5.7.2.2 Redshift space effects

Our next step is to move to redshift space, considering RSD, redshift errors and the FOG smearing effect. As usual, for the sake of comparison, we will use the bispectrum

RSD model with and without the trispectrum bias term given in Eq. (5.32). Regarding theoretical errors, only the diagonal part of the error covariance [Eq. (5.64)] will be used in redshift space, due to the high computational cost. The results are presented as a function of redshift bins in Figure 5.17 for Euclid and DESI, while the rest are plotted in Figure 5.18. We use the spectroscopic sample of these two surveys, therefore the effect of the redshift uncertainties is small (see Secs. 5.5.2.1 and 5.5.2.2 for details). Qualitatively, our real space monopole approximation results are confirmed. These surveys can produce improvements on current *Planck* bounds for the local shape, but not for the other two, mostly due to theoretical errors. Adding trispectrum corrections has a minimal effect because such corrections need very large scales to be effective and, contrary to radio surveys, the probed volumes are here too small to make a difference.

The situation changes for LSST and SPHEREx. These surveys probe much larger volumes, but at the same time are affected by large photometric redshift errors. Due to the latter, all PNG predicted constraints are now degraded (Figure 5.15) with respect to the real space forecast. The full redshift space forecasts, coming from the integrated signal over the entire redshift range, are presented in Table 5.11 for the galaxy power spectrum, bispectrum and their combination. Both cases, with and without the trispectrum term, are shown. To better quantify the effect of redshift uncertainties on our final $f_{\rm NL}$ constraints, we present also the results of the RSD model, taking $\sigma_z(z) = 0$. For the Euclid and DESI surveys, the spectroscopic redshift uncertainties only contribute a few percent in the final RSD constraints on all three PNG types, both for the case of power spectrum and bispectrum. This is not the case though, as we also discussed before, for the photometric sample of LSST and the two configuration of SPHEREx. For both surveys we consider larger redshift uncertainties than the spectroscopic samples and hence the effect has a bigger impact on the final constraints. The forecasts coming from the bispectrum are affected the most by redshift errors, especially for equilateral PNG.

In the case of the SPHEREx samples, the two configurations we consider have redshift

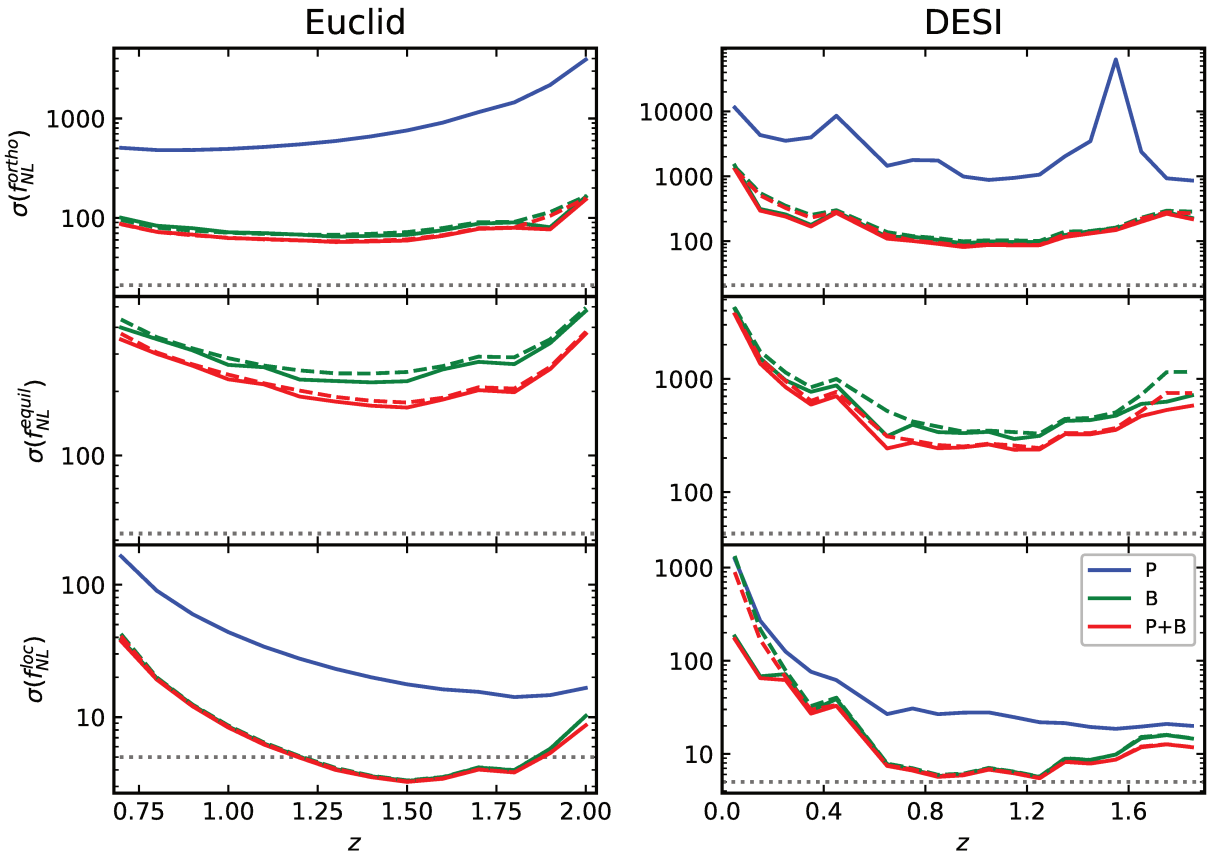

Figure 5.17 – Fisher forecasts on the amplitude of the three PNG types considered here in the case of a Euclid survey (left) and a DESI on (right). The dashed lines represent the RSD model, given by Eqs. (5.28) and (5.29) for the power spectrum and bispectrum respectively, without the presence of the trispectrum term [Eq. (5.32)] in the galaxy bispectrum. Solid lines represent the same model but with the trispectrum correction included. The constraints from the power spectrum are plotted in blue, from the bispectrum in green and from both power spectrum and bispectrum in red, without taking into account their cross term in the covariance. The FOG effect, as well as the redshift error, is taken into account in both models. Only the diagonal part of the theoretical errors covariance is used here.

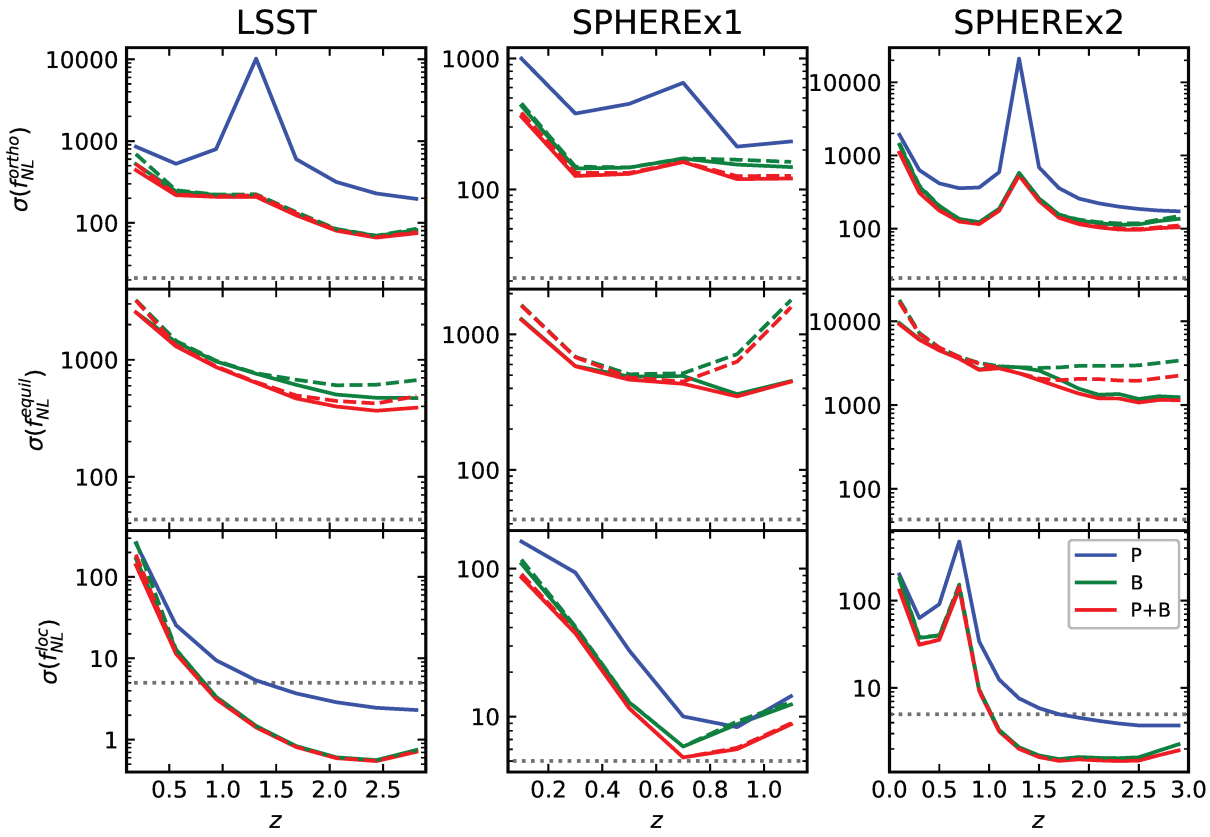

Figure 5.18 – Same as in Figure 5.17, but for the LSST (left) and the two configurations of a SPHEREx surveys (middle and right).

uncertainties differing by two orders of magnitude, with SPHEREx1 being the most precise. This can explain the better performance of SPHEREx1 with respect to SPHEREx2 for equilateral PNG, which is the type affected the most by redshift uncertainties (see Sec. 5.7.1 for a detailed discussion). Even though SPHEREx2 has a wider redshift range than SPHEREx1, its larger redshift errors prevent an improvement over the SPHEREx1 orthogonal PNG forecasts. The local PNG case is affected the least by redshift uncertainties and therefore the observed improvement in the $f_{\rm NL}^{\rm loc}$ constraints of SPHEREx2 is justified. The SPHEREx2 constraining power is significantly better than that of *Planck* , for bins with $z \gtrsim 1$. The same is observed also for LSST constraints on $f_{\rm NL}^{\rm loc}$, with a better performance than *Planck* in the majority of redshift bins. Adding the trispectrum correc-

	RSD[$\sigma_z(z)=0$]					RSD					RSD+trispectrum				
	Euclid	DESI	LSST	SPHEREx1	SPHEREx2	Euclid	DESI	LSST	SPHEREx1	SPHEREx2	Euclid	DESI	LSST	SPHEREx1	SPHEREx2
P(loc)	5.588	6.209	1.161	5.441	1.01	5.602	6.226	1.301	5.715	1.441	5.601	6.225	1.301	5.715	1.441
B(loc)	1.214	1.957	0.082	1.66	0.164	1.349	2.147	0.322	4.448	0.563	1.337	2.111	0.322	4.376	0.563
P+B(loc)	1.186	1.865	0.081	1.586	0.162	1.311	2.027	0.312	3.469	0.523	1.3	1.998	0.312	3.435	0.523
P(equil)	-	-	-	-	-	-	-	-	-	-	-	-	-	-	-
B(equil)	73.56	111.73	31.07	151.75	35.5	77.69	117.78	276.11	284.13	853.02	72.75	104.2	229.27	202.86	475.3
P+B(equil)	55.63	79.56	17.15	104.45	20.27	59.58	85.31	207.28	260.36	638.89	57.29	79.43	184.26	193.32	424.79
P(ortho)	172.92	339.48	87.38	118.33	38.92	173.39	340.67	124.42	133.73	72.1	173.36	340.63	124.42	133.73	72.1
B(ortho)	20.39	33.38	7.58	28.05	6.94	21.26	35.24	40.71	70.24	40.46	20.71	32.59	39.76	67.28	39.34
P+B(ortho)	17.77	29.49	6.94	26.08	6.59	18.62	31.0	38.42	59.63	34.82	18.24	29.31	37.63	57.35	34.07

Table 5.11 – Forecast marginalised 1σ results for the three PNG type considered here, originating from Euclid, DESI, LSST and SPHEREx. The full RSD model for both power spectrum and bispectrum is considered [Eqs. (5.28) and (5.29)]. Three different versions of the model are examined here: without considering the redshift uncertainties ("RSD[$\sigma_z(z)=0$]"), including the redshift errors ("RSD") and adding to the latter the trispectrum contribution ("RSD+trispectrum"). Regarding the theoretical errors, only the diagonal part of the covariance is used.

tion has a minimal impact on the bispectrum forecasts for the orthogonal and local types, while it can have an overall improvement in the equilateral results of the large-volume surveys. Still, large redshift errors make the trispectrum contribution far from enough to improve over current bounds.

We remind again that, in the analysis of this section, we generally use only the diagonal part of the theoretical error covariance. However, as we show in Sec. 5.7.2.1, the effect is expected to be small for surveys with wide redshift range. In order to quantify the effect of neglecting off-diagonal terms, we performed a full error covariance analysis for Euclid. The survey volume size shrinks in this case the computational effort tremendously, compared to radio continuum cases, and makes a full numerical analysis feasible. The deterioration level in the final PNG constraints is consistent with what reported for radio continuum. More specifically, we observe a $< 1\%$ and $\sim 7\%$ degradation for local and equilateral PNG cases respectively.

The results under "RSD+trispectrum" in Table 5.11 are considered as our final forecasts on the three PNG types originating from the optical surveys. Comparing these results with those available in the literature, we see that our power spectrum Euclid constraints, after excluding the theoretical errors, are consistent with the forecasts in Ref.

(Giannantonio et al, 2012) for the local and orthogonal PNG. On the other hand our forecasts on the local type, coming from Euclid and DESI, are slightly worse than those reported in (Tellarini et al, 2016). The difference originates from the fact that we take into account the presence of theoretical errors, as well as the effect of redshift uncertainties. The differences are slightly higher for redshift space bispectrum forecasts, owing to the higher impact of theoretical errors and to the inclusion of redshift errors (small, but not completely negligible also for spectroscopic surveys).

As done for the radio analysis, we also tested the effect of neglecting NG corrections in the bispectrum variance, by using Eq. (5.62). In the case of Euclid, a degradation of $\sim 42\%$ and $\sim 20\%$ is observed in the forecasts for the local and equilateral PNG types respectively. For LSST we get a deterioration of $\sim 32\%$ and $\sim 10\%$, while for the SPHEREx2 configuration $\sim 57\%$ and $\sim 21\%$, for the final constraints on local and equilateral PNG respectively. Again these results agree with the trend observed before, indicating that, in order to generate realistic forecast from future LSS surveys on the local PNG amplitude, one has to take into account the higher order terms in the diagonal of the bispectrum covariance matrix.

5.8 Conclusions

In this chapter we have investigated constraints on the amplitude of the non-Gaussian parameters $f_{\rm NL}$ for three types of PNG shapes – local, equilateral and orthogonal – and on galaxy bias parameters, through galaxy power spectrum and bispectrum measurements on large scales using a Fisher matrix approach. We thoroughly accounted for a large number of effects in modelling the gravitational NG contributions, including a full second order treatment of bias and RSD. We carefully investigated the propagation of theoretical uncertainties, following the approach introduced in (Baldauf et al, 2016) and extending it to bias loop-corrections. All these effects were to a various extent included in previous literature, but never consistently accounted for at once in a single forecast analysis. The

cross-correlation between power spectrum and bispectrum was ignored in this work, and the bispectrum covariance approximated as diagonal. However, for the large scales considered here, we expect this to have small impact, based on recent results in the literature (Chan and Blot, 2017). We also employed, as standardly done, a Gaussian approximation for the bispectrum variance. We presented an explicit estimate of the effect of ignoring NG contributions to the variance, by considering leading NG corrections, see Eq. (5.62). We found that, in the worst case scenario, such corrections can degrade our constraints by a factor $\sim 50\%$. A more detailed study of the bispectrum covariance, including NG corrections, will be included in future work. Likewise, it will be important to account in the future for the effect of relativistic corrections on the bispectrum, especially for large volume surveys (see *e.g.* (Di Dio et al, 2016; Umeh et al, 2017; Bertacca et al, 2017)).

In addition to the previous ingredients, we improved the modelling of the galaxy bispectrum by considering a complete second order bias expansion, which includes for the first time the trispectrum term [Eq. (5.1)]. We only consider the zeroth order (tree-level) expansions in the matter fields, because we are only interested in the large-scale contributions. For dark matter, we have used the MPTbreeze perturbation theory, based on Renormalised Perturbation Theory, which provides a natural cut-off in the non-linear regime, such that ultraviolet divergences are automatically removed. The final bispectrum model used for our forecast is represented by Eqs. (5.19) and (5.29), in real and redshift space respectively. These are the starting point of our numerical analysis.

Our constraints are based on radio surveys – with 10 μJy and 1 μJy flux limits, and optical surveys – two spectroscopic and two photometric. For the radio surveys, we considered radio continuum datasets and assumed that the redshift of radio sources would be estimated via clustering based methods.

We have summarised our main results in Table 5.12, where we have reported the constraints derived when considering RSD, redshift and theoretical errors for the three non-Gaussian shapes, together with the *Planck* temperature and polarisation constraints

	Planck	SKA	EMU	Euclid	DESI	LSST	SPHEREx1	SPHEREx2
Local	5.0	0.181	0.632	1.3	1.998	0.312	3.435	0.523
Equilateral	43	244.06	273.78	57.29	79.43	184.26	193.32	424.79
Orthogonal	21	17.94	29.11	18.24	29.31	37.63	57.35	34.07

Table 5.12 – Summary of 1σ forecasts for the three PNG types considered (local, equilateral and orthogonal), from radio (SKA and EMU) and galaxy surveys (Euclid, DESI, LSST and SPHEREx) derived from combining the power spectrum and bispectrum and accounting for RSD, redshift uncertainties, the trispectrum term and theoretical errors.

(Planck Collaboration et al, 2016a), for reference.

It is clear that for all surveys, important improvements over current CMB bounds are possible for the local shape and that the bispectrum gives a very important contribution, improving the expected $f_{\rm NL}^{\rm loc}$ bound by a factor $\sim$ 4-5 in most cases. On the other hand, other shapes, especially equilateral, would be poorly constrained. It is interesting to investigate this aspect more in detail. On one hand, it is well known that the power spectrum cannot place constraints on equilateral NG, leaving the bispectrum as the only useful statistic. For forthcoming optical surveys (spectroscopic and photometric), the main limiting factors are provided by the relatively small number of modes available in the linear regime and by theoretical errors, which peak in the equilateral limit, since this is the most affected by late-time evolution. Including mildly non-linear scales in the analysis of course addresses the former problem, but strongly exacerbates the latter and it will require exquisitely accurate modelling of late-time non-linearities. This, at present, is of course the object of a significant amount of scientific activity. Larger future optical and radio surveys (*e.g.* LSS, SKA) will, on the other hand, provide access to much larger volumes and higher redshifts.

Owing to this, it would be therefore natural to expect improvements in the bispectrum forecasts, for all shapes, even in presence of significant theoretical errors. The trade-off for these surveys is however represented by large errors in the determination of redshifts. We find indeed that redshift errors massively degrade the final forecasts, especially for equilateral scenarios (large wavenumbers in squeezed triangles are less affected). When we

neglect them, in our monopole approximation model, we actually see that large improvements (e.g. up to a factor ~ 5 for SKA) with respect to *Planck* equilateral constraints can be achieved. Notably, this constraining power mostly comes from very large scales and trispectrum contributions, which display a $\sim k^{-2}$ scale-dependence in the equilateral case. Such contributions therefore deserve further attention.

It is therefore clear that developing strategies for better determination of redshifts in future photometric and radio surveys could be a powerful approach toward the goal of significantly improving PNG bounds, beyond local models. Another possibility, which will be explored in a forthcoming work, is to rely on intensity mapping.

Chapter 6 | *The modal estimator*

6.1 Introduction

The most stringent constrains on primordial non-Gaussianity comes from the measurements of the CMB bispectrum (Planck Collaboration et al, 2016a). Future LSS surveys promise to deliver big enough volumes to match the constraining power of the CMB, in some case even surpass it (see Chapter 5). Measuring, however, the bispectrum of LSS is a challenging and computationally demanding task, due to the three dimensional nature of the dataset. In fact the measurements of a three-point correlator need $\mathcal{O}(N^6)$ operations, where N is the number of modes per dimension inside a simulation box or LSS survey. The approach followed is based on the *modal estimation* formalism, which was developed and applied extensively for both temperature and polarization CMB maps (Fergusson and Shellard, 2009; Fergusson et al, 2010a,b; Regan et al, 2010; Fergusson et al, 2012). In a nutshell, modal methods consist in finding a suitable basis of bispectrum templates and write higher order correlations as a linear combination of such templates ("modes"). By properly choosing the templates, it is always possible to work with separable bispectra (see Sec. 6.2) and to achieve fast convergence. It was extended for LSS in (Fergusson et al, 2012) and used to measure $f_{\rm NL}$ from N-body simulations with non-Gaussian initial conditions in (Schmittfull et al, 2013). In addition, it was used for measuring the bispectrum of simulations and compare predictions from different perturbation theories in (Lazanu et al, 2016).

The reduction of the numerical cost within this method is dramatic ($\mathcal{O}(n_{\rm max}N^3)$). Although, the modal estimator was developed for measuring the primordial non-Gaussian

amplitude, its appealing features make it ideal to extract any kind of galaxy bispectrum (separable or not) from a simulation or LSS survey dataset, for each redshift slice of interest. The modal decomposition applies both to the theoretical bispectra of interest, as well as to the three-point function extracted from data or simulations. One can expand both, using the same basis, and achieve a fast, efficient comparison by only comparing the coefficient of the expansion, *i.e.* without the need of measuring all the Fourier mode triangles. This allows for massive data compression (from billions of triangles to hundred/thousand coefficients). In this chapter we will show results on the measured gravitational bispectrum, reconstructed from the modal estimator, for simulations with Gaussian initial conditions. Moreover, we will present measurements of the primordial and the effective gravitational $f_{\rm NL}$ parameters for a few realizations with non-Gaussian initial conditions of the local type. This way we can show the power of the modal estimator to separate these two contributions and clean the primordial signal from the late-time gravitational non-Gaussianity . Finally, we will test the modal estimator for measurements of the gravitational bispectrum of Gaussian simulations, when dark energy couples to matter, providing us with an example of how it can be used in order to test dark energy and modified gravity models.

We begin with an introduction to the statistical estimators and terminology that it will be used later on (a detailed review on the subject can be found in any textbook for statistics *e.g.* (Barlow, 1989)). We proceed with the review of the modal estimator itself. Finally, we present details on the N-body simulations and the methodology used here to extract the bispectrum of gravity, as well as PNG, in addition to the simulation bispectrum and $f_{\rm NL}$ results. The last part is dedicated to the work in progress and potential future applications of the estimator in various LSS fields.

6.2 Statitical estimator

A *statistical estimator* is a procedure used to measure a property from a data sample or a parent distribution. All the statistical moments needed to describe the PDF of a field or dataset are based on the ensemble average over all possible realizations of the system. Practically this is not possible and therefore what we actual measure is the estimated value of the quantity by applying the estimator on the sample. We saw this in Sec. 3.5.1, where we discussed that the ergodic assumption can shift the problem of calculating the ensemble of a stochastic process (*e.g.* primordial density fluctuations) from integrating over infinite realisations to a spatial integration over all the infinite volume. Although, due to the fact that we do not have an infinite volume in the Universe, what we actually measure with the ensemble average of the density field is an estimation of its mean and not the true value of the first moment.

We define α to be the parameter that we want to measure in a sample and $\hat{\alpha}$ is a function of the data, which provides our statistical estimate of α. As we discussed already, what we will measure will not be the true value (*i.e.* it will be the expected value of the estimator), due to the statistical fluctuations. As N goes to infinity these effects will be smaller and smaller, in the case of independent measurements, and the expected value will approach the true. Hence, one of the characteristics of an estimator is *consistency*, defined as:

$$\lim_{N\to\infty} \langle \hat{\alpha} - \alpha \rangle = 0. \tag{6.1}$$

For a finite number of independent measurements, we cannot be sure if the expected value of the estimator represents exactly the true value (it might be larger or smaller). If this offset is somehow balanced around the true value, we can say that the estimator is *unbiased*. In other words, for an unbiased estimator the expected value is equal to the true, $\langle \hat{\alpha} \rangle = \alpha$. Although, by the law of large numbers, if an estimator is consistent, it will

be bias free as we increase the number of trials and the expected value approaches more and more the true. The variance of the estimator measures the spread of the estimated value around the expected, which depends on the dataset at hand. Therefore, for a good estimation of the true values we would like the estimator to have as small as possible spread for each different realization. An estimator is *efficient* if its variance is small.

Lets say that we have a dataset $\{x_1, x_2, \ldots, x_n\}$, where the probability of each individual set is drawn from a PDF, given the true value of parameter α to be $P(x_i;\alpha)$. The probability density function of the whole dataset will be given by the joint probability density function of all subset realization. The *likelihood* function of the full dataset is defined as

$$L(x_1, x_2, \ldots, x_n; \alpha) = L(\mathbf{x};\alpha) = \prod_i P(x_i;\alpha). \tag{6.2}$$

Now the expectation value of the one-point n-th moment is given as in Sec. 3.5.1, from:

$$\langle\, \hat{\alpha}^n(\mathbf{x}) \,\rangle = \int \hat{\alpha}^n(\mathbf{x}) L(\mathbf{x};\alpha) d\mathbf{x}. \tag{6.3}$$

Assuming that the estimator at hand is unbiased we can write:

$$\langle\, \hat{\alpha} \,\rangle = \int \hat{\alpha} L(\mathbf{x};\alpha) d\mathbf{x}. \tag{6.4}$$

Since the estimator depends only on the dataset, we can differentiate the above with respect to the true value of the parameter and get

$$1 = \int \hat{\alpha} \frac{dL(\mathbf{x};\alpha)}{d\alpha} d\mathbf{x} \quad \Rightarrow \quad 1 = \int \hat{\alpha} L(\mathbf{x};\alpha) \frac{d\ln L(\mathbf{x};\alpha)}{d\alpha} d\mathbf{x}. \tag{6.5}$$

The integral over the dataset of the likelihood must be equal to unity and therefore differentiating it, like the above, we can get:

$$\int L(\mathbf{x};\alpha)d\mathbf{x}=1 \quad \Rightarrow \quad \int \frac{d\ln L(\mathbf{x};\alpha)}{d\alpha}L(\mathbf{x};\alpha)d\mathbf{x}=\left\langle \frac{d\ln L(\mathbf{x};\alpha)}{d\alpha}\right\rangle =0. \tag{6.6}$$

Multiplying the above with α, subtracting it from Eq. (6.5) and using the Schwartz inequality we get:

$$\left(\int(\hat{\alpha}-\alpha)^2 L(\mathbf{x};\alpha)d\mathbf{x}\right)\left(\int\left[\frac{d\ln L(\mathbf{x};\alpha)}{d\alpha}\right]^2 L(\mathbf{x};\alpha)d\mathbf{x}\right)\geq 1. \tag{6.7}$$

The first part is the variance of the estimator and hence we can write the above as:

$$\langle(\hat{\alpha}-\alpha)^2\rangle\left\langle \frac{d\ln L(\mathbf{x};\alpha)}{d\alpha}\right\rangle \geq 1. \tag{6.8}$$

If we differentiate Eq. (6.6) and substitute the result to the above, we can get the Cramer-Rao inequality:

$$\langle(\hat{\alpha}-\alpha)^2\rangle \geq -\frac{1}{\left\langle \frac{d^2\ln L(\mathbf{x};\alpha)}{d\alpha^2}\right\rangle}. \tag{6.9}$$

This states that an estimator has a lower bound in its accuracy. For any unbiased estimator this inequality is always satisfied.

The *maximum likelihood* estimation method states that, we can determine the value of a parameter α that maximizes $\ln L(\mathbf{x};\alpha)$ and gives the highest probability of actually obtaining the dataset $\mathbf{x}$ as high as possible, *i.e.* it makes our data the most likely. The estimator that takes this value is called a *maximum likelihood estimator*

$$\frac{d\ln L(\mathbf{x};\alpha)}{d\alpha}\Big|_{\alpha=\hat{\alpha}}=0. \tag{6.10}$$

Given the likelihood for a sample we can solve, sometimes, the above and get an equation for the maximum likelihood estimator of the parameter α. In the case we cannot achieve that, a numerical derivation must be applied. For large samples the maximum likelihood estimator, if consistent, saturates the Cramer-Rao bound and the inequality becomes

equality. In addition, any unbiased estimator, whose variance has the exact lower bound, is a maximum likelihood estimator.

6.3 Modal estimation formalism

The main idea of the modal estimator comes from the separability of some primordial non-Gaussian shapes (*e.g.* local, equilateral, orthogonal) predicted by a class of inflationary models. This characteristic, which can be written schematically as $B(k_1, k_2, k_3) = X(k_1)Y(k_2)Z(k_3)$, can reduce the operational cost from $\mathcal{O}(N^6)$ to $\mathcal{O}(N^3)$ as it was shown in (Komatsu et al, 2005) (later on KSW). However, these shapes are not the only ones predicted by the plethora of inflationary models. A large amount of non-separable shapes are considered in the literature, which should be measured in order to extend our constraining power to the whole inflationary landscape. The numerical task we need to undergo is extremely demanding. To address this issue, in the work of (Fergusson and Shellard, 2009; Fergusson et al, 2010a,b) and (Fergusson et al, 2012; Regan et al, 2012; Schmittfull et al, 2013) for the CMB and LSS respectively, the idea of separability is extended to an arbitrary primordial shape by proposing the *modal estimator*. This formalism is based on an expansion of the bispectrum on a set of separable modes forming a basis. The convergence of the expansion can be achieved with a small number of coefficients ($n_{\max} \sim \mathcal{O}(50)$), where now the information is compressed into them. The computational speed up for measuring the bispectrum from simulations or LSS surveys is reduced tremendously ($\mathcal{O}(N^3)$). The modes are now used instead of the full bispectrum for all the formed Fourier modes triangles. This way a massive data compression is achieved.

The expansion coefficients of the theoretical bispectrum can be compared against those coming from simulations, in order to constrain the non-Gaussian amplitude in a fast and accurate way. In the case which the full bispectrum in the standard form (*i.e.* $B(k_1, k_2, k_3)$) is the one desired, the translation between the two "languages" is a mere loop over the triangles of interest. Within each iteration, a simple small matrix ($n_{\max} \times n_{\max}$)

multiplication with a vector of the same size takes place. Even though the modal estimator was developed for measuring primordial non-Gaussianity, one can use it to extract in a quick and simple way the bispectrum of simulations or even mock catalogues, by taking advantage the quick convergence and the reduced computational requirements of the modal decomposition. In addition, as it was shown in the work of (Regan et al, 2012), the modal decomposition technique can be used to generate non-Gaussian initial conditions for simulations for any shape desired. Finally, in the work of (Regan et al, 2010; Fergusson et al, 2010b, 2012) the modal estimator was expanded to cover also the planar trispectrum of CMB and LSS, *i.e.* the projection of the full trispectrum on the plane with four and five degrees of freedom in the case of the single diagonal or non-diagonal respectively.

6.3.1 The modal estimator

We start by introducing the maximum likelihood estimator, for measuring the non-Gaussian amplitude, with an optimal signal-to-noise weighting as (Fergusson et al, 2012; Regan et al, 2012; Schmittfull et al, 2013):

$$\hat{f}_{\rm NL}^{\rm th} = (2\pi)^3 \int \frac{d^3k_1}{(2\pi)^3}\frac{d^3k_2}{(2\pi)^3}\frac{d^3k_3}{(2\pi)^3}(2\pi)^3\delta_D\left(\mathbf{k}_1+\mathbf{k}_2+\mathbf{k}_3\right)\frac{B^{th}(k_1,k_2,k_3)[\delta_{\mathbf{k}_1}\delta_{\mathbf{k}_2}\delta_{\mathbf{k}_3}-3\langle\,\delta_{\mathbf{k}_1}\delta_{\mathbf{k}_2}\,\rangle\delta_{\mathbf{k}_3}]}{P_\delta(k_1)P_\delta(k_2)P_\delta(k_3)}, \tag{6.11}$$

where $P_\delta(k) = P(k) + 1/\overline{n}_g$ is the matter power spectrum, predicted by perturbation theory or measured by the simulation itself, with the absorbed Poisson shot noise term, while $\delta(\mathbf{k})$ is the non-linear overdensity field coming from observations/simulations. In order to improve the efficiency of the estimator towards the smaller non-linear scales in reconstructing the simulation bispectrum, as well as measuring the effective non-Gaussian amplitude generated by the late-time gravitational evolution, we will use here the non-linear matter power spectrum predicted by the HALOFIT model. The theoretical bispectrum, $B^{th}(k_1,k_2,k_3)$, is the one we wish to test upon the sample. Moreover, the linear term $\langle\,\delta_{\mathbf{k}_1}\delta_{\mathbf{k}_2}\,\rangle\delta_{\mathbf{k}_3}$ takes into account any kind of inhomogeneities coming from systematic effects

in the dataset at hand. In the case of a homogeneous field ($\delta_{\mathbf{k}=0} = 0$), as assumed for the simulations used here, such term disappears. Furthermore, the signal-to-noise weighting uses only the diagonal part of the bispectrum estimator covariance (*i.e.* $P(k_1)P(k_2)P(k_3)$ term in the denominator). A brute force implementation of the bispectrum estimator, as it appears in the above equation, is not very useful since it needs $\mathcal{O}(N^6)$ operations. This can be seen after applying the triangle condition, imposed by the translation invariance of the three point correlator in a homogeneous and isotropic Universe.

The expected value of the estimator above, considering a large set of realizations of the observed density field $\delta(\mathbf{k})$, is given by:

$$\langle\, \hat{f}_{\rm NL}^{\rm th} \,\rangle = \frac{(2\pi)^3}{N_{\rm th}} \int \frac{d^3k_1}{(2\pi)^3}\frac{d^3k_2}{(2\pi)^3}\frac{d^3k_3}{(2\pi)^3}(2\pi)^6\delta_D^2(\mathbf{k}_1+\mathbf{k}_2+\mathbf{k}_3)\frac{B^{\rm th}(k_1,k_2,k_3)B^{\rm obs}(k_1,k_2,k_3)}{P_\delta(k_1)P_\delta(k_2)P_\delta(k_3)}, \quad (6.12)$$

where we substituted the expected value of the three-point function of the observational density field with its respective bispectrum [Eq. (3.98)]. For now the normalisation $N_{\rm th}$ is just a value, but shortly we will derive an expression for it coming from the estimator itself. In addition, we can substitute one of the two Dirac deltas with $\delta_D\,(\mathbf{0}) = V/(2\pi)^3$, where V is the volume of the simulation, since only one is need to impose the triangle condition. The final step is to perform the angular integration, after taking into advantage the expansion of the Dirac delta into spherical harmonics, given by:

$$\begin{aligned}\delta_D\,(\mathbf{k}_1+\mathbf{k}_2+\mathbf{k}_3) = 8\int d^3x \sum_{l_1m_1} i^{l_1} j_{l_1}(k_1x)Y_{l_1m_1}(\hat{\mathbf{k}}_1)Y^*_{l_1m_1}(\hat{\mathbf{x}}) \\ \times \sum_{l_2m_2} i^{l_2} j_{l_2}(k_2x)Y_{l_2m_2}(\hat{\mathbf{k}}_2)Y^*_{l_2m_2}(\hat{\mathbf{x}}) \sum_{l_3m_3} i^{l_3} j_{l_3}(k_3x)Y_{l_3m_3}(\hat{\mathbf{k}}_3)Y^*_{l_3m_3}(\hat{\mathbf{x}}). \quad (6.13)\end{aligned}$$

If we apply the above in Eq. (6.12), we get a constant term from $\int d\Omega_{\hat{\mathbf{k}}_i} Y_{l,m}(\hat{\mathbf{k}}_i)Y_{00}(\hat{\mathbf{k}}_i) = 2\sqrt{\pi}\delta_{l0}\delta_{m0}$ and a factor from the integration over $\int d\Omega_{\hat{\mathbf{x}}} Y^*_{00}(\hat{\mathbf{x}})Y^*_{00}(\hat{\mathbf{x}})Y^*_{00}(\hat{\mathbf{x}}) = G^{000}_{000} = 1/(2\sqrt{\pi})$, where $G^{l_1l_2l_3}_{m_1m_2m_3}$ is the Gaunt integral. The integration over the Bessel functions is the one imposing the triangle condition on the Fourier modes, generating a factor of $(\pi/4)k_1k_2k_3$ for a closed triangle and zero otherwise. Combining all these together, the

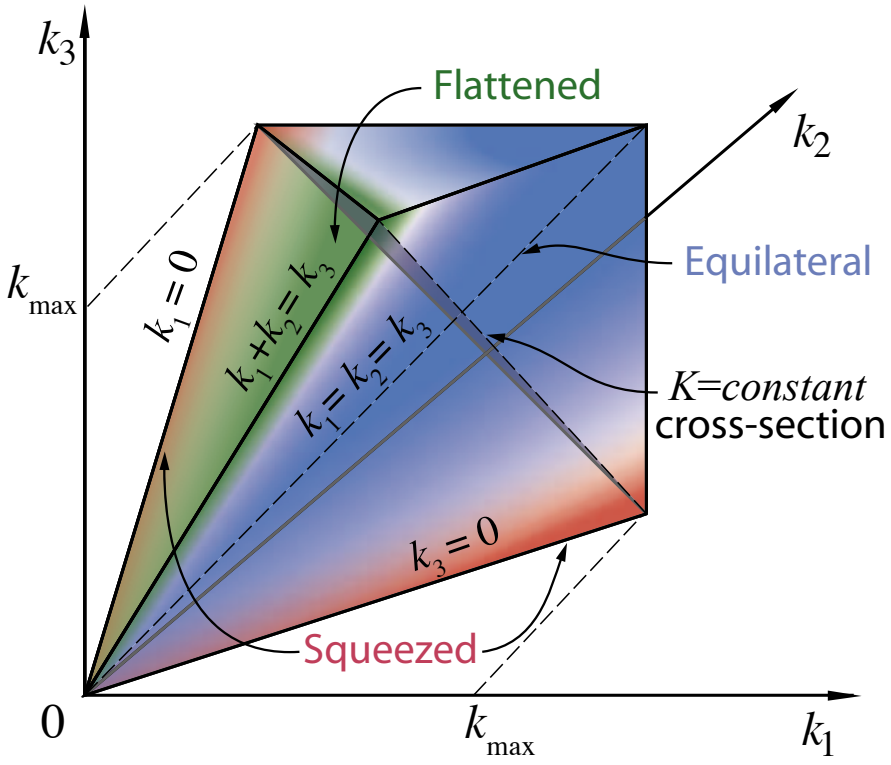

Figure 6.1 – The tetrahedral domain as defined by the triangle condition, $k_1 \geq k_2 \geq k_3$. The volume is bounded in each side towards the small scales from the maximum wavevector value we consider. Here it is assumed that the minimum mode value is zero. In a simulation of survey large scales are also bounded by the observed volume hence there is in principle a cut in the corner of the plot (large scales) defined by $k_{\rm min}$. The regions where different configurations reside are highlighted. Source: Lazanu et al (2016).

expected value of the estimator becomes simply:

$$\langle \hat{f}_{\rm NL}^{\rm th} \rangle = \frac{1}{N_{\rm th}} \frac{V}{\pi} \int_{\mathcal{V}_B} dk_1 dk_2 dk_3 \frac{k_1 k_2 k_3 B^{\rm th}(k_1,k_2,k_3) B^{\rm obs}(k_1,k_2,k_3)}{P_\delta(k_1) P_\delta(k_2) P_\delta(k_3)}. \tag{6.14}$$

Demanding the above to be equal to unity in the case of $B^{\rm obs} = B^{\rm th}$, we get the normalisation factor to be:

$$N_{\rm th} = \frac{V}{\pi} \int_{\mathcal{V}_B} dk_1 dk_2 dk_3 \frac{k_1 k_2 k_3 [B^{\rm th}(k_1,k_2,k_3)]^2}{P_\delta(k_1) P_\delta(k_2) P_\delta(k_3)}. \tag{6.15}$$

The integration is done over a tetrahedral volume $\mathcal{V}_B$, a visualization of which can be found in Figure 6.1. The domain is defined from the triangle condition (*i.e.* $k_1 \geq k_2 \geq k_3$), where the minimum magnitude value of each mode is bounded by the large scale limit of the simulating box (*i.e.* the fundamental frequency $k_f = k_{\rm min} = 2\pi/V^{1/3}$). On the other hand, its maximum value is defined by the resolution of the simulation at hand. The form of the domain is a tetrahedron with a glued triangular pyramid on top of it. Although, the full shape is shown in Figure 6.1, we only need a sixth of it due to the symmetries of the bispectrum. Taking advantage the form of the estimator's expected value [Eq. (6.14)], we can define an inner product for two functions on the tetrahedral domain as:

$$T[f,g] = \langle f,g \rangle = \frac{V}{\pi} \int_{\mathcal{V}_B} f(k_1,k_2,k_3) g(k_1,k_2,k_3) w(k_1,k_2,k_3) dV_k, \tag{6.16}$$

where the fundamental cell is $dV_k = dk_1\, dk_2\, dk_3$ and $w(k_1,k_2,k_3)$ is a weight function defined appropriately. One can easily obtain the volume of the tetrahedral domain as $T[1] = k_{\rm max}^3/2$. The inner product of two signal-to-noise weighted bispectra can be used to achieve a comparison between a bispectrum coming from the simulation/survey with the theoretical prediction (Babich et al, 2004; Fergusson et al, 2012). It is given as

$$\langle B_i, B_j \rangle \equiv \frac{V}{\pi} \int_{\mathcal{V}_B} dV_k \frac{B_i(k_1,k_2,k_3) B_j(k_1,k_2,k_3)}{P_\delta(k_1) P_\delta(k_2) P_\delta(k_3)}, \tag{6.17}$$

and the shape correlator is given by:

$$C(B_i,B_j) = \frac{\langle B_i, B_j \rangle}{\sqrt{\langle B_i, B_i \rangle \langle B_j, B_j \rangle}}. \tag{6.18}$$

where it defines how similar two bispectrum shapes are and can be used to compare theoretical and simulated bispectra. Furthermore, it can be used to test the convergence of the modal expansion, indicating the performance of the modal decomposition. Moreover, if we take the norm of the inner product, we can get the signal-to-noise squared for the bispectrum as

$$|B|^2 = \frac{V}{(2\pi)^3}\int_{\mathcal{V}_B} dV_k \frac{s_B B^2(k_1,k_2,k_3)}{\Delta B^2(k_1,k_2,k_3)} = \frac{\langle B,B\rangle}{6(2\pi)^3}, \tag{6.19}$$

where the diagonal part of the bispectrum variance is denoted as ΔB^2 and is given by (Scoccimarro et al, 1998; Scoccimarro et al, 2004):

$$\Delta B^2(k_1,k_2,k_3) = (2\pi)^3 \frac{s_B P_\delta(k_1)P_\delta(k_2)P_\delta(k_3)}{8\pi^2 k_1 k_2 k_3}, \tag{6.20}$$

where the parameter s_B is equal to 6 if the formed triangle is an equilateral, 2 if it is isosceles and unity otherwise. Therefore we can see that the signal-to-noise ratio of the estimator is consistent with the work of (Scoccimarro et al, 1998; Scoccimarro et al, 2004; Sefusatti et al, 2012).

6.3.2 Modal decomposition

Having defined the inner product of two bispectra, we can now expand any 3D bispectrum on a basis $Q_n(k_1,k_2,k_3)$, defined on the tetrahedral domain, compressing the information of the full bispectrum into the coefficients of the expansion. We can write the noise weighted bispectrum as:

$$\frac{\sqrt{k_1k_2k_3}B^{\rm th}(k_1,k_2,k_3)}{\sqrt{P_\delta(k_1)P_\delta(k_2)P_\delta(k_3)}} = \sum_{n=0}^{n_{\rm max}-1} \alpha_n^Q Q_n(k_1,k_2,k_3). \tag{6.21}$$

The convergence of the estimator depends on the size of the basis, *i.e.* $n_{\rm max}$, and the desired accuracy is achieved with only a small number of coefficients (Schmittfull et al, 2013) of $\mathcal{O}(50-100)$. This means that increasing the number of modes contributes negligible corrections to the reconstructed theory bispectrum. The reason that we choose to project the weighted signal-to-noise bispectrum will become clear later on, however note that a no-weight expansion can be chosen.

The basis $Q_n(k_1,k_2,k_3)$ is constructed on the same domain to the one generated by the non-separable bispectrum we wish to expand, while the desired separability should be

taken into account. This is done by creating one dimensional functions $q_r(k_i)$ in the *ith* direction, which are orthogonal and well behaved over the full tetrahedral domain. The choice of the modal functions does not affect the final outcome of the decomposition, as it was shown in the work of (Fergusson et al, 2010a), where they test the convergence and results for a variety of different basis. An efficient choice of basis is a type of one dimensional polynomials on the tetrahedral domain, similar to the Legendre polynomials. These functions are constructed by taking the inner product $T[f]$ for a unit interval and using the weight $w(x) = x(4-3x)/2$. It is useful to use the modes under the transformation $x = k_1/k_{\rm max}$, $y = k_2/k_{\rm max}$ and $z = k_3/k_{\rm max}$, in order to acquire a basis on the normalised domain that could be easily generalised to any different scale limits. The orthogonal polynomials are build from the following determinant (Fergusson et al, 2010a):

$$q_n(x) = \frac{1}{\mathcal{N}} \begin{vmatrix} 1/2 & 7/24 & 1/5 & ... & w_n \\ 7/24 & 1/5 & 3/20 & ... & w_{n+1} \\ ... & ... & ... & ... & ... \\ w_{n-1} & w_n & w_{n+1} & ... & w_{2n-1} \\ 1 & x & x^2 & ... & x^n \end{vmatrix}, \tag{6.22}$$

where

$$w_n \equiv T[x^n] = \frac{n+6}{2(n+3)(n+2)}. \tag{6.23}$$

The normalisation of the modal functions is chosen in such a way that the inner product $\langle q_n(x), q_m(x) \rangle = 1$, *i.e.* we choose $q_n(x)$ to be orthogonal in one dimension:

$$\langle q_n, q_p \rangle = \int_{\mathcal{V}_B q_n(x)} q_p(x)\, d\mathcal{V}_B = \delta_{np}. \tag{6.24}$$

From these well behaved polynomials, where we present the first few of them in Figure 6.2, we can build the three-dimension separable mode basis Q_n, which will be ultimately used to decompose the bispectrum of interest, from:

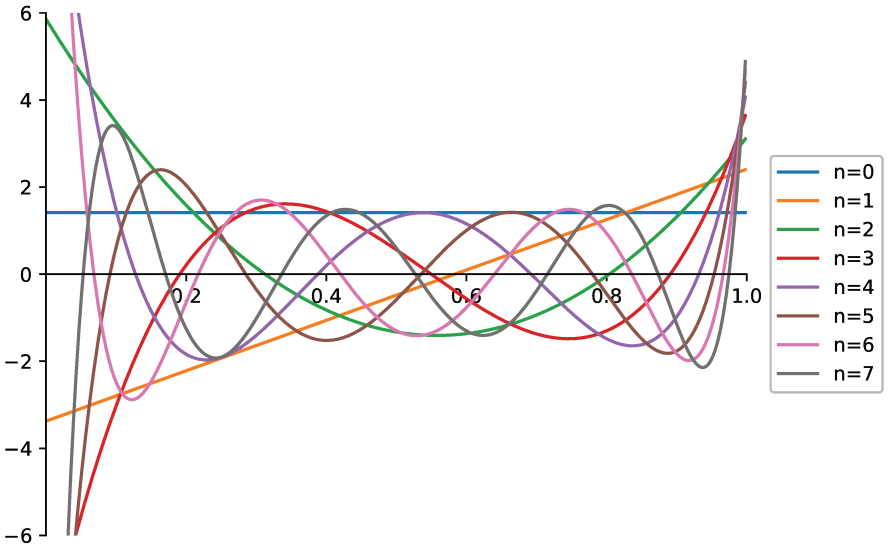

Figure 6.2 – The first eight orthogonal one dimensional polynomials $q_n(x)$ defined on the tetrahedral. They are well defined and well behaved within the boundaries of the domain. Source: (Fergusson et al, 2010a)

$$Q_n(x,y,z) = \frac{1}{6}[q_p(x)q_r(y)q_s(z) + q_r(x)q_s(y)q_p(z) + q_s(x)q_p(y)q_r(z) + \ 3 \ \text{perm}] = q_{\{p}q_s q_{r\}}, \tag{6.25}$$

where the label of the basis is given by $n = p + r + s$ and the indices p, r, s denote the degree of the constructed polynomial, while $\{prs\}$ means symmetrization over the indices. The mapping between a triplet prs and the basis label n is done by ordering the triplet in such a way that Q_n are grouped by the total order of the polynomials that they came from (see (Fergusson et al, 2010a) for details on the ordering). Having constructed the basis we can define its inner product as:

$$\gamma_{nm} \equiv \langle Q_n, Q_m \rangle = \frac{V}{\pi} \int_{\mathcal{V}_B} dV_k Q_n(k_1,k_2,k_3) Q_m(k_1,k_2,k_3). \tag{6.26}$$

The matrix γ_{nm} is not in general diagonal, it displays though partial orthogonality. The construction of the γ_{nm} matrix exploits the separability of the basis Q_n and thus its

calculation can be computationally affordable. However, its numerical cost might be increased in the case of a large number of modes, *i.e.* large basis. Nevertheless, γ_{nm} matrix must be computed only ones, saved and reused for any desirable decomposition.

The γ matrix is not diagonal (nearly orthogonal), therefore we would like to have the convenience of an orthogonal basis. We proceed to its orthonormalization, by choosing the Cholesky decomposition, due to its numerical stability. The γ matrix will be decomposed into its associated upper and lower triangular matrices as:

$$\gamma_{nm} = \sum_{r}^{n_{\max}} \lambda_{nr}^{-1} (\lambda_{rm}^{-1})^T, \tag{6.27}$$

where λ_{nm} is the lower triangular matrix. We can use this now to make the basis orthogonal as

$$R_m(k_1, k_2, k_3) = \sum_{p=0}^{n_{\max}} \lambda_{mp} Q_p(k_1, k_2, k_3), \tag{6.28}$$

where

$$\langle R_m, R_n \rangle = \delta_{nm}. \tag{6.29}$$

Any theoretical bispectrum can now be decomposed in a separable basis, by calculating the coefficients with respect to the orthogonal basis as

$$\alpha_n^R = \left\langle R_n, \frac{\sqrt{k_1 k_2 k_3} B^{\rm th}(k_1, k_2, k_3)}{P_\delta(k_1) P_\delta(k_2) P_\delta(k_3)} \right\rangle. \tag{6.30}$$

The above is equivalent to

$$\alpha_n^Q = \sum_{p=0}^{n_{\max}} \lambda_{pm} \alpha_p^R. \tag{6.31}$$

The derived coefficients can be used now in Eq. (6.21) to get the reconstructed bispectrum. Note that, in order to calculate α_n^R in the case of a non-separable bispectrum, the

3D integral over the tetrahedral domain must be performed. Therefore, there is some computational effort to orthonormalise the basis and to derive α_n^R ($\mathcal{O}(n_{\rm max}N^3)$ operations). However, it needs to be done only ones, while the derived coefficients can be used for any domain bounds, since the γ matrix is calculated for the normalised tetrahedron. Note that, there is a trade off between the Q and R basis. More specifically, Q_n is not orthogonal, but its elements are separable templates, while R_n is orthogonal but non-separable. Therefore, the Q-basis is ideal for template-fitting and extracting modal coefficients from data, while the R-basis is well-suited for the theoretical interpretation of the results [see Eqs. (6.37), (6.38) and (6.38)]. In the case of a separable shape, it is faster and easier to calculate first the coefficients of the Q_n basis from:

$$\alpha_n^Q = \sum_{p=0}^{n_{\rm max}} \gamma_{np}^{-1} \left\langle Q_n, \frac{\sqrt{k_1k_2k_3}B^{\rm th}(k_1,k_2,k_3)}{P_\delta(k_1)P_\delta(k_2)P_\delta(k_3)} \right\rangle, \tag{6.32}$$

and then derive the modes of the orthogonal basis from

$$\alpha_n^R = \sum_{p=0}^{n_{\rm max}} \lambda_{pn}^{-1}\alpha_p^Q. \tag{6.33}$$

Both the above, are equivalent and give the final decomposition of the theoretical bispectrum.

The most powerful result of the modal decomposition is the reduction of the calculations, regarding the simulation or survey bispectrum. If we substitute the modal decomposition of the theory in the optimal estimator of Eq. (6.12) and expand the Dirac delta in plane waves we get:

$$\hat{f}_{\rm NL}^{\rm th} = \frac{(2\pi)^3}{N_{\rm TH}} \sum_n \alpha_n^Q \int d\mathbf{x}^3 [M_p(\mathbf{x})M_r(\mathbf{x})M_s(\mathbf{x})], \tag{6.34}$$

where

$$M_p(\mathbf{x}) = \int \frac{d^3\mathbf{k}}{(2\pi)^3} \frac{\delta_{\mathbf{k}} q_p(k)}{\sqrt{k P_\delta(k)}}. \tag{6.35}$$

The above can be calculated in an efficient way by using a Fourier transformation. The coefficients of the decomposition for the simulation is now given by:

$$\beta_n^Q = \int d\mathbf{x}^3 [M_p(\mathbf{x}) M_r(\mathbf{x}) M_s(\mathbf{x})], \tag{6.36}$$

which only adds a 3D integration over position space in the computational burden. The final operations are $\mathcal{O}(N^3)$ (Schmittfull et al, 2013). We can then transform the coefficients to the orthogonal frame just by using Eq. (6.33). The bispectrum of the dataset can be now derived for a single realization, given sufficient signal-to-noise, as (Fergusson et al, 2012; Regan et al, 2012)

$$\begin{aligned} B^{\rm obs}(k_1,k_2,k_3) &= \frac{\sqrt{P_\delta(k_1)P_\delta(k_2)P_\delta(k_3)}}{\sqrt{k_1 k_2 k_3}} \sum_n \beta_n^R R_n(k_1,k_2,k_3) \\ &= \frac{\sqrt{P_\delta(k_1)P_\delta(k_2)P_\delta(k_3)}}{\sqrt{k_1 k_2 k_3}} \sum_n \beta_n^Q Q_n(k_1,k_2,k_3), \end{aligned} \tag{6.37}$$

which is a simple summation over the number of modes (Schmittfull et al, 2013). For a desired set of configurations it can be calculated though a triangle loop with a negligible computational cost, *i.e.* only a small vector-vector multiplication for each iteration. In the standard approach one needs to go through all the possible triangles formed in the simulation grid, which bares a tremendous computational effort. Although, all the above relations are done assuming a continuous field, the transformation to the discreet version is simple, *e.g.* when we use Eq. (6.35) the applied algorithm is the discrete Fourier transformation, being consistent with the resolution of the simulation.

The coefficients of the projected theoretical bispectrum, obviously, depend on the model. However this is not true for the coefficients of the simulation, since the model dependence introduced in the form of power spectrum is cancelled as shown in Eq. (6.37).

Therefore, the reconstruction of the bispectrum is done in a model independent manner (Fergusson et al, 2012). Now it is clear why we decomposed the weighted bispectrum in the first place. By doing this we are able to remove the explicit dependence on signal-to-noise weight, coming from the estimator itself. The estimator is reduced now in the following simple summation

$$\hat{f}_{\rm NL}^{\rm th} = \frac{1}{N_{\rm th}} \sum_m \alpha_m^R \beta_m^R, \tag{6.38}$$

whose expectation value is given by

$$\langle \hat{f}_{\rm NL}^{\rm th} \rangle = \frac{1}{N_{\rm th}} \sum_m [\alpha_m^R]^2. \tag{6.39}$$

The above two equations imply that

$$\langle \beta_n^R \rangle = \alpha_n^R. \tag{6.40}$$

In addition we can define the shape correlation between the theory and simulations from Eq. (6.18) as

$$C_{\beta,\alpha} = C(B^{\rm obs}, B^{\rm th}) = \frac{\sum_n \alpha_n^R \langle \beta_n^R \rangle}{\sqrt{\sum_m (\alpha_m^R)^2 \sum_p \langle \beta_p^R \rangle^2}}. \tag{6.41}$$

6.3.3 Testing the pipeline and the modal expansion

The shape correlator defined in Eq. (6.18) can be used to test the convergence and accuracy of the modal decomposition of a theoretical bispectra. Substituting B_i with the decomposed theoretical bispectrum on the modal basis and B_j with the actual theoretical prediction, we can define

$$C^{\rm th} = C(\sqrt{\frac{P_\delta(k_1)P_\delta(k_2)P_\delta(k_3)}{k_1 k_2 k_3}} \sum_n \alpha_n^Q Q_n(k_1,k_2,k_3), B^{\rm th} k_1 k_2 k_3). \tag{6.42}$$

We measure the shape correlator for an increasing number of modes, to test the efficiency of the modal expansion, for three theoretical bispectra. We choose four separable shapes, *i.e.* the tree-level matter bispectrum [Eq. (3.103)] and the three types primordial bispectrum considered throughout this thesis (*i.e.* local, equilateral and orthogonal; see Sec. 2.4.4). As we have already discussed, very few bispectra share the characteristic of separability. Therefore, in order to have a more complete picture on the convergence of the modal decomposition, we choose also a non-separable theoretical bispectrum, *i.e.* the 1-loop matter bispectrum, predicted by SPT, for Gaussian initial conditions (see Sec. 3.5.3.1). The resulting shape correlators, $C^{\rm th}$, are presented in Figure 6.3 as a function of the number of modes considered in the expansion. For these tests, we do not perform any stabilization, *i.e.* the mode ordering is generated by the mapping $n = p + r + s$, without any index reshuffling.

The correlation results, between the decomposed bispectrum and the original theoretical prediction, show that the modal decomposition converges rapidly for a few three-dimensional modes. More specifically, for the local primordial bispectrum we need 23 modes to achieve a $\sim 98\%$ correlation, while for the equilateral and the tree-level matter bispectrum the correlation is $\sim 99\%$ with just 17 modes. The reason for the faster convergence of the equilateral and tree-level bispectrum with respect to local is the structure of the basis itself, which picks more signal from configurations that do not approach the squeezed triangles. On the other hand, additional modes are needed for the modal expansion to start picking signal from the squeezed configurations and accurately decompose the local primordial bispectrum. The 1-loop matter bispectrum can be decomposed by just 14 modes, where the correlation is greater than 99% at that stage. Finally, the orthogonal case is the one that needs the most modes, *i.e.* 25 modes to accomplish 97% correlation. The more modes we consider the higher the correlation and thus the efficiency of the decomposition. This indicates that beyond 40-50 modes all these bispectra can be decomposed with 99.9% correlation, which shows the great amount of compression

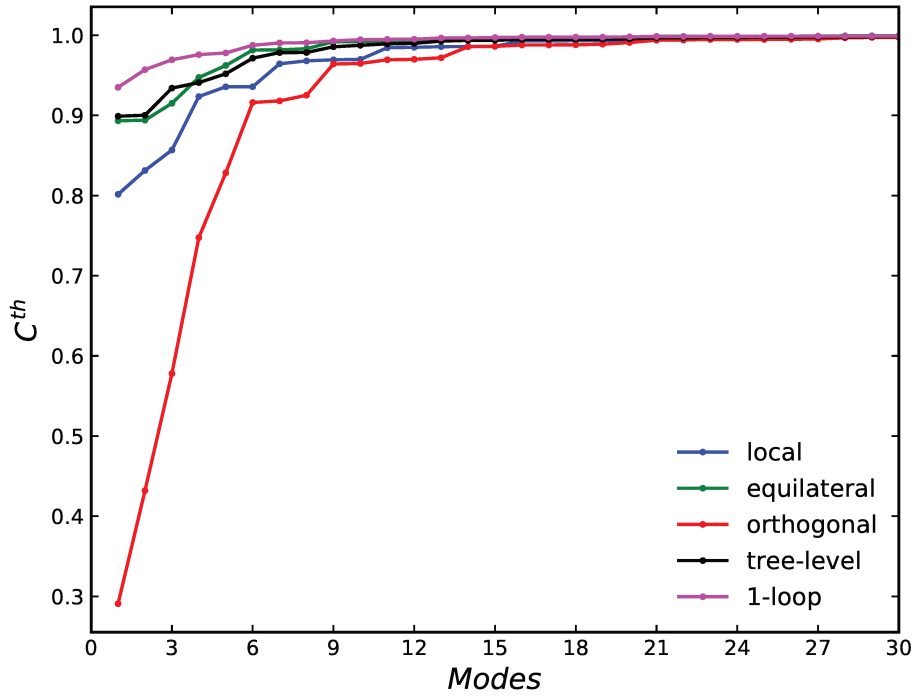

Figure 6.3 – The shape correlation, $C^{\rm th}$ [Eq. (6.42)], of the reconstructed bispectra to the original up to a given mode n. The plot includes the primordial bispectra for the local, equilateral and orthogonal PNG shapes, as well as the gravitational induced tree-level matter bispectrum, which are all separable. In addition, we show a non-separable case, which is the 1-loop matter bispectrum (see Sec. 3.5.3.1). All cases demonstrate a rapid convergence, where for 20 modes we have a correlation greater than 99%.

achieved with the modal expansion. Note that, even with 10 modes we can achieve more than 90% correlation.

The efficiency and convergence of the modal decomposition is based to the numerical stability of the γ_{nm} matrix. The measurement of the bispectrum from simulations/surveys with a large number of Fourier modes needs a larger basis for the modal expansion to converge and give accurate results. However, a large γ_{nm} matrix, inevitably, has modes that are not linearly independent (negative eigenvalues), as needed for a numerically stable decomposition. Therefore, the developed pipeline devotes a small amount of its computational time into turning γ_{nm} into a positive-defined and stable matrix.

Two methods were developed to achieve this:

Stabilization Method 1: An approach to stabilize the γ_{nm} matrix is to normalize each column and then repeatedly apply a pseudo Principal Component Analysis (PCA). Starting from one mode of the γ_{nm} matrix (*e.g.* here we start from the constant γ_{00} element[1]), we form a 1x1 γ'_{nm} sub-matrix. We proceed by increasing the element number of the square γ'_{nm} sub-matrix by one, for each step of the loop. In each iteration a different mode n, which is mapped to the triplet p, r, s in a unique way, is added from the mode pool, until all the combinations are completed. For example, in the first iteration γ'_{nm} becomes a 2x2 sub-matrix of γ_{nm}, where the mode indices (*i.e.* m and n) can take the value of the starting element (*i.e.* in our case 0) and a value that remains inside the pool of mode numbers. This first step of the loop finishes when all the unique 2x2 γ' sub-matrices, formed by all the index combinations of the initial γ_{nm} matrix, have been generated, *e.g.* $\gamma'_{nm} = \gamma_{01}$, $\gamma'_{nm} = \gamma_{02}$,..., $\gamma'_{nm} = \gamma_{010}$, *etc.*. For each iteration of element loop, the eigenvalues are calculated and the smallest is compared to a positive threshold. The index combination that is kept to form the 2x2 γ'_{nm} sub-matrix is the one that has the largest minimum eigenvalue, which is above the chosen threshold. In the next step we increase again the number of elements of the square sub-matrix by one (*i.e.* in our example it will be a 3x3) and repeat the process. If at any step of the process a mode generates a negative minimum eigenvalue, the index number is removed from the mode pool. The process stops when we reach the adopted threshold. The resulting γ'_{nm} sub-matrix, formed by the original γ_{nm}, is now stable (no negative eigenvalues) and it will be the one used for the modal decomposition algorithm.

Stabilization Method 2: An alternative would be to follow the opposite direction from the previous method. We start with the full γ_{nm} matrix and in each iteration we remove one mode index. In the first iteration, one by one, every n-th mode is removed, generating $n_{\max} - 1$ different $n_{\max} - 1 \times n_{\max} - 1$ sub-matrices (γ'_{nm}), originating from the initial γ_{nm} matrix. The sub-matrix that is kept for the next loop step corresponds to the one

[1]The zero-zero element of γ_{nm} is a constant, since it corresponds to the product of zero degree polynomials (see Figure 6.2), *i.e.* $\gamma_{00} = q_0^6 T[1] = q_0^6 k_{\max}^3/2$

with the largest minimum eigenvalue (above some chosen threshold) with respect to the rest. The same process continues until the sub-matrix γ'_{nm} has a minimum eigenvalue that is just above the positive threshold. The resulting γ'_{nm} matrix is now, like in the previous method, positive-defined and numerically stable. This method is much slower than the former, since for the first couple of iterations the γ'_{nm} sub-matrix is large and therefore the eigenvalue decomposition can be numerically cumbersome.

In order to test the efficiency of these two methods in numerically stabilizing the modal expansion, we choose a large number of modes (*e.g.* ~ 200) that devise a numerically unstable γ_{nm} matrix which is still positive-defined. We use the shape correlator [Eq. (6.42)] to test the performance and speed of the two stabilization methods on improving the convergence and accuracy of the modal decomposition. The results are presented for the test basis in Figure 6.4, where we consider the effect of the stabilization techniques on the decomposition of the primordial bispectrum for the local, equilateral and orthogonal PNG. We also consider, separately, the tree-level and 1-loop matter bispectrum.

The improvement of both methods over the results generated by the numerical unstable basis is significant for all bispectra tested. The unstabilised results show a saturation in the correlation results beyond the 10th mode, which indicates that the modal expansion does not converge. In addition, the values of $C^{\rm th}$, for all cases, are larger than 60%, which shows that the numerical unstable basis does not efficiently reconstruct the theoretical bispectra. The *Stabilization Method 1* improves immediately the correlation results, starting from the first few modes, by $\sim 30-40\%$, achieving a rapid convergence. The *Stabilization Method 2* exhibit a slower convergence (*i.e.* more modes need to be added) over the previous method, while at the same time the correlation values increase by $\sim 20-30\%$ over the unstable results. In addition, the second method takes about two orders of magnitude more time to finish than the first, as expected. For this small basis, it does not impose a problem, since both of them take a very small amount of time over the total load needed for the pipeline to finish. Further tests were performed, indicating that for larger basis

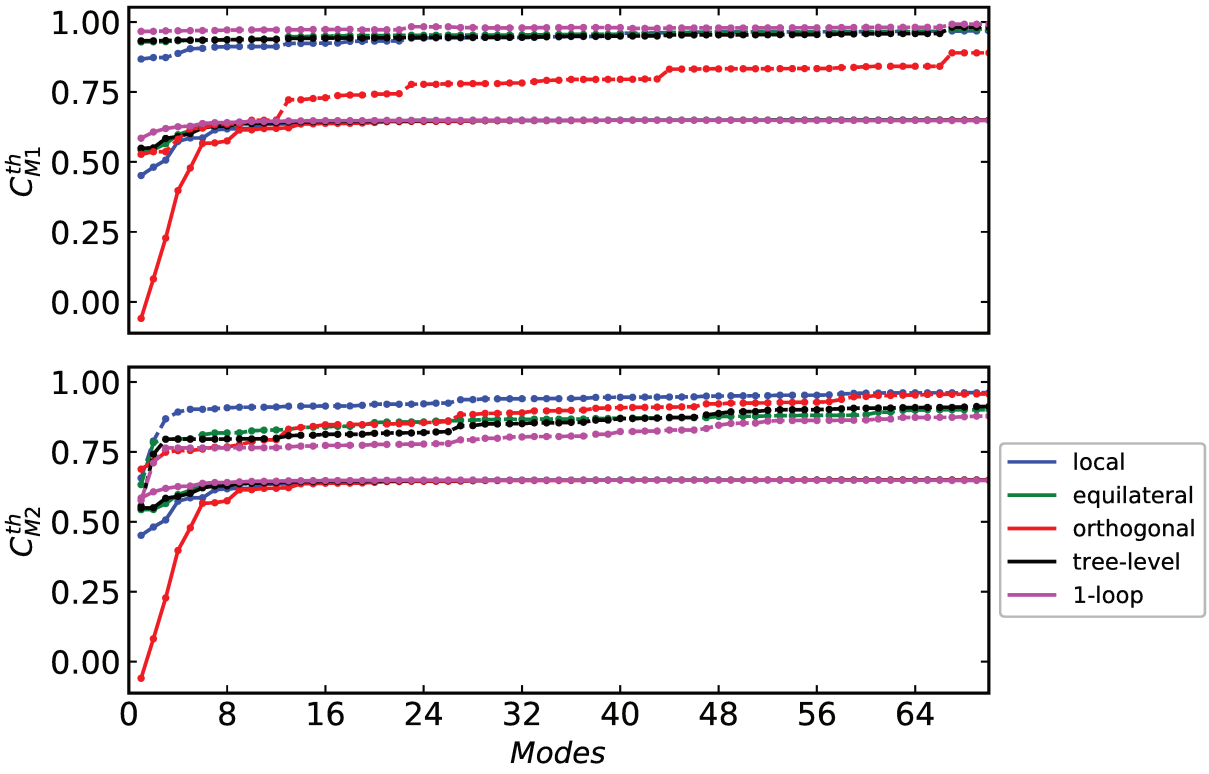

Figure 6.4 – The shape correlation of the reconstructed bispectra to the original as a function of the number of modes considered. A test basis is chosen, which is numerically unstable. Two stabilization methods are used (see main text for a description) to improve the convergence of the decomposition. The upper plot shows the effect of the *Stabilization Method 1* (C^{th}_{M1}), while the lower corresponds to *Stabilization Method 2* (C^{th}_{M2}). The solid lines represent the shape correlation results, when the unstable basis is used, while the dashed line represents the results after the stabilization is applied. The improvement over the unstable results is significant. The plot includes the primordial bispectra for the local, equilateral and orthogonal PNG shapes, as well as the gravitational induced tree-level and 1-loop matter bispectrum.

the second method can become computationally inefficient. Taking advantage of the a priori knowledge that the final stable γ_{nm} sub-matrix must be smaller than the initial, we choose the first method as our main approach.

A finally ingredient in the process of creating the most stable basis is that we start from a very large set of modes in order to produce a numerically stable γ'_{nm} sub-matrix, since we can generate a basis made from modes that are completely independent from each other.

6.4 Measuring the bispectrum from N-body simulations

Perturbation theory (Sec. 3) can provide an adequate description for the evolution of structures in the Universe up to a semi-nonlinear regime. Beyond that point, the non-linear fluctuations can become large, marking the scales at which any perturbative approach breaks down. In this non-linear regime the use of cosmological simulations is necessary in order to follow the dynamics. The main idea is to derive a numerical solution for the equations that govern the evolution of matter [Eq. (3.1)-(3.3)] in phase space. Cosmological dark matter simulations treat all matter as collisionless and neglect any physics coming from baryons, *i.e.* all matter is considered dark matter. The matter density field is sampled by partitioning phase space into N elementary cells ("particles"), that have velocities, positions and usually the same masses. These N-body particles evolve with gravity in a comoving coordinate system and depending their number we can define the mass resolution of the simulation. The main steps of the numerical simulation is first to give the initial condition of the particles. One can use (Sec. 3.3) the ZA approximation or the second order solution (2LPT) and take advantage the relations between the gravitational potential and the displacement field, that is the bases of this formalism, in order to give initial velocity and position to the particles. Usually the initial time is taken to be at some large redshift ($z \gtrsim 50$) during the matter domination era. The next step is to calculate the gravitational force from the Poisson equation in each particle due to the mass of the other particles. The derived acceleration is used to update the positions and velocities of the particles. The process is repeated in a time step fashion approaching the present, till it reaches the desired redshift. At every step tests on the conservation of energy and momentum are made as diagnostics (besides the diagnostics of the pipeline).

The differences between the various methods of performing an N-body simulations

mainly focus on the different ways of solving the Poisson equation. The naive way of calculating the force on each particle from all the neighbours, *i.e.* Particle Particle method (PP). Although the calculations are exact the computational effort scales like $\mathcal{O}(N^2)$, making it extremely challenging for a large numbers of particles. Many alternative have been proposed and the reader can find a state of the art review in (Kuhlen et al, 2012; Baldi, 2012) and reference within. For explicit details on the N-body simulations the reader is addressed to (Hockney and Eastwood, 1988). Here we will just summarize the main two algorithms used in cosmology.

The first method for improving the PP algorithm is to organize the distribution of particles in a hierarchical way, *i.e.* a tree structure (Barnes and Hut, 1986). The main idea of the tree-like division is to slit the volume in nodes, where each node is divided in equal volume subcells (eight in the case of the Octree as in (Barnes and Hut, 1986)) and each of them is splitted again in the same number as the parent node. This process continues till there is one particle or zero in each subcell. The gravitational potential is calculated by taking advantage the fact that the contribution on a particle coming from distant particles can be approximated at lower level by a multipole expansion, *i.e.* treat the particles in the distant cells as a single particle. The individual contributions are now calculated only for the neighbouring cells. This process reduces the computational cost to $\mathcal{O}(N \log N)$, while keeping the error of the approximation under control. An improvement in the speed of the algorithm of $\mathcal{O}(N)$ is possible if one chooses the Fast Multipole Method (Greengard and Rokhlin, 1997). In this case the force is computed between tree nodes and not individual particles and nodes. In order to avoid numerical divergences, a *softening length* is introduced to suppress the gravitational interactions between particles that come too close to each other. This length can give the spatial resolution of the simulation.

An other type of algorithm is the *Particle Mesh* (PM) (Hockney and Eastwood, 1988) where in order to define a density field the particles are placed on a mesh. The gravitational forces are then calculated from a Fast Fourier transformation on the grid and

they are interpolated back to particles. The resulting computational effort is again $\mathcal{O}(N_g \log N_g)$, only the number of grid points is usually 2^3 times larger than the particles (Kuhlen et al, 2012). In this case the softening length is defined by the mesh size L/N_g, where L is the size of the box. For a length big enough to avoid numerical divergences and achieve good resolution, a large number of particles and grid cells must be chosen making this method computationally and memory demanding. Hybrid methods have been introduced that combine the desired characteristics from both methods. Adaptive mesh techniques (Couchman, 1991) can improve the resolution of the PM method by introducing an adaptive mesh that is refined using a tree algorithm in regions that demand higher accuracy in the calculation of the gravitational force. One of the most widely used tree-PM code is $\mathrm{G}_{\mathrm{ADGET}}$ (Springel, 2005) and it will be the one used for the simulations listed in the next section.

6.4.1 Modal decomposed bispectrum and PNG measurements

In order to measure the bispectrum from a set of cosmological simulations we need to define the overdensity field in Fourier space, which is assumed in theoretical prediction to be a continuous random field. This is not the case for N-body simulations where we have N_p discrete particles. The density is defined in such case as

$$\rho(\mathbf{x}) = \sum_{i=1}^{N_p} m_i \delta_D \left(\mathbf{x} - \mathbf{x}_i\right), \tag{6.43}$$

and the overdensity will be

$$\delta(\mathbf{x}) = \frac{1}{\overline{n}} \sum_{i=1}^{N_p} m_i \delta_D \left(\mathbf{x} - \mathbf{x}_i\right) - 1, \tag{6.44}$$

where $\overline{n}$ is the mean number of particles inside the cubic volume $V = L^3$ (*i.e.* $\overline{n} = N_p/V$). In order to take advantage of the Fast Fourier transformation technique we need to interpolate the density field into a grid of size N_g in each direction. The derived overdensity

field will give a Fourier coefficient, where its maximum accessible is the Nyquist frequency, $k_{\rm Nyq} = N_p k_f/2$, which k_f being the fundamental frequency of the volume (*i.e.* $k_f = 2\pi/L$). The distribution of the particles to the nearby grid points is called a *mass assignment scheme* and is done by applying a *shape function*, which quantifies how the mass is distributed on the grid. The assigned density field will be given by

$$\rho(\mathbf{x}) = \int d^3x' \rho(\mathbf{x}') W(\mathbf{x} - \mathbf{x}'), \tag{6.45}$$

where the window function $W(\mathbf{x} - \mathbf{x}')$ defines the amount of density distributed at a grid point $\mathbf{x}^g$ with a separation $\mathbf{x}$. Therefore, the interpolated overdensity field on the grid is given by

$$\delta(\mathbf{x}_j^g) = \frac{1}{\overline{n}} \sum_{i=1}^{N_p} W(\mathbf{x}_j^g - \mathbf{x}_i) - 1. \tag{6.46}$$

The window function can be calculated for each distribution scheme from the integral over the cell volume of the shape function

$$W(\mathbf{x}_j^g - \mathbf{x}_i) = \frac{1}{H^3} \int_{\mathbf{x}_j^g} d^x S(\mathbf{x} - \mathbf{x}_i), \tag{6.47}$$

where $H = L/N_g$ is the grid spacing. The are mainly three schemes widely used, categorized according to number of grid points each particle is assigned to. The simplest is the Nearest Grid Point (NGP) where the particle is assigned only to the cell that contains it, which is obviously a very crude assignment scheme. In this case the window function is the top-hat given in one-dimension as:

$$W(d) = \begin{cases} 1, & \text{if } \left|\dfrac{d}{H}\right| \leq \dfrac{1}{2} \\ 0, & \text{otherwise,} \end{cases} \tag{6.48}$$

where $d = |x^g - x_i|$ is the distance of the particle from a grid point. Its Fourier transform

is

$$W_{NGP}(k) = \frac{\sin(\pi k)}{2k_{\mathrm{Nyq}}}. \tag{6.49}$$

The most commonly used scheme is the Cloud-in-Cell (CIC), where each particle is assigned to the two neighbouring grid points (eight in the 3D case). The window function is given by:

$$W(d) = \begin{cases} 1 - \dfrac{d}{H}, & \text{if } d \leq H \\ 0, & \text{otherwise,} \end{cases} \tag{6.50}$$

and its Fourier coefficient is given by

$$W_{CIC}(k) = W_{NGP}^2 = \left(\frac{\sin(\pi k)}{2k_{\mathrm{Nyq}}} \right)^2. \tag{6.51}$$

Finally the Triangular Shaped Cloud (TSC) distributes the point to three neighbouring grid cells (28 for the 3D case) and is the smoothest of these three. The window function is given by

$$W(d) = \begin{cases} \dfrac{3}{4} - \left(\dfrac{d}{H} \right)^2, & \text{if } d \leq \dfrac{H}{2} \\ \dfrac{1}{2} \left(\dfrac{3}{2} - \dfrac{d}{H} \right)^2, & \text{if } \dfrac{H}{2} \leq d \leq \dfrac{3H}{2} \\ 0, & \text{otherwise,} \end{cases} \tag{6.52}$$

its Fourier transformation is given by

$$W_{TSC} = W_{NGP}^3 = \left(\frac{\sin(\pi k)}{2k_{\mathrm{Nyq}}} \right)^3, \tag{6.53}$$

all the above are easily generalised for a three-dimensional grid for the real and Fourier

space as

$$W(\mathbf{d}) = W(d_1)W(d_2)W(d_3), \tag{6.54}$$

$$W(\mathbf{k}) = \left(\frac{\sin(\pi k_1)}{2k_{\rm Nyq}}\frac{\sin(\pi k_2)}{2k_{\rm Nyq}}\frac{\sin(\pi k_3)}{2k_{\rm Nyq}}\right)^p, \tag{6.55}$$

where $p = 1, 2, 3$ for the NGP, CIC and TSC respectively. The final overdensity at each grid point will be given in three dimensions by

$$\rho(\mathbf{x}_g) = \frac{\sum_{i=1}^{N_p} m_i W(|d_x|)W(|d_y|)W(|d_z|)}{H^3}. \tag{6.56}$$

The above means that the overdensity contrast will be now the convolved one with the window function and not the actual overdensity. Therefore ,we need to deconvolve the Fourier coefficients by simply dividing the resulting overdensity with the Fourier transform of the window function, *i.e.* $\delta_{\mathbf{k}} = \delta^g_{\mathbf{k}}/W(\mathbf{k})$ with $\delta^g_{\mathbf{k}}$ being the interpolated overdensity contrast on the grid. The final step is to remove from the measured correlators the Poisson noise.

Here we will present the bispectrum results coming from 20 N-body with 512^3 number of particles in a box of side $L = 2400\,$Mpc/h. The simulations start from redshift $z = 49$, where the Gaussian initial conditions are generated by using 2LPT method (Crocce et al, 2006), which applies an initial displacement field to the particles as discussed in Sec. 3.3. The evolution of the N-body towards $z = 0.5$ is done by using $\rm G_{ADGET}$ 2 (Springel, 2005). The final overdensity field at the desired redshift is interpolated on a grid by using the CIC mass assignment scheme. A Fast Fourier transformation is applied to get $\delta_{\mathbf{k}}$, which is later deconvolved with the kernel $W_{CIC}(\mathbf{k})$ [Eq. (6.55)]. The cosmology used in this section differs from the rest of this work, where we assume a flat ΛCDM cosmology with $\Omega_m = 0.223$, $\Omega_b = 0.047$, $h = 0.7$, $\Delta^2_\zeta = 2.5887 \times 10^{-9}$ and $n_s = 0.95$. Finally in order to avoid aliasing effects that can affect the results near the Nyquist frequency, we stay well bellow that at $|\mathbf{k}| \leq 0.3 k_{\rm Nyq}$. The main objective here is to test the efficiency and the

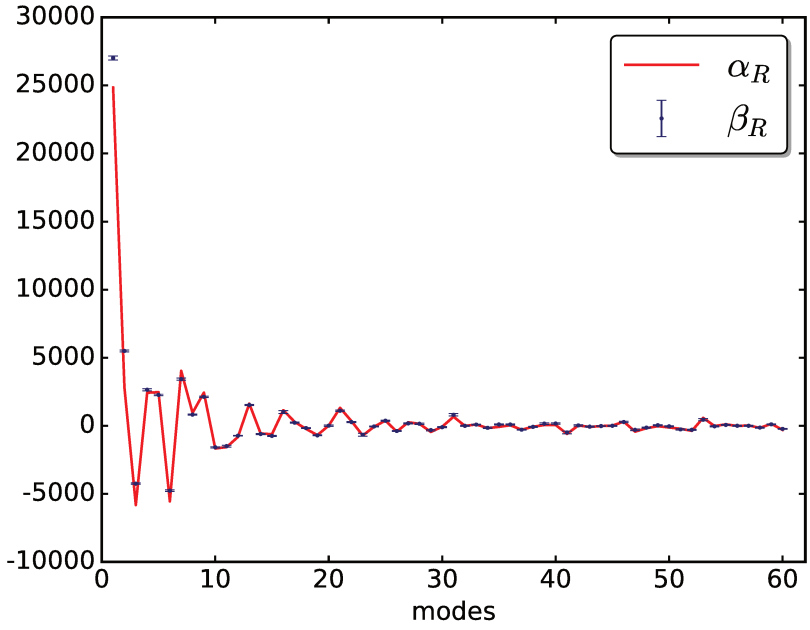

Figure 6.5 – The coefficient of the theory α_R (red solid line) and simulations β_R (blue points) with respect to the number of modes, after the decomposition on the orthonormal basis R_n as given by Eqs. (6.30) and (6.37) respectively. Errors are plotted as well. The shape correlation between the two [Eq. (6.41)] is $C_{\beta,\alpha} = 0.992$

convergence of the pipeline and not to test any PT theoretical predictions, although a comparison is performed.

The bispectrum is decomposed into the polynomial basis defined on the tetrahedron, as given by Eq. (6.37) together with Eq. (6.36)eq:Mmat. In Figure 6.5 we present the coefficients of the theory and simulations coming from the modal decomposition on the same three dimensional orthonormal basis R_n. The shape correlation between the two is $C_{\beta\alpha} = 0.992$, indicating a good agreement. The number of modes needed to fully reconstruct the bispectrum of simulations is $n_{\rm max} = 60$. Having precomputed the γ matrix needed for the decomposition, the pipeline takes 2-3 minutes on a single core to fully decompose the bispectrum of each single simulation realization up to the $k_{\rm max}$ considered here. From the derived coefficients we can now reconstruct the bispectrum of simulations for any desired triangle configurations with the computational cost of a vector summation

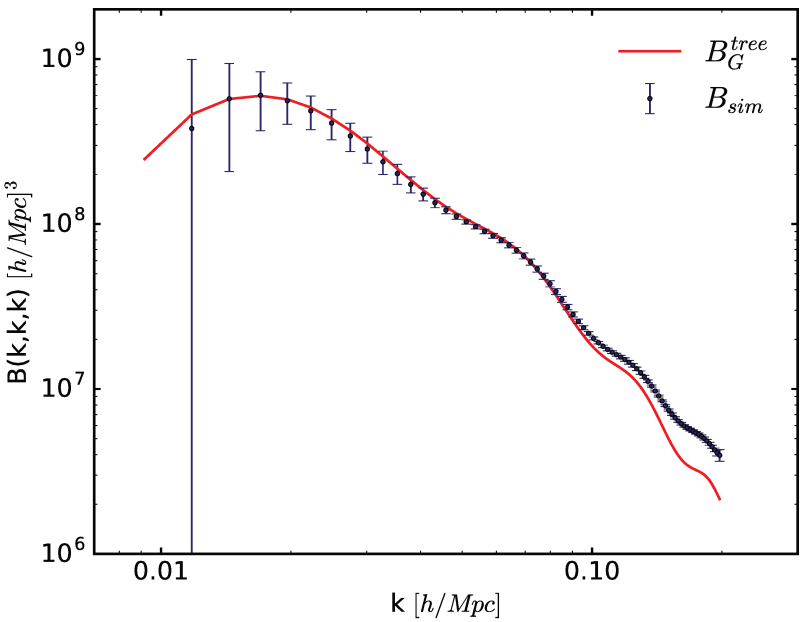

Figure 6.6 – The bispectrum derived from Gaussian dark matter N-body simulations (blue points) at $z = 0.5$ for the equilateral configurations. The red solid line is the tree level bispectrum of matter as generated from the non-linear nature of gravity. The errors are given by the samples standard deviation, where we assume that each simulation is independent from the other (*i.e.* diagonal covariance).

inside a loop over the triangles of interest.

Following this procedure we reconstruct the bispectrum of simulations for the equilateral configurations and present the results in Figure 6.6. In addition the tree level gravitational bispectrum from SPT [Eq. (3.103)] is also plotted for comparison. The results show that the tree level prediction deviates $\mathcal{O}(20\%)$ from the simulation results at $k \simeq 0.13\,\mathrm{h/Mpc}$. Although the resolution of the simulations is small, we are in agreement with the findings of (Lazanu et al, 2016), where they use the modal estimator to decompose the bispectrum from a set of simulations with different resolutions and compare with a variety of PT models. These results are not surprising since the bispectrum is sensitive to non-linearities induced by the gravitational evolution and higher order corrections are needed to improve the fit with simulations as we progress towards the semi-nonlinear

tree-level bispectrum		1-loop bispectrum	
$f_{\rm NL}$	$C_{\beta\alpha}$	$f_{\rm NL}$	$C_{\beta\alpha}$
1.25	0.91	1.07	0.984

Table 6.1 – Measurements of the effective non-Gaussianity, generated by the gravitational evolution, from a single realization. Two theoretical templates are fitted, *i.e.* the tree-level and the 1-loop matter bispectrum.

regime (up to the scales of validity of SPT).

Finally, up to the scale considered, we measure the effective $f_{\rm NL}$ value, corresponding to the late-time gravitational evolution. Since we have normalized the estimator already to the effective theoretical $f_{\rm NL}$ value, we expect the results to be close to unity if the decomposition of both the theoretical and observational bispectrum was accurate. Indeed that is what we measure, $f_{\rm NL}^{\rm eff} = 1.058 \pm 0.005$, where the deviation from unity can be attributed to the fact that the tree-level bispectrum, used to normalise the estimator deviates towards the smaller scales (Figure 6.6).

The pipeline is further tested on a single box simulation with side $L = 600\,{\rm Mpc/h}$ and 512^3 number of particles. The simulations starts again at redshift $z = 49$, where the initial conditions are Gaussian. The final redshift of the realisation is $z = 0$, while the cosmology is now slightly different than before, *i.e.* $\Omega_m = 0.2241$, $\Omega_b = 0.047$, $h = 0.703$. As done before, we use CIC scheme to assign the particles on the grid and measure $\delta_{\mathbf{k}}$ from a fast Fourier transformation. We limit the scale range up to $k_{\rm max} = k_{\rm Nyq}/8 \approx 0.335\,{\rm h/Mpc}$, in order to retain the analysis inside the linear regime. The coefficients of the modal decomposition are plotted in Figure 6.7, where we have considered both the tree-level bispectrum, as well as the 1-loop predictions.

The coefficient comparison show a good agreement with each other, where $\alpha_R^{\text{1-loop}}$ seems to agree more with the modal coefficients of the simulation. In order to quantify this, we show in Table 6.1 the results of the effective $f_{\rm NL}$ parameter measured by the fitting of the two theoretical templates.

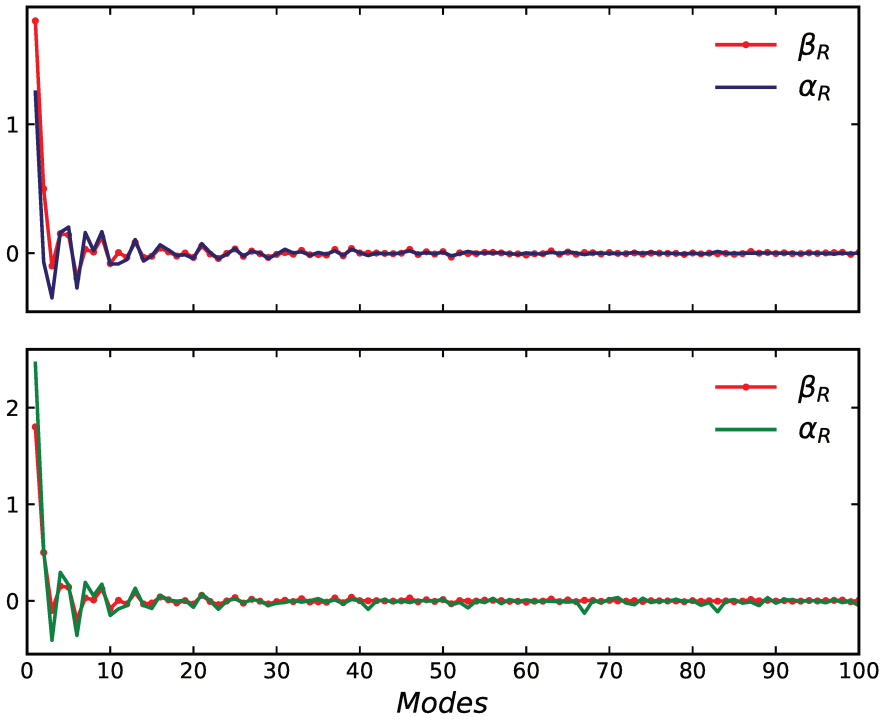

Figure 6.7 – The coefficient of the simulation β_R (red solid line) and theory α_R with respect to the number of modes, after the decomposition on the orthonormal basis R_n as given by Eqs. (6.30) and (6.37) respectively. The blue line represents the coefficients corresponding to the decomposed tree-level bispectrum, while the green to the 1-loop predictions.

Moreover, the pipeline is tested also in the case of a realization with non-Gaussian initial conditions of the local type. The results of the coefficient, for both the theoretical predictions (gravitational and primordial bispectrum) and the simulation, are presented in Figure 6.8.

In order to measure the primordial non-Gaussian signal, we remove from the simulation coefficients , those that correspond to the theoretical Gaussian predictions, *i.e.* $\beta_n = \beta_n^{tot} - \alpha_n^G$. These coefficients are now used in Eq. (6.38) in order to separate the late-time gravitational component from the primordial signal. The normalisation of the estimator is then the sum of the coefficients corresponding to the theoretical primordial non-Gaussian bispectrum. The measured $f_{\rm NL}^{\rm loc}$, as well as the shape correlator, are presented in Table 6.2. We are aware that the value of $f_{\rm NL}^{\rm loc}$ used to generate the non-Gaussian initial conditions is

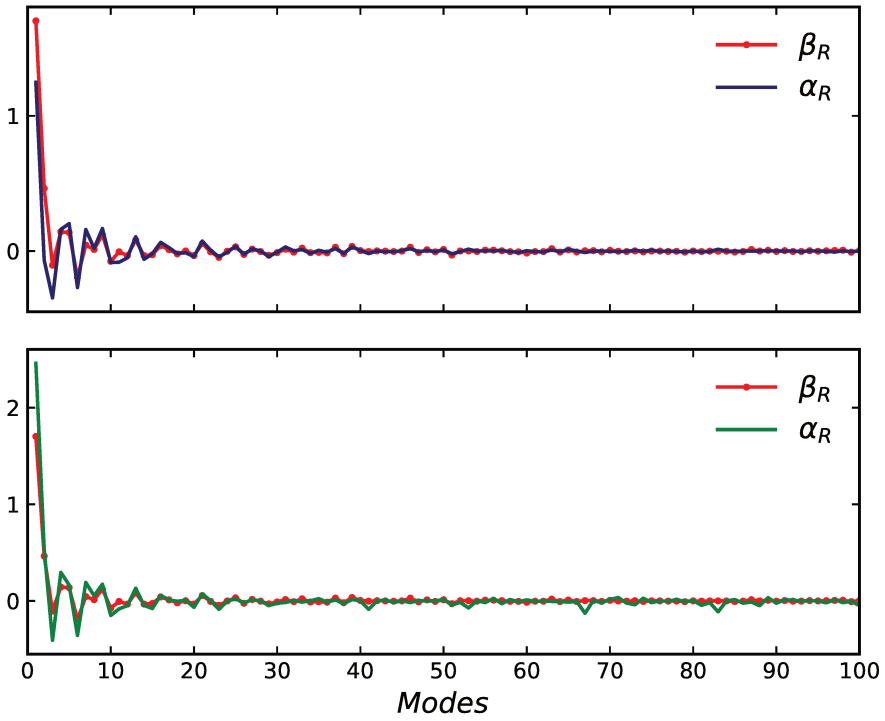

Figure 6.8 – The coefficient of the simulation β_R (red solid line) and theory α_R with respect to the number of modes. The blue line represents the coefficients corresponding to the decomposed tree-level and primordial bispectrum, while the green to the 1-loop predictions, as well as the primordial contribution.

$f_{\rm NL}^{\rm loc} = -200$. Comparing this to the values measured from the simulations, after removing the gravitational component, we see that when the 1-loop bispectrum is used as the theoretical template $f_{\rm NL}^{\rm loc}$ is closer to the expected value. The reason for this is that, up to the scales considered, 1-loop bispectrum fits better to the simulation bispectrum and therefore the removal of the gravitational late-time non-Gaussianity is more accurate than in the case where the tree-level predictions are considered. The remaining discrepancy could be eliminated from the estimated error on $f_{\rm NL}^{\rm loc}$, if a series of realizations was available to us.

tree-level bispectrum		1-loop bispectrum	
$f_{\rm NL}^{\rm loc}$	$C_{\beta\alpha}$	$f_{\rm NL}^{\rm loc}$	$C_{\beta\alpha}$
-321	0.92	-205	0.985

Table 6.2 – Measurements of the amplitude of local non-Gaussianity, after separating the late-time gravitational signal. The latter is achieved after considering two different theoretical templates, *i.e.* the tree-level and the 1-loop matter bispectrum.

Chapter 7 | *Conclusion*

In this thesis we have investigated the higher-order statistics of LSS. The main focus is the potential of the LSS bispectrum, and in particular the bispectrum of galaxies, in providing constraints on primordial non-Gaussianity, as well as probing the non-linear regime of structure growth.

The approach followed was threefold:

We started by modelling the galaxy power spectrum and bispectrum, thoroughly accounting for a large number of effects. We considered the tree-level expansions in the matter fields, since the analysis is restricted on the large-scale regime, while we used a full second order treatment for redshift space distortion. Moreover, a complete second order bias expansion was considered, taking into account the recent developments in the literature. In addition, we improved the modelling of the galaxy bispectrum, by including the trispectrum bias term, which was extended, for the first time, for redshift space.

In the next step, we have investigated the constraining power of two large volume radio continuum surveys (*i.e.* SKA and EMU), as well as for two spectroscopic and two photometric optical surveys, on forecasting the non-Gaussian parameters $f_{\rm NL}$ for three types of PNG shapes – local, equilateral and orthogonal– and on galaxy bias parameters. The statistical tools used were the galaxy power spectrum and bispectrum on large scales, without taking into account the cross-correlation between the two, while the forecasting was achieve through the Fisher matrix approach. We have carefully studied the propagation of theoretical uncertainties, where we have considered the impact of theoretical errors, up to loop-corrections in the matter and bias expansions, on the forecasts.

The forecast results, for most surveys considered, have shown an improvement over current CMB bounds for the local shape, by a factor $\sim$ 4-5, while we have verified that the

bispectrum gives a very important contribution for all PNG shapes. On the other hand, other shapes, especially equilateral, would be poorly constrained. This was mainly due to the fact that, the power spectrum cannot place constraints on equilateral PNG, leaving the bispectrum as the only source of signal. Additional limiting factors were, the theoretical errors, which peak in the equilateral limit, and the small volumes of some surveys (few optical cases). We have shown that larger optical and radio surveys could improve the constraints not only for equilateral, but for all shapes considered. However, the trade-off for these surveys is the presence of large redshift errors, which indeed massively degraded the final forecasts (especially for equilateral PNG). In a very idealised case, where galaxy redshift could be accurately known for all objects, even in presence of significant theoretical errors, large improvements (*e.g.* up to a factor ~ 5 for radio) with respect to *Planck* equilateral constraints were obtained. The source of such non-Gaussian signal was mostly from the trispectrum contributions, which display a $\sim k^{-2}$ scale-dependence even in the equilateral case. An additional observation was that the trispectrum bias corrections, in the case of small surveys, degraded the forecasts for equilateral PNG, due to the enhancement of degeneracies between $f_{\rm NL}^{\rm eq}$ and the bias parameters. These two points indicate that the trispectrum term is an important ingredient for forecasting equilateral PNG, through Fisher matrix formalism, and therefore deserves further attention.

The main conclusion from this part of the thesis was that, in order to improve current PNG bounds, beyond the local case, future LSS surveys should improve the strategies of redshift determination, while larger volumes is an attractive feature that can increase the PNG signal.

In the final step of this thesis, we developed a pipeline that can measure the bispectrum of simulations and LSS datasets, based on the modal estimation formalism. It reduces the massive computational effort ($\mathcal{O}(N^6)$) of the numerical calculations to a manageable size ($\mathcal{O}(N^3)$), while we have shown that it efficiently compresses all the information of the three-point correlator into a small set of modes. Different tests, for improving the

convergence and efficiency of the modal decomposition were performed. Moreover, we have shown the power of this formalism not only in reconstructing the bispectrum of a simulation/LSS survey, but also to effortlessly measure the effective non-Gaussianity, generated by the non-linear evolution, and separating it from the inflationary non-Gaussian signal.

Bibliography

Acquaviva V, Bartolo N, Matarrese S, Riotto A (2003) Gauge-invariant second-order perturbations and non-Gaussianity from inflation. Nuclear Physics B 667:119–148, DOI 10.1016/S0550-3213(03)00550-9, arXiv:astro-ph/0209156

Afshordi N, Tolley AJ (2008) Primordial non-Gaussianity, statistics of collapsed objects, and the integrated Sachs-Wolfe effect. *Phys. Rev. D*78, 0806.1046

Agarwal N, Ho S, Shandera S (2014) Constraining the initial conditions of the Universe using large scale structure. *Journal of Cosmology and Astro-Particle Physics*2:038, DOI 10.1088/1475-7516/2014/02/038, 1311.2606

Albrecht A, Steinhardt PJ (1982) Cosmology for grand unified theories with radiatively induced symmetry breaking. Phys Rev Lett 48:1220–1223, DOI 10.1103/PhysRevLett.48.1220, URL http://link.aps.org/doi/10.1103/PhysRevLett.48.1220

Alishahiha M, Silverstein E, Tong D (2004) DBI in the sky: Non-Gaussianity from inflation with a speed limit. *Phys. Rev. D*70(12):123505, DOI 10.1103/PhysRevD.70.123505, arXiv:hep-th/0404084

Alonso D, Ferreira PG (2015) Constraining ultralarge-scale cosmology with multiple tracers in optical and radio surveys. *Phys. Rev. D*92(6):063525, DOI 10.1103/PhysRevD.92.063525, 1507.03550

Amendola L, Appleby S, Bacon D, Baker T, Baldi M, Bartolo N, Blanchard A, Bonvin C, Borgani S, Branchini E, Burrage C, Camera S, Carbone C, Casarini L, Cropper M, de Rham C, Di Porto C, Ealet A, Ferreira PG, Finelli F, García-Bellido J, Giannantonio T, Guzzo L, Heavens A, Heisenberg L, Heymans C, Hoekstra H, Hollenstein L, Holmes R, Horst O, Jahnke K, Kitching TD, Koivisto T, Kunz M, La Vacca G, March M, Majerotto E, Markovic K, Marsh D, Marulli F, Massey R, Mellier Y, Mota DF, Nunes NJ, Percival W, Pettorino V, Porciani C, Quercellini C, Read J, Rinaldi M, Sapone D, Scaramella R, Skordis C, Simpson F, Taylor A, Thomas S, Trotta R, Verde L, Vernizzi F, Vollmer A, Wang Y, Weller J, Zlosnik T (2013) Cosmology and Fundamental Physics with the Euclid Satellite. Living Reviews in Relativity 16:6, DOI 10.12942/lrr-2013-6, 1206.1225

Angulo R, Fasiello M, Senatore L, Vlah Z (2015) On the statistics of biased tracers in the Effective Field Theory of Large Scale Structures. *Journal of Cosmology and Astro-Particle Physics*9:029, DOI 10.1088/1475-7516/2015/09/029, 1503.08826

Assassi V, Baumann D, Green D, Zaldarriaga M (2014) Renormalized Halo Bias. JCAP 1408:056, DOI 10.1088/1475-7516/2014/08/056, 1402.5916

Assassi V, Baumann D, Schmidt F (2015) Galaxy Bias and Primordial Non-Gaussianity. JCAP 1512(12):043, DOI 10.1088/1475-7516/2015/12/043, 1510.03723

Audren B, Lesgourgues J, Bird S, Haehnelt MG, Viel M (2013) Neutrino masses and cosmological parameters from a Euclid-like survey: Markov Chain Monte Carlo forecasts including theoretical errors. Journal of Cosmology and Astroparticle Physics 2013(01):026–026, DOI 10.1088/1475-7516/2013/01/026, URL http://arxiv.org/abs/1210.2194, arXiv: 1210.2194

Babich D, Creminelli P, Zaldarriaga M (2004) The shape of non-Gaussianities. *Journal of Cosmology and Astro-Particle Physics*8:009, DOI 10.1088/1475-7516/2004/08/009, astro-ph/0405356

Baldauf T, Seljak U, Senatore L (2011) Primordial non-Gaussianity in the bispectrum of the halo density field. *Journal of Cosmology and Astro-Particle Physics*4, 1011.1513

Baldauf T, Seljak U, Desjacques V, McDonald P (2012) Evidence for quadratic tidal tensor bias from the halo bispectrum. *Phys. Rev. D*86, 1201.4827

Baldauf T, Mirbabayi M, Simonović M, Zaldarriaga M (2016) LSS constraints with controlled theoretical uncertainties. ArXiv e-prints 1602.00674

Baldi M (2012) Dark Energy simulations. Physics of the Dark Universe 1:162–193, DOI 10.1016/j.dark.2012.10.004, 1210.6650

Ballinger WE, Peacock JA, Heavens AF (1996) Measuring the cosmological constant with redshift surveys. *MNRAS*282:877, DOI 10.1093/mnras/282.3.877, astro-ph/9605017

Bardeen JM, Bond JR, Kaiser N, Szalay AS (1986) The statistics of peaks of Gaussian random fields. *ApJ*304:15–61

Barlow RJ (1989) Statistics: A Guide to the Use of Statistical Methods in the Physical Sciences (Manchester Physics Series), reprint edn. WileyBlackwell

Barnes J, Hut P (1986) A hierarchical O(N log N) force-calculation algorithm. *Nature*324:446–449, DOI 10.1038/324446a0

Bartolo N, Komatsu E, Matarrese S, Riotto A (2004a) Non-Gaussianity from inflation: theory and observations. Physics Reports 402:103–266, DOI 10.1016/j.physrep.2004.08.022, arXiv:astro-ph/0406398

Bartolo N, Matarrese S, Riotto A (2004b) Non-Gaussianity in the curvaton scenario. *Phys. Rev. D*69(4):043503, DOI 10.1103/PhysRevD.69.043503, arXiv:hep-ph/0309033

Baumann D (2009) TASI Lectures on Inflation. arXiv:09075424 [astro-ph, physics:gr-qc, physics:hep-ph, physics:hep-th] ArXiv: 0907.5424

Baumann D, Nicolis A, Senatore L, Zaldarriaga M (2012) Cosmological non-linearities as an effective fluid. *Journal of Cosmology and Astro-Particle Physics*7:051, DOI 10.1088/1475-7516/2012/07/051, 1004.2488

Bernardeau F (1992) The Gravity induced quasi-Gaussian correlation hierarchy. Astrophys J 392:1–14, DOI 10.1086/171398

Bernardeau F, Colombi S, Gaztanaga E, Scoccimarro R (2002) Large scale structure of the universe and cosmological perturbation theory. Phys Rept 367:1–248, astro-ph/0112551

Bernardeau F, Crocce M, Scoccimarro R (2008) Multipoint propagators in cosmological gravitational instability. *Phys. Rev. D*78(10):103521, DOI 10.1103/PhysRevD.78.103521, 0806.2334

Bernardeau F, Crocce M, Scoccimarro R (2012) Constructing regularized cosmic propagators. *Phys. Rev. D*85(12):123519, DOI 10.1103/PhysRevD.85.123519, 1112.3895

Bertacca D, Raccanelli A, Bartolo N, Liguori M, Matarrese S, Verde L (2017) Relativistic wide-angle galaxy bispectrum on the light-cone. ArXiv e-prints 1705.09306

Bock J, SPHEREx Science Team (2016) SPHEREx: An All-Sky Spectral Survey. In: American Astronomical Society Meeting Abstracts, American Astronomical Society Meeting Abstracts, vol 227, p 147.01

Bond JR, Cole S, Efstathiou G, Kaiser N (1991) Excursion set mass functions for hierarchical Gaussian fluctuations. *ApJ*379:440–460, DOI 10.1086/170520

Bouchet FR (1996) Introductory Overview of Eulerian and Lagrangian Perturbation Theories. In: Bonometto S, Primack JR, Provenzale A (eds) Dark Matter in the Universe, p 565, astro-ph/9603013

Bouchet FR, Colombi S, Hivon E, Juszkiewicz R (1995) Perturbative Lagrangian approach to gravitational instability. A&A296:575, astro-ph/9406013

Buchbinder EI, Khoury J, Ovrut BA (2008) Non-Gaussianities in new ekpyrotic cosmology. Phys Rev Lett 100:171,302, 0710.5172

Buchert T (1989) A class of solutions in Newtonian cosmology and the pancake theory. A&A223:9–24

Buchert T, Melott AL, Weiss AG (1994) Testing higher-order Lagrangian perturbation theory against numerical simulations I. Pancake models. A&A288:349–364, astro-ph/9309056

Byrnes CT, Choi KY (2010) Review of Local Non-Gaussianity from Multifield Inflation. Advances in Astronomy 2010, DOI 10.1155/2010/724525, 1002.3110

Byrnes CT, Tasinato G (2009) Non-Gaussianity beyond slow roll in multi-field inflation. *Journal of Cosmology and Astro-Particle Physics*8:016, DOI 10.1088/1475-7516/2009/08/016, 0906.0767

Byrnes CT, Choi KY, Hall LMH (2008) Conditions for large non-Gaussianity in two-field slow-roll inflation. *Journal of Cosmology and Astro-Particle Physics*10:008, DOI 10.1088/1475-7516/2008/10/008, 0807.1101

Byrnes CT, Choi KY, Hall LMH (2009) Large non-Gaussianity from two-component hybrid inflation. *Journal of Cosmology and Astro-Particle Physics*2:017, DOI 10.1088/1475-7516/2009/02/017, 0812.0807

Camera S, Santos MG, Ferreira PG, Ferramacho L (2013) Cosmology on Ultralarge Scales with Intensity Mapping of the Neutral Hydrogen 21 cm Emission: Limits on Primordial Non-Gaussianity. Physical Review Letters 111(17):171302, DOI 10.1103/PhysRevLett.111.171302, 1305.6928

Camera S, Raccanelli A, Bull P, Bertacca D, Chen X, Ferreira P, Kunz M, Maartens R, Mao Y, Santos M, Shapiro PR, Viel M, Xu Y (2015) Cosmology on the Largest Scales with the SKA. Advancing Astrophysics with the Square Kilometre Array (AASKA14) 25, 1501.03851

Carrasco JJM, Hertzberg MP, Senatore L (2012) The effective field theory of cosmological large scale structures. Journal of High Energy Physics 9:82, DOI 10.1007/JHEP09(2012)082, 1206.2926

Catelan P, Lucchin F, Matarrese S, Porciani C (1998) The bias field of dark matter halos. Mon Not Roy Astron Soc 297:692–712, DOI 10.1046/j.1365-8711.1998.01455.x, astro-ph/9708067

Catelan P, Porciani C, Kamionkowski M (2000) Two ways of biasing galaxy formation. Mon Not Roy Astron Soc 318:39, DOI 10.1046/j.1365-8711.2000.04023.x, astro-ph/0005544

Chan KC, Blot L (2017) Assessment of the Information Content of the Power Spectrum and Bispectrum. Physical Review D 96(2), DOI 10.1103/PhysRevD.96.023528, URL http://arxiv.org/abs/1610.06585, arXiv: 1610.06585

Chan KC, Scoccimarro R, Sheth RK (2012) Gravity and large-scale nonlocal bias. *Phys. Rev. D*85, 1201.3614

Chen X, Easther R, Lim EA (2007) Large non-Gaussianities in single-field inflation. *Journal of Cosmology and Astro-Particle Physics*6:023, DOI 10.1088/1475-7516/2007/06/023, arXiv:astro-ph/0611645

Cheung C, Fitzpatrick AL, Kaplan J, Senatore L, Creminelli P (2008) The effective field theory of inflation. Journal of High Energy Physics 3:014-014, DOI 10.1088/1126-6708/2008/03/014, 0709.0293

Cole S, Kaiser N (1989) Biased clustering in the cold dark matter cosmogony. *MNRAS*237:1127–1146

Coles P (1990) Second-order evolution of cold dark matter perturbations. *MNRAS*243:171–176, DOI 10.1093/mnras/243.2.171

Coles P, Lucchin F (2002) Cosmology: The Origin and Evolution of Cosmic Structure. John Wiley and Sons

Colless M, et al (2001) The 2dF Galaxy Redshift Survey: Spectra and redshifts. Mon Not Roy Astron Soc 328:1039, DOI 10.1046/j.1365-8711.2001.04902.x, astro-ph/0106498

Conroy C, Wechsler RH, Kravtsov AV (2006) Modeling Luminosity-dependent Galaxy Clustering through Cosmic Time. *ApJ*647, astro-ph/0512234

Cooray A, Sheth R (2002) Halo models of large scale structure. *Phys. Rep.*372, astro-ph/0206508

Couchman HMP (1991) Mesh-refined P3M - A fast adaptive N-body algorithm. *ApJ*368:L23–L26, DOI 10.1086/185939

Creminelli P (2003) On non-Gaussianities in single-field inflation. JCAP 0310:003, astro-ph/0306122

Creminelli P, Zaldarriaga M (2004) A single-field consistency relation for the three-point function. *Journal of Cosmology and Astro-Particle Physics*10:006, DOI 10.1088/1475-7516/2004/10/006, astro-ph/0407059

Creminelli P, Nicolis A, Senatore L, Tegmark M, Zaldarriaga M (2006) Limits on non-gaussianities from wmap data. JCAP 0605:004, astro-ph/0509029

Crocce M, Scoccimarro R (2006a) Memory of initial conditions in gravitational clustering. Phys Rev D73:063,520, DOI 10.1103/PhysRevD.73.063520, astro-ph/0509419

Crocce M, Scoccimarro R (2006b) Renormalized cosmological perturbation theory. Phys Rev D73:063,519, DOI 10.1103/PhysRevD.73.063519, astro-ph/0509418

Crocce M, Pueblas S, Scoccimarro R (2006) Transients from initial conditions in cosmological simulations. *MNRAS*373:369–381, DOI 10.1111/j.1365-2966.2006.11040.x, astro-ph/0606505

Crocce M, Scoccimarro R, Bernardeau F (2012) MPTBREEZE: a fast renormalized perturbative scheme. *MNRAS*427:2537–2551, DOI 10.1111/j.1365-2966.2012.22127.x, 1207.1465

Dalal N, Doré O, Huterer D, Shirokov A (2008) Imprints of primordial non-Gaussianities on large-scale structure: Scale-dependent bias and abundance of virialized objects. *Phys. Rev. D*77, 0710.4560

Dawson KS, Schlegel DJ, Ahn CP, Anderson SF, Aubourg É, Bailey S, Barkhouser RH, Bautista JE, Beifiori A, Berlind AA, Bhardwaj V, Bizyaev D, Blake CH, Blanton MR, Blomqvist M, Bolton AS, Borde A, Bovy J, Brandt WN, Brewington H, Brinkmann J, Brown PJ, Brownstein JR, Bundy K, Busca NG, Carithers W, Carnero AR, Carr MA, Chen Y, Comparat J, Connolly N, Cope F, Croft RAC, Cuesta AJ, da Costa LN, Davenport JRA, Delubac T, de Putter R, Dhital S, Ealet A, Ebelke GL, Eisenstein DJ, Escoffier S, Fan X, Filiz Ak N, Finley H, Font-Ribera A, Génova-Santos R, Gunn JE, Guo H, Haggard D, Hall PB, Hamilton JC, Harris B, Harris DW, Ho S, Hogg DW, Holder D, Honscheid K, Huehnerhoff J, Jordan B, Jordan WP, Kauffmann G, Kazin EA, Kirkby D, Klaene MA, Kneib JP, Le Goff JM, Lee KG, Long DC, Loomis CP, Lundgren B, Lupton RH, Maia MAG, Makler M, Malanushenko E, Malanushenko V, Mandelbaum R, Manera M, Maraston C, Margala D, Masters KL, McBride CK, McDonald P, McGreer ID, McMahon RG, Mena O, Miralda-Escudé J, Montero-Dorta AD, Montesano F, Muna D, Myers AD, Naugle T, Nichol RC, Noterdaeme P, Nuza SE, Olmstead MD, Oravetz A, Oravetz DJ, Owen R, Padmanabhan N, Palanque-Delabrouille N,

Pan K, Parejko JK, Pâris I, Percival WJ, Pérez-Fournon I, Pérez-Ràfols I, Petitjean P, Pfaffenberger R, Pforr J, Pieri MM, Prada F, Price-Whelan AM, Raddick MJ, Rebolo R, Rich J, Richards GT, Rockosi CM, Roe NA, Ross AJ, Ross NP, Rossi G, Rubiño-Martin JA, Samushia L, Sánchez AG, Sayres C, Schmidt SJ, Schneider DP, Scóccola CG, Seo HJ, Shelden A, Sheldon E, Shen Y, Shu Y, Slosar A, Smee SA, Snedden SA, Stauffer F, Steele O, Strauss MA, Streblyanska A, Suzuki N, Swanson MEC, Tal T, Tanaka M, Thomas D, Tinker JL, Tojeiro R, Tremonti CA, Vargas Magaña M, Verde L, Viel M, Wake DA, Watson M, Weaver BA, Weinberg DH, Weiner BJ, West AA, White M, Wood-Vasey WM, Yeche C, Zehavi I, Zhao GB, Zheng Z (2013) The Baryon Oscillation Spectroscopic Survey of SDSS-III. *AJ*145:10, DOI 10.1088/0004-6256/145/1/10, 1208.0022

Dekel A, Lahav O (1999) Stochastic nonlinear galaxy biasing. Astrophys J 520:24–34, DOI 10.1086/307428, astro-ph/9806193

DESI Collaboration, Aghamousa A, Aguilar J, Ahlen S, Alam S, Allen LE, Allende Prieto C, Annis J, Bailey S, Balland C, et al (2016) The DESI Experiment Part I: Science,Targeting, and Survey Design. ArXiv e-prints 1611.00036

Desjacques V, Seljak U (2010) Primordial Non-Gaussianity in the Large-Scale Structure of the Universe. Advances in Astronomy 2010:908640, DOI 10.1155/2010/908640, 1006.4763

Desjacques V, Seljak U, Iliev IT (2009) Scale-dependent bias induced by local non-Gaussianity: a comparison to N-body simulations. *MNRAS*396, 0811.2748

Desjacques V, Jeong D, Schmidt F (2011a) Accurate predictions for the scale-dependent galaxy bias from primordial non-Gaussianity. *Phys. Rev. D*84(6):061301, DOI 10.1103/PhysRevD.84.061301, 1105.3476

Desjacques V, Jeong D, Schmidt F (2011b) Non-Gaussian Halo Bias Re-examined:

Mass-dependent Amplitude from the Peak-Background Split and Thresholding. *Phys. Rev. D*84(6):063512, DOI 10.1103/PhysRevD.84.063512, 1105.3628

Desjacques V, Jeong D, Schmidt F (2016) Large-Scale Galaxy Bias 1611.09787

Di Dio E, Durrer R, Marozzi G, Montanari F (2016) The bispectrum of relativistic galaxy number counts. *Journal of Cosmology and Astro-Particle Physics*1:016, DOI 10.1088/1475-7516/2016/01/016, 1510.04202

Dimastrogiovanni E, Bartolo N, Matarrese S, Riotto A (2010) Non-Gaussianity and Statistical Anisotropy from Vector Field Populated Inflationary Models. Advances in Astronomy 2010:752670, DOI 10.1155/2010/752670, 1001.4049

Doré O, Bock J, Ashby M, Capak P, Cooray A, de Putter R, Eifler T, Flagey N, Gong Y, Habib S, Heitmann K, Hirata C, Jeong WS, Katti R, Korngut P, Krause E, Lee DH, Masters D, Mauskopf P, Melnick G, Mennesson B, Nguyen H, Öberg K, Pullen A, Raccanelli A, Smith R, Song YS, Tolls V, Unwin S, Venumadhav T, Viero M, Werner M, Zemcov M (2014) Cosmology with the SPHEREX All-Sky Spectral Survey. ArXiv e-prints 1412.4872

Dvali G, Gruzinov A, Zaldarriaga M (2004) Cosmological perturbations from inhomogeneous reheating, freezeout, and mass domination. Phys Rev D69:083,505, astro-ph/0305548

Feldman HA, Frieman JA, Fry JN, Scoccimarro R (2001) Constraints on Galaxy Bias, Matter Density, and Primordial Non-Gaussianity from the PSCz Galaxy Redshift Survey. Physical Review Letters 86:1434–1437, DOI 10.1103/PhysRevLett.86.1434, astro-ph/0010205

Fergusson JR, Shellard EPS (2009) Shape of primordial non-Gaussianity and the CMB bispectrum. *Phys. Rev. D*80(4):043510, DOI 10.1103/PhysRevD.80.043510, 0812.3413

Fergusson JR, Liguori M, Shellard EPS (2010a) General CMB and primordial bispectrum estimation: Mode expansion, map making, and measures of F_{NL}. *Phys. Rev. D*82(2):023502, DOI 10.1103/PhysRevD.82.023502, 0912.5516

Fergusson JR, Regan DM, Shellard EPS (2010b) Optimal Trispectrum Estimators and WMAP Constraints. ArXiv e-prints 1012.6039

Fergusson JR, Liguori M, Shellard EPS (2012) The CMB bispectrum. *Journal of Cosmology and Astro-Particle Physics*12:032, DOI 10.1088/1475-7516/2012/12/032, 1006.1642

Font-Ribera A, McDonald P, Mostek N, Reid BA, Seo HJ, Slosar A (2014) DESI and other Dark Energy experiments in the era of neutrino mass measurements. *Journal of Cosmology and Astro-Particle Physics*5:023, DOI 10.1088/1475-7516/2014/05/023, 1308.4164

Fosalba P, Gaztanaga E (1998) Cosmological perturbation theory and the spherical collapse model: Part 1. Gaussian initial conditions. Mon Not Roy Astron Soc 301:503–523, DOI 10.1046/j.1365-8711.1998.02033.x, astro-ph/9712095

Friedmann A (1922) Über die Krümmung des Raumes. Zeitschrift fur Physik 10:377–386, DOI 10.1007/BF01332580

Fry JN (1984) The Galaxy correlation hierarchy in perturbation theory. *ApJ*279:499–510, DOI 10.1086/161913

Fry JN (1994) Gravity, bias, and the galaxy three-point correlation function. Physical Review Letters 73:215–219, DOI 10.1103/PhysRevLett.73.215

Fry JN, Gaztanaga E (1993) Biasing and hierarchical statistics in large-scale structure. *ApJ*413:447–452, astro-ph/9302009

Gabrielli A (2005) Statistical Physics for Cosmic Structures. Springer Science & Business Media

Gabrielli A, Sylos Labini F (2001) Fluctuations in galaxy counts: A new test for homogeneity vs. fractality. EPL (Europhysics Letters) 54:286–292, DOI 10.1209/epl/i2001-00239-3, astro-ph/0012097

Gabrielli A, Sylos Labini F, Durrer R (2000) Biasing in Gaussian Random Fields and Galaxy Correlations. *ApJ*531:L1–L4, DOI 10.1086/312528, astro-ph/9905183

Gaite J, Domínguez A, Pérez-Mercader J (1999) The Fractal Distribution of Galaxies and the Transition to Homogeneity. *ApJ*522:L5–L8, DOI 10.1086/312204, astro-ph/9812132

Gamow G (1946) Expanding Universe and the Origin of Elements. Physical Review 70:572–573, DOI 10.1103/PhysRev.70.572.2

Ganc J, Komatsu E (2010) A new method for calculating the primordial bispectrum in the squeezed limit. *Journal of Cosmology and Astro-Particle Physics*12:009, DOI 10.1088/1475-7516/2010/12/009, 1006.5457

Gangui A, Lucchin F, Matarrese S, Mollerach S (1994) The Three point correlation function of the cosmic microwave background in inflationary models. Astrophys J 430:447–457, astro-ph/9312033

Giannantonio T, Porciani C (2010) Structure formation from non-Gaussian initial conditions: Multivariate biasing, statistics, and comparison with N-body simulations. *Phys. Rev. D*81(6), 0911.0017

Giannantonio T, Porciani C, Carron J, Amara A, Pillepich A (2012) Constraining primordial non-Gaussianity with future galaxy surveys. *MNRAS*422:2854–2877, DOI 10.1111/j.1365-2966.2012.20604.x, 1109.0958

Gil-Marín H, Wagner C, Verde L, Porciani C, Jimenez R (2012) Perturbation theory approach for the power spectrum: from dark matter in real space to massive haloes in redshift space. *Journal of Cosmology and Astro-Particle Physics*11:029, DOI 10.1088/1475-7516/2012/11/029, 1209.3771

Gil-Marín H, Wagner C, Noreña J, Verde L, Percival W (2014) Dark matter and halo bispectrum in redshift space: theory and applications. *Journal of Cosmology and Astro-Particle Physics*12:029, DOI 10.1088/1475-7516/2014/12/029, 1407.1836

Gil-Marín H, Percival WJ, Verde L, Brownstein JR, Chuang CH, Kitaura FS, Rodríguez-Torres SA, Olmstead MD (2017) The clustering of galaxies in the SDSS-III Baryon Oscillation Spectroscopic Survey: RSD measurement from the power spectrum and bispectrum of the DR12 BOSS galaxies. *MNRAS*465:1757–1788, DOI 10.1093/mnras/stw2679, 1606.00439

Gnedenko BV (1998) Theory of Probability. CRC Press

Goroff MH, Grinstein B, Rey SJ, Wise MB (1986) Coupling of modes of cosmological mass density fluctuations. *ApJ*311:6–14, DOI 10.1086/164749

Greengard L, Rokhlin V (1997) A fast algorithm for particle simulations. Journal of Computational Physics 135(2):280 – 292, DOI http://dx.doi.org/10.1006/jcph.1997.5706, URL http://www.sciencedirect.com/science/article/pii/S0021999197957065

Grossi M, Verde L, Carbone C, Dolag K, Branchini E, Iannuzzi F, Matarrese S, Moscardini L (2009) Large-scale non-Gaussian mass function and halo bias: tests on N-body simulations. *MNRAS*398:321–332, DOI 10.1111/j.1365-2966.2009.15150.x, 0902.2013

Guth AH (1981) Inflationary universe: A possible solution to the horizon and flatness problems. Phys Rev D 23:347–356, DOI 10.1103/PhysRevD.23.347, URL http://link.aps.org/doi/10.1103/PhysRevD.23.347

Heavens A (2009) Statistical techniques in cosmology. ArXiv e-prints 0906.0664

Heavens AF, Matarrese S, Verde L (1998) The Nonlinear redshift-space power spectrum of galaxies. Mon Not Roy Astron Soc 301:797–808, DOI 10.1046/j.1365-8711.1998.02052.x, astro-ph/9808016

Hockney RW, Eastwood JW (1988) Computer simulation using particles

Hogg DW (1999) Distance measures in cosmology. ArXiv Astrophysics e-prints astro-ph/9905116

Hogg DW, Eisenstein DJ, Blanton MR, Bahcall NA, Brinkmann J, Gunn JE, Schneider DP (2005) Cosmic homogeneity demonstrated with luminous red galaxies. Astrophys J 624:54–58, DOI 10.1086/429084, astro-ph/0411197

Hubble E (1929) A Relation between Distance and Radial Velocity among Extra-Galactic Nebulae. Contributions from the Mount Wilson Observatory, vol 3, pp23-28 3:23–28

Ivezic Z, Tyson JA, Abel B, Acosta E, Allsman R, AlSayyad Y, Anderson SF, Andrew J, Angel R, Angeli G, Ansari R, Antilogus P, Arndt KT, Astier P, Aubourg E, Axelrod T, Bard DJ, Barr JD, Barrau A, Bartlett JG, Bauman BJ, Beaumont S, Becker AC, Becla J, Beldica C, Bellavia S, Blanc G, Blandford RD, Bloom JS, Bogart J, Borne K, Bosch JF, Boutigny D, Brandt WN, Brown ME, Bullock JS, Burchat P, Burke DL, Cagnoli G, Calabrese D, Chandrasekharan S, Chesley S, Cheu EC, Chiang J, Claver CF, Connolly AJ, Cook KH, Cooray A, Covey KR, Cribbs C, Cui W, Cutri R, Daubard G, Daues G, Delgado F, Digel S, Doherty P, Dubois R, Dubois-Felsmann GP, Durech J, Eracleous M, Ferguson H, Frank J, Freemon M, Gangler E, Gawiser E, Geary JC, Gee P, Geha M, Gibson RR, Gilmore DK, Glanzman T, Goodenow I, Gressler WJ, Gris P, Guyonnet A, Hascall PA, Haupt J, Hernandez F, Hogan C, Huang D, Huffer ME, Innes WR, Jacoby SH, Jain B, Jee J, Jernigan JG, Jevremovic D, Johns K, Jones RL, Juramy-Gilles C, Juric M, Kahn SM, Kalirai JS, Kallivayalil N, Kalmbach B, Kantor

JP, Kasliwal MM, Kessler R, Kirkby D, Knox L, Kotov I, Krabbendam VL, Krughoff S, Kubanek P, Kuczewski J, Kulkarni S, Lambert R, Le Guillou L, Levine D, Liang M, Lim K, Lintott C, Lupton RH, Mahabal A, Marshall P, Marshall S, May M, McKercher R, Migliore M, Miller M, Mills DJ, Monet DG, Moniez M, Neill DR, Nief J, Nomerotski A, Nordby M, O'Connor P, Oliver J, Olivier SS, Olsen K, Ortiz S, Owen RE, Pain R, Peterson JR, Petry CE, Pierfederici F, Pietrowicz S, Pike R, Pinto PA, Plante R, Plate S, Price PA, Prouza M, Radeka V, Rajagopal J, Rasmussen A, Regnault N, Ridgway ST, Ritz S, Rosing W, Roucelle C, Rumore MR, Russo S, Saha A, Sassolas B, Schalk TL, Schindler RH, Schneider DP, Schumacher G, Sebag J, Sembroski GH, Seppala LG, Shipsey I, Silvestri N, Smith JA, Smith RC, Strauss MA, Stubbs CW, Sweeney D, Szalay A, Takacs P, Thaler JJ, Van Berg R, Vanden Berk D, Vetter K, Virieux F, Xin B, Walkowicz L, Walter CW, Wang DL, Warner M, Willman B, Wittman D, Wolff SC, Wood-Vasey WM, Yoachim P, Zhan H, for the LSST Collaboration (2008) LSST: from Science Drivers to Reference Design and Anticipated Data Products. ArXiv e-prints 0805.2366

Jain B, Bertschinger E (1994) Second-order power spectrum and nonlinear evolution at high redshift. *ApJ*431:495–505, DOI 10.1086/174502, astro-ph/9311070

Jarvis M, Bacon D, Blake C, Brown M, Lindsay S, Raccanelli A, Santos M, Schwarz DJ (2015) Cosmology with SKA Radio Continuum Surveys. Advancing Astrophysics with the Square Kilometre Array (AASKA14) 18, 1501.03825

Jeong D, Komatsu E (2006) Perturbation Theory Reloaded: Analytical Calculation of Nonlinearity in Baryonic Oscillations in the Real-Space Matter Power Spectrum. *ApJ*651:619–626, DOI 10.1086/507781, astro-ph/0604075

Jeong D, Komatsu E (2009) Primordial Non-Gaussianity, Scale-dependent Bias, and the Bispectrum of Galaxies. *ApJ*703:1230–1248, DOI 10.1088/0004-637X/703/2/1230, 0904.0497

Johnston S, Taylor R, Bailes M, Bartel N, Baugh C, Bietenholz M, Blake C, Braun R, Brown J, Chatterjee S, Darling J, Deller A, Dodson R, Edwards P, Ekers R, Ellingsen S, Feain I, Gaensler B, Haverkorn M, Hobbs G, Hopkins A, Jackson C, James C, Joncas G, Kaspi V, Kilborn V, Koribalski B, Kothes R, Landecker T, Lenc E, Lovell J, Macquart JP, Manchester R, Matthews D, McClure-Griffiths N, Norris R, Pen UL, Phillips C, Power C, Protheroe R, Sadler E, Schmidt B, Stairs I, Staveley-Smith L, Stil J, Tingay S, Tzioumis A, Walker M, Wall J, Wolleben M (2008) Science with ASKAP. The Australian square-kilometre-array pathfinder. Experimental Astronomy 22:151–273, DOI 10.1007/s10686-008-9124-7, 0810.5187

Kaiser N (1984) On the spatial correlations of Abell clusters. *ApJ*284:L9–L12, DOI 10.1086/184341

Kaiser N (1987) Clustering in real space and in redshift space. *MNRAS*227:1–21, DOI 10.1093/mnras/227.1.1

Karagiannis D, Shanks T, Ross NP (2014) Search for primordial non-Gaussianity in the quasars of SDSS-III BOSS DR9. *MNRAS*441:486–502, DOI 10.1093/mnras/stu590, 1310.6716

Karciauskas M, Dimopoulos K, Lyth DH (2009) Anisotropic non-Gaussianity from vector field perturbations. *Phys. Rev. D*80(2):023509, DOI 10.1103/PhysRevD.80.023509, 0812.0264

Khoury J, Ovrut BA, Steinhardt PJ, Turok N (2001) The Ekpyrotic universe: Colliding branes and the origin of the hot big bang. Phys Rev D64:123,522, hep-th/0103239

Kofman L, Pogosyan D (1995) Dynamics of gravitational instability is nonlocal. *ApJ*442:30–38, DOI 10.1086/175419, astro-ph/9403029

Kolb EW, Turner MS (1990) The Early Universe. Front Phys 69:1–547

Komatsu E, Spergel DN (2001) Acoustic signatures in the primary microwave background bispectrum. Phys Rev D 63:063,002

Komatsu E, Spergel DN, Wandelt BD (2005) Measuring Primordial Non-Gaussianity in the Cosmic Microwave Background. *ApJ*634:14–19, DOI 10.1086/491724, astro-ph/0305189

Komatsu E, Afshordi N, Bartolo N, Baumann D, Bond JR, Buchbinder EI, Byrnes CT, Chen X, Chung DJH, Cooray A, Creminelli P, Dalal N, Dore O, Easther R, Frolov AV, Khoury J, Kinney WH, Kofman L, Koyama K, Leblond L, Lehners JL, Lidsey JE, Liguori M, Lim EA, Linde A, Lyth DH, Maldacena J, Matarrese S, McAllister L, McDonald P, Mukohyama S, Ovrut B, Peiris HV, Riotto A, Rodrigues Y, Sasaki M, Scoccimarro R, Seery D, Sefusatti A, Smith KM, Starobinsky AA, Steinhardt PJ, Takahashi F, Tegmark M, Tolley AJ, Verde L, Wandelt BD, Wands D, Weinberg S, Wyman M, Yadav APS, Zaldarriaga M (2009) Non-Gaussianity as a Probe of the Physics of the Primordial Universe and the Astrophysics of the Low Redshift Universe. astro2010: The Astronomy and Astrophysics Decadal Survey 2010:158, 0902.4759

Kovetz ED, Raccanelli A, Rahman M (2016) Cosmological Constraints with Clustering-Based Redshifts. ArXiv e-prints 1606.07434

Kuhlen M, Vogelsberger M, Angulo R (2012) Numerical simulations of the dark universe: State of the art and the next decade. Physics of the Dark Universe 1:50–93, DOI 10.1016/j.dark.2012.10.002, 1209.5745

Labini FS (2010) Characterizing the large scale inhomogeneity of the galaxy distribution. In: Alimi JM, Fuözfa A (eds) American Institute of Physics Conference Series, American Institute of Physics Conference Series, vol 1241, pp 981–990, DOI 10.1063/1.3462744, 0910.3833

Labini FS, Vasilyev NL, Pietronero L, Baryshev YV (2009) Absence of self-averaging

and of homogeneity in the large scale galaxy distribution. Europhys Lett 86(4):49,001, DOI 10.1209/0295-5075/86/49001, 0805.1132

Langlois D (2010) Inflation and Cosmological Perturbations. In: Wolschin G (ed) Lecture Notes in Physics, Berlin Springer Verlag, Lecture Notes in Physics, Berlin Springer Verlag, vol 800, pp 1–57, DOI 10.1007/978-3-642-10598-21, 1001.5259

Laureijs R, Amiaux J, Arduini S, Augueres J, Brinchmann J, Cole R, Cropper M, Dabin C, Duvet L, Ealet A, et al (2011) Euclid Definition Study Report. ArXiv e-prints 1110.3193

Lazanu A, Giannantonio T, Schmittfull M, Shellard EPS (2016) Matter bispectrum of large-scale structure: Three-dimensional comparison between theoretical models and numerical simulations. Phys Rev D93(8):083,517, DOI 10.1103/PhysRevD.93.083517, 1510.04075

Lazanu A, Giannantonio T, Schmittfull M, Shellard EPS (2017) Matter bispectrum of large-scale structure with Gaussian and non-Gaussian initial conditions: Halo models, perturbation theory, and a three-shape model. *Phys. Rev. D*95(8):083511, DOI 10.1103/PhysRevD.95.083511, 1511.02022

Lehners JL (2010) Ekpyrotic Nongaussianity: A Review. Advances in Astronomy 2010:903907, DOI 10.1155/2010/903907, 1001.3125

Lehners JL, Steinhardt PJ (2008) Non-Gaussian density fluctuations from entropically generated curvature perturbations in Ekpyrotic models. Phys Rev D77:063,533

Lehners JL, Steinhardt PJ (2008) Non-Gaussian density fluctuations from entropically generated curvature perturbations in ekpyrotic models. *Phys. Rev. D*77(6):063533, DOI 10.1103/PhysRevD.77.063533, 0712.3779

Leistedt B, Peiris HV, Roth N (2014) Constraints on Primordial Non-Gaussianity from 800 000 Photometric Quasars. Physical Review Letters 113(22):221301, DOI 10.1103/PhysRevLett.113.221301, 1405.4315

Lemaître G (1927) Un Univers homogène de masse constante et de rayon croissant rendant compte de la vitesse radiale des nébuleuses extra-galactiques. Annales de la Société Scientifique de Bruxelles 47:49–59

Levi M, Bebek C, Beers T, Blum R, Cahn R, Eisenstein D, Flaugher B, Honscheid K, Kron R, Lahav O, McDonald P, Roe N, Schlegel D, collaboration rtD (2013) The DESI Experiment, a whitepaper for Snowmass 2013. arXiv:13080847 [astro-ph] ArXiv: 1308.0847

Lewis A, Challinor A, Lasenby A (2000) Efficient computation of CMB anisotropies in closed FRW models. Astrophys J 538:473–476, astro-ph/9911177

Liddle AR, Lyth DH (2000) Cosmological Inflation and Large-Scale Structure. Cambridge University Press

Liguori M, Sefusatti E, Fergusson JR, Shellard EPS (2010) Primordial Non-Gaussianity and Bispectrum Measurements in the Cosmic Microwave Background and Large-Scale Structure. Advances in Astronomy 2010:980523, DOI 10.1155/2010/980523, 1001.4707

Linde A (1982) A new inflationary universe scenario: A possible solution of the horizon, flatness, homogeneity, isotropy and primordial monopole problems. Physics Letters B 108(6):389 – 393, DOI 10.1016/0370-2693(82)91219-9, URL http://www.sciencedirect.com/science/article/pii/0370269382912199

Linde A (2005) Particle Physics and Inflationary Cosmology. ArXiv High Energy Physics - Theory e-prints arXiv:hep-th/0503203

Linde AD, Mukhanov VF (1997) Nongaussian isocurvature perturbations from inflation. Phys Rev D56:535–539, astro-ph/9610219

LoVerde M, Smith KM (2011) The non-gaussian halo mass function with f nl , g nl and tau nl. Journal of Cosmology and Astroparticle Physics 2011(08):003

LoVerde M, Miller A, Shandera S, Verde L (2008) Effects of Scale-Dependent Non-Gaussianity on Cosmological Structures. JCAP 0804:014, 0711.4126

LSST Science Collaboration, Abell PA, Allison J, Anderson SF, Andrew JR, Angel JRP, Armus L, Arnett D, Asztalos SJ, Axelrod TS, et al (2009) LSST Science Book, Version 2.0. ArXiv e-prints 0912.0201

Lyth DH, Wands D (2002) Generating the curvature perturbation without an inflaton. *Phys. Lett.* *B*524:5–14, DOI 10.1016/S0370-2693(01)01366-1, arXiv:hep-ph/0110002

Ma Z, Hu W, Huterer D (2006) Effects of Photometric Redshift Uncertainties on Weak-Lensing Tomography. *ApJ*636:21–29, DOI 10.1086/497068, astro-ph/0506614

Maartens R (2011) Is the Universe homogeneous? Philosophical Transactions of the Royal Society of London Series A 369:5115–5137, DOI 10.1098/rsta.2011.0289, 1104.1300

Makino N, Sasaki M, Suto Y (1992) Analytic approach to the perturbative expansion of nonlinear gravitational fluctuations in cosmological density and velocity fields. Phys Rev D 46:585–602

Maldacena J (2003) Non-gaussian features of primordial fluctuations in single field inflationary models. Journal of High Energy Physics 5:13, DOI 10.1088/1126-6708/2003/05/013, arXiv:astro-ph/0210603

Marín FA, Blake C, Poole GB, McBride CK, Brough S, Colless M, Contreras C, Couch W, Croton DJ, Croom S, Davis T, Drinkwater MJ, Forster K, Gilbank D, Gladders M, Glazebrook K, Jelliffe B, Jurek RJ, Li Ih, Madore B, Martin DC, Pimbblet K, Pracy

M, Sharp R, Wisnioski E, Woods D, Wyder TK, Yee HKC (2013) The WiggleZ Dark Energy Survey: constraining galaxy bias and cosmic growth with three-point correlation functions. *MNRAS*432:2654–2668, DOI 10.1093/mnras/stt520, 1303.6644

Martin J, Ringeval C, Vennin V (2014) Encyclopædia Inflationaris. Phys Dark Univ 5-6:75–235, DOI 10.1016/j.dark.2014.01.003, 1303.3787

Matarrese S, Verde L (2008) The Effect of Primordial Non-Gaussianity on Halo Bias. *ApJ*677, 0801.4826

Matsubara T (1999) Stochasticity of bias and nonlocality of galaxy formation: Linear scales. Astrophys J 525:543–553, DOI 10.1086/307931, astro-ph/9906029

McDonald P (2006) Clustering of dark matter tracers: Renormalizing the bias parameters. Phys Rev D74:103,512, DOI 10.1103/PhysRevD.74.103512,10.1103/PhysRevD.74.129901, [Erratum: Phys. Rev.D74,129901(2006)], astro-ph/0609413

McDonald P (2008) Primordial non-Gaussianity: large-scale structure signature in the perturbative bias model. Phys Rev D78:123,519, DOI 10.1103/PhysRevD.78.123519, 0806.1061

McDonald P, Roy A (2009) Clustering of dark matter tracers: generalizing bias for the coming era of precision LSS. *Journal of Cosmology and Astro-Particle Physics*8, 0902.0991

Melott AL, Buchert T, Weib AG (1995) Testing higher-order Lagrangian perturbation theory against numerical simulations. 2: Hierarchical models. A&A294:345–365, astro-ph/9404018

Ménard B, Scranton R, Schmidt S, Morrison C, Jeong D, Budavari T, Rahman M (2013) Clustering-based redshift estimation: method and application to data. ArXiv e-prints 1303.4722

Mirbabayi M, Schmidt F, Zaldarriaga M (2015) Biased Tracers and Time Evolution. JCAP 1507(07):030, DOI 10.1088/1475-7516/2015/07/030, 1412.5169

Mo HJ, White SDM (1996) An analytic model for the spatial clustering of dark matter haloes. *MNRAS*282, astro-ph/9512127

Mo HJ, Jing YP, White SDM (1996) The correlation function of clusters of galaxies and the amplitude of mass fluctuations in the Universe. *MNRAS*282, astro-ph/9602052

Mostek N, Coil AL, Cooper M, Davis M, Newman JA, Weiner BJ (2013) The DEEP2 Galaxy Redshift Survey: Clustering Dependence on Galaxy Stellar Mass and Star Formation Rate at z ˜ 1. *ApJ*767:89, DOI 10.1088/0004-637X/767/1/89, 1210.6694

Mukhanov V (2005) Physical Foundations of Cosmology. Cambridge University Press

Mukhanov VF, Steinhardt PJ (1998) Density perturbations in multifield inflationary models. *Phys. Lett. B*422:52–60, DOI 10.1016/S0370-2693(98)00032-X, arXiv:astro-ph/9710038

Newman JA (2008) Calibrating Redshift Distributions beyond Spectroscopic Limits with Cross-Correlations. *ApJ*684:88-101, DOI 10.1086/589982, 0805.1409

Nikoloudakis N, Shanks T, Sawangwit U (2013) Clustering analysis of high-redshift luminous red galaxies in Stripe 82. *MNRAS*429:2032–2051, 1204.3609

Norris RP, Hopkins AM, Afonso J, Brown S, Condon JJ, Dunne L, Feain I, Hollow R, Jarvis M, Johnston-Hollitt M, Lenc E, Middelberg E, Padovani P, Prandoni I, Rudnick L, Seymour N, Umana G, Andernach H, Alexander DM, Appleton PN, Bacon D, Banfield J, Becker W, Brown MJI, Ciliegi P, Jackson C, Eales S, Edge AC, Gaensler BM, Giovannini G, Hales CA, Hancock P, Huynh MT, Ibar E, Ivison RJ, Kennicutt R, Kimball AE, Koekemoer AM, Koribalski BS, López-Sánchez ÁR, Mao MY, Murphy T, Messias H, Pimbblet KA, Raccanelli A, Randall KE, Reiprich TH, Roseboom IG,

Röttgering H, Saikia DJ, Sharp RG, Slee OB, Smail I, Thompson MA, Urquhart JS, Wall JV, Zhao GB (2011) EMU: Evolutionary Map of the Universe. PASA28:215–248, DOI 10.1071/AS11021, 1106.3219

Orsi A, Baugh CM, Lacey CG, Cimatti A, Wang Y, Zamorani G (2010) Probing dark energy with future redshift surveys: a comparison of emission line and broad-band selection in the near-infrared. *MNRAS*405:1006–1024, DOI 10.1111/j.1365-2966.2010.16585.x, 0911.0669

Padmanabhan N, Schlegel DJ, Seljak U, Makarov A, Bahcall NA, Blanton MR, Brinkmann J, Eisenstein DJ, Finkbeiner DP, Gunn JE, Hogg DW, Ivezić Ž, Knapp GR, Loveday J, Lupton RH, Nichol RC, Schneider DP, Strauss MA, Tegmark M, York DG (2007) The clustering of luminous red galaxies in the Sloan Digital Sky Survey imaging data. *MNRAS*378:852–872, arXiv:astro-ph/0605302

Passaglia S, Manzotti A, Dodelson S (2017) Cross-correlating 2D and 3D galaxy surveys. *Phys. Rev. D*95(12):123508, DOI 10.1103/PhysRevD.95.123508, 1702.03004

Peacock JA, Dodds SJ (1994) Reconstructing the Linear Power Spectrum of Cosmological Mass Fluctuations. *MNRAS*267:1020, DOI 10.1093/mnras/267.4.1020, astro-ph/9311057

Peebles PJE (1980) The large-scale structure of the universe

Peebles PJE (1993) Principles of physical cosmology. Princeton University Press

Penzias AA, Wilson RW (1965) A Measurement of Excess Antenna Temperature at 4080 Mc/s. *ApJ*142:419–421, DOI 10.1086/148307

Pietroni M (2008) Flowing with Time: a New Approach to Nonlinear Cosmological Perturbations. JCAP 0810:036, DOI 10.1088/1475-7516/2008/10/036, 0806.0971

Pillepich A, Porciani C, Hahn O (2010) Universal halo mass function and scale-dependent bias from N-body simulations with non-Gaussian initial conditions. Mon Not Roy Astron Soc 402:191–206, 0811.4176

Planck Collaboration, Ade PAR, Aghanim N, Arnaud M, Arroja F, Ashdown M, Aumont J, Baccigalupi C, Ballardini M, Banday AJ, et al (2016a) Planck 2015 results. XVII. Constraints on primordial non-Gaussianity. A&A594:A17, DOI 10.1051/0004-6361/201525836, 1502.01592

Planck Collaboration, Ade, P A R, Aghanim, N, Arnaud, M, Ashdown, M, Aumont, J, Baccigalupi, C, Banday, A J, Barreiro, R B, Bartlett, J G, Bartolo, N, Battaner, E, Battye, R, Benabed, K, Benoît, A, Benoit-Lévy, A, Bernard, J-P, Bersanelli, M, Bielewicz, P, Bock, J J, Bonaldi, A, Bonavera, L, Bond, J R, Borrill, J, Bouchet, F R, Boulanger, F, Bucher, M, Burigana, C, Butler, R C, Calabrese, E, Cardoso, J-F, Catalano, A, Challinor, A, Chamballu, A, Chary, R-R, Chiang, H C, Chluba, J, Christensen, P R, Church, S, Clements, D L, Colombi, S, Colombo, L P L, Combet, C, Coulais, A, Crill, B P, Curto, A, Cuttaia, F, Danese, L, Davies, R D, Davis, R J, de Bernardis, P, de Rosa, A, de Zotti, G, Delabrouille, J, Désert, F-X, Di Valentino, E, Dickinson, C, Diego, J M, Dolag, K, Dole, H, Donzelli, S, Doré, O, Douspis, M, Ducout, A, Dunkley, J, Dupac, X, Efstathiou, G, Elsner, F, Enßlin, T A, Eriksen, H K, Farhang, M, Fergusson, J, Finelli, F, Forni, O, Frailis, M, Fraisse, A A, Franceschi, E, Frejsel, A, Galeotta, S, Galli, S, Ganga, K, Gauthier, C, Gerbino, M, Ghosh, T, Giard, M, Giraud-Héraud, Y, Giusarma, E, Gjerløw, E, González-Nuevo, J, Górski, K M, Gratton, S, Gregorio, A, Gruppuso, A, Gudmundsson, J E, Hamann, J, Hansen, F K, Hanson, D, Harrison, D L, Helou, G, Henrot-Versillé, S, Hernández-Monteagudo, C, Herranz, D, Hildebrandt, S R, Hivon, E, Hobson, M, Holmes, W A, Hornstrup, A, Hovest, W, Huang, Z, Huffenberger, K M, Hurier, G, Jaffe, A H, Jaffe, T R, Jones, W C, Juvela, M, Keihänen, E, Keskitalo, R, Kisner, T S, Kneissl, R, Knoche, J, Knox, L, Kunz, M, Kurki-Suonio, H, Lagache, G, Lähteenmäki, A, Lamarre, J-M, Lasenby, A, Lattanzi, M,

Lawrence, C R, Leahy, J P, Leonardi, R, Lesgourgues, J, Levrier, F, Lewis, A, Liguori, M, Lilje, P B, Linden-Vørnle, M, López-Caniego, M, Lubin, P M, Macías-Pérez, J F, Maggio, G, Maino, D, Mandolesi, N, Mangilli, A, Marchini, A, Maris, M, Martin, P G, Martinelli, M, Martínez-González, E, Masi, S, Matarrese, S, McGehee, P, Meinhold, P R, Melchiorri, A, Melin, J-B, Mendes, L, Mennella, A, Migliaccio, M, Millea, M, Mitra, S, Miville-Deschênes, M-A, Moneti, A, Montier, L, Morgante, G, Mortlock, D, Moss, A, Munshi, D, Murphy, J A, Naselsky, P, Nati, F, Natoli, P, Netterfield, C B, Nørgaard-Nielsen, H U, Noviello, F, Novikov, D, Novikov, I, Oxborrow, C A, Paci, F, Pagano, L, Pajot, F, Paladini, R, Paoletti, D, Partridge, B, Pasian, F, Patanchon, G, Pearson, T J, Perdereau, O, Perotto, L, Perrotta, F, Pettorino, V, Piacentini, F, Piat, M, Pierpaoli, E, Pietrobon, D, Plaszczynski, S, Pointecouteau, E, Polenta, G, Popa, L, Pratt, G W, Prézeau, G, Prunet, S, Puget, J-L, Rachen, J P, Reach, W T, Rebolo, R, Reinecke, M, Remazeilles, M, Renault, C, Renzi, A, Ristorcelli, I, Rocha, G, Rosset, C, Rossetti, M, Roudier, G, Rouillé d'Orfeuil, B, Rowan-Robinson, M, Rubiño-Martín, J A, Rusholme, B, Said, N, Salvatelli, V, Salvati, L, Sandri, M, Santos, D, Savelainen, M, Savini, G, Scott, D, Seiffert, M D, Serra, P, Shellard, E P S, Spencer, L D, Spinelli, M, Stolyarov, V, Stompor, R, Sudiwala, R, Sunyaev, R, Sutton, D, Suur-Uski, A-S, Sygnet, J-F, Tauber, J A, Terenzi, L, Toffolatti, L, Tomasi, M, Tristram, M, Trombetti, T, Tucci, M, Tuovinen, J, Türler, M, Umana, G, Valenziano, L, Valiviita, J, Van Tent, F, Vielva, P, Villa, F, Wade, L A, Wandelt, B D, Wehus, I K, White, M, White, S D M, Wilkinson, A, Yvon, D, Zacchei, A, Zonca, A (2016b) Planck 2015 results - xiii. cosmological parameters. A&A594:A13, DOI 10.1051/0004-6361/201525830, URL https://doi.org/10.1051/0004-6361/201525830, 1502.01589

Polarski D, Starobinsky AA (1994) Isocurvature perturbations in multiple inflationary models. *Phys. Rev. D*50:6123–6129, DOI 10.1103/PhysRevD.50.6123, arXiv:astro-ph/9404061

Press WH, Schechter P (1974) Formation of galaxies and clusters of galaxies by selfsimilar

gravitational condensation. Astrophys J 187:425–438

Raccanelli A, Zhao GB, Bacon DJ, Jarvis MJ, Percival WJ, Norris RP, Röttgering H, Abdalla FB, Cress CM, Kubwimana JC, Lindsay S, Nichol RC, Santos MG, Schwarz DJ (2012) Cosmological measurements with forthcoming radio continuum surveys. *MNRAS*424:801–819, DOI 10.1111/j.1365-2966.2012.20634.x, 1108.0930

Raccanelli A, Shiraishi M, Bartolo N, Bertacca D, Liguori M, Matarrese S, Norris RP, Parkinson D (2017) Future constraints on angle-dependent non-Gaussianity from large radio surveys. Physics of the Dark Universe 15:35–46, DOI 10.1016/j.dark.2016.10.006, 1507.05903

Regan DM, Shellard EPS, Fergusson JR (2010) General CMB and primordial trispectrum estimation. *Phys. Rev. D*82(2):023520, DOI 10.1103/PhysRevD.82.023520, 1004.2915

Regan DM, Schmittfull MM, Shellard EPS, Fergusson JR (2012) Universal non-Gaussian initial conditions for N-body simulations. *Phys. Rev. D*86(12):123524, DOI 10.1103/PhysRevD.86.123524, 1108.3813

Rigopoulos GI, Shellard EPS, van Tent BJW (2006) Large non-Gaussianity in multiple-field inflation. *Phys. Rev. D*73(8):083522, DOI 10.1103/PhysRevD.73.083522, arXiv:astro-ph/0506704

Robertson HP (1935) Kinematics and World-Structure. *ApJ*82:284, DOI 10.1086/143681

Salopek DS, Bond JR (1990) Nonlinear evolution of long-wavelength metric fluctuations in inflationary models. Phys Rev D 42:3936–3962

Sarkar P, Yadav J, Pandey B, Bharadwaj S (2009) The scale of homogeneity of the galaxy distribution in SDSS DR6. *MNRAS*399:L128–L131, DOI 10.1111/j.1745-3933.2009.00738.x, 0906.3431

Sasaki M, Väliviita J, Wands D (2006) Non-Gaussianity of the primordial perturbation in the curvaton model. *Phys. Rev. D*74(10):103003, DOI 10.1103/PhysRevD.74.103003, arXiv:astro-ph/0607627

Schmidt F (2016) Towards a self-consistent halo model for the nonlinear large-scale structure. Phys Rev D93(6):063,512, DOI 10.1103/PhysRevD.93.063512, 1511.02231

Schmidt F, Hui L (2013) Cosmic Microwave Background Power Asymmetry from Non-Gaussian Modulation. Phys Rev Lett 110:011,301, DOI 10.1103/PhysRevLett.110.059902,10.1103/PhysRevLett.110.011301, [Erratum: Phys. Rev. Lett.110,059902(2013)], 1210.2965

Schmidt F, Kamionkowski M (2010) Halo clustering with nonlocal non-Gaussianity. *Phys. Rev. D*82(10):103002, DOI 10.1103/PhysRevD.82.103002, 1008.0638

Schmidt F, Jeong D, Desjacques V (2013) Peak-background split, renormalization, and galaxy clustering. *Phys. Rev. D*88(2):023515, DOI 10.1103/PhysRevD.88.023515, 1212.0868

Schmittfull MM, Regan DM, Shellard EPS (2013) Fast estimation of gravitational and primordial bispectra in large scale structures. *Phys. Rev. D*88(6):063512, DOI 10.1103/PhysRevD.88.063512, 1207.5678

Schneider M, Knox L, Zhan H, Connolly A (2006) Using Galaxy Two-Point Correlation Functions to Determine the Redshift Distributions of Galaxies Binned by Photometric Redshift. *ApJ*651:14–23, DOI 10.1086/507675, astro-ph/0606098

Scoccimarro R (1997) Cosmological perturbations: Entering the nonlinear regime. Astrophys J 487:1, astro-ph/9612207

Scoccimarro R (1997) Cosmological Perturbations: Entering the Nonlinear Regime. *ApJ*487:1–17, DOI 10.1086/304578, astro-ph/9612207

Scoccimarro R, Colombi S, Fry JN, Frieman JA, Hivon E, Melott A (1998) Nonlinear Evolution of the Bispectrum of Cosmological Perturbations. *ApJ*496:586–604, DOI 10.1086/305399, astro-ph/9704075

Scoccimarro R, Couchman HMP, Frieman JA (1999) The Bispectrum as a Signature of Gravitational Instability in Redshift Space. *ApJ*517:531–540, DOI 10.1086/307220, astro-ph/9808305

Scoccimarro R, Feldman HA, Fry JN, Frieman JA (2001a) The Bispectrum of IRAS Redshift Catalogs. *ApJ*546:652–664, DOI 10.1086/318284, astro-ph/0004087

Scoccimarro R, Sheth RK, Hui L, Jain B (2001b) How Many Galaxies Fit in a Halo? Constraints on Galaxy Formation Efficiency from Spatial Clustering. *ApJ*546:20–34, DOI 10.1086/318261, astro-ph/0006319

Scoccimarro R, Sefusatti E, Zaldarriaga M (2004) Probing primordial non-Gaussianity with large - scale structure. Phys Rev D69:103,513, DOI 10.1103/PhysRevD.69.103513, astro-ph/0312286

Scoccimarro R, Hui L, Manera M, Chan KC (2012) Large-scale Bias and Efficient Generation of Initial Conditions for Non-Local Primordial Non-Gaussianity. Phys Rev D85:083,002, DOI 10.1103/PhysRevD.85.083002, 1108.5512

Scrimgeour MI, Davis T, Blake C, James JB, Poole GB, Staveley-Smith L, Brough S, Colless M, Contreras C, Couch W, Croom S, Croton D, Drinkwater MJ, Forster K, Gilbank D, Gladders M, Glazebrook K, Jelliffe B, Jurek RJ, Li Ih, Madore B, Martin DC, Pimbblet K, Pracy M, Sharp R, Wisnioski E, Woods D, Wyder TK, Yee HKC (2012) The WiggleZ Dark Energy Survey: the transition to large-scale cosmic homogeneity. *MNRAS*425:116–134, DOI 10.1111/j.1365-2966.2012.21402.x, 1205.6812

Sefusatti E (2009) One-loop perturbative corrections to the matter and galaxy bis-

pectrum with non-Gaussian initial conditions. *Phys. Rev. D*80(12):123002, DOI 10.1103/PhysRevD.80.123002, 0905.0717

Sefusatti E, Komatsu E (2007) Bispectrum of galaxies from high-redshift galaxy surveys: Primordial non-Gaussianity and nonlinear galaxy bias. *Phys. Rev. D*76(8), 0705.0343

Sefusatti E, Crocce M, Pueblas S, Scoccimarro R (2006) Cosmology and the bispectrum. *Phys. Rev. D*74(2):023522, DOI 10.1103/PhysRevD.74.023522, astro-ph/0604505

Sefusatti E, Crocce M, Desjacques V (2012) The halo bispectrum in N-body simulations with non-Gaussian initial conditions. *MNRAS*425, 1111.6966

Senatore L (2015) Bias in the Effective Field Theory of Large Scale Structures. JCAP 1511(11):007, DOI 10.1088/1475-7516/2015/11/007, 1406.7843

Senatore L, Smith KM, Zaldarriaga M (2010) Non-Gaussianities in Single Field Inflation and their Optimal Limits from the WMAP 5-year Data. JCAP 1001:028, 0905.3746

Seo HJ, Eisenstein DJ (2003) Probing Dark Energy with Baryonic Acoustic Oscillations from Future Large Galaxy Redshift Surveys. The Astrophysical Journal 598(2):720–740, DOI 10.1086/379122, URL http://arxiv.org/abs/astro-ph/0307460, arXiv: astro-ph/0307460

Sheth RK, Tormen G (1999) Large scale bias and the peak background split. Mon Not Roy Astron Soc 308:119, astro-ph/9901122

Sheth RK, Chan KC, Scoccimarro R (2013) Nonlocal Lagrangian bias. *Phys. Rev. D*87(8):083002, DOI 10.1103/PhysRevD.87.083002, 1207.7117

Slipher VM (1914) The Radial Velocity of the Andromeda Nebula. Popular Astronomy 22:19–21

Slipher VM (1915) Spectrographic Observations of Nebulae. Popular Astronomy 23:21–24

Slosar A, Hirata C, Seljak U, Ho S, Padmanabhan N (2008) Constraints on local primordial non-Gaussianity from large scale structure. *Journal of Cosmology and Astro-Particle Physics*8, 0805.3580

Smith RE, Peacock JA, Jenkins A, White SDM, Frenk CS, Pearce FR, Thomas PA, Efstathiou G, Couchman HMP (2003) Stable clustering, the halo model and non-linear cosmological power spectra. *MNRAS*341:1311–1332, DOI 10.1046/j.1365-8711.2003.06503.x, astro-ph/0207664

Smith RE, Scoccimarro R, Sheth RK (2007) Scale dependence of halo and galaxy bias: Effects in real space. *Phys. Rev. D*75(6):063512, DOI 10.1103/PhysRevD.75.063512, astro-ph/0609547

Song YS, Taruya A, Oka A (2015) Cosmology with anisotropic galaxy clustering from the combination of power spectrum and bispectrum. *Journal of Cosmology and Astro-Particle Physics*8:007, DOI 10.1088/1475-7516/2015/08/007, 1502.03099

Springel V (2005) The cosmological simulation code GADGET-2. *MNRAS*364:1105–1134, DOI 10.1111/j.1365-2966.2005.09655.x, astro-ph/0505010

Suto Y, Sasaki M (1991) Quasinonlinear theory of cosmological self-gravitating systems. Physical Review Letters 66:264–267, DOI 10.1103/PhysRevLett.66.264

Szalay AS (1988) Constraints on the biasing of density fluctuations. *ApJ*333:21–23, DOI 10.1086/166721

Takahashi R, Sato M, Nishimichi T, Taruya A, Oguri M (2012) Revising the Halofit Model for the Nonlinear Matter Power Spectrum. *ApJ*761:152, DOI 10.1088/0004-637X/761/2/152, 1208.2701

Taruya A, Soda J (1999) Stochastic biasing and galaxy mass density relation in the weakly nonlinear regime. Astrophys J 522:46–58, DOI 10.1086/307612, astro-ph/9809204

Taruya A, Koyama K, Matsubara T (2008) Signature of primordial non-Gaussianity on the matter power spectrum. *Phys. Rev. D*78(12):123534, DOI 10.1103/PhysRevD.78.123534, 0808.4085

Tegmark M, Peebles PJE (1998) The Time Evolution of Bias. *ApJ*500:L79–L82, DOI 10.1086/311426, astro-ph/9804067

Tellarini M, Ross AJ, Tasinato G, Wands D (2015) Non-local bias in the halo bispectrum with primordial non-Gaussianity. JCAP 1507(07):004, DOI 10.1088/1475-7516/2015/07/004, 1504.00324

Tellarini M, Ross AJ, Tasinato G, Wands D (2016) Galaxy bispectrum, primordial non-Gaussianity and redshift space distortions. *Journal of Cosmology and Astro-Particle Physics*6:014, DOI 10.1088/1475-7516/2016/06/014, 1603.06814

Tinker JL, Weinberg DH, Zheng Z, Zehavi I (2005) On the Mass-to-Light Ratio of Large-Scale Structure. *ApJ*631, astro-ph/0411777

Umeh O, Jolicoeur S, Maartens R, Clarkson C (2017) A general relativistic signature in the galaxy bispectrum: the local effects of observing on the lightcone. *Journal of Cosmology and Astro-Particle Physics*3:034, DOI 10.1088/1475-7516/2017/03/034, 1610.03351

Verde L, Matarrese S (2009) Detectability of the effect of inflationary non-gaussianity on halo bias. The Astrophysical Journal Letters 706(1):L91

Verde L, Heavens AF, Matarrese S, Moscardini L (1998) Large scale bias in the universe. 2. Redshift space bispectrum. Mon Not Roy Astron Soc 300:747–756, DOI 10.1046/j.1365-8711.1998.01937.x, astro-ph/9806028

Verde L, Wang LM, Heavens A, Kamionkowski M (2000) Large scale structure, the cosmic microwave background, and primordial non-gaussianity. Mon Not Roy Astron Soc 313:L141–L147, astro-ph/9906301

Verde L, Heavens AF, Percival WJ, Matarrese S (2002) The bias of galaxies and the density of the universe from the 2dF galaxy redshift survey. ArXiv Astrophysics e-prints astro-ph/0212311

Wagner C, Verde L, Boubekeur L (2010) N-body simulations with generic non-Gaussian initial conditions I: power spectrum and halo mass function. *Journal of Cosmology and Astro-Particle Physics*10:022, DOI 10.1088/1475-7516/2010/10/022, 1006.5793

Wagner C, Schmidt F, Chiang CT, Komatsu E (2015) The angle-averaged squeezed limit of nonlinear matter N-point functions. JCAP 1508(08):042, DOI 10.1088/1475-7516/2015/08/042, 1503.03487

Walker AG (1937) On milne's theory of world-structure*. Proceedings of the London Mathematical Society s2-42(1):90–127, DOI 10.1112/plms/s2-42.1.90, URL http://dx.doi.org/10.1112/plms/s2-42.1.90

Wang Y (2006) Dark Energy Constraints from Baryon Acoustic Oscillations. *ApJ*647:1–7, DOI 10.1086/505384, astro-ph/0601163

Weinberg S (1972) Gravitation and Cosmology. John Wiley & Sons

Weinberg S (2008) Cosmology. Cosmology, OUP Oxford, URL https://books.google.gr/books?id=nqQZdg020fsC

Wittman DM, Tyson JA, Kirkman D, Dell'Antonio I, Bernstein G (2000) Detection of weak gravitational lensing distortions of distant galaxies by cosmic dark matter at large scales. Nature 405:143–149, DOI 10.1038/35012001, astro-ph/0003014

Xia JQ, Bonaldi A, Baccigalupi C, De Zotti G, Matarrese S, Verde L, Viel M (2010a) Constraining primordial non-Gaussianity with high-redshift probes. *Journal of Cosmology and Astro-Particle Physics*8:013, DOI 10.1088/1475-7516/2010/08/013, 1007.1969

Xia JQ, Viel M, Baccigalupi C, De Zotti G, Matarrese S, Verde L (2010b) Primordial Non-Gaussianity and the NRAO VLA Sky Survey. *ApJ*717:L17–L21, 1003.3451

Xia JQ, Viel M, Baccigalupi C, De Zotti G, Matarrese S, Verde L (2010c) Primordial Non-Gaussianity and the NRAO VLA Sky Survey. *ApJ*717:L17–L21, DOI 10.1088/2041-8205/717/1/L17, 1003.3451

Xia JQ, Baccigalupi C, Matarrese S, Verde L, Viel M (2011) Constraints on primordial non-Gaussianity from large scale structure probes. *Journal of Cosmology and Astro-Particle Physics*8:033, 1104.5015

Yokoyama S, Soda J (2008) Primordial statistical anisotropy generated at the end of inflation. *Journal of Cosmology and Astro-Particle Physics*8:5, DOI 10.1088/1475-7516/2008/08/005, 0805.4265

York DG, et al (2000) The Sloan Digital Sky Survey: Technical Summary. Astron J 120:1579–1587, DOI 10.1086/301513, astro-ph/0006396

Zaldarriaga M (2004) Non-Gaussianities in models with a varying inflaton decay rate. Phys Rev D69:043,508, astro-ph/0306006

Zel'dovich YB (1970) Gravitational instability: An approximate theory for large density perturbations. A&A5:84–89

Zentner AR (2007) The Excursion Set Theory of Halo Mass Functions, Halo Clustering, and Halo Growth. International Journal of Modern Physics D 16:763–815, DOI 10.1142/S0218271807010511, arXiv:astro-ph/0611454

Zhan H (2006) Cosmic tomographies: baryon acoustic oscillations and weak lensing. *Journal of Cosmology and Astro-Particle Physics*8:008, DOI 10.1088/1475-7516/2006/08/008, astro-ph/0605696

Zhan H, Tyson JA (2017) Cosmology with the Large Synoptic Survey Telescope. ArXiv e-prints 1707.06948